

Notice 1

Under the Copyright Act 1968, this thesis must be used only under the normal conditions of scholarly fair dealing. In particular no results or conclusions should be extracted from it, nor should it be copied or closely paraphrased in whole or in part without the written consent of the author. Proper written acknowledgement should be made for any assistance obtained from this thesis.

Notice 2

I certify that I have made all reasonable efforts to secure copyright permissions for third-party content included in this thesis and have not knowingly added copyright content to my work without the owner's permission.

A Study of Nanomaterials Enhanced Epoxy as Adhesives for CFRP-Steel Bonding

HAYDAR FALEH

B.Sc Eng (1st class, Honours)

M.Sc (1st class, Honours)

Submitted in total fulfilment of the requirements for the
degree of Doctor of Philosophy

Department of Civil Engineering



MONASH University

Victoria, Australia

January, 2011

DECLARATION

The candidate herein declares that the research work presented in this thesis contains no material which has been accepted for the award of any other degree or diploma in any university or other institutions. I affirm that to the best of my knowledge, the thesis contains no material previously published or written by another person, except where due reference is made in the text in the thesis.

Haydar Faleh

ACKNOWLEDGMENTS

I would like to express my sincere appreciation to my Supervisors Professor Riadh Al-Mahaidi , Dr. Luming Shen and Profwssor Xiao Ling Zhao for their enthusiasm, patience, encouragement and support that kept me working on the right track with a high spirit. Without their continuous inspiration, guidance and advice throughout the entire span of the research project, the work in this thesis would have never been completed.

I gratefully acknowledge Monash University for providing me with a Monash Graduate Scholarship (MGS).

The journey to complete a PhD research project is perilous and fraught with complex problems. One would certainly require sincere assistance from many people in an attempt to complete the journey with success. I express my sincere gratitude to laboratory staff members Long Goh, Alan Taylor and Kevin Nievaart, and of the Civil Engineering Laboratory for their sincere assistance for the experiments. I wish to thank Mr. Alex McKnight and Dr. Con Adam for their help. I would like to thank all the academic and administrative staff in the Civil Engineering Department for their support. The assistance given to me by Jenny Manson, the postgraduate admissions officer, is particularly unforgettable.

I would like to thank all staff and my fellow postgraduates of the Department of Civil Engineering, Monash University, for their friendship, encouragement and support. I

am grateful to my friends Ahmed Al-Shawaf ,Sabrina Fawzia, Mark Sentry and Rawaa Al-Safi for their support in different aspects of the experiments.

I am indebted to my wife Saja for her endless patience, sacrifice, and understanding.

Finally I remain indebted to “Allah” who made my research easy for me during my whole candidature.

SUMMARY

The successful retrofitting of steel structures by using CFRP significantly depends on the performance and integrity of the CFRP-steel joints, and the effectiveness of the adhesive used. However, the adhesives are usually much weaker than the adherents they join. To improve bonding performance, one possibility is to consider toughened adhesives. It is a common practice to enhance the epoxy by adding nanoparticles to it. This thesis reports a detailed investigation of infusing different types and amounts of nano-particles onto different adhesives used in CFRP-steel joint.

It is a common practice to use nanoparticles to strengthen polymers in general and adhesives in particular. Literature review shows that sonication is widely used technique to infuse nanoparticles onto composites.

A series of coupons tests was carried out to study the effect of adding different types and percentages of multi wall carbon nan-tubes (MWCNT) and SiC nano-powder on the properties of Araldite-420 and Sikadur-30 adhesives.

Scanning electron microscope was used to evaluate the dispersion of the nanoparticles inside the epoxy. Sonication alone increased the homogeneity of the epoxies and enhanced Sikadur-30 properties with no effect on Araldite-420.

MWCNT increased the strength and elastic modulus for Araldite-420 in different percentages depending on nanoparticles amounts. SiC nanoparticles had no or minor effect on strength and elastic modulus for Araldite-420. Adding nanoparticles to Sikadur-30 had no, or even negative effect, on strength and elastic modulus. The transition glass temperature doesn't affected by adding nanoparticles. Also, test to find the properties of steel and CFRP plates were carried out

Same results were repeated when enhanced epoxies used to attach CFRP plates on steel with single lap joint. 2% MWCNT was the optimum percentage for Araldite-420 joint strength. As the nanoparticles percentages reach the optimum values, the failure mode changed from epoxy failure to a delamination failure.

Photogrammetry technique were used to calculate strains on the top of CFRP bond length and compared with classical strain gages. Due to its simplicity and efficiency, photogrammetry was adopted to collect the strain along bonding length.

The delamination failure type of the CFRP-steel joint, which include full separation of particle complicated. A mesh-less simulation method called material point method, easily simulates the exact shape of failure with reasonably good prediction of experimental results.

The simulation method was verified with the results from experimental tests carried out in this research as well as tests available in the literature. The model predicts the ultimate load, displacements and strain distribution reasonably well. Also, using this method provide the ability to study the effect of loading rate on CFRP-steel joints.

Finally, a bond slip model and bond stress values for different percentages and types of nanoparticles were conducted for better understanding of bonding mechanism.

Table of Contents

Declaration	ii
Acknowledgments	iii
Summary	v
Table of Contents	vii
List of Figures	xii
List of Tables	xx
List of Publications	xxi

Chapter One: Introduction

1.1 Background	1
1.2 Nanomaterial CFRP composites	2
1.3 The aim the research	4
1.4 Structure of the thesis	5

Chapter Two: Literature Review

2.1 Introduction	7
2.2 CFRP in Construction	8
2.2.1 Background	8
2.2.2 Advantages and disadvantages of CFRP strengthening	9

2.2.3 Behaviour of CFRP with different element materials	10
2.2.4 Adhesive thickness and nature	11
2.2.5 Properties and Types of the CFRP	12
2.2.6 CFRP joints validation and types	13
2.2.7 Failure types of CFRP-steel joints	17
2.3 Carbon nano tubes (CNT)	18
2.3.1 Background and history	18
2.3.2 CNT nature	19
2.3.3 CNT properties	21
2.3.4 CNT manufacturing methods	26
2.3.4.1 Arc-discharge	27
2.3.4.2 Laser-ablation	28
2.3.4.3 Chemical vapour deposition (CVD)	30
2.3.5 CNT functionalization	32
2.3.5.1 Non-covalent attachment	33
2.3.5.2 Covalent attachment	33
2.3.6 SiC nanoparticle	34
2.3.6.1 SiC fabrication methods	35
2.4 Nanoparticles enhancing polymers	37
2.4.1 Mixing methods	38
2.4.1.1 Challenges of mixing process	39
2.4.1.2 Ultrasonic mixing	41
2.4.1.3 High shear mixing	44
2.4.1.4 Three mill way	45
2.4.1.5 Chemical modification	46
2.4.2 Effects of nano-particles on epoxy properties	47
2.5 Using nanoparticles to enhance FRP systems	53
2.5.1 Introduction	53
2.5.2 Multiscale composite fabrication methods	54

2.6 Material Point Method	58
2.6.1 Background	58
2.6.2 MPM fundamentals	59
2.6.3 Why MPM?	60
2.6.4 Application of material point method in engineering	61
2.7 Summary	63

Chapter Three: Material Properties

3.1 Introduction	64
3.2 Nanoparticle Additives to the Epoxy	
3.2.1 Background	65
3.2.2 Adhesive property	65
3.2.3 Nano-additives types	66
3.2.4 Mixing method	68
3.2.5 Effect of Sonication on the epoxies	71
3.2.6 Araldite-420 enhanced by MWCNT	73
3.2.7 Sikadur-30 enhanced by MWCNT	80
3.2.8 SiC-epoxy composites	82
3.2.9 Dispersion analysis	90
3.2.10 Glass transition temperature tests	92
3.3 Carbon fibre reinforced polymer	97
3.3.1 General	97
3.3.2 Measured properties of CFRP	98
3.4 Measuring properties of steel	101
3.5 Summary	103

Chapter Four: Experimental investigation of CFRP-steel joint using different nanoparticles enhanced epoxy

4.1 Introduction	104
4.2 Specimens materials, preparation and testing setup	105
4.3 Evaluation of testing setup	108
4.4 Strain calculation method Photogramatry	109
4.4.1 Introduction	109
4.4.2 Principles and component of Photogrammetry system	111
4.4.3 Comparing Photogrammetry and strain gages results	113
4.5 Effect of mixing method	117
4.6 Effect of adding nanoparticles	124
4.6.1 Effect of MWCNT	125
4.6.2 Effect of different type of MWCNT	132
4.6.3 MWCNT specimens failure	136
4.7 Effect of Adding SiC	137
4.8 Summary	147

Chapter Five: A Model-Based Simulation of CFRP-Steel Bond Failure Using the Material Point Method

5.1 Introduction	149
5.2 Material point method	150
5.2.1 Background	150
5.2.2 MPM governing equations and their weak forms	151
5.3 MPM Evaluation	158
5.3.1 Pre-tested Specimens Simulation	158
5.3.2 Simulation results	161

5.3.2.1 Bond length effect	161
5.3.2.2 Loading rate effect	172
5.4 MPM simulation of different epoxies specimens	177
5.5. Summary	184

Chapter Six: Nanomaterial Enhanced CFRP-steel systems Bond Slip Models

6.1 Introduction	186
6.2 MPM simulation of nanomaterial enhanced specimens	187
6.3 Bond slip model for nanomaterial enhanced specimens	195
6.3.1 Shear stress distribution	195
6.3.2 Bond slip model	200
6.3.3 Bond slip relationship	202
6.4 Summary	206

Chapter Seven Conclusions and Future Work

7.1 Research summary	208
7.2 Conclusions	210
7.3 Future research	213

References	214
-------------------	-----

Appendices	A-1 to A-12
-------------------	-------------

List of Figures

Figure 2.1 CFRP on steel plate (Miller et al., 2001)	14
Figure 2.2 Double-lap joint	14
Figure 2.3 Compression shear lap tests (El Damatty and Abushagur,2003)	15
Figure 2.4 Single lap joint (Xia and Teng,2005)	16
Figure 2.5 Disc pull-off and torsional test	16
Figure 2.6 Failure types of CFRP-steel joints	17
Figure 2.7 different types of carbon forms(Lau and Hue, 2002)	20
Figure 2.8 Tensile loading for individual MWCNT and loading stages (Yu et al,2000a)	24
Figure 2.9 TEM image and computer simulation for MWCNT buckling(Iijima et al., 1996)	25
Figure 2.10 Schematic illustration of the arc-discharge technique (Saito et al. 1996)	27
Figure 2.11 Schematic of the laser ablation process (Collins and Avouris,2000)	29
Figure 2.12 Schematic for CVD process	32
Figure 2.13 Ultrasonic Mixing machine	43
Figure 2.14 Three- Roll Mill Machine (Yasmin et al.,2006)	46
Figure 2.15 VARTM procedure scheme and procedure (Bekyarova et al.,2007)	56
Figure 2.16 Deposition of carbon nanotubes on a carbon fibre surface by electrophoresis. (Bekyarova et al., 2007)	58
Figure 3.1 Coupons naming scheme.	68
Figure 3.2 Epoxy coupon Teflon mould	70
Figure 3.3 Adhesive coupon dimensions	70
Figure 3.4 Comparison between three mixing methods of Araldite-420	72
Figure 3.5 Comparison between mixing types of Sikadur-30	73
Figure 3.6 Effect of MWCNT on Araldite-420	74
Figure 3.7 MWCNT effects on Araldite-420 strength	75

Figure 3.8 MWCNT effects on Araldite-420 elastic modulus	76
Figure 3.9 MWCNT particle surrounded by Araldite-420 bundles.	77
Figure 3.10 3 % MWCNT particle surrounded by epoxy bundles.	78
Figure 3.11 Behaviour of MWCNT inside epoxy	79
Figure 3.12 Effect of MWCNT on Sikadur-30	80
Figure 3.13 MWCNT effect on Sikadur-30 strength	81
Figure 3.14 MWCNT effect on Sikadur-30 elastic modulus	82
Figure 3.15 Effect of SiC on Araldite-420	83
Figure 3.16 Effect of SiC powder and vacuuming on Araldite-420	84
Figure 3.17 Effect of SiC on Araldite-420 strength	86
Figure 3.18 Effect of SiC on Araldite-420 elastic modulus	87
Figure 3.19 Effect of SiC on Sikadur-30	88
Figure 3.20 Effect of SiC on Sikadur-30 strength	89
Figure 3.21 Effect of SiC on Sikadur-30 elastic modulus	89
Figure 3.22 Hand-mixed Araldite-420 under SEM	90
Figure 3.23 1% MWCNT embedded in Araldite-420 under SEM	91
Figure 3.24 3% MWCNT embedded in Araldite-420 under SEM	91
Figure 3.25 Dynamic Mechanical Thermal Analysis (DMTA) machine	93
Figure 3.26 $\tan\Delta$ variation with temperature for various MWCNT % in Araldite-420	94
Figure 3.27 $\tan\Delta$ variations with temperature for various MWCNT % in Sikadur-30	94
Figure 3.28 $\tan\Delta$ variations with temperature for various SiC% in Araldite-420	95
Figure 3.29 $\tan\Delta$ variations with temperature for various SiC % in Sikadur-30	95
Figure 3.30 Schematic view of CFRP coupon (not to scale)	99
Figure 3.31 Test set-up on the Shimidzu testing machine	99
Figure 3.32 Failure modes of the CFRP laminate coupon specimens	100
Figure 3.33 Stress strain curve for CFRP laminate and mild steel (measured)	101
Figure 3.34 Strain curve for CFRP laminate in two perpendicular directions	101

Figure 3.35 Tested steel coupon specimen	102
Figure 3.36 Stress-strain curve of the tested steel	102
Figure 4.1 schematic view of a specimen	106
Figure 4.2 Specimen coding scheme	107
Figure 4.3 Top-view for CAH03 specimen	108
Figure 4.4 Strain from top and bottom sides of the specimen	109
Figure 4.5 ARAMIS photogrammetry system	112
Figure 4.6 Specimen fixed to test machine ready for testing with aid of strain gauges and ARAMIS system.	114
Figure 4.7 Strain distribution of CAH01 specimen along CFRP laminate surface by strain gauges and ARAMIS system	115
Figure 4.8 ARAMIS stages for CAH01	115
Figure 4.9 Strain distribution of CAH02 specimen along CFRP laminate surface by strain gauges and ARAMIS system	116
Figure 4.10 ARAMIS stages for CAH02	116
Figure 4.11 Effect of different mixing methods on Araldite-420 pure epoxy	118
Figure 4.12 Failure surface of Araldite-420 pure specimens	119
Figure 4.13 Strain distribution along pure sonicated Araldite-420 specimens	120
Figure 4.14 Effect of different mixing methods on Sikadur-30 pure epoxy	121
Figure 4.15 Failure surface of Sikadur-30 pure specimens	122
Figure 4.16 Strain distribution along pure sonicated and hand-mixed Sikadur-30 specimens	123
Figure 4.17 Effect of adding MWCNT to Araldite-420	126
Figure 4.18 Failure surface of CAC1	127
Figure 4.19 Failure surface of CAC2	128
Figure 4.20 Failure surface of CAC3	129
Figure 4.21 Strain distribution along CAC specimens	131
Figure 4.22 Effect of “NTP” MWCNT type on Araldite-420	133
Figure 4.23 Strain distribution along CACN specimens	133

Figure 4.24 Effect of adding MWCNT to Sikadur-30	134
Figure 4.25 Strain distribution along CSC specimens	135
Figure 4.26 Failure surfaces of CSC specimens	136
Figure 4.27 Effect of different SiC percentages on Araldite-420 specimens	138
Figure 4.28 Failure surface of CAS1	139
Figure 4.29 Failure surface of CAS2 specimens	140
Figure 4.30 Failure surface of CAS3	141
Figure 4.31 Strain distribution along CAS specimens	142
Figure 4.32 Effect of SiC on Sikadur-30	143
Figure 4.33 Failure surface of CSS1	144
Figure 4.34 Failure surface of CSS2	145
Figure 4.35 Failure surface of CSS3 specimens	145
Figure 4.36 Strain distribution along CSS specimens	146
Figure 5.1 Side view of the CFRP-steel double lap joint tested in (Fawzia,2007)	158
Figure 5.2 Schematic of (Fawzia,2007) specimens modelled using the MPM.	159
Figure 5.3 An elasto-plasticity model with linear hardening and softening laws for epoxy layer.	160
Figure 5.4 Linear elasto-plasticity constitutive model for steel and combined CFRP-epoxy layer	161
Figure 5.5.Comparison of load displacement behaviour of bond length 40mm.	162
Figure 5.6.Comparison of load displacement behaviour of bond length 50mm.	162
Figure 5.7.Comparison of load displacement behaviour of bond length 70mm.	163
Figure 5.8 Comparison of load displacement behaviour of bond length 80mm.	163
Figure 5.9 Load displacement behaviour of simulated bond length 90mm	164
Figure 5.10 Load displacement behaviour of simulated bond length 100mm	164
Figure 5.11 Normal strain distribution in the combined CFRP/epoxy layer with bond length of 70mm.	165
Figure 5.12 Normal strain distribution in the combined CFRP/epoxy layer with bond length of 80mm.	165

Figure 5.13 Deformed shapes for 40mm bond length at different times.	166
Figure 5.14 Deformed shape for 50mm bond length at different times	166
Figure 5.15 Deformed shape for 70mm bond length at different times.	167
Figure 5.16 Deformed shape for 80mm bond length at different times.	167
Figure 5.17 Experimental failure mode for 50 and 70 mm bond length (Fawzia,2007)	168
Figure 5.18. Shear stress distribution along 40 mm bond length samples at the failure layer.	169
Figure 5.19. Shear stress distribution along 50 mm bond length samples at the failure layer.	170
Figure 5.20. Shear stress distribution along 70 mm bond length samples at the failure layer.	170
Figure 5.21. Shear stress distribution along 80 mm bond length samples at the failure layer.	170
Figure 5.22 Loading rate effect on the load-deflection curve of 40 mm bonding length	172
Figure 5.23. Deformed shape for 40mm bond length under 20mm/min loading speed at different times	173
Figure 5.24. Deformed shape for 40mm bond length under 200mm/min loading speed at different times	173
Figure 5.25. The effect of loading rate on the load-deflection curve of 50mm bonding length	174
Figure 5.26. The effect of loading rate on the load-deflection curve of 70mm bonding length	174
Figure 5.27. The effect of loading rate on the load-deflection curve of 80mm bonding length	175
Figure 5.28. The effect of loading rate on the load-deflection curve of 90mm bonding length	175

Figure 5.29. The effect of loading rate on the load-deflection curve of 100mm bonding length	175
Figure 5.30 Loading rate effect on various bonding lengths	176
Figure 5.31 Schematic of Chapter four specimens modelled using the MPM.	178
Figure 5.32 MPM modelling compared with experimental results for sonicated-only mixed Araldite-420 specimens	179
Figure 5.33 MPM modelling compared with experimental results for hand-mixed Sikadur-30 specimens	179
Figure 5.34 MPM modelling compared with experimental results for sonication mixed Sikadur-30 specimens	179
Figure 5.35 MPM model failure shape (side view) and failure image(top view) for CAM specimens	180
Figure 5.36 MPM model failure shape (side view) and failure image(top view) for CSH specimens	181
Figure 5.37 MPM model failure shape (side view) and failure image(top view) for CSM specimens	182
Figure 5.38 Normal strain distribution in the CFRP plate surface for CAM specimens.	183
Figure 5.39 Normal strain distribution in the CFRP plate surface for CSH specimens.	183
Figure 5.40 Normal strain distribution in the CFRP plate surface for CSM specimens.	184
Figure 6.1 MPM specimens compared with experimental results for Araldite+1%SiC samples	189
Figure 6.2 MPM-experimental strain distribution on CFRP surface along bonding length for CFRP-Araldite+1%SiC	189
Figure 6.3 MPM specimens compared with experimental results for Araldite+2%MWCNT samples.	190

Figure 6.4 MPM-experimental strain distribution on CFRP surface along bonding length for CFRP-Araldite+2%MWCNT	190
Figure 6.5 MPM specimens compared with experimental results for Sikadur-30+1%SiC samples	191
Figure 6.6 Compared MPM-experimental strain distribution on CFRP surface along bonding length for CFRP-Sikadur-30 +1%SiC	191
Figure 6.7 MPM specimens compared with experimental results for Sikadur-30+2%MWCNT samples	192
Figure 6.8 Compared MPM-experimental strain distribution on CFRP surface along bonding length for CFRP-Sikadur-30 +2%MWCNT	192
Figure 6.9 MPM specimens of oven-vacuumed specimens compared with experimental and MPM results of Araldite-420 +1%SiC	194
Figure 6.10 MPM specimens of oven-vacuumed specimens compared with experimental and MPM results of Araldite-420 +2%SiC	194
Figure 6.11 MPM specimens of oven-vacuumed specimens compared with experimental and MPM results of Araldite-420 +3%SiC	194
Figure 6.12 Shear stress distribution along CFRP bond length of Araldite-420 hand- mixed specimen	197
Figure 6.13 Shear stress distribution along CFRP bond length of Sikadur-30 sonicated-mixed specimen	198
Figure 6.14 Shear stress distribution along CFRP bond length of Araldite-420+ 1%SiC specimen	198
Figure 6.15 Shear stress distribution along CFRP bond length of Araldite-420+ 2%MWCNT specimen	199
Figure 6.16 Shear stress distribution along CFRP bond length of Sikadur-30+ 1%SiC specimen	199
Figure 6.17 Shear stress distribution along CFRP bond length of Sikadur-30+ 2%MWCNT specimen	200
Figure 6.18 Bilinear bond-slip model approximation (Xia and Teng, 2005)	201

Figure 6.19 Comparison of the bond-slip model between CFRP strengthened concrete structure, Lu et al (2005) and steel structure, Xia and Teng (2005)	202
Figure 6.20 Effects of MWCNT percentages on bond-slip relationship of Araldite-420 specimens	203
Figure 6.21 Effects of SiC percentages on bond-slip relationship of Araldite-420 specimens	204
Figure 6.22 Effects of SiC percentages on bond-slip relationship of Sikadur-30 specimens	204
Figure 6.23 Effects of MWCNT percentages on bond-slip relationship of Sikadur-30 specimens	205
Figure 6.24 Effects of different nanoparticle types and percentages on bond strength of Araldite-420 specimens	205
Figure 6.25 Effects of different nanoparticle types and percentages on bond strength of Sikadur-30 specimens	206

List of Tables

Table 2.1 Material properties of different fibre materials	13
Table 2.2 Effects of nano-particles on mechanical properties of epoxies	48
Table 2.3 Effects of nanoparticles on Tg of epoxies	51
Table 3.1 Mechanical properties of adhesives as given by the manufacturer (Huntsman advanced Materials, Sika Australia Pty Ltd)	66
Table 3.2 Coupon samples tests scheme	67
Table 3.3 Tg results for different epoxies and different nanomaterials	96
Table 3.4 Test results of CFRP laminate (BASF Construction Chemicals)	100
Table 4.1 specimen test programme	107
Table 4.2 Ultimate strength of pure epoxy specimens	117
Table 4.3 Ultimate strength of MWCNT specimens	125
Table 4.4 Ultimate strength of new MWCNT type specimens	132
Table 4.5 Ultimate strength of CSC specimens	134
Table 4.6 Ultimate strength of CAS specimens	138
Table 4.7 Ultimate strength of CSS specimens	143
Table 5.1. Mechanical properties for the materials of double lap shear specimens	161
Table 5.2 Comparisons of experimental data and MPM results	164
Table 5.3 Mechanical properties of the materials of single lap shear specimens	177
Table 6.1 Mechanical properties for tested epoxy used in MPM simulation	188
Table 6.2 Mechanical properties of ASO epoxy	193

List of Publications

During my candidature, the following Journal papers were published:

1. Haydar, F., Al-Mahaidi, R., and Shen, L. (2011), "A numerical investigation of CFRP-steel bond failure using material point method", *Advanced Structural Engineering* (Accepted).
2. Haydar, F., Al-Mahaidi, R., and Shen, L. (2011), "Fabrication and mechanical characterization of carbon nanotubes-enhanced epoxy", *Advanced Materials Research* (Accepted).
3. Haydar, F., Al-Mahaidi, R., and Shen, L. (2011), "Fabrication and Characterization of Nano-Particle-Enhanced Epoxy", *Composites Part B*, (Submitted).

During my candidature, the following Conference papers were published:

1. Haydar, F., Al-Mahaidi, R., and Shen, L., "A model-based simulation of CFRP-steel bond failure with material point method", 14th International Conferences on Composite Structures (CICE2006), 19-21 November, 2007, Melbourne, Victoria, Australia.
2. Faleh, H., Al-Mahaidi, R. And Shen, L., "Simulation of bond behaviour between CFRP and steel using the material point method", First scientific conference on nanotechnology, advanced materials and their applications, 13-14 Oct, 2009, University of Technology, Baghdad, Iraq.
3. Haydar, F., Al-Mahaidi, R., and Shen, L., "Fabrication and Mechanical Characterization of Carbon Nanotubes-Enhanced Epoxy" , International conference on structures and building materials (ICSBM 2011), January, 2011, Guangzhou, China

The following papers are under preparation:

1. Haydar, F., Al-Mahaidi, R., and Shen, L. (2011), "CFRP-steel joints using different nanoparticle-enhanced epoxies: experimental investigation", *Composites Part B*.
2. Haydar, F., Al-Mahaidi, R., and Shen, L. (2011), "CFRP-steel joints using different nanoparticle-enhanced epoxies: numerical model", *Composites Part B*.

Chapter One

Introduction

1.1 Background

As the number of defective structures and structures requiring rehabilitation has increased around the world, new strategies and practices are necessary to deal with the demand for remediation .

Steel bridges were among the structures most recommended for improvement based on the National Bridge Inventory (NBI) report (Klaiber et al, 1987). Design errors, sub-standard materials, poor workmanship and lack of proper maintenance are the main factors that contribute to the weakening of structures, potentially leading to serious damage and in the worst case, to collapse. Without appropriate remediation, such bridges may have inadequate capacity to carry legal traffic loads and be load-restricted or even require replacement (Giancaspro et al, 2009). In Australia, more than 50 % of bridges are now more than 60 years old, and most of these bridges are estimated to be inadequate, particularly those already damaged (Al-Mahaidi, 2002).

Replacement of part of the structure is often not economically feasible. Indeed, conventional methods of reinforcement and repair are costly, time-consuming, not aesthetic and may not provide effective results. Whilst the addition of an external strengthening member to these structures is a common practice, this technique has many disadvantages when using heavy and bulky materials. Due to their low weight-to-strength ratio, easy handling requirements, and their compatibility with different

materials, carbon fibre-reinforced polymers (CFRPs) have become more widely-used than heavy and bulky steel plates in retrofitting old or damaged steel structures.

Multi-functionality has been a focus of rehabilitation technology in recent decades, and design parameters such as mass reduction with increased system efficiency demand multifunctional approaches.

However, with our continuing quest for lighter and stronger composites, the demand for new types of materials is increasing. No longer can traditional fibrous composites fulfil our stringent requirements, nor can they be engineered at the continuum level, which controls properties at the molecular or atomic level.

Therefore, this thesis argues that “multi-scale” rehabilitation approaches should be developed to make use of developments in nano-phase enhancing technology.

1.2 Nano-material CFRP composites

Since the discovery of the strongest ever material known by mankind in 1991, the applications of carbon nano-tubes have been extended and stronger, tougher and lighter composites have been developed. Nano-crystalline materials are exceptionally strong, hard, and ductile at high temperatures, wear-resistant, corrosion-resistant, and chemically very active.

Unfortunately, to date these superior properties of nano-particles could not be used directly in a separate material. The only practical way to transfer their very valuable properties to other materials has been to add them as fillers to enhance the properties of composites.

These composites are now being considered for a wide range of applications including packaging and coating in the electronics, automotive and aerospace industries. While

nano-particles have attractive attributes, their usage in structural composites which are relatively large in dimension is almost non-existent (Chisholm et al, 2005).

The evolution of construction materials has required civil engineers to combine such materials into their construction or rehabilitation, projects. The main application in civil engineering for nano-particles is to add them as fillers in structural adhesives.

The emerging use of nano-fillers in conventional CFRPs introduces the possibility of improving the already high mechanical efficiency in CFRPs rehabilitation techniques. However, the transfer of the properties of nano-particles to CFRP rehabilitation systems is limited by the amount of nano-particles inside the composite. The extensive surface area of nano-particles plays a major role in transferring their great properties to the surrounding composite. However, the high surface area encourages these nano-particles to agglomerate, thus preventing them from spreading in high percentages inside composites. Therefore, it is essential to spread these particles inside composites without creating agglomeration to make full use of their superior properties.

Most past simulations of CFRP system behaviour (Fawzia et al., 2006; Wu et.al., 1998; Rahimi and Hutchinson, 2001) have been conducted using the Finite Element Method (FEM) to model the failure stages. However, the FEM is a mesh-based method and may have difficulties in modelling the transition from continuous to discontinuous failure mode involved in the process of CFRP delamination from the steel plate. Therefore, the Material Point Method (MPM), which is a mesh-less method that does not employ fixed mesh connectivity, is adopted in the present study to model the discontinuous failure of the CFRP-steel bond.

1.3 The aim the research

For the last 10 years, many attempts have been made to combine nano-particles and CFRP (Hsiao et al ,2003 ; Qiu et.al 2007). None have used these systems in actual structures.

The major component of the present study is therefore to study the effects of adding different nano-particles to different structural epoxies used to attach CFRP plates to steel plates.

The outcome of this study will contribute the establishment of basic knowledge of how nano-particles affect the behaviour of CFRP-steel systems, and the ultimate joint capacities with different types and percentages of nano-particles. This knowledge will be used to establish appropriate guidelines for the use of nano-particles in CFRP-steel joint systems. In particular, the aims of this thesis are:

1. To experimentally investigate the effect of using the ultra-sonication mixing method on the strength, elastic modulus and glass transition temperature of structural adhesives.
2. To experimentally investigate the effect of different nano-particles at different percentages on the strength, elastic modulus and glass transition temperature of different structural adhesives.
3. To study the effect of different nano-particles at different percentages in different adhesives on the bond behaviour between steel and CFRP plates, the strain distribution along and across the bond length, and on bond and shear stress slip relationships.

4. To develop numerical models using MPM for single lap joints to increase the knowledge of CFRP-steel system behaviour through different loading stages up to failure, and to validate the model by experimental results.
5. To establish a model using MPM to identify the effects of loading rate and bond length on the ultimate strength of double-lap CFRP-steel specimens.
6. To propose a suitable bond-slip model for different enhanced epoxy specimens based on the experimental studies.

1.4 Structure of the thesis

This thesis comprises seven chapters. The content of these chapters is outlined in this section.

Chapter 2 is an overview of CFRP composites and the nano-particles usually used to enhance these composites. The importance of the strengthening of steel structures and key issues affecting this process are outlined. The types of nano-particles, their properties, the synthesis process, the various different mixing methods used to infuse them in composites and their challenges are briefly discussed in this chapter. The effects of adding nano-particles to composites, specially CFRP systems, are also reviewed. This chapter also focusses on modelling the failure of CFRP-steel systems and explains how a mesh-free simulation method like MPM has many advantages over the traditional finite element method.

Chapter 3 presents an investigation of the material properties of different adhesives enhanced by different types and percentages of nano-particles. The effects of different

preparation methods are reported in this chapter. The results of tests under tension of steel and CFRP plate coupons are also provided.

Chapter 4 presents an experimental investigation of the bond behaviour of CFRP plates attached to steel plates using various types and percentages of nano-particles in single lap joints. The test specimen configurations, instrumentation, test set-up and test results are described. The results include the failure modes, load carrying capacity and strain distribution along bonding length using photogrammetry techniques.

Chapter 5 evaluates MPM by means of its governing equations and a series of double-lap CFRP-steel samples tested by previous researchers. A parametric study of the effect of different bonding lengths and loading rates for double lap CFRP-steel samples is reported in this chapter.

Chapter 6 is concerned with the simulation of nano-particle-enhanced samples using MPM. The MPM results are validated with the experimental results obtained in Chapter Four. Results of shear strength tests along the bonding length and bond-slip models for different types and percentages of nano-particles are presented in this chapter.

Finally, Chapter 7 presents the conclusions drawn from the findings of this research, including the experimental investigations and numerical analyses. It also discusses research recommended for further investigation.

Chapter Two

Literature Review

2.1 Introduction

Their high strength-to-weight ratio, excellent corrosion resistance, relatively low preparation and application costs and superior fatigue life time make carbon fibre-reinforced polymers (CFRPs) an excellent choice for the retrofitting and rehabilitation of defective steel structures.

CFRP patches work perfectly to a certain loading limit. To increase this limit, the strengthening of the joining adhesives is a practical option. The addition of fillers such as nano-particles is a very common technique to enhance epoxy properties(Chisholm et al., 2005;Zhu et al., 2004)

Most past simulations of CFRP system behaviour (Fawzia et al., 2006; Wu et.al., 1998; Rahimi and Hutchinson, 2001) have used the Finite Element Method (FEM) to model the failure stages. The FEM is a mesh-based method and may have difficulties in modelling the transition from continuous to discontinuous failure mode involved in the process of CFRP delamination from the steel plate. Therefore, the Material Point Method (MPM), which is a mesh-less methods that does not employ fixed mesh connectivity, is adopted in the present study to model the discontinuous failure of CFRP-steel bonds.

The literature review is presented in three main sections. The first section provides an overview of CFRP-steel retrofitting systems and demonstrates the importance of the

strengthening of steel structures, provides details of strengthening materials and different tests procedures, and explains the advantages of using epoxy attached joints. The second section reviews the nano-particles used to enhanced epoxies, their types, properties, synthesis techniques, and methods of blending them into the epoxy, the effects of these additives on epoxies and on CFRP composites. Finally, a review of a mesh-free simulation method used to model CFRP-steel systems is discussed, including a historical timeline, its most common usages and the advantages of this method over mesh-based methods.

2.2 CFRP in Construction

2.2.1 Background

As the first decade of the 2nd millennium finished, the number of highly deficient structures was rapidly increasing. These structures varied from infrastructure, bridges, and other types of structures including, in some cases, significant historical buildings.

Structures, specially bridges, suffer from increased traffic volumes and loads, diminished capacity through environmental degradation and age, more stringent design code regulations. The need for major retrofitting in some parts of the world has necessitated the repair and rehabilitation of existing infrastructure (Al-Mahaidi and Hii,2007).

As it is time-consuming and expensive to replace these structures, it is essential to develop low-cost and convenient solutions to lengthen the useful life of these structures by strengthening and rehabilitation. However, the requirement to ensure the safety of civil infrastructure necessitates the assurance of integrity and service-life durability of

any rehabilitation procedure. In the case of bonded repair of metallic systems, there is thus a need for the continuous in-service assessment of bond performance and integrity under various harsh environmental and load conditions (Matta et al., 2006).

Many strengthening solutions have been successfully implemented to upgrade steel members to increase their working life by increasing their capacity or reducing stress levels in areas of stress concentration within those members.

2.2.2 Advantages and disadvantages of CFRP strengthening

The addition of members, external supports, increasing member cross-sections, post-tensioning or attachment of external laminates, are among the most common methods to rehabilitate defective members.

Although all these methods perform well technically, they are costly, time-consuming and have some drawbacks in terms of optimisation of structural behaviour. Other prime disadvantages include the following:

- The heavy weight of additional members requires the use of extensive and complex scaffolding and adds extra dead load that may necessitate additional calculations.
- Steel patches are very weak against corrosion and fatigue failure.
- Installation requires the use of heavy equipment and machinery, and the implementation of time-consuming and labour-intensive procedures. In addition, the installation process includes welding which may create residual stress and damage in the member.

Therefore, many different types of patches have been used to overcome these shortcomings. Since its first use, carbon fibre-reinforced polymer (CFRP) has become a preferred method to strengthen structures.

2.2.3 Behaviour of CFRPs with different element materials

CFRPs are widely used for the strengthening of concrete structures and extensive research has already been conducted (see, for example Teng and Lam,2004; Rizkalla et al., 2003; Al-Mahaidi and Hii,2007; and Pham and Al-Mahaidi,2004). These studies build on general theories of how CFRPs perform when used in the strengthening of concrete elements.

When CFRP is used to strengthen steel elements, many concerns should be taken into consideration if the developed CFRP-concrete theories are to be used:

- The elongation of CFRP is less than 10% of that of steel but in the same order as that of concrete.
- The tensile strength of adhesive is much less than that of steel, whereas that of adhesive is much larger than that of concrete. Therefore, CFRP-concrete debonding failure is caused by concrete fracture, whereas debonding in CFRP-steel tends to be at the interface between the CFRP and steel plate.
- Welding is often used to join steel members but this method is not applicable to concrete.

The blind application of existing theories from CFRP-concrete systems to CFRP-steel systems may result in unsafe structures.

The steps to prepare steel surfaces prior to the application of CFRP composites are similar to those used to prepare concrete surfaces in terms of surface abrasion and surface cleaning. Surface preparation of the steel must be undertaken to ensure complete chemical bonding between the steel and the adhesive. This typically involves the removal of surface paint, mill scale, rust and surface cleaning. The most effective way of achieving a chemically-active surface is by chemical and mechanical cleaning. Chemical cleaning includes cleaning the surface with acetone and chemicals that can dissolve the rust without harsh effects on the steel surface. However, environmental constraints may limit the use of such solvents.

Mechanical cleaning includes removing the inactive oxide and hydroxide layers on the surface of the steel by cutting and deformation of the base material. Sand blasting should be carried out until a “white metal” surface with a rough texture is achieved. To minimize oxidization and re-contamination of the cleaned surface, application of the CFRP should take place as soon as possible after the surface preparation.

2.2.4 Adhesive: thickness and nature

As CFRP composites are non-metallic materials, this restricts the attachment methods to metallic (and non-metallic surfaces) to mechanical attaching (net or rivets) or adhesives. Adhesive joints have the advantages of low cost, flexibility to create complex joints, distribution of the stress over the attached area, and avoidance of thermal distortion related to the welding process.

To achieve the required properties of the epoxy, the application procedures should be strictly followed. Researchers report premature failure in CFRP-steel systems

(Tavakkolizadeh and Saadatmanesh,2003), or even the same performance as bare steel samples due to improper mixing ratio (Jones and Civajan,2003).

The disadvantages of adhesive joints include the difficulty of investigating them, the effects of thermal cycling and high humidity and temperature on strength, and the special surface treatment necessary. Therefore, shear strength and bond durability are major concerns in choosing the adhesive process.

The adhesive transfers the stress from the structural element to the CFRP. Therefore, to prevent stress concentration inside the adhesive, the thickness should be between 0.5 and 2mm. The appropriate adhesive thickness can be achieved using specially-shaped trowels to spread the adhesive onto the surfaces. Bond line spacer beads can also be mixed with the adhesive or attached to the metal surface to achieve the desired bond line thickness (Photiou et al., 2006)

2.2.5 Properties and Types of CFRP

CFRP composites are commonly used in two forms: CFRP plates and CFRP sheets. The mechanical properties of CFRPs commercially available for civil engineering applications compared with other fibre materials are shown in Table 1. To confirm these properties, the ASTM:D 3039 procedures have been conducted by various researchers(Moy, 2001;Fawzia et al.,2005).

Table 2.1 Material properties of different fibre materials

	Carbon fibre			Aramid fibre	E-glass fibre
	High-strength (HS)	High-modulus (HM)	Ultra-high modulus (UHM)		
Modulus of Elasticity (GPa)	230-240	295-390	440-640	125-130	70-85
Tensile strength (MPa)	4300-4900	2740-5940	2600-4020	3200-3600	2460-2580
Strain to failure (%)	1.9-2.1	0.7-1.9	0.4-0.8	2.4	3.5
Density (kg/m³)	1800	1730-1810	1910-2120	1390-1470	2600
Coefficient of thermal expansion (parallel to fibre), (x 10⁻⁶/°C)	-0.38	-0.83	-1.1	2.1	4.9

2.2.6 CFRP joint validation and types

Before a bonding system can be used with confidence, it is necessary to undertake an experimental validation of the effectiveness of the joining technique to be used in practice. These experimental joints check the bonding strength between CFRP and the steel, and determine the best epoxy thickness, bonding length, and the failure type that the joint will suffer.

On-site tests should be simple and can conduct the data directly. Therefore, three types of testing system have been adopted:

- Loading is directly applied to steel element.
- Loading is directly applied to CFRP.
- Pull-off adhesive testing.

Many arrangements have been adopted to test CFRP joints by applying force through the steel plate.

The first arrangement, as can be shown in Figure 2.1, is CFRP attached to continuous steel plate (Miller et al., 2001), which can be considered as strengthening rather than bonding between steel and CFRP. Study of the bond behaviour is not easy in this arrangement because the steel plate may yield before debonding occurs.



Figure 2.1 CFRP on steel plate (Miller et al., 2001)

Another arrangement which has been used widely is shown in Figure 2.2 and consists of double-lap joints (Fawzia et al., 2006; Al-Shawaf et al., 2006; Lenwari et al., 2002; Schnerch et al., 2004; Lam and Cheng, 2004; Colombi and Poggi, 2006; Tavakkolizadeh and Saadatmanesh, 2003; Jones and Civjan, 2003; Hollaway and Cadei, 2002). The uncertainty of the location of debonding failure makes observation and the experimental instrument more complicated. Fawzia et al, (2006) therefore used unequal bond length to force the debonding failure to occur in the shorter bond length.

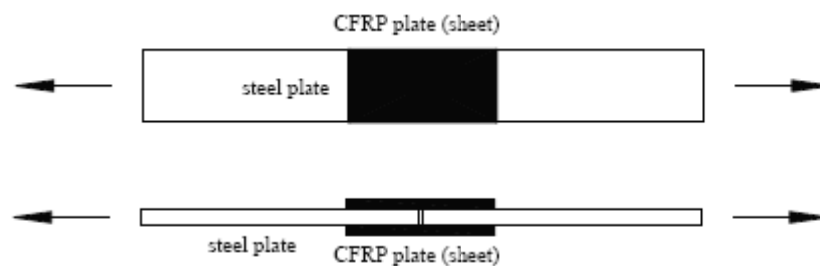


Figure 2.2 Double-lap joint

El Damatty and Abushagur (2003) tested compressive formation by applying force through the CFRP attached to a square hollow section as shown in Figure 2.3. The CFRP plate may locally fail in compression testing due to the small compressive strength of the CFRP plate compared with its high tensile strength.

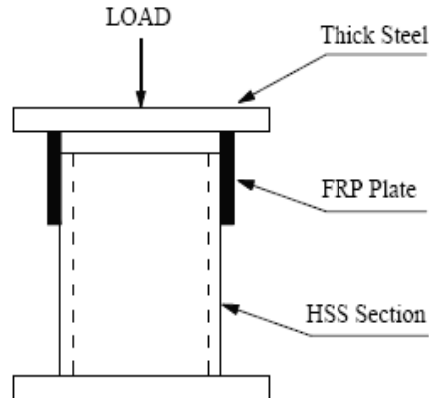


Figure 2.3 Compression shear lap tests (El Damatty and Abushagur,2003)

In their single-lap joint testing Jiao and Zhao (2004) and Xia and Teng (2005) applied tensile force to CFRP plates directly as shown in Figure 2.4. This method gives a better lock in the joint and provides direct indications regarding the bond strength. However, the application of the force to the CFRP directly requires additional attention to the CFRP end grippers, which is very difficult if CFRP-sheets are used. This method is widely used to study the bond behaviour of CFRP and concrete. Special preparations should be made to ensure that no moment is created through the loading process.

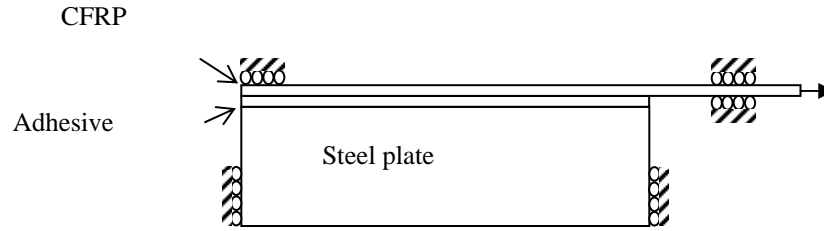


Figure 2.4 Single lap joint (Xia and Teng,2005)

Figure 2.5 shows another type of test adopted to test CFRP bond strength by use of a disc pull-off test. Torsion is applied to a disc attached on a CFRP surface attached to a steel surface. This method can be considered as a prediction of the condition of the CFRP-steel joint through the greatest perpendicular force that a surface area can withstand in tension before a plug of material is detached, or whether the surface remains intact at a prescribed force.

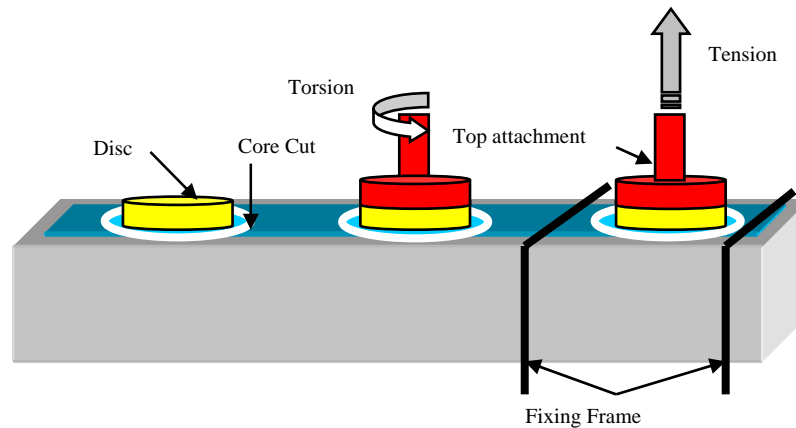


Figure 2.5 Disc pull-off and torsional test

Of the above test types, the double lap joint test is the most convenient type for a study focussed on joint behaviour.

2.2.7 Failure types of CFRP-steel joints

Depending on adhesive thickness, CFRP elastic modulus and strength, bond length, and the surrounding environment, many failure schemes have been reported for CFRP-steel joints:

- Steel and adhesive interface failure.
- Adhesive layer failure.
- CFRP plate and adhesive interface failure.
- CFRP plate delamination.
- CFRP plate rupture.
- Steel yielding.

Thickness and type of adhesive will control failure mode (Xia and Teng,2005). Figure 7 summarises these failure types.

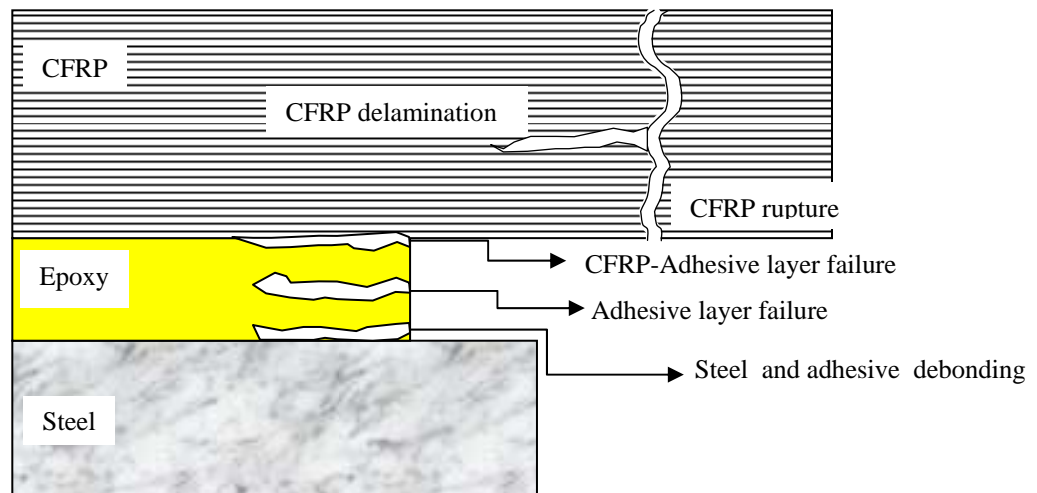


Figure 2.6 Failure types of CFRP-steel joints

Failure will occur in the adhesive if a thin adhesive layer used, and delamination if a thicker layer is used. Also, if the CFRP layer has a high elastic modulus, the CFRP tends to rupture instead of a combination of adhesive and rupture failure if a normal elastic modulus CFRP is used (Jiao and Zhao,2004).

2.3 Carbon nano-tubes (CNT)

2.3.1 Background and history

In the mid 1980s, Smalley and co-workers at Rice University developed the chemistry of fullerenes and were awarded the Nobel Prize for their discovery. Fullerenes are geometric cage-like structures of carbon atoms that are composed of hexagonal and pentagonal faces. The first closed, convex structure formed was the C₆₀ molecule. Named after the architect known for designing geodesic domes, R. Buckminster Fuller, Buckminster fullerene is a closed cage of 60 carbon atoms where each side of a pentagon is the adjacent side of a hexagon similar to a soccer ball and the C₆₀ molecule is often referred to as a Bucky ball(Mraz,2005).

A few years later, their valuable work led Iijima(1991) to the first observation of multiwalled carbon nano-tubes (MWCNT), and the synthesis of single-walled carbon nano-tubes (SWCNT) by (Iijima and Ichlhashi,1993 and Bethune et al,1993) working independently.

The discovery of carbon nano-tubes(CNT) in the last decade of the past century does not mean that that did not exist and be used previously. A 2006 study published in National Geographic (Inman,2006)determined that some carbon nano-tubes are present in

Damascus steel, possibly helping to account for the legendary strength of the ancient swords made of it.

CNT are long, slender fullerenes where the walls of the tubes are hexagonal carbon graphite structures, often capped at each end. These cage-like forms of carbon have been shown to exhibit exceptional material properties that are a consequence of their symmetric structure.

Due to the valuable mechanical properties of the CNT, a variety of structures has been proposed, ranging from everyday items like clothes and sports gear to combat jackets and smart weapons.

2.3.2 The nature of CNTs

CNTs are often visualized as looking like rolls of graphite chicken wire, but actually, CNTs are part of the fullerene family; they are essentially Buckyballs expanded from the centre into cylinders.

Unlike diamonds, where a 3-D diamond cubic crystal structure is formed with each carbon atom having the four nearest neighbours arranged in a tetrahedron, graphite is formed as a 2-D sheet of carbon atoms arranged in a hexagonal array. The properties of nano-tubes depend on their atomic arrangement (how the sheets of graphite are 'rolled'), the diameter and length of the tubes, and their morphology, or nano-structure.

Heptagons allow for concave areas within the nano-tube. Thus, the heptagonal defects in nano-tubes can result in many possible equilibrium shapes. Indeed, most nano-tubes are

not straight cylinders with hemispherical caps. Figure 2.7 shows different types of carbon forms.

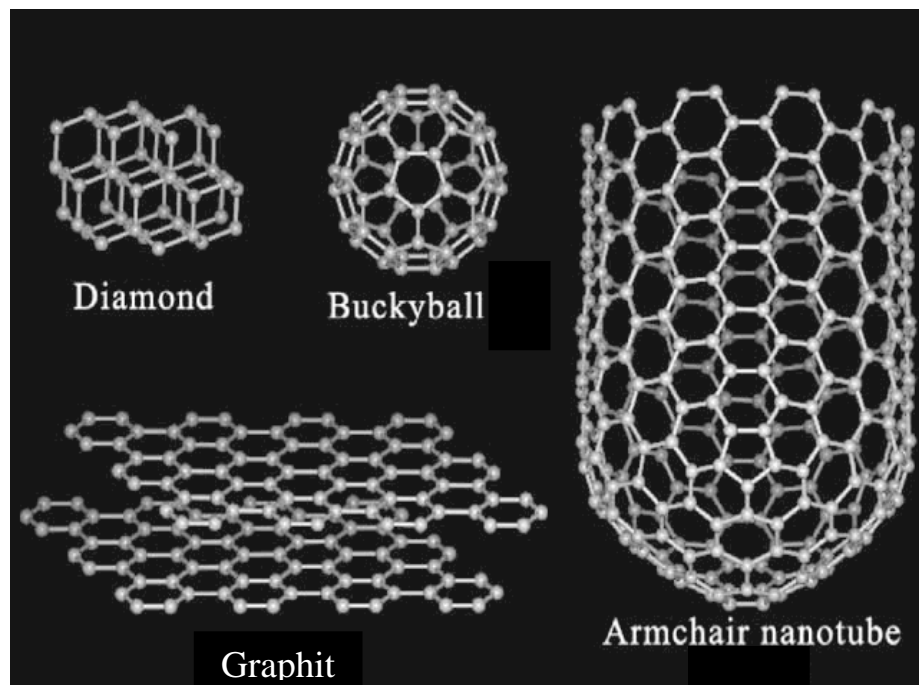


Figure 2.7 different types of carbon forms(Lau and Hue, 2002)

CNTs exist as either single-walled or multi-walled structures:

Single-Walled Carbon Nano-tube (SWCNT) is a one-atom thick sheet of graphite rolled up into a seamless cylinder with a diameter in the order of a nanometre. This results in a nano-structure in which the length-to-diameter ratio exceeds 1,000,000.

Multi-Walled Nano-tubes (MWCNT) consist of multiple layers of graphite rolled in on themselves to form a tube shape. These concentric nano-tubes are held together by secondary, van der Waals bonding. MWCNT are several microns in length and 5–50 nm in diameter depending on the number of layers.

Due to their structural perfection and strong carbon-carbon bonds, CNTs are expected to have excellent mechanical properties.

2.3.3 CNT properties

Since their first observation nearly two decades ago by Iijima, (1991), CNTs have been the focus of considerable research. Many researchers have reported mechanical properties of CNTs that exceed any previously known materials. Indeed, if the reported mechanical properties are accurate, CNTs may result in an entire new class of advanced materials.

Significant challenges exist in both the micro-mechanical characterization of nano-tubes and the modelling of the elastic and fracture behaviour at the nano-scale.

Any characterization process of nano-tubes or their composites faces many challenges.

These challenges include

- complete lack of micro-mechanical characterization techniques for direct property measurement,
- uncertainty of data obtained from indirect measurements,
- remarkable limitations on specimen size, and

- inadequacy in test specimen preparation techniques and lack of control in nanotube alignment and distribution.

Although there are varying reports in the literature on the exact properties of CNTs, theoretical and experimental results show extremely high elastic modulus, greater than 4 TPa (the elastic modulus of diamond is 1.2 TPa) and reported strengths 10–100 times higher than the strongest steel at a fraction of the weight(García et al .,2007). Since CNTs have a low density for a solid of 1.3-1.4 g/cm³(Collins and Avouris 2000) , their specific strength of up to 48,000 kN·m/kg is the best of known materials, compared to high-carbon steel's 154 kN·m/kg.

In addition to the exceptional mechanical properties associated with CNTs, they also possess superior thermal and electric properties, being thermally stable up to 2800 °C in vacuum, having thermal conductivity about twice as high as diamond, and electric-current-carrying capacity 1000 times higher than copper wires (Collins and Avouris, 2000).

Experimental methods for the measurement of the mechanics of individual CNTs include

- measuring the lateral bending of suspended MWCNTs (Salvetat et al,1999) or of SWCNT ropes (Walters et al,1999) with atomic force microscopy (AFM).
- measuring axial compression with tapping-mode AFM, and examining the pattern of mechanically deformed MWCNTs in polymer composites with a transmission electron microscope (TEM) (Lourie et al,1998).

- observing the thermally-induced or electric field-induced vibration of “cantilevered” nano-tubes inside a TEM. (Treacy et al.,1996; Poncharal et al.,1999)

Axial elastic modulus values ranging from 200 to 4000 GPa, combined with average bending strength of 14 GPa and axial compressive strengths of 100 GPa for MWCNTs, with strain at failure of 0.05 for SWCNT ropes were obtained from the above-mentioned studies.

Wong et al., (1997) were the first to perform direct measurement of the stiffness and strength of individual, structurally-isolated MWCNT using AFM. The nano-tube was pinned at one end to molybdenum disulfide surfaces and load was applied to the tube by means of the AFM tip. The bending force was measured through the displacement along the unpinned length, and a value of 1.26 TPa was obtained for the elastic modulus. The average bending strength measured was 14.2-8 GPa.

Yu et al, (2000a) applied the force to the MWCNT by a manipulation tool that can also be used as a mechanical loading device. The AFM probes used in testing CNTs provide a sharp end for picking up and mounting each nano-tube and they act as force sensors by imaging of the cantilever deflection. The individual CNTs were picked up and then attached at each end of a section length onto the opposing tips of AFM cantilever probes. Each nano-tube section was then stress-loaded and observed in situ in the TEM. By recording the whole tensile loading experiment, both the deflection of the soft cantilever and the length change of the nano-tube were simultaneously obtained. Figure 2.8 shows the loading mechanism and stages of MWCNT. The experimentally-calculated tensile

strengths of the outermost layer ranged from 11 to 63 GPa and the elastic modulus ranged from 270 to 950 GPa.

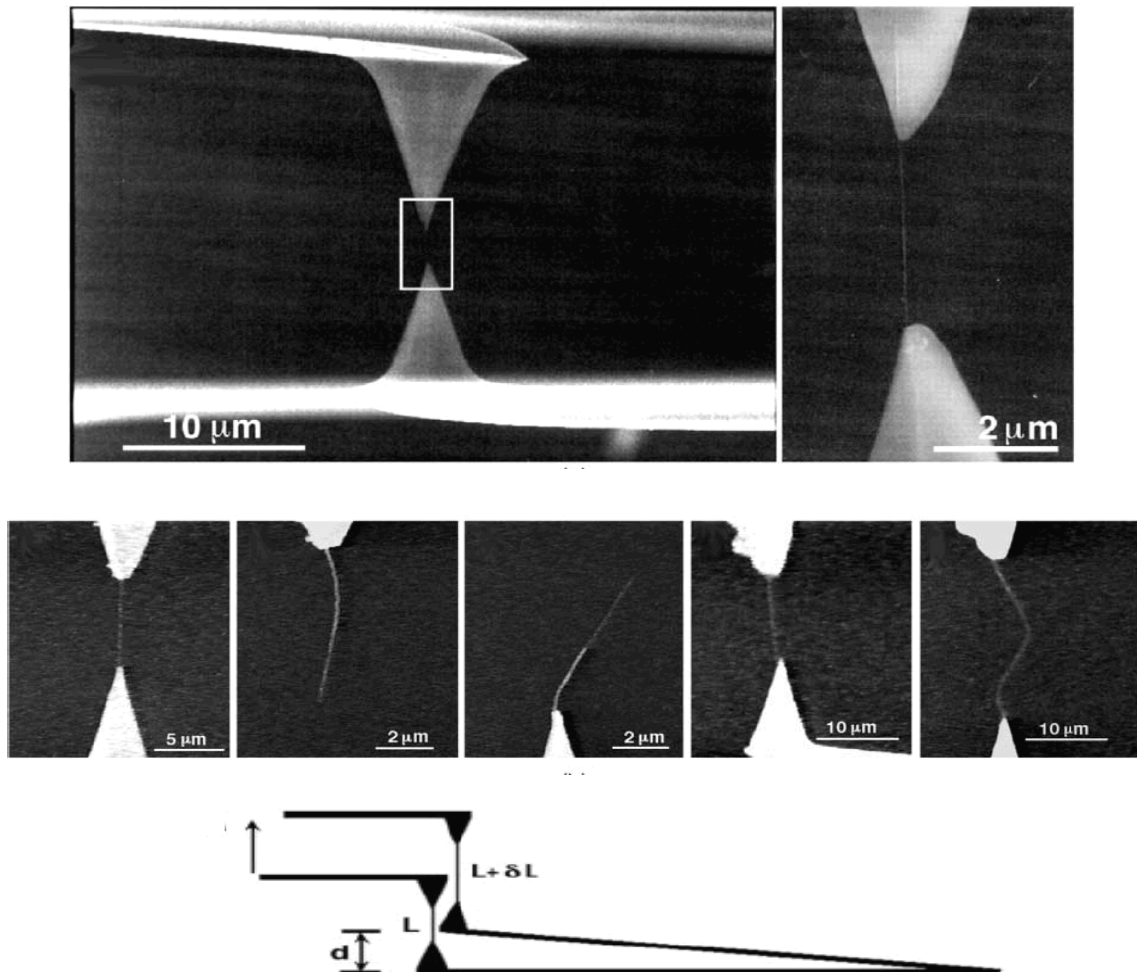


Figure 2.8 Tensile loading for individual MWCNT and loading stages (Yu et al,2000a)

Xie et al., (2000) also tested ropes of MWCNT in tension. The tensile strength and modulus were 3.6 and 450 GPa, respectively. In their subsequent investigation of SWCNT ropes, Yu et al., (2000b) assumed that only the outermost tubes assembled in the

rope carried the load during the experiment, and they calculated tensile strengths of 13 to 52 GPa and average elastic moduli of 320 to 1470 GPa.

Lu (1997), adopted an empirical lattice dynamics model to predict the elastic properties of SWCNT. His study suggested that elastic properties are insensitive to different combinations of parameters, such as tube radius and number of layers. Also, the elastic properties are the same for all nano-tubes with a radius larger than one nm. The predicted Young's modulus was about 1 TPa, the shear modulus up to 0.45 TPa, and the bulk modulus 0.74 TPa.

In addition to their experimental observations, Iijima et al., (1996) examined the flexibility of nano-tubes under compression using molecular dynamic simulations. Their experimental and theoretical results show that nano-tubes are remarkably flexible. The bending is completely reversible up to angles in excess of 110° , despite the formation of complex kink shapes, as shown in Figure 2.9.

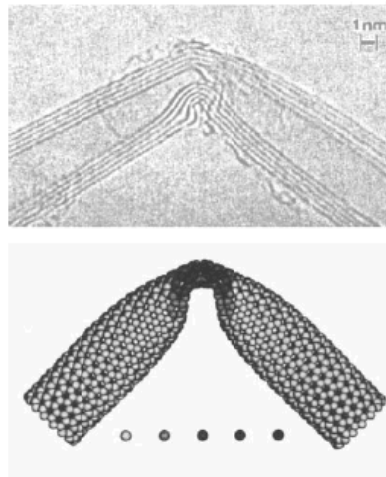


Figure 2.9 TEM image and computer simulation for MWCNT buckling(Iijima et al., 1996)

It is suggested that, unlike the strongly anisotropic thermal expansion in conventional carbon fibres and graphite, the thermal expansion of CNT is essentially isotropic. However, the thermal conductivity of nano-tubes is believed to be highly anisotropic, and its magnitude along the axial direction is perhaps higher than that of any other material.

Dramatic recent advances have fuelled speculation that nano-tubes will be useful for downsizing circuit dimensions. For example, current-induced electro-migration cause's conventional metal wire interconnects to fail when the wire diameter becomes too small. The covalently bonded structure of CNT militates against similar breakdown of nano-tube wires, and because of ballistic transport, the intrinsic resistance of the nano-tube should essentially vanish. (Liang et al.,2001 and Yao et al ,2000)

Experimental results show that metallic SWCNTs can carry up to 10^9 A/cm², whereas the maximum current densities for normal metals are 10^5 A/cm² (Liang et al., 2001;Yao et al., 2000). Unfortunately, the ballistic current-carrying capability is less useful for presently- envisioned applications because of necessarily large contact resistances. Contacting all layers in a MWCNT could reduce this contact resistance, but it cannot be totally eliminated(Baughman et al., 2002).

2.3.4 CNT manufacturing methods

Today, there are around 44 producers worldwide of CNT products ranging from SWCNT to nano-fibres. All the types of CNTs are produced mainly by three techniques: arc-discharge (Iijima,1991), laser-ablation (Rinzler et al., 1998), and catalytic growth from

carbon monoxide and chemical vapour deposition (CVD) from hydrocarbon methods (Inami et al., 2007)

2.3.4.1 Arc-discharge

Iijima (1991) first observed nano-tubes synthesized from the electric-arc discharge technique. Shown schematically in Figure 2.10, the arc discharge technique generally involves the use of two high-purity graphite rods as the anode and cathode.

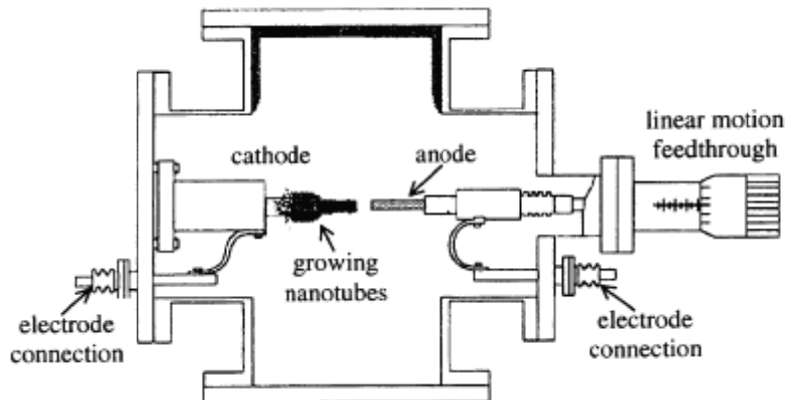


Figure 2.10 Schematic illustration of the arc-discharge technique (Saito et al. 1996)

The pure graphite rod, used as anode, is drilled and filled with graphite and Y-Ni alloy powder. The cathode is a sharp ended, pure graphite rod. The rods are brought together under a helium atmosphere of a 500 Torr pressure and a voltage of 40 A d.c is applied until a stable arc is achieved.

After the arc discharge, most of the soot condenses on the inner wall of chamber and forms a thick cloth-like film. The cloth-like soot is collected and dispersed in ethanol.

The build-up consists of an outside shell of fused material and a softer fibrous core containing nano-tubes and other carbon particles. The exact process variables depend on the size of the graphite rods. As the anode is consumed, a constant gap between the anode and cathode is maintained by adjusting the position of the anode.

To achieve SWCNT, the electrodes are doped with a small amount of metallic catalyst particles (Iijima et al., 1993; Bethune et al., 1993; Shi et al., 2000; Saito and Nishikubo 1996 among others).

2.3.4.2 Laser-ablation

Laser ablation was first used for the initial synthesis of fullerenes. The first attempt to produce MWCNT by laser was by Gue et al., (1995a), who were producing various metal molecules by blasting metals using lasers. They changed the metal to graphite and the results were MWCNT. Later that year the same team added different metal particles to the graphite catalyst (the best yield was from a cobalt and nickel mixture) to synthesize SWCNT (Gue et al., 1995b). Over the years, the technique has been improved to allow the production of SWCNT (Rinzler et al., 1998; Zhang and Iijima, 1999).

To produce CNT by this technique, a graphite target doped with cobalt and nickel catalyst (Rinzler et al., 1998) is vaporized by a pulsed laser in a high-temperature reactor, while an inert argon gas is bled into the chamber. The nano-tubes develop on the cooler surfaces of the reactor as the vaporized carbon condenses. A water-cooled surface may be included in the system to collect the nano-tubes. The laser ablation method can produce more homogenous products compared with the arc-discharge method.

The general set-up for laser ablation is shown in Figure 2.11.

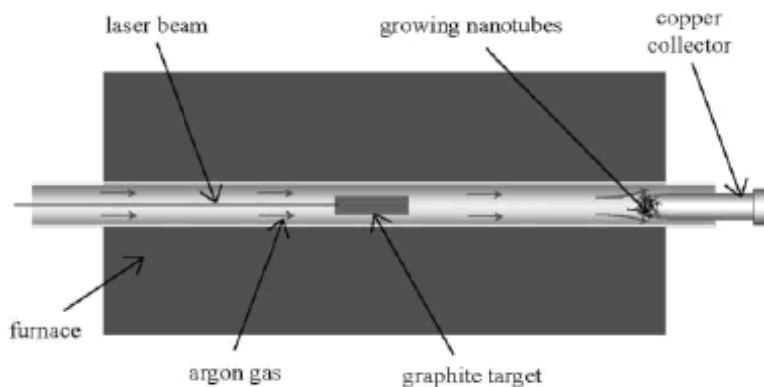


Figure 2.11 Schematic of the laser ablation process (Collins and Avouris,2000)

Zhang and Iijima (1999) developed a model to explain the CNT formation process in the laser ablation method. In this model, carbon species are first ablated from the target and form a plasma zone. The plasma then begins to cool down through expansion. Finally, carbon species are further cooled down by collision with argon gas until a thermal dynamic equilibrium is established. The CNTs are believed to form in the second step where the plasma zone is still dense and hot.

The high temperature of 1200 °C restricts the cooling rate of carbon species, and thus sustains the necessary kinetic energy for them to decompose into precursors and to arrive at the growth site of nano-tubes.

2.3.4.3 Chemical vapour deposition (CVD)

All currently known synthesis methods for CNTs result in major concentrations of impurities, which are typically removed by acid treatment. These treatments may introduce other impurities, degrade nano-tube length and perfection, and add to costs. Another problem, especially for electronic devices, is that the usual synthetic routes result in mixtures of various semi-conducting and metallic nano-tubes.

These limitations have motivated the development of gas-phase techniques, such as chemical vapour deposition (CVD), in which nano-tubes are formed by the decomposition of a carbon-containing gas. Of the various means for nano-tube synthesis, CVD shows the most promise for industrial-scale deposition. Since the carbon source is continually replaced by flowing gas, the option of continuous production is offered. In addition, CVD is capable of growing nano-tubes directly on a desired substrate, whereas the nano-tubes must be collected in the other growth techniques. The growth sites are controllable by careful deposition of the catalyst. The final purity of the as-produced nano-tubes can be quite high, minimizing subsequent purification steps.

During CVD, a substrate is prepared with a layer of metal catalyst particles, most commonly nickel, cobalt (Inami et al., 2007), iron, or a combination (Ishigami et al., 2008). These particles increase the surface area for higher yield of the catalytic reaction of the carbon feedstock with the metal particles.

The diameters of the nano-tubes that are to be grown are related to the size of the metal particles. This can be controlled by patterned (or masked) deposition of the metal,

annealing, or by plasma etching of a metal layer. The substrate is heated to approximately 700°C.

To initiate the growth of nano-tubes, two gases are bled into the reactor: a process gas (such as ammonia, nitrogen or hydrogen) and a carbon-containing gas (such as acetylene, ethylene, ethanol or methane). Nano-tubes grow at the sites of the metal catalyst; the carbon-containing gas is broken apart at the surface of the catalyst particle, and the carbon is transported to the edges of the particle, where it forms the nano-tubes. The catalyst particles can stay at the tips of the growing nano-tube during the growth process, or remain at the nano-tube base, depending on the adhesion between the catalyst particle and the substrate.

Figure 2.12 shows a scheme for the CVD process. One issue in this synthesis route is the removal of the catalyst support via an acid treatment, which sometimes could destroy the original structure of the carbon nano-tubes. However, alternative catalyst supports that are soluble in water have proven effective for nano-tube growth.(Eftekhari et al., 2006)

If plasma is generated by the application of a strong electric field during the growth process (plasma-enhanced CVD), then the nano-tube growth will follow the direction of the electric field (Ren et al., 1998).

Nikolaev et al. (1999) describe the gas-phase growth of SWCNT with carbon monoxide as the carbon source. Catalysts for SWCNT growth form in situ by thermal decomposition of iron pentacarbonyl in a heated flow of carbon monoxide at pressures of 1–10 atm and temperatures of 800–1200°C.

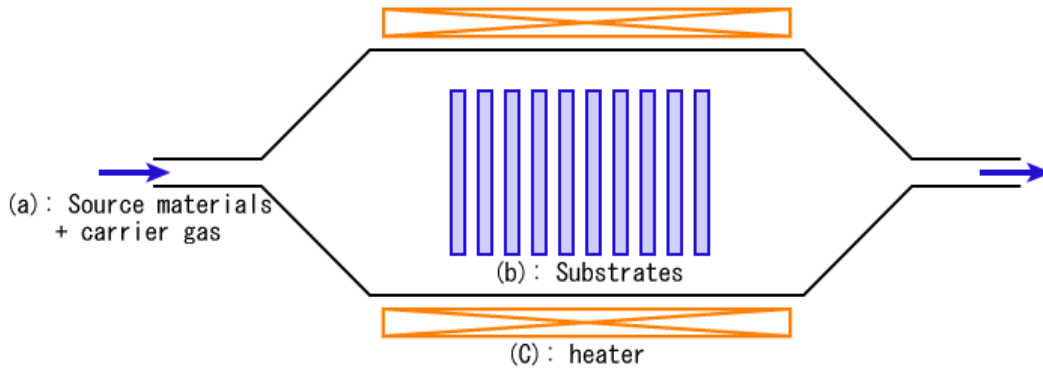


Figure 2.12 schematic for CVD process

2.3.5 CNT functionalization

The manufactured CNTs usually contain agglomerate structures that can be very difficult to breakdown physically. There are regions with more CNTs, and regions with fewer CNTs . More CNTs are observed within agglomerates. What is observed in the mechanical properties, when CNT works as reinforcement, reflects the average containing contributions from the whole sample (Gong et al., 2000).

Van der Waals forces work as intermolecular interactions, which encourage the formation of agglomerates. When mixed into an epoxy resin, these large agglomerates considerably increase the viscosity of the compound. After functionalization, which is modifying the surface of the CNT by adding a chemical group, the CNT surfaces are partly polarised so that the resin can more easily penetrate into the agglomerates and individualise the CNTs. Nevertheless, the matrix cannot properly wet the individualised CNTs because of their non-polar surfaces. Therefore, the CNTs re-agglomerate, but with a modified structure (Jacobs et al., 2006).

Two main approaches are considered for the surface modification of CNTs:

- (1) non-covalent attachment of molecules;
- (2) covalent attachment of functional groups to the walls of the nano-tubes.

2.3.5.1 Non-covalent attachment

Non-covalent attachment is based mainly on van der Waals forces, and is controlled by thermodynamic criteria (O'Connell et al., 2001). Non-covalent attachment, which for some polymer chains is called wrapping, can alter the nature of the CNT's surface and make it more compatible with the polymer matrix.

Chemical oxidation and amine treatment are the techniques used to achieve this attachment. The CNTs are opened at the end and the terminal carbons are converted to carboxylic acids by oxidation in concentrated sulphuric and nitric acids.

2.3.5.2 Covalent attachment

This type of functionalization includes gas plasma treatment. Plasma treatment is a useful method because it permits the fixation of different chemical groups on the surface. Moreover, this kind of treatment is used to modify the surface without changing the characteristics of CNTs. It can be carried out by applying cold gas plasma for a short period of time. The plasma is also known as glow discharge plasma, which is obtained when the gas is exposed to an electromagnetic field of radio frequencies at low temperature and low pressure (Zhang et al., 2009).

The advantage of non-covalent attachment is that as the perfect structure of the nano-tube is not altered, its mechanical properties should not change. The main potential disadvantage of non-covalent attachment is that the forces between the wrapping molecule and the nano-tube may be weak, thus if used as a filler in a composite the efficiency of the load transfer may be low. The boiling in nitric acid damages the outer graphite layers and produces notches.

The covalent attachment of functional groups to the surface of nano-tubes can improve the efficiency of load transfer. However, it must be noted that these functional groups may introduce defects on the walls of the perfect structure of the nano-tubes. These defects will lower the strength of the reinforcing component. Therefore, there will be a trade-off between the strength of the interface and the strength of the nano-tube filler. (Eitan et al., 2003)

Qiu et al, (2007) functionalized MWCNTs by strong acid oxidation. MWCNTs were added to a mixture of concentrated nitric acid and sulphuric acid, shaken in an ultrasonic water bath and refluxed for 30 min. After cooling, the mixture was washed with distilled water on a sintered glass filter until the washings showed no acidity.

2.3.6 SiC nano-particles

Silicon carbide (SiC) is a compound of silicon and carbon. found naturally in a mineral phase of the extremely rare mineral moissanite. Bulk SiC is known as a ceramic material with high hardness, wear resistance, high temperature stability, and chemical inertness.

Due to its high abrasion resistance, SiC powder has been mass-produced since 1893 for use as an abrasive.

Covalent ceramic materials like SiC have been recognized as potential candidates for structural applications because of their superior mechanical properties (strength, stiffness and hardness), chemical properties (oxidation and corrosion resistance) and thermal stability at high temperatures (Yong and Hahn, 2004).

2.3.6.1 SiC fabrication methods

The conventional method for the production of SiC is the Acheson process, in which carbo-thermic reduction of silicon dioxide (SiO₂) by carbon is carried out at temperatures ranging from 2000 to 3000 °C for about one week (Krstic, 1992). SiC powders derived from this process have large particle size because of the high reaction temperature and long reaction time. Therefore, extensive milling is needed to convert the as-synthesized products to sinterable powders with particle sizes ranging from a few micrometers to sub-micrometers.

Many other methods can be used to produce SiC powders, including arc-discharge (Seeger et al., 2000), carbo-thermal reduction (Shen et al., 2006), and chemical vapour deposition (Borowiak-Palen et al., 2005). Of the possible preparation methods, self-propagation high-temperature synthesis (SHS) is considered to be an attractive method due to its proven advantages: lower energy requirement, simpler and cheaper equipment, higher product purity, and finer and well-sintered starting powders.

However, the synthesis of SiC from Si and C elements by the SHS process cannot be realized under normal combustion conditions. The reason is that the Si/C system has a low adiabatic combustion temperature of 1327°C–1427°C. Therefore, an additional energy source is required for the Si/C system to realize the SHS reaction. Much research has been carried out on the provision of the additional energy source, such as adding chemical promoter (Yang et al., 2007a) using microwave energy (Peng et al., 2001) or carrying out preheating treatment (Yang et al., 2007b and Larpiattaworn et al., 2006, among others)

The major part of the fabrication process is carried out at high temperatures, 1200–1250°C. Borowiak-Palen et al. (2005), used a shape memory synthesis method, in which CNTs (as templates) react with silicon (produced by the disproportionation reaction of a SiO vapour). These researchers produced SiC nano-tubes based on a high-temperature (1350 °C) and high vacuum reaction between silicon powder and 15-50 nm diameter MWCNT. The source of silicon was silicon powder.

Kinemuchi et al. (1997) used a carbon-coated Si_3Ni_4 powder to thermally decompose CH_4 gas. The SiC particles had less than 50 nm diameter in a relatively cheap method. 900°C was used to ease the decomposition process.

Yang et al., (2007a) used a mechanical activation process to produce SiC powder with an average size of 0.5-1 μm . Silicon powders, carbon black polytetrafluoroethylene powders and NH_4Cl powders were mechanically milled using steel balls as the milling media. The mixture was loosely packed in a graphite crucible which was then placed in a SHS

reactor. Evacuation was performed up to a vacuum. The powder mixture was then ignited with a tungsten coil by passing a 15A electrical current through it.

2.4 Nano-particle-enhanced polymers

Over the years, many attempts have been made to modify epoxies by adding either rubber particles (Imanaka et al., 2003; Chikhi et al., 2002) or fillers (Xian et al., 2006; Vasconcelos et al., 2005) to improve the composite properties of the polymers.

The fibre-like structure of CNTs makes them particularly attractive for reinforcement of composite materials. Great progress has been achieved in the development of epoxy-based nano-composites with nano-particles as a reinforcing structural element. The keys for such development are the usage of different epoxy resins, types and percentages of nano-particles, and different processing techniques and parameters.

The dispersion of nano-particles, that restricts the mobility of polymer chains under loading, improves the modulus and strength at small loadings. The high aspect ratio, high modulus, the strength of nano-particles, and good interfacial adhesion between the nanoparticles and matrix also contribute to the reinforcement. However, the contribution is restricted by the degree of dispersion of the nanoparticles across the polymer and the existence of aggregates inside the composites. Therefore, the dispersion method and its effectiveness are vital in any attempt to reinforce polymers using nano-particles.

2.4.1 Mixing methods

The transition from micro to nano-particles leads to changes in their physical as well as chemical properties. These changes include increases in the ratio of the surface area to volume. Although large surface area is a desirable property for nano-particles, and is necessary for its work as an interface for stress transfer, this property undesirably induces strong attractive forces between the nano-particles themselves, leading to excessive agglomeration behaviour.

Moreover, if the centre of the nano-particles is close to the radius of gyration of the polymer bundles, the number of atoms at the surface will increase significantly. This in turn will enhance the reactivity between the particle and the polymer. More reactivity will translate into increased changes in polymer properties such as cross-linking, rate of cure, and other thermal properties. If the dispersion level is low, this association will increase nano-particle size, and create larger agglomerates that decrease the mobility of the polymer molecules, increase nano-particle suspension viscosity and even prevent the completion of the polymerization process. This leads to problems in blend dispersion, workability, and, consequently, in composite manufacturing. Therefore, the incorporation of CNT as reinforcement in polymers will enhance the mechanical properties of the polymers but it will also modify their processing behaviour (Visco et al., 2009).

Although the state of dispersion is one of the most important issues, there is no reasonable method to evaluate it over the whole specimen. In most research efforts, optical microscopic, scanning electron microscopic, and transmission electron microscopic image-analysis have been employed to qualitatively assess the state of

dispersion. However, these methods cannot yield the overall dispersion since the images show only very small fractions of the sample's cross-section (Kim et al., 2009b)

2.4.1.1 Challenges of mixing process

Since the first successful attempt to disperse MWCNT into epoxy resin in 1998 (Scadler et al., 1998), strong interfacial bonding has been found to be a necessary condition to obtain full advantage of the extraordinary properties of nano-materials for the reinforcement of composites.

All previous studies indicate that as nano-particle concentrations decrease, more uniform dispersal is achieved, while higher concentrations tend to disperse and form a network because of increased nano-particle self-interactions (Lozano et al., 2001).

To characterize the dispersion quality, two major aspects should be considered: particle size distribution and homogeneous spatial distribution (Gojny et al., 2005).

First, exfoliation of the nano-particles, i.e. the gradual separation of individual nano-tubes from agglomerates, has to be achieved, which is highly dependent on the chosen dispersing method and the processing parameters applied.

In a common milling technique, separation of particles is achieved in a top-down approach by breaking up larger particles. Nano-particle processing needs a non-destructive dispersing method to maintain a minimal critical fibre length, which is necessary in order to preserve efficient load transfer within the composite material.

Because of their pseudo-aromatic C–C bonds, CNTs show only low reactivity with other chemical agents, but due to van der Waals interactions they show a distinct tendency to form aggregates. These strong intrinsic van der Waals forces oblige CNTs to hold together as ropes and bundles with a very low solubility in most solvents, which leads to poor dispersion when mixed into a polymer matrix.

To gradually separate the individual CNTs from agglomerates, the CNTs are usually added to a solvent such as chloroform (Wang and Qui, 2009), ethanol (Song and Youn, 2005; Wang et al., 2008; Ma et al., 2007), acetone (Kim et al., 2009b; Ganguli et al., 2006) to de-agglomerate the CNTs from each other.

After their synthesis, CNTs are usually obtained as mechanically-entangled solid bodies or subsequently associate themselves into aggregates (Nadler et al., 2008). To remove the unwanted amorphous carbon and metal catalyst, acids like sulphuric acid or nitric acid (Wang et al., 2008) or even a combination of acids (Guo et al., 2007), have been mixed with CNTs in different concentrations.

The second issue in the development of nano-particle/polymer composites is the interfacial adhesion between the nano-particles and the matrix polymer. A sufficient stress transfer from the matrix to the tubes is required to efficiently exploit the potential of CNTs as structural reinforcement. Moreover, the atomically smooth surface of nano-tubes and the lack of interfacial bonding limit load transfer from the polymer matrix to the nano-tubes.

The rigorous mixing of nano-particles with resin produces highly reactive volatile vapour bubbles at the initial stage of the reaction between resin and hardener. If these bubbles are

not removed, they detrimentally affect the properties of the final product by creating voids. Therefore, vacuuming should be applied until all bubbles are completely removed.

The nano-particle dispersion on other epoxy parts such as resin (Song et al.,2005,Wang et al., 2008, Chisholm et al., 2005,Nhuapeng et al., 2008) or the curing agent (Wang and Qui,2009)depends on the reactivity to the mixing method.

There are various techniques to disperse the nano-materials homogeneously throughout the epoxy:

- Ultrasonic mixing
- High Shear mixing
- Chemical mixing and modification

2.4.1.2 Ultrasonic mixing

Many researchers (Nhuapeng et al., 2008; Nadler et al.,2008; Kim et al.,2009a; Ganguli et al., 2006 ; Zhou et al., 2007; Eskin,2001; Niyogi et al., 2003;Chisholm et al., 2005, among many others) have used this method to distribute nano-particles into polymers due to its simplicity compared with other methods.

A pulsed ultrasound separates the nano-particles within agglomerates and disperses them in the matrix effectively. However, this method is only manageable for small batches due to the extreme reduction of the vibrational energy with increasing distance from the ultrasound probe.

In this method, the application of alternating acoustic pressure above the cavitation threshold creates numerous cavities in the liquid. Some of these cavities oscillate at a frequency of the applied field (usually 20 kHz) while the gas content inside these cavities remains constant. However, some other cavities grow intensely under tensile stresses while yet another portion of these cavities which are not completely filled with gas start to collapse under the compression stresses of the sound wave. In the latter case, the collapsing cavity generates tiny particles of “debris” and the energy of the collapsed cavity is transformed into pressure pulses. It is noteworthy that the formation of the “debris” further facilitates the development of cavitation. It is assumed that acoustic cavitation in liquids develops according to a chain reaction. Therefore, individual cavities on real nuclei develop so rapidly that within a few microseconds an active cavitation region is created close to the source of the ultrasound probe. The development of cavitation processes in the ultrasonically processed melt creates favourable conditions for the intensification of various physio-chemical processes. Acoustic cavitation accelerates heat and mass transfer processes such as diffusion, wetting, isolation, dispersion and emulsification. Recently it has been reported that there is a clear acceleration of polymer reaction under ultrasound in both catalysed and un-catalysed reactions (Price,2003). Figure 2.13 shows an ultrasonic probe mixing machine.



Figure 2.13 Ultrasonic Mixing machine

In general, use of ultra-sonication enhances the homogeneity of the epoxy by helping the epoxy components to mix molecules together and format reactive species, which ultimately leads to increased cross-linking in the polymer. This effect is more prominent when each of the highly reactive surfaces of the nano-particle is efficiently coated with epoxy resin and reacts with the hardener of the resin. (Chisholm et al., 2005; Visco et al., 2009)

Parameters affecting the dispersing result are energy input, power density, ultrasonic frequency, temperature and viscosity of the fluid, and colloidal stability.

The time for the sonication varies from 10 min (Chen et al., 2007a), 30 min (Kim et al., 2009a; Chisholm et al., 2005; Rodgers et al., 2005), 1hr (Song et al., 2008; Song and Youn, 2005; Zhou et al., 2007; Ma et al., 2007), 2hrs (Wang et al., 2008), 3hrs (Wang and

Qui , 2009; Nhuapenget al., 2008) and up to 4hrs (Guo et al., 2007). Intense sonication varies from 12W to 30-40W (Wang and Qui,2009) and up to 600W(Guo et al., 2007).

In order to avoid a temperature rise during the sonication process, external cooling is employed by submerging the beaker containing the mixture in an ice bath. (Kim et al., 2009a; Chisholm et al., 2005; Zhou et al., 2009). Another technique to control mixing temperature is to stop sonication every certain period to allow the heat energy to disperse. These periods depend on the polymer viscosity and the safe temperature range. Sonication usually varies from 3s on, 1s off (Kim et al., 2009b) , 30 s on, 15 s off(Chen et al., 2007a) and 25s on, 50s off (Zhou et al., 2009; 2007).

The polymer temperature is controlled through the mixing period and is not allowed to exceed 80°C (Song and Youn, 2005;Zhou et al, 2009;2007), or 100°C(Song et al., 2008).

However, ultrasound should be avoided after activation of the CNTs in concentrated nitric acid. It is suspected that this pre-treatment causes some damage in the outer shells of the CNTs, and that the high stress fields in the sonication process cause partial fracture of the pre-damaged CNTs(Lu et al., 1996; Shelimov et al., 1998; Zhang et al., 2001).

2.4.1.3 High shear mixing

Stirring is a common technique used to disperse particles in different matrices such as colour pigments for cosmetics or lacquers, and can also be used to disperse nanoparticles, but with higher shear forces to achieve a fine dispersion. The size and shape of the propeller and the mixing speed control the dispersion result (Sandler et al., 1999).

For the efficient manufacture of larger amounts of nano-composites, many researchers have adopted high shear mixing to disperse nano-particles in epoxy (Gojny and Schulte, 2004; Gojny et al., 2005; 2006; Wichmann et al., 2006; Kostopoulos et al., 2009; Thostenson and Chou, 2002, among others) .

In this method, a dual asymmetric centrifuge (Chen et al., 2007a), or a three-roll mill (Yasmin et al., 2003;2006), is used to mix the nano-particles into the hardener or the resin. The stirrers rotate at a high speed of 2000rpm(Wang and Qui,2009; Barrau et al, 2005), 3000rpm(Chen et al., 2007a; 2007b) 3500rpm(Ganguli et al., 2006) for different times from 15 min up to 1hr for the main mix(Barrau et al., 2005). During mixing, the sample is exposed to high shear forces and impacts, while only little air is introduced into the mixture. Due to the elevated temperature created in the epoxy during the high speed process, the properties of the epoxy may be affected. (Lozano et al., 2001).

2.4.1.4 Three-roll milling

The three-roll mill is an alternative dispersing method commonly used in the ink and electronic industries and has been successfully used to disperse CNTs in epoxy (Gojny et al., 2004; Thostenson and Chou, 2006b).

Shear forces are applied to the agglomerates while they are passing through the gap between two rolls rotating in opposite directions with different velocities. Unlike stirring, that can cause breakage of individual tubes (Andrews et al., 2002), this method has little destructive effect on the CNTs. Relevant processing parameters are the viscosity of the

fluid, and the gap width and velocity of the rolls. The dwell time of each batch of suspension on the rolls is in the range of minutes.

A first primary dispersion of the agglomerates is performed in the knead vortexes, whereas the final distribution of the nano-particles occurs in the thin gap between the rolls(Fiedler et al., 2006). The gap between the rolls usually ranges around 5 μm and the velocity of the three rolls ranges from 20/60/180 rpm resulting in roller circumferential speeds of 8.4×10^{-2} / 2.5×10^{-1} / 7.5×10^{-1} m/s. To ensure that each agglomerate passes the gap at least once per processing step, the mixing process is usually done in discontinuous mode. Figure 2.14 shows a three mill machine. However, mixing nano-particles with epoxy resin using this method will produce a foamy and viscous solution that makes degassing quite difficult.

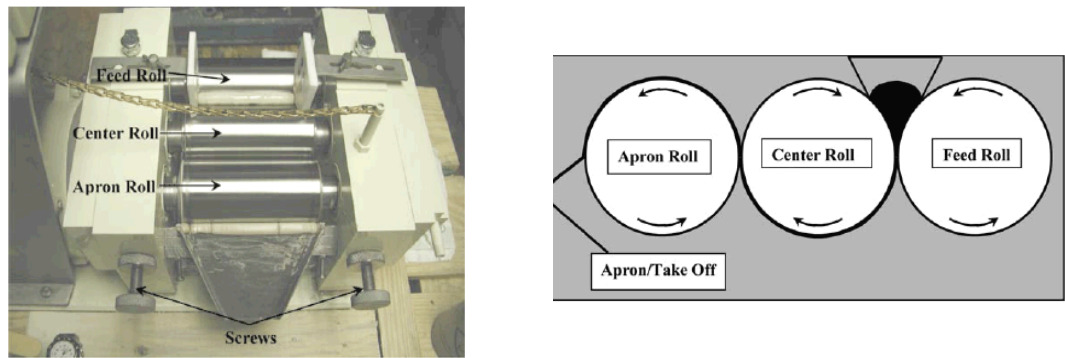


Figure 2.14 Three- Roll Mill Machine (Yasmin et al., 2006)

2.4.1.5 Chemical modification

The chemical methods are aimed at creating surface functionalities on CNTs, thereby improving their chemical compatibility/interactions with a polymer or solvent, leading to enhanced dispersion. The CNTs are dissolved in an organic solvent followed by mixing

with epoxy resin and curing agent. In this system CNTs are covalently integrated into the epoxy and become part of the cross-linked structure rather than remaining a separate component (Zhu et al., 2004). Two major drawbacks in chemical functionalization are recognized:

(1) most methods are aggressive, especially the oxidation process using concentrated acids (Park et al., 2005; Kim et al., 2005), and generate structural defects negatively affecting the intrinsic properties of CNTs;

(2) although some milder functionalization processes have been developed, such as UV/ozone treatment or plasmas (Sham and Kim, 2006; Seo et al., 2005), followed by amine (Sham and Kim, 2006; Gabriel et al., 2006) silane (Ma et al., 2006) or fluorine treatments (Lee et al., 2003), the limited active sites on the CNT surface (mostly at the defects and end caps) may lead to a low efficiency of functionalization, thus slightly altering the dispersibility of CNTs in a polymer (Geng et al., 2008).

2.4.2 Effects of nano-particles on epoxy properties

Advanced composite materials have been developed over the years to satisfy the increased demand for low density high-quality and multifunctional materials. A number of experimental investigations have demonstrated that nano-particles are inherently multifunctional and the addition of nano-particles significantly improves the electrical, thermal, optical and mechanical properties of nano-composites at low concentrations (Qiu et al., 2007) The variation in the extent of improvement may be due to factors such as the state of dispersion of nano-particles as well as the interface between the particles

and the matrix. Table 2.2 summarizes some of the research on polymer reinforcement by various researchers.

Table 2.2 Effects of nano-particles on mechanical properties of epoxies

Reference	Addition	Percentages	Effect	Mixing method
He and Tian, 2009	CNT-Al ₂ O ₃	1% wt	Tensile strength:34% Young's modulus: 47%	Mechanical mixing
Ganguli et al., 2006	MWCNT	0.15wt%	fracture toughness40%	Ball-milled
Guo et al.,2007	MWCNT	1–3 wt. %.	decreased 10–20% tensile strength and elastic modulus	Sonication
	Acid treated MWCNTs	8 wt. %	Strength (+11.65%) Fracture strain at break (+127.8%)	
Zhu et al.,2004;2003	SWCNT	1 wt.%,4%	an increased strength and Young's modulus and elongation by 30-70%	Sonication
Nhuapeng et al., 2008	SiC NWs	15 vol%	Hardness increased by 384% tensile strength increased by 341% wear track decreased to 40%	Sonication
Chisholm et al., 2005	micro and nano sized SiC filler	1.5 and 3% by weight	Stiffness increased by45% Strength increased by 13%	Sonication
Allaoui et al., 2002	CNTs.	1 % wt	Young's modulus increased from 118MPa to 236 MPa ,yield strength from 118MPa to 465 MPa	Hand mixing
Jia et al., 1999	MWCNT	3 wt%	Hardness increased from 10.76 kg/m ² to 26.9 kg/m ² .	Mechanical mixing
Andrews et al.,1999	SWCNT	5 wt%	elastic modulus increased from 34 GPa to 78 GPa , Tensile strength increased from 490 MPa to 850	Mechanical and sonication

Continued on the next page

Li et al.,2004	SWCNT	1, 3, and 5 wt%	Increase in elastic modulus by 75% and hardness by 30%	Sonication
Qian et al., 2000	MWCNT	1 wt%	Increased tensile strength 25% and the elastic modulus increased 42%	Sonication
Thostenson and Chou, 2002	MWCNT	5 wt%	Increased the tensile modulus, yield strength and ultimate strengths	Mechanical mixing
Song and Youn,2005	MWCNT	0.5,1,1.5%wt	Tensile modulus increased from 68MPa for 0.5% wt to 80MPa for 1.5%wt.	Sonication
Visco et al., 2009	CNT	0.5-1.5%	Elastic modulus increased by 35% Failure stress increased from 2000MPa to 2750MPa.	Sonication, Mechanical mixing
Zhou et al., 2007	MWCNT	0.1,0.2,0.3,0.4%	Tensile modulus increased by 11.7% Tensile strength increased by28.3%	Sonication +Mechanical mixing
Bondar et al., 2005	SWCNT ,MWCNT	0.5%, 1%, 1.5%,	No major differences	Sonication

The variation in the extent of improvement is due to factors such as the state of dispersion and percentage of CNT particles as well as the interface between the particles and the matrix.

From the above-mentioned studies, it is clear that the content of nano-particles used in the matrix does not exceed 8% wt.

It is widely believed that with 3% loading, the number of nano-particles is very high, which allows particle-to-particle interaction rather than the intended particle-to-polymer interaction. Once the loading reaches this state, the particles begin to agglomerate and

form lumps which eventually affect the van der Waals interaction between the polymer chains, reduce cross-linking and increase void content in the nano-composite. The resulting mechanical properties are hence degraded. A possible reason for these relatively high percentage weight losses is the continuous loss of void content in the system.

On the other hand, if small percentages are used, the nano-particles work as reinforcement inside the polymer. During the failure process, the crack propagation changes direction as it crosses nano-particles. The bridge effect, which prevents crack opening, increases strength in the nano-particle/epoxy matrix. The decreased cleavage plane size and the increased surface roughness imply that the path of the crack tip is distorted because of the CNTs, making crack propagation more difficult and requiring more energy to continue.

Further discussion of nano-particles dispersed in epoxy can be found in Chapter Three.

In addition to the effect of nano-particles on the mechanical properties (modulus, strength) of polymers, the dispersion of nano-particles into polymers also affects their thermal properties.

One effective thermal property of adhesive structural joint is the glass transition temperature, (T_g), which is the temperature indicating the phase change of a material from a glassy to a rubbery state. For structural applications, it provides the limiting temperature of their mechanical service after which the epoxy changes from a rigid to a rubbery or viscous state. As a result, the mechanical properties of the adhesive are dramatically decreased since the modulus of the resin, and hence the FRP composite, decreases. The polymer then begins to lose its ability to transfer stresses from the

structural element to the fibres(ACI 440 2008). Therefore, it is desirable to have a high T_g .

The T_g of composites is usually measured by a dynamic mechanical-thermal analyser (DMTA) or differential scanning calorimeter (DSC). Many researchers have studied the effect of adding nano-particles to various polymers on their T_g . Table 2.3 summarises some of these studies.

Table 2.3 Effects of nanoparticles on T_g of epoxies

Reference	Addition	Percentages	Effect	Mixing method
Cho et al., 2008	MWCNT	0.5-1%	T_g increased to 200°C from 160°C	Mechanical mixing
Tao et al., 2006	SWCNT	1%	T_g decreased to 119°C from 149°C	Hand mixing
Zhou et al., 2005	Nano-particles SiC	5,10,20%	T_g decreased to 154°C from 140°C	Sonication
Zhou et al., 2007	MWCNT	0.1,0.2,0.3 0.4%	22 °C increase in T_g	Sonication+ mechanical mixing
Barrau et al., 2005	Mixed MWCNT and SWCNT	0.04-0.4%	no change in T_g	Mechanical mixing
Guadagno et al., 2009	MWCNT	0.5,2 and 3%	T_g was raised 25%	Sonication
Evseeva and Tanaeva, 2008	SWCNT, MWCNT	0.1,1%	T_g increased to 125 °C from 100°C	Sonication+ Mechanical mixing

It is clear from Table 2.3 that nano-particles have varying effects on the T_g . This variation in effect is due to the way that nano-particles effect epoxy molecular internal motion.

The mechanism of the effect of nano-particles on T_g depends on:

- (i) cross-link density

The molecules of epoxy resin measure are of the same order of magnitude as nano-particles. As the nano-particles disperse in the epoxy, due to their high surface area, each particle will fasten more to the epoxy backbone, and generate higher cross-link density in the microscopic area surrounding the nano-particles.

This will increase viscosity, which inhibits the cure reaction, resulting in a lower cross-linking density during the curing process. This leads to less energy being needed to transfer the particles from the solid to the rubbery phase, i.e. lower T_g . (Tao et al., 2006, Gojny and Schulte, 2004; Zouet al., 2008).

On the other hand, if viscosity is not affected, increasing the cross-link density will increase the amount of energy needed for the transformation process, which leads to higher T_g .

(ii) restriction in molecular motion at the molecular level

Dispersing the nano-particles in resin and adding the hardener improves interfacial strength between the nano-particles and the epoxy matrix, thus reducing the mobility of the matrix molecules.

Less moluculer motion increases the transformation energy from glass to rubber, i.e. higher T_g .

(iii) free volume

When the nano-particles are dispersed in epoxy they will create larger particles and start to agglomerate. This agglomeration will cause a free volume that decreases T_g , because it will need less energy to free the particles from the glassy to the rubber phase.

Thus, in epoxy nano-composites, two competing processes proceed: nano-particles limit the mobility of epoxy resin macromolecules and inhibit the curing process, but simultaneously reduce the cross-linking density and increase the free volume inside the epoxy (Sangermano et al., 2008).

With each T_g sample, a trade-off will occur between the negative and positive factors affecting T_g . This trade-off depends on the initial viscosity of the epoxy, nano-particle number and size, and dispersion quality.

2.5 Use of nano-particles to enhance CFRP systems

2.5.1 Introduction

With the continuing quest for lighter and stronger composites, the demand for new types of materials is increasing. No longer can traditional fibrous composites fulfil our strengthening requirements, nor can they be engineered at the continuum level, which controls properties at the molecular or atomic level.

The replacement of CFRPs by nano-composites can be regarded as unrealistic, due to the highly-developed and well-established conventional fibre-reinforcement of polymers and their still unmatched level of material properties. Nevertheless, if the outstanding properties of nano-particles can be transferred to conventional fibre-reinforcements (e.g. carbon-, glass- or aramid-fibres) by means of nano-tube-modified epoxy or matrix, this could lead to a new generation of multi-functional composite systems (Sandler et al., 2003).

However, most efforts so far have only achieved limited success in obtaining specific functional requirements (Fan et al., 2004;Yokozeki et al.,2007;Du et al.,2004, among others). The current critical challenge is the processing techniques of materials because of the typically small size and large specific surface area of nano-particles.

Moreover, these improvements must be achieved through conventional processing techniques without any detrimental effects on process ability, appearance, density and aging performance of the matrix (Chisholm et al.,2005).

Some attempts have been made to develop advanced synthesis processes of CNTs with macroscopic lengths, while other efforts have focussed on grafting shorter CNTs into longer and more widely applied composite fibres (Zheng et al., 2004; Dalton et al., 2003;2004; Vigolo et al., 2000) or into composite sheets (Wang et al.,2004;Lahiffet al.,2004;Mamedov et al.,2002).

However, as these studies are still at the initial stage of development and are difficult for mass production, simpler and more cost-effective fabrication methods are highly desirable.

2.5.2 Multi-scale composite fabrication methods

Although improvements in the mechanical properties of multi-scale composites are achieved with the addition of CNTs, the transferability of improved matrix properties into continuous-fibre-reinforced composites is a challenging task limited by many factors (Wichmann et al., 2006).

In order to utilize the exceptional properties of nano-particles in polymer composites, an applied load must be effectively transferred from the matrix to both nano-particles and fibres to achieve a significant improvement of the composite properties.

The simplest way to enhance CFRP systems with nano-particles is by reinforcing the system adhesive (or matrix). Many researchers have focussed on reinforcing the epoxy with nano-particles, and then adding this to FRP systems (Iwahori et al.,2005;Song et al.,2008;Liao et al.,2006, among others) due to the simplicity and effectiveness of such an approach.

In this approach, nano-particles and epoxy are mixed according to the different mixing methods outlined in previous sections. Then, the enhanced epoxy is used as an adhesive to attach CFRP plates or is hand laid into the fibres before drying.

Using this method, and with a low CNT loading of 0.3 wt% in the epoxy, improvements in flexural modulus, strength, and percentage strain to break of 11.6%, 18.0%, and 11.4%, respectively, were reported by Kim et al. (2009a).

In 2003, Hsiao et al. used different weight fractions of MWCNT(1 and 5%wt) dispersed in epoxy to produce toughened adhesives. The reinforced adhesives were used to bond two CFRP plates in a single lap joint. The bond strength was enhanced by 31.2% for the 1wt% and 45.6% for the 5wt %.

Qiu et al, (2007) mixed MWCNT with epoxy for use as a matrix in fibreglass composite and found a 27.2% increase in Young's modulus along fibre orientation and a 15.9% increase in tensile strength.

These property enhancements are due to that the presence of nano-particles in the matrix of fibres, which makes the matrix more conductive and lowers the contact resistance between the fibres.

Another method used by other researchers (Gojny et al.,2005; Wichmann et al.,2006; Haque et al.,2003;Thostenson and Chou,2006a) is to spread the enhanced epoxy onto the fibres by integrating the enhanced epoxy and firer fabric by vacuum-assisted resin transfer moulding (VARTM).In this method, the CNT/ carbon fibre preform is sealed in a vacuum bag, and the epoxy resin is then infused into the carbon fibres under vacuum.

Figure 2.15 shows the scheme of procedure.

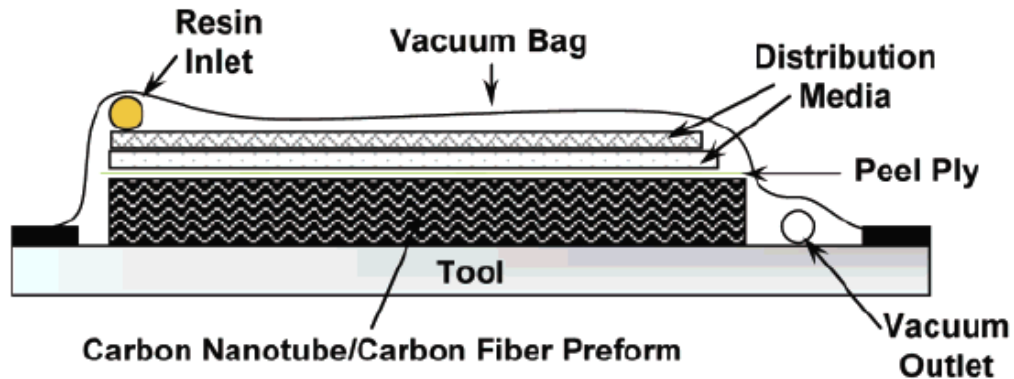


Figure 2.15 VARTM procedure scheme and procedure (Bekyarova et al.,2007)

The CNT/epoxy mixture is processed into a small thickness film by using compression moulding. After the nano-composite film is prepared, the film is placed between the fibre preforms and the distribution medium. Finally, the fibre preform is fully impregnated before the epoxy resin is cured. (Song,2007)

In 2007, Bekyarova et al. used another method to fabricate multi-scale hybrid composites in which the nano-tubes were grown (or deposited) on the carbon fibres by the CVD method or electrophoresis.

Although the CVD process is an efficient technique for the growth of CNTs on a variety of surfaces, the use of high temperatures and pre-deposited catalysts, taken together with the difficulties in processing large panels, imposes serious limitations on the practical application of this technique for the fabrication of CNT-reinforced structural composites. Furthermore, high-temperature processing with CVD removes any sizing that may be applied to the fibre during manufacturing, and the CVD reaction may also degrade fibre strength.

As shown in Figure 2.16, the CNTs are dispersed in water by ultra-sonication. The carbon fibre is fixed in a stainless steel frame, and two stainless steel plates are positioned on both sides of the carbon fabric as counter electrodes. The carbon fabric is immersed in the nano-tube dispersion, and a positive potential is applied to the carbon fabric. After this process, the matrix (nano-particle-enhanced or pure) is added to the enhanced CFRP by hand lay-up or VARTM, and left for curing.

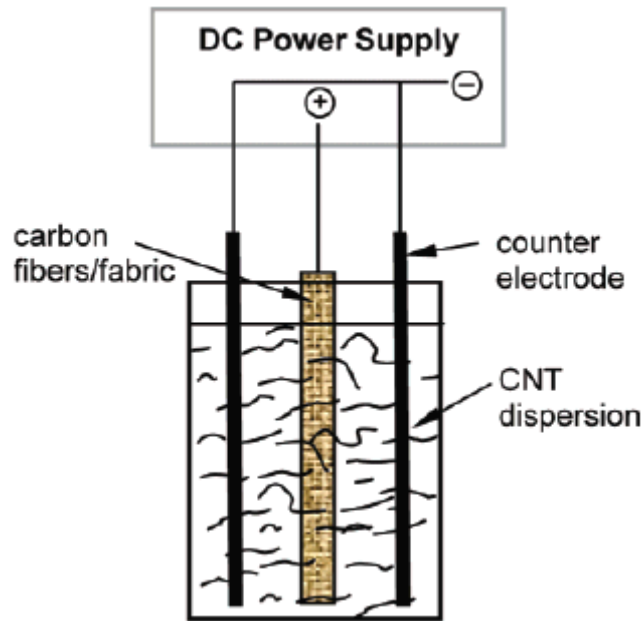


Figure 2.16 Deposition of carbon nanotubes on a carbon fibre surface by electrophoresis.
(Bekyarova et al., 2007)

2.6 Material Point Method

2.6.1 Background

Previous simulations of the dynamic failure of CFRP-steel joint systems (Fawzia et al., 2006; Liu et al., 2008; Teng and Hu, 2007; Wu et al., 1998; Rahimi and Hutchinson, 2001; Yin and Wu, 2001, among others) were mainly performed using the Finite Element Method (FEM). The FEM is a mesh-based method and may have difficulties in modelling the transition from the continuous to discontinuous failure modes involved in the process of CFRP delamination from steel plate.

As an innovative spatial discretization method, MPM is an extension to the solid mechanics problems of a hydrodynamics code called FLIP (Brackbill and Ruppel, 1986; Brackbill et al., 1988) that, in turn, evolved from the Particle-in-Cell Method dating back to the pioneering work of Harlow (1964). The motivation of the development was to

simulate the challenging solid mechanics problems such as impact/contact, penetration, fragmentation and machine processing with history-dependent internal state variables (Chen et al., 2002). The essential idea is to take advantage of both the Eulerian and Lagrangian methods, while avoiding the shortcomings of each.

In 1994 Sulsky et al. outlined the MPM equations, and foreshadowed the future applications, limitations and the development that might come from using this method in certain history-dependent applications. MPM has been considered as an extension to the Particle-in-Cell method with particles interpreted to be material points that are followed through the complete loading process.

2.6.2 MPM fundamentals

The MPM is an evaluation of particle in cell methods which utilize two meshes: a material or Lagrangian mesh defined over the material of the body under consideration, and a special or Eulerian mesh defined over the computational domain. Each material point carries its material properties while it is processed. MPM starts with transferring the information from the material points to a grid, the information being used to solve the equation of motion in an updated Lagrangian frame on the grid. The particles are then updated and the grid is redefined. Detailed algorithms have been studied in Chapter Five.

2.6.3 Why MPM?

The main special features of MPM that differentiate it from FEM can be summarized as follows:

1. The material points, where constitutive equations are applied, move from one element to another rather than remain at the centre or Gauss points of an element.
2. The use of the point mass representation for the mass density results in the appearance of point masses in expressions for the internal and external force vectors.
3. The specific stress is used to provide a convenient form of the equation of motion in which the stress is evaluated only at the material point.
4. Matrices are never developed for any step in MPM procedure. Instead, nodal variables are accumulated by sweeping over material elements.
5. The traditional mesh based methods (Eulerian scheme) are handicapped when dealing with problems their constitutive equations are history dependent. On the other hand, purely Lagrangian methods typically result in severe mesh distortion, and the consequence is ill-conditioning of the element stiffness matrix leading to mesh lock-up or entanglement.

The MPM is more convenient than other mesh-based methods if the problems include:

- Localised large deformations: the MPM can model without mesh distortion or tangling, due to the mapping process from material point to cell nodes and from cell nodes to material points involved in each time

step. Therefore, mesh tangling is avoided while material variables are tracked through the complete deformation history.

- Propagation of cracks and separation of continuum: the MPM is preferred due to the use of the same set of continuous shape functions in both mappings, which results in a natural no-slip contact/impact scheme.
6. Advection of history-dependent variables like plastic strain and strain hardening parameters is straightforward, since the variables are defined on material points which themselves advect through the Eulerian mesh. Thus, numerical dissipation normally associated with an Eulerian method is avoided.
 7. It helps the multiple materials to be performed easily since each material point retains its identity -material properties-throughout the computation.

2.6.4 Application of material point method in engineering

Since its appearance in 1994, MPM has been used to simulate many structural problems that have history-dependent variables. These problems are:

- The upsetting of billets and the Taylor problem of cylinders impacting a rigid wall (Sulsky and Schreyer, 1996).
- Vibration and impact (Sulsky et al., 1994).
- Cylinder rebounding from a rigid wall (Sulsky et al., 1995).
- Thin membrane motion objects like springs, pendulum strings with initial shock (York et al., 1999).
- The behaviour of granular materials (Bardenhagen et al., 2000).

- Dynamic failure with damage diffusion (Chen et al., 2002).
- Decohesion failure: Schreyer et al.(2002) explored the energy implementation of material softening in a thermodynamic framework. The model assumes the delamination occurs when the dissipated energy (fracture energy) is greater than the plastic work of the traction on the failure surface. This model is better than the FEM model in the attributes of no mesh deformation so that re-meshing is not necessary and the continuous tracking of material points avoids the need for re-mapping history variables such as decohesion. Compatibility is invoked in a weak sense with the result that no special algorithms are needed for mesh realignment along crack surfaces or for double nodes.
- Delamination of tungsten film from the silicon substrate (Shen and Chen,2004). The model proposed a bifurcation-based decohesion model which is formulated within the framework of continuum mechanics. The molecular dynamics simulate single crystal tungsten under tension to investigate the effect of specimen size and loading rate on the material properties. The proposed decohesion model is then calibrated by applying a molecular dynamic simulation of a single tungsten crystal block under tension and using available experimental data to account for the size effect.
- Bifurcation-based decohesion model to simulate the transition from localization to decohesion involved in the delamination process of compressed films (Chen et al., 2005). The onset and orientation of discontinuous failure are identified from the discontinuous bifurcation analysis. The MPM is developed to accommodate the multi-scale discontinuities involved in film delamination.

2.7 Summary

From the above literature review many conclusions can be drawn including the following:

- Many types of nano-particles can be added to enhance epoxy behaviour.
- The effects of adding small amounts of nano-particles varies from positive to negative on strength and T_g , depending on the agglomeration and distribution status.
- The distribution of nano-particles can be done by many mixing methods. The ultrasonic mixing method is adopted for the purposes of the present study owing to its simplicity and efficacy.
- The effects of nano-particle-enhanced epoxy depends on the epoxy type. Therefore, the effects of different nano-particles with different content percentages on strength and thermal properties should be studied.
- The effects of adding small amounts of nano-particles to different types of adhesives used in CFRP enhancing systems need more studies to find the effects on over-all CFRP-steel systems.
- To understand the CFRP-steel joint behaviour, an active model is needed focusing on the epoxy. The key factors for such a model are the bond-slip relationship and strength of joint. MPM will be used to simulate the failure pattern owing to its ability to simulate discontinuous failures.

Chapter Three

Material Properties

3.1 Introduction

The successful retrofitting of steel structures by using CFRP significantly depends on the performance and integrity of the CFRP-steel joints, and the effectiveness of the adhesive used. In order to improve the performance of the whole system, the enhancement of the adhesive properties is the most preferred option. Various applications are anticipated for nanomaterials/polymer composites such as electrostatic painting (Baughman, et al.,2002), antistatic shielding on aeroplane wings (Milne,et al., 2004) or for transparent electronic conductors (Park,et al.,2002).

This chapter presents the work on an experimental program to study the mechanical and thermal characteristics of two types of epoxies, used as structural commercial adhesives, reinforced by two types of nanoparticle additions. The program involved the following components:

- Testing in direct tension a total of 60 epoxy coupons with different types and percentages of nano-additives;
- Testing the effect of adding different nano-additives in different percentages for the two epoxies on the glass transition temperature T_g , and;
- Evaluating the dispersion method used to mix the nano-additives into the epoxies.

- To find the degree of strengthening, all of the materials used in the bonding process should undergo quality assessment by material property testing. Therefore, CFRP plates and steel coupons were tested.

3.2 Nanoparticle additives to the epoxy

3.2.1 Background

Using adhesive bonding for joining composite parts provides many advantages, such as low cost, high strength-to-weight ratio, low stress concentration, fewer processing requirements and good fatigue and environmental resistance (Ferreira, et al., 2002). However, the adhesives are usually much weaker than the adherents they join. To improve bonding performance, one possibility is to consider toughened adhesives. It is a common practice to enhance the epoxy by adding nanoparticles to it.

In order to utilize the exceptional properties of nanoparticles on polymer composites, the applied load must be effectively transferred from the matrix to the nanoparticles to achieve a significant improvement of the composite properties. Moreover, these improvements should be achieved through conventional processing techniques without any detrimental effects on process ability, appearance, density and aging performance of the matrix.

3.2.2 Adhesive properties

The most frequently used epoxies to attach CFRP plates on steel are Araldite-420 and Sikadur-30. These epoxies have a high mechanical strength, are easy to apply and cure within 16-24 hours with no requirement for elevated temperature. The

disadvantage of these adhesives is the limited working time, which ranges around 60 minutes. To achieve the required properties of the epoxy, the application procedures should be strictly followed (Fawzia, 2007). Table 3.1 below gives the manufacturer's properties of these epoxies.

Table 3.1 Mechanical properties of adhesives as given by the manufacturer
(Huntsman Advanced Materials, Sika Australia Pty Ltd)

	Araldite-420	Sikadur-30
Specific gravity	1.2	1.77
Tensile strength	32MPa	33MPa
Ultimate strain	0.04	0.003
Elastic Modulus	1.9 GPa	12.8GPa

It is a common practice to obtain measured material properties such as tensile strength, modulus of elasticity and ultimate strain rather than relying on the values supplied by the manufacturer (Fawzia, 2007). It is also necessary to create reference properties to be compared with those for nano-particle-enhanced epoxies.

Due to the nano-meter's dimensions and high superficial area of the nanotubes, a small amount is enough to increase the viscosity of the nanomaterial/matrix blend. This causes problems in blend dispersion, workability, and, consequently, in composite manufacture (Wang, et al. 2004).

3.2.3 Nano-additives types

In general, comparison of results reported is often difficult, due to the usage of different epoxy matrices, with different processing techniques and parameters, as well as the choice of nanoparticles from various sources with different types and qualities. Therefore, all results should be compared to reference materials, as the neat

epoxy matrix. Keeping most variables constant, it was the aim of this study to compare the influence of these different percentages of nanoparticles on the mechanical properties and to appraise the real potential of nanoparticles as structural modifiers of epoxy-based composites.

To study the effect of additive types on the chosen epoxies, two types of nanomaterials (Multi-wall carbon nanotubes (MWCNT), diameter 110-170nm, length 5-9micrometer and 90+% purity and silicon carbide nanopowder (SiC) particle size < 100nm, density 3.22 g/ml at 25 °C, both manufactured by Sigma-Aldrich Co.) were added at different weight percentages (0%, 1%, 2% and 3%) as summarised in Table 3.2. Ultrasonic mixer (VCX 500 from Sonics & Materials, Inc.) was used to ensure the uniformity of the nanomaterials in the epoxy.

Table 3.2 Coupon samples tests scheme

		Araldit-420	Sikadur-30
Multi-wall Carbon Nanotubes (MWCNT)	0% Hand mixing	3samples	3samples
	1%	3samples	3samples
	2%	3samples	3samples
	3%	3samples	N/A
Silicon Carbide nanopowder (SiC)	0% Ultrasonic mix	3samples	3samples
	1%	3samples	3samples
	2%	3samples	3samples
	3%	3samples	3samples
	0% Ultrasonic mix (Vacuumed)	3samples	N/A
	1%(Vacuumed)	3samples	N/A
	2%(Vacuumed)	3samples	N/A
	3%(Vacuumed)	3samples	N/A

The addition of nanoparticles to a cement-like epoxy of Sikadur-30 increased its viscosity to the extent that the 3%MWCNT-epoxy mix became so dense that hand pre-mixing was very difficult and could not be continued.

Due to the differences between the specimens in the epoxies used, the nanoparticles (type and percentage) and the mixing methods, the specimens were given a naming scheme as follows. The first letter indicates the epoxy type (A for Araldite-420 and S for Sikadur-30). The second letter stands for the additive, C for MWCNT and S for SiC powder. Then, the mixing method is indicated by M for mechanical-ultrasonic mixing without additives, H for normal hand mixing without additives and O for the vacuumed oven specimens. The number indicates the weight concentrations by percentage of additives (1%, 2% and 3%). Therefore the code AS2 is for an Araldite-420 sample with 2% SiC powder. Figure 3.1 briefs the naming scheme for epoxy coupons.

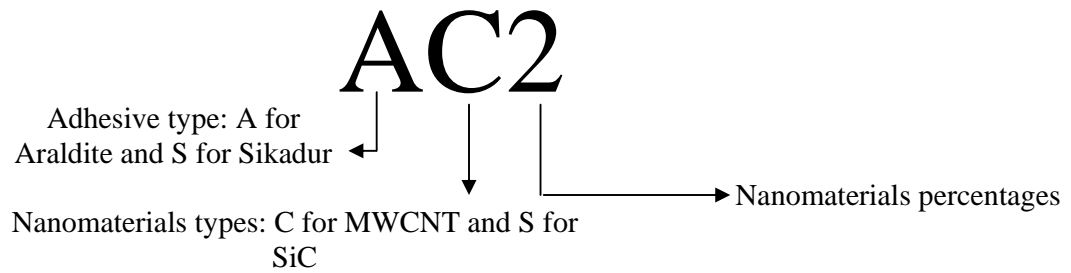


Figure 3.1 Coupons naming scheme

3.2.4 Mixing method

The dispersion of the nanoparticles in the epoxy plays an important role as homogeneous dispersion guarantees uniform load-sharing by the reinforcing particles. The achievement of homogeneous dispersion of nanoparticles is regarded as a prerequisite for composites.

Many researchers (Eskin, 2001, Niyogi, et al. 2003 and Chisholm, et al. 2005, among others) use the ultrasonic mixing method due to its simplicity compared with other

methods. In the present study, ultrasonic mixing was employed to infuse MWCNT and SiC nanopowder into part-A of the Araldite 420 adhesive.

Due to the strong intrinsic van der Waals forces, MWCNTs tend to hold together as ropes and bundles that have very low solubility in most solvents, which leads to poor dispersion when mixed into a polymer matrix. To break these bonds, the MWCNT was mixed with ethanol (99% pure) at a 1:10 concentration then left for curing for 48 hrs in the vacuum chamber. Then it was ready to be mixed with the part-A of the epoxy.

The nanoparticles were dispersed in part A since this part is less reactive to ultrasound irradiation than part B.

Due to the small-sized particles and thin needle shape, which make the material like asbestos, there is a danger of lung cancer.. Therefore, all necessary precautions were taken when dealing with the nano-particles. All weighing of the pre-calculation nano-particles and hand pre-mixing of the nanoparticles with epoxies part-A was done inside a sealed glass box in a vacuum chamber while the researcher was wearing a gas mask and double latex gloves. After the nano-particles were fully hand mixed with epoxy part-A in the vacuum chamber, it was safe to deal with it in the open air.

Then, a conical ultrasonicator was used for the main dispersion of nanoparticles. At a 55% energy density, ultrasonic waves were applied for 50 min at an amplitude of 30 s every 50 s to prevent the applied energy from increasing the mix temperature over the limit. In order to avoid any rise in temperature during sonication, the temperature was monitored and controlled by the mixer temperature probe and submerging the mixing beaker in a mixture of ice and water so that the mix temperature did not reach 55°C.

At the end of the mixing time, the dispersion of nanoparticles appeared uniform on visual inspection.

In the next step, Part-B of the epoxy was added to the mixture at the recommended ratio and the mixing was carried out by hand for about 4 min.

The shape of the specimen was engraved into the Teflon mould following ASTM:D 638-01 standards, as can be seen in Figures 3.2 and 3.3.

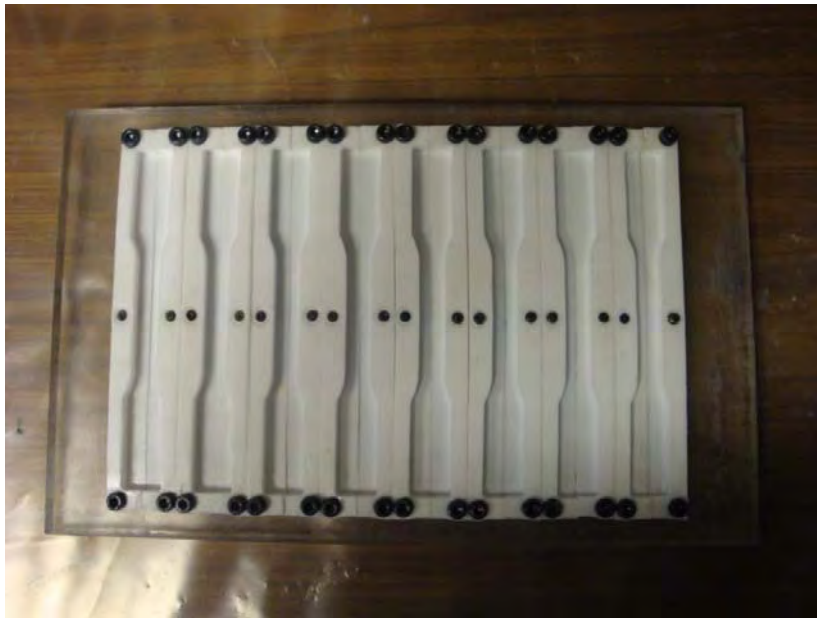


Figure 3.2 Epoxy coupon Teflon mould

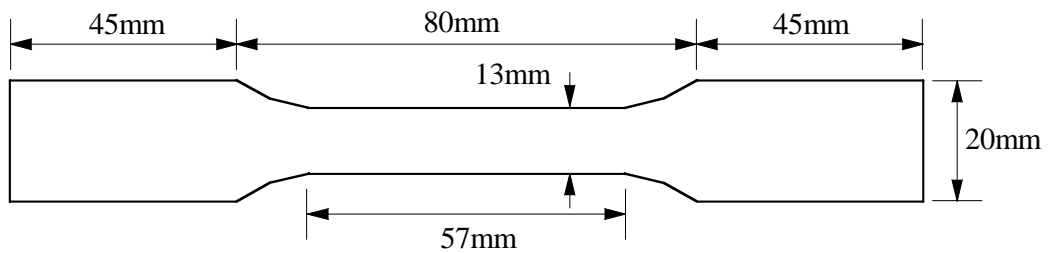


Figure 3.3 Adhesive coupon dimensions

The rigorous mixing of part A and part B produced highly reactive volatile vapour bubbles at the initial stage of the reaction, which if not removed could detrimentally affect the properties of the final product by creating voids. Therefore, the vibrating table was used for 10 min on the mould while the epoxy was poured into mould's grooves.

A uniformly-distributed load of 800 kg/m^2 was then applied over the epoxy for 24 hours to assure the uniformity of the coupons. Then, the coupons were de-moulded and the extra epoxy ground and tested 7 days after the casting.

The specimens were tested using an Instron testing machine at the rate of 2 mm/min. Strain was measured using strain gauges attached longitudinally to the two opposite sides of the specimen.

3.2.5 Effect of sonication on the epoxies

To study the effect of using sonication alone on the epoxy part A, and to create reference data that can be used to find the effect of nanoparticles only, a set of samples from both epoxies was prepared and tested using the same previously-mentioned mixing procedures without nanoparticles.

Figure 3.4 shows that using sonication mixing alone on Araldite-420 part A caused a negligible decrement in strength from 26.7 MPa for the hand mixed to 26.4MPa for the sonicated samples. The modulus of elasticity was not affected by sonication and remained 1.87MPa. Sonication did not increase the modulus of elasticity but increased the elastic limit from 16MPa to 21MPa as can be seen in Figure 3.3.

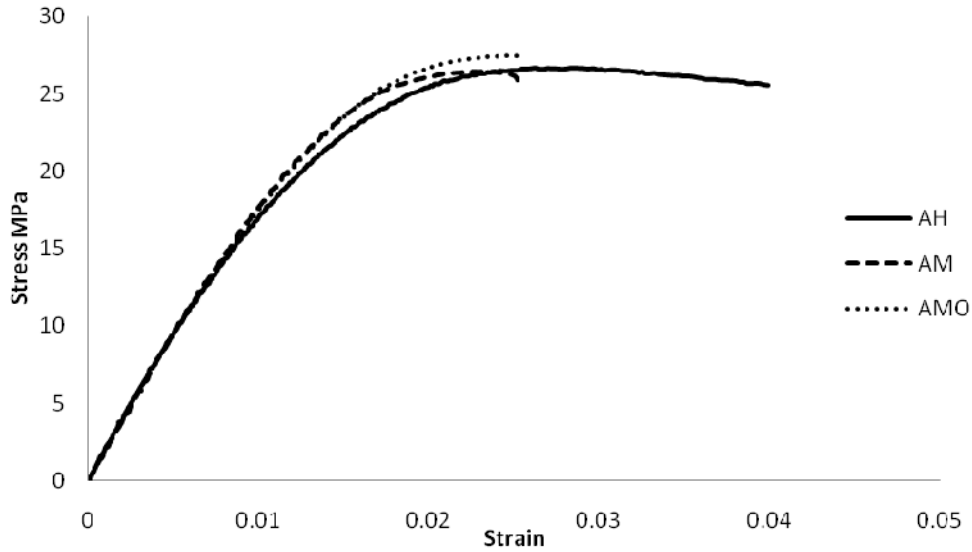


Figure 3.4 Comparison between three mixing methods of Araldite-420

A possible reason for such a negligible and unexpected difference is the micro air-bubbles created during the sonication process which the vibration table could not remove. Another possible reason is that the components of Araldite-420 part A are homogeneous and any additional mixing will not assist part-A particles in obtaining extra energy that can be used when part-B is added.

To confirm which of these reasons is correct, a new set of Araldite-420 samples was prepared with the same procedures except that sonicated part A was placed in a vacuum oven at a temperature of 55°C for 2hrs.

The vacuumed samples showed a small increment in strength of 2.5% from the hand mixing as can be seen in Figure 3.4. This small increment showed that the bubbles inside were so small that the vacuum oven could not remove them.

Therefore, part-A particles are not affected by sonication energy and its homogeneity was not enhanced.

The situation in relation to Sikadur-30 supports this theory.

The strength increased from 18.6 MPa for a hand mixed sample to 22.8MPa for sonication neat samples as seen in Figure 3.5, and the modulus of elasticity of the sonicated sample decreased from 13.48 MPa for the hand mixed to 9.29MPa for the sonicated net Sikadur-30 samples.

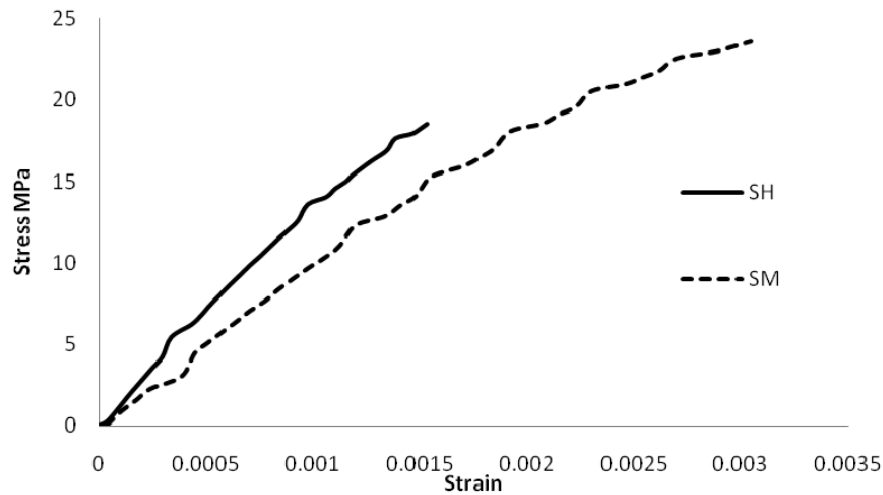


Figure 3.5 Comparison between mixing types of Sikadur-30

The reason for such change in stiffness derives from the fact that ultrasound irradiation enhances the homogeneity of the reaction mixture in part-A of the epoxy resin. Ultrasound irradiation helps in the molecular mixing of part-A components and the formation of reactive species which ultimately leads to increased cross-linking in the polymer when mixed with part B.

3.2.6 Araldite-420 enhanced by MWCNT

Carbon nanotubes (CNTs) are the strongest and stiffest materials on earth, in terms of tensile strength and elastic modulus. Their excellent mechanical properties

and superior length-to-diameter ratio make CNTs very attractive for composite reinforcement (Zhu, et al., 2004).

Due to the excellent mechanical properties of CNTs, a variety of structures have been proposed ranging from everyday items like clothes and sports gear to combat jackets and swords.

Adding MWCNT to Araldite-420 increased the strength from 26.7MPa for hand mixing, and 26.4 MPa for sonicated neat specimens to 27.9MPa for 1wt % MWCNT. As the percentage of the MWCNT increased to 2wt%, the strength increased to 30.9MPa, which is the optimum strength as shown in Figure 3.6. Beyond 2wt%, the strength returned to 27.2MPa.

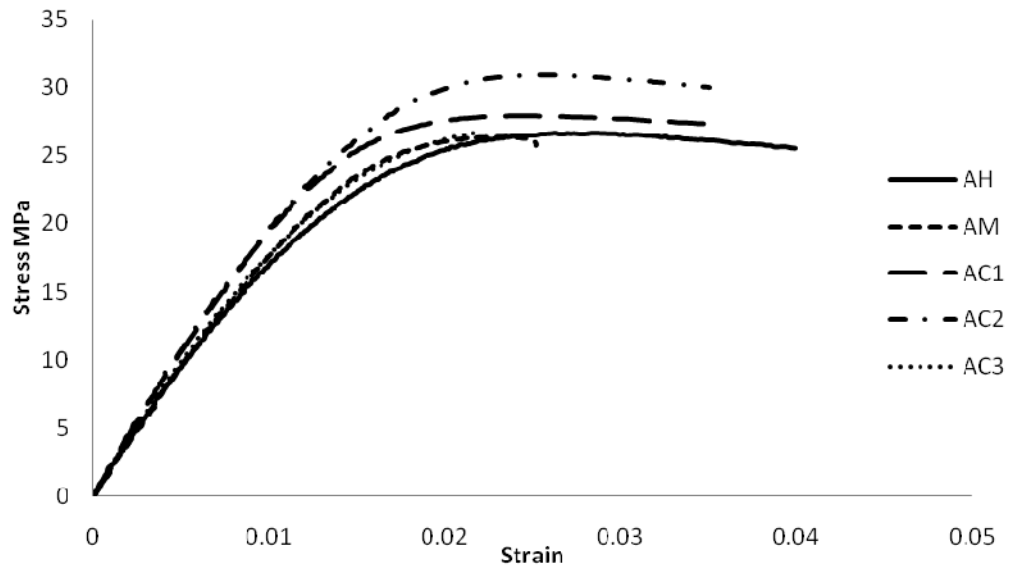


Figure 3.6 Effect of MWCNT on Araldite-420

However, adding MWCNT to Araldite-420 increased the stiffness with the same patron as the strength shows: the modulus of elasticity increased from 1.87MPa for

hand and neat sonicated epoxy to 2.1MPa for 1wt%, 2.13MPa for 2% and 1.92 for the 3wt%MWCNT.

The elastic limit also increased according to the same pattern: from 16MPa for hand mixing and 21MPa for sonicated neat to 23 MPa, 25 MPa then back to 21 MPa for 1, 2 and 3% MWCNT respectively.

Figures 3.7 and 3.8 summarize the effects of adding MWCNT to Araldite-420.

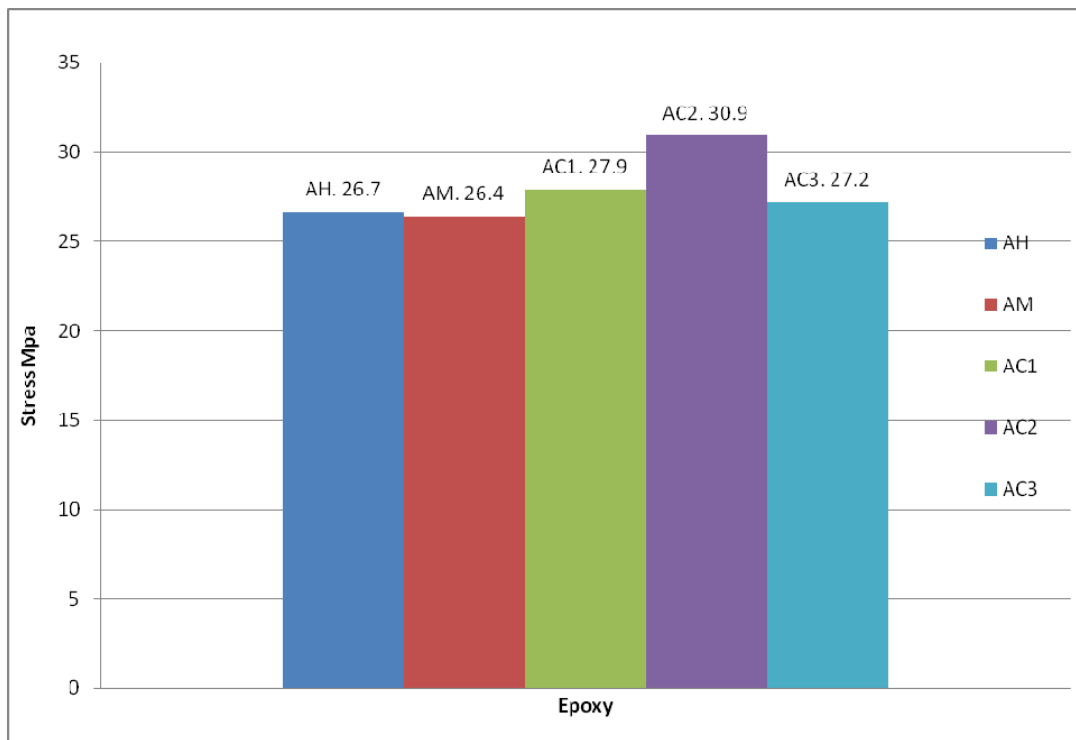


Figure 3.7 MWCNT effects on Araldite-420 strength

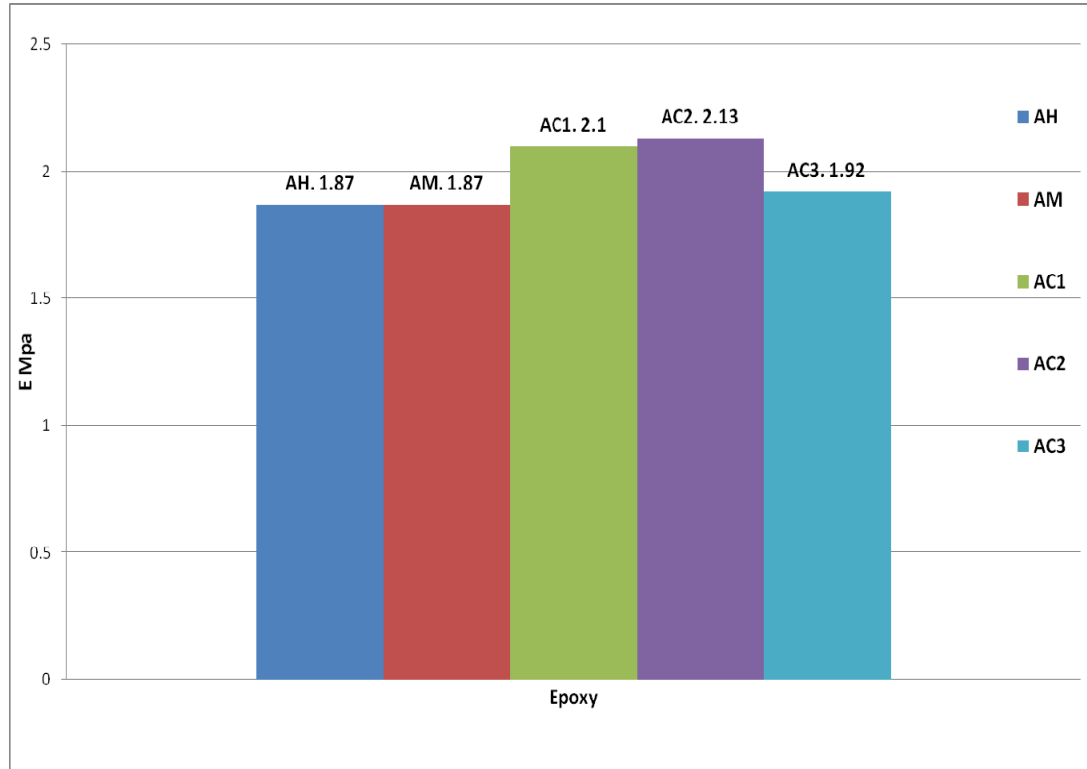


Figure 3.8 MWCNT effects on Araldite-420 elastic modulus

To clarify these results, it is necessary to understand the MWCNT behaviour inside the epoxy. When the MWCNT infuses inside the epoxy, due to its needle-like shape, it tends to surround itself by a thin layer of epoxy that attaches strongly to the outer wall of the nanotube, due to its high surface area, as shown in Figure3.9.

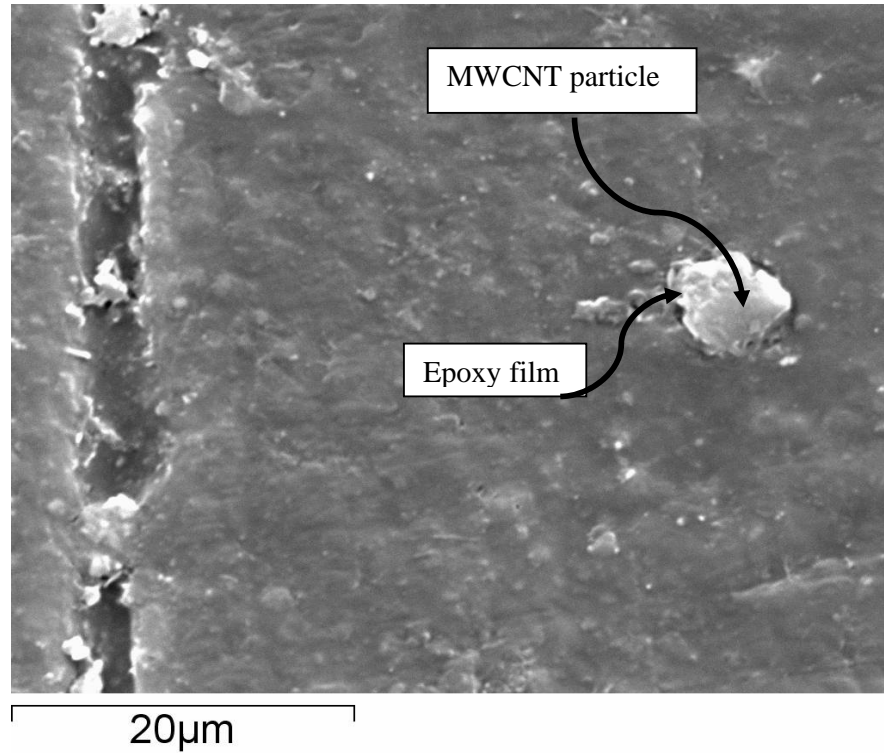


Figure 3.9 MWCNT particle surrounded by Araldite-420 bundles.

This combination starts to work as a reinforcing item and prevents the nanotubes from agglomerating at the same time. These reinforcing particles decrease the crack width by bridging the gap between the sides and its length because the crack now needs to move a longer distance around these items, which needs more energy.

Also, when nanotubes are positioned between the resin molecules, an obstacle is created to molecular motion which increases brittleness. (Zhou et al.,2007)

This effect will last until the concentration of the MWCNT increases to a degree that the strong, thin epoxy film has no space to form, as can be seen in Figure 3.10, and the agglomeration starts to form larger bundles of MWCNT surrounded by a layer of epoxy (Lozano, et al.,2001). This layer still attaches strongly to the nanotubes, but the nanotubes have a very weak connection between each other. The brittle forces

attached to the nanotubes inside the agglomeration weaken reinforcing action and help to shorten the crack length through the agglomeration of the nanotubes. Figure 3.11 summarises the above mechanism.

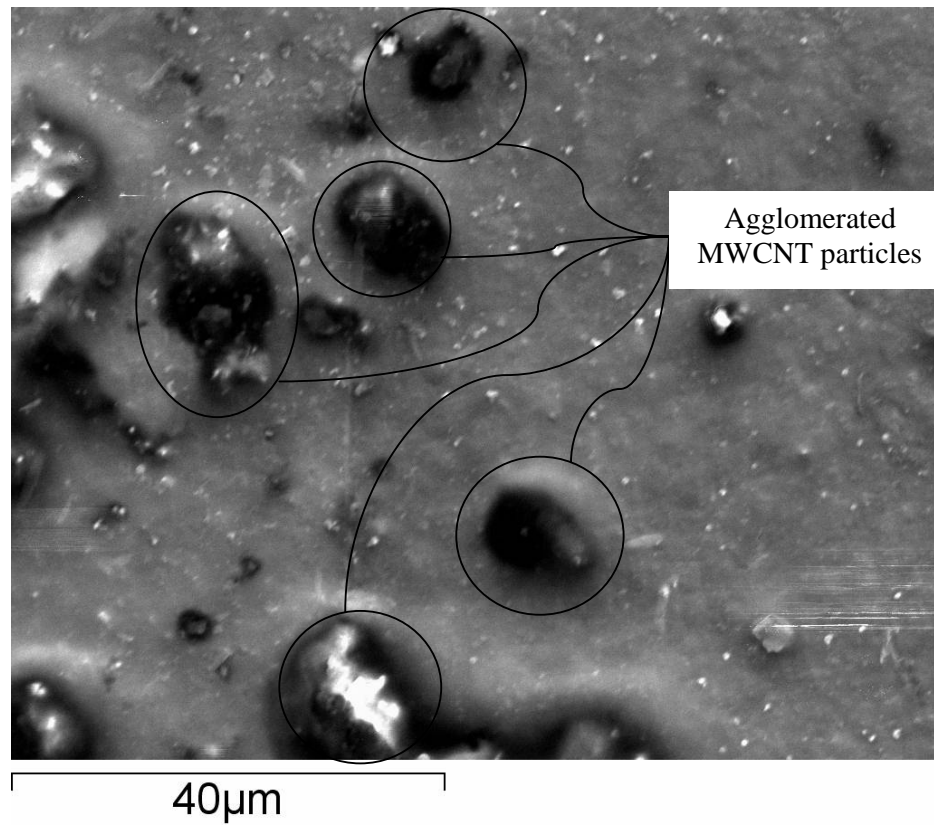
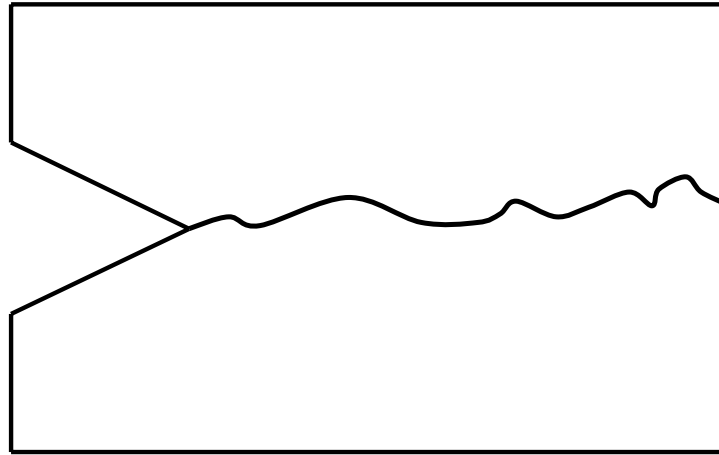
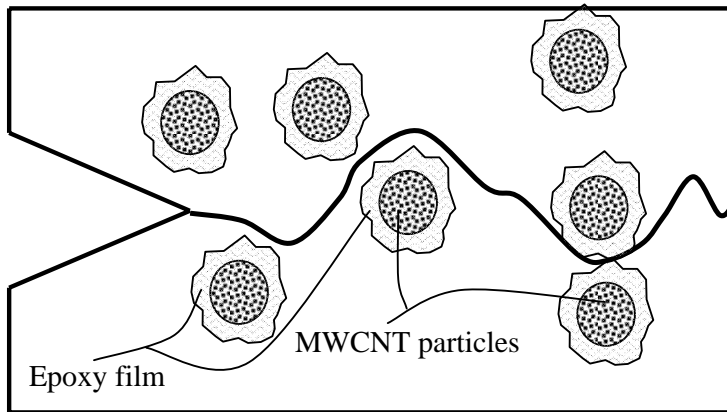


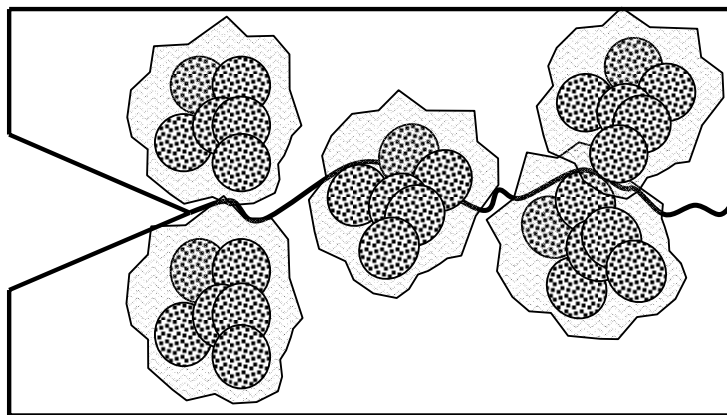
Figure 3.10 3 % MWCNT particle surrounded by epoxy bundles.



a) Crack through un-reinforced epoxy section



b) Crack through under reinforced epoxy



c) Crack through over-reinforced epoxy

Figure 3.11 Behaviour of MWCNT inside epoxy

3.2.7 Sikadur-30 enhanced by MWCNT

Sikadur-30 is a cement-like epoxy used widely in attaching CFRP laminates to steel. Adding MWCNT to Sikadur-30 has a different effect than that on Araldite-420: Figure 3.12 shows that the major strength gain came from the sonication only; 1% of MWCNT to the Sikadur-30 will increase the strength from 22.8 MPa in the neat sonicated specimen to 23.5MPa and 17.7MPa for the 1% and 2%MWCNT respectively.

Also, the modulus of elasticity will be 12.37MPa and 10.84MPa for the 1%and 2%MWCNT respectively from 9.29MPa and 13.48MPa for sonicated and hand-mixed samples.

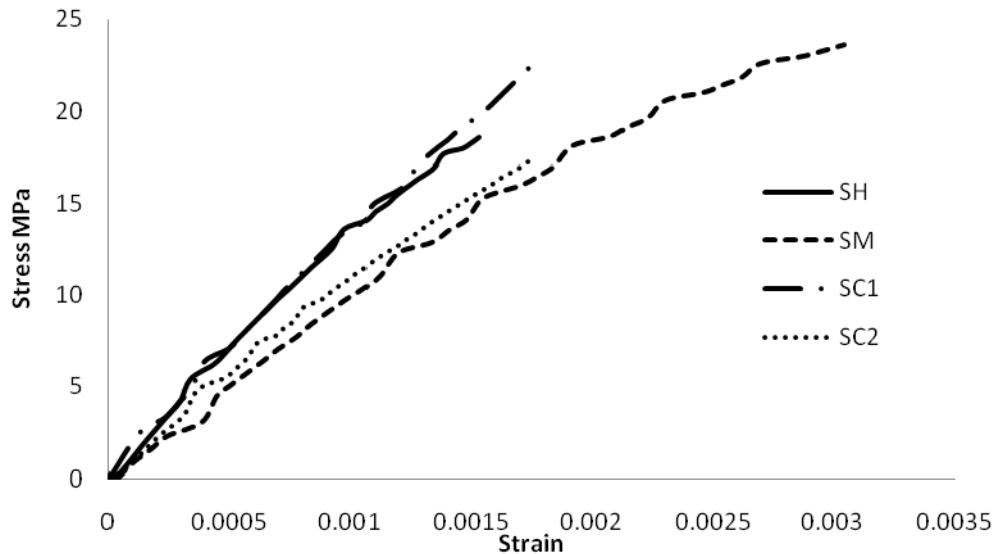


Figure 3.12 Effect of MWCNT on Sikadur-30

Sikadur-30 part-A has many agglomerated filling materials, which has no role in chemical reaction when added to part-B (which also contains filling materials which do not have any role in the chemical reaction). Therefore, sonication will

increase the homogeneity of these particles in part-A by breaking their agglomerations, thus helping part-B particles to create stronger bonds.

However, these bonds still have non-reactive particles which create the same effect of adding high percentages of MWCNT to Araldite-420, and prevent the epoxy forming the strong, thin film around the nanoparticles. Therefore, MWCNT has a neglected effect on strength, and even starts to work as impurities which are poorly adherent to epoxy particles and concentrate stress at their tips.

The effect of MWCNT on Sikadur-30 can be summarized in Figures 3.13 and 3.14.

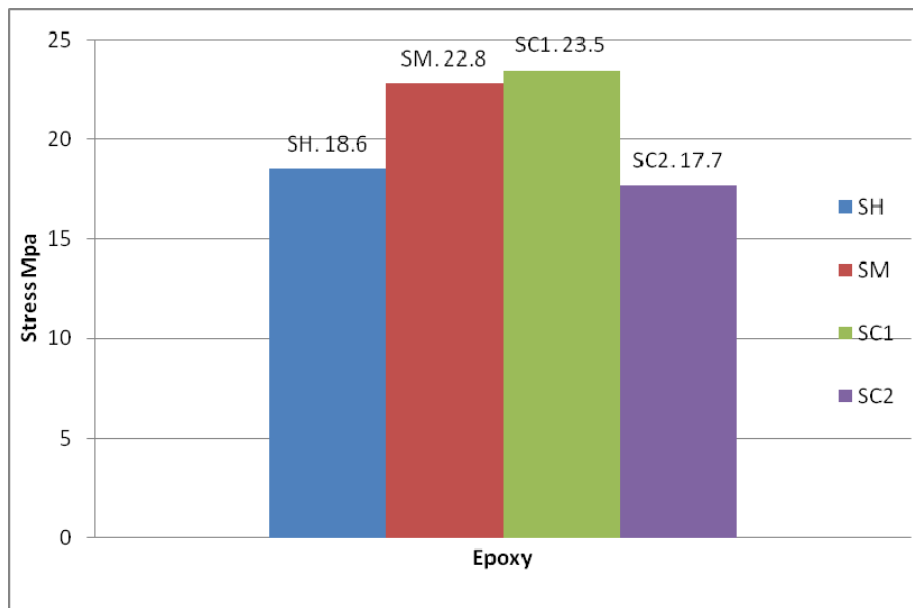


Figure 3.13 MWCNT effect on Sikadur-30 strength

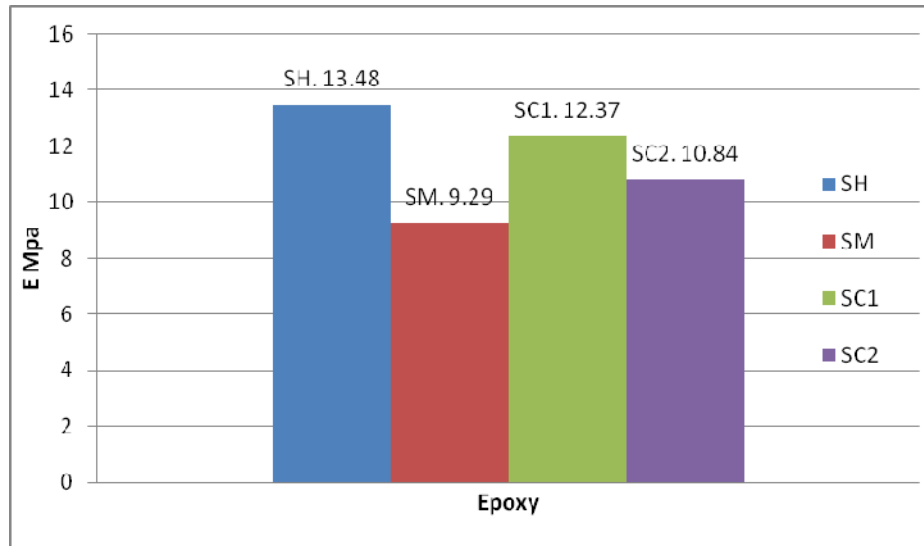


Figure 3.14 MWCNT effect on Sikadur-30 elastic modulus

3.2.8 SiC-epoxy composites

Among reinforcement materials, SiC is one of the most-used in anti-wear applications. Friction properties of SiC (in dry and lubricated conditions) have been widely studied because it is often used in such applications as bearings, bushings, and other mechanical devices. Bulk SiC is known as a ceramic material with high hardness, wear resistance, high temperature stability and chemical inertness. Accordingly, SiC nanoparticles were employed in the preparation of nanocomposites in the hope of imparting the excellent properties of SiC to the composite materials. (Abenojar et al.2009)

To find the effect of adding SiC nanopowder into the CFRP-steel commonly used epoxies, three coupon series were prepared: SiC+Araldite-420, SiC+Araldite-420+vacuum oven, and SiC+Sikadur-30.

SiC nano-powder was added to the Araldite-420, tested under tension and compared to hand-mixed and sonication mixed neat epoxy.

As Figure 3.15 indicates, SiC nanopowder has a small or even a negative effect on strength compared with the hand-mixed samples. An increment in strength compared with neat epoxy samples (26.7MPa for hand mixed and 26.4MPa for sonication) occurred when 1 % of SiC was used(27.9MPa) and a decrement occurred when 2% (23.5MPa)and 3% (25.9MPa) were used.

The modulus of elasticity followed the same pattern: a slight increase when 1%SiC was added (from1.87MPa for the neat epoxy, hand-mixed and sonicated, to 1.93MPa for 1%SiC) then a sharp decrease with 2%SiC (1.77MPa) followed by a slight decrease with the 3%SiC (1.85MPa).

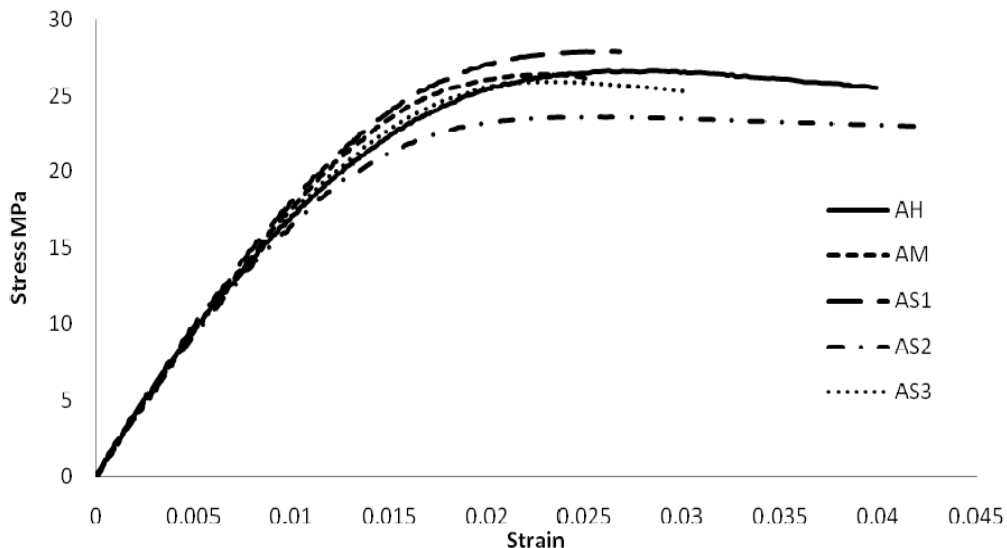


Figure 3.15 Effect of SiC on Araldite-420

To study the effect of the air bubbles that may be created in the mixing process, Araldite-420 part-A was vacuumed according to the previous procedure.

The vacuumed-SiC samples were tested and the previous pattern was repeated. The strengths were compared between the SiC-Araldite samples with and without vacuum oven. Vacuuming increased the strength, as can be shown in Figure 3.16, from 27.9, 23.5 and 25.9 MPa for 1%, 2% and 3% SiC to 28.9, 24.3 and 27.7MPa for 1%, 2% and 3% SiC respectively.

The increments in strength due to SiC addition were still less than 10% for the 1% of SiC.

As reported previously for neat-vacuumed Araldite samples, SiC had a better effect on modulus of elasticity which increased to 2.75MPa, 2.06MPa and 2.27 MPa for vacuumed epoxy with 1%, 2% and 3% SiC respectively.

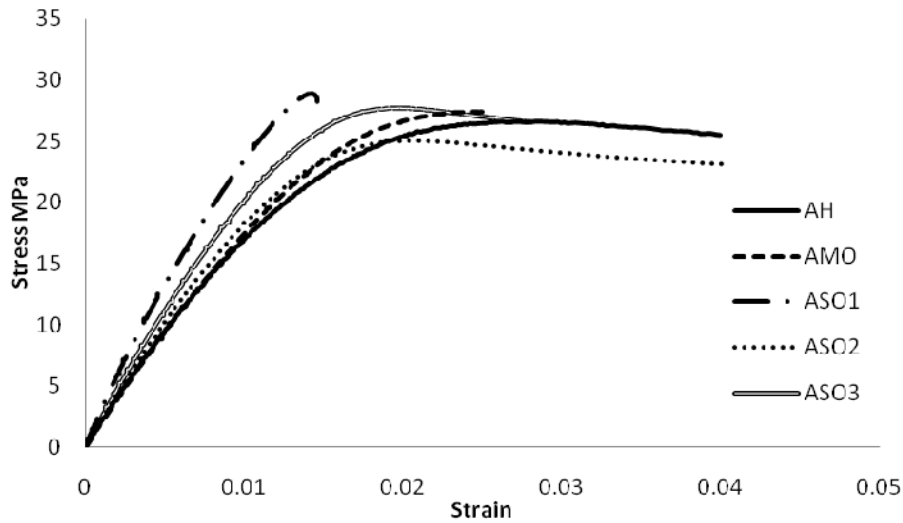


Figure 3.16 Effect of SiC powder and vacuuming on Araldite-420

Due to the high surface area of the SiC, its particles can embed inside the Araldite-420 bundles and create a thin, strong film around them. However, compared

with nanotubes, the SiC has less effect on Araldite-420 strength. The morphology of the SiC particles has a great influence: on nanotubes, the needle shape and circular cross-section give the optimum surface area which increases the amount of reinforcing particles. With SiC nanopowder, its irregular shapes decrease the amount of reinforcing particles and when the amount is increased, it starts to work as a stress concentrator and micro-crack initiator, reducing the strength of the composite. If the number of particles increases, they start to agglomerate and create better shaped agglomerate that can attach itself better to the epoxies, but the bonds between these particles remain less than those between SiC particles and epoxy bundles.

The increase in the modulus of elasticity is due to the irregular shape of the SiC , which prevent the epoxy bundles from sliding on each other. Therefore, the strain amount will decrease, which increases the modulus of elasticity. The effect of SiC on Araldite-420 can be summarized in Figures 3.17and 3.18.

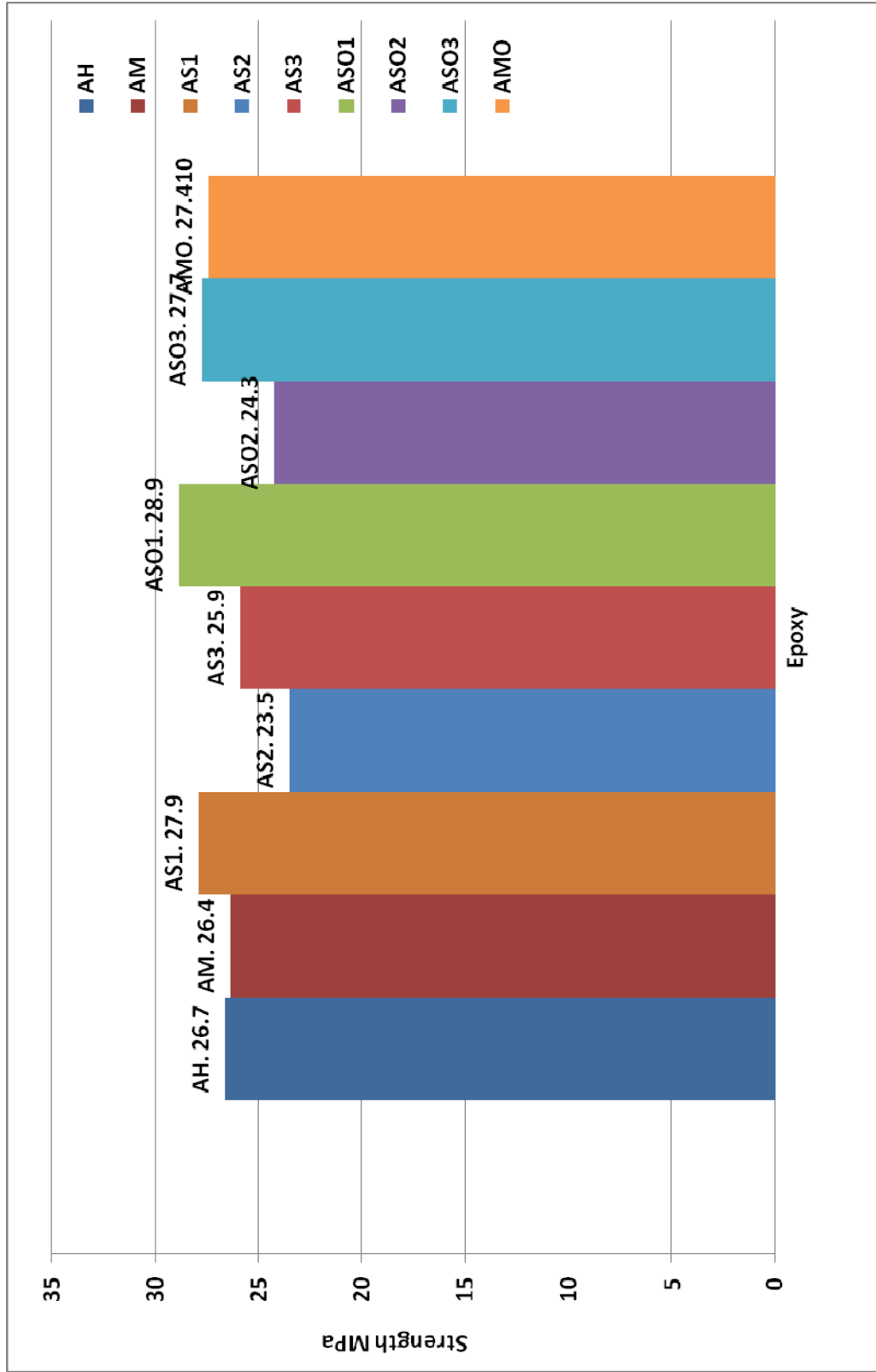


Figure 3.17 Effect of SiC on Araldite-420 strength

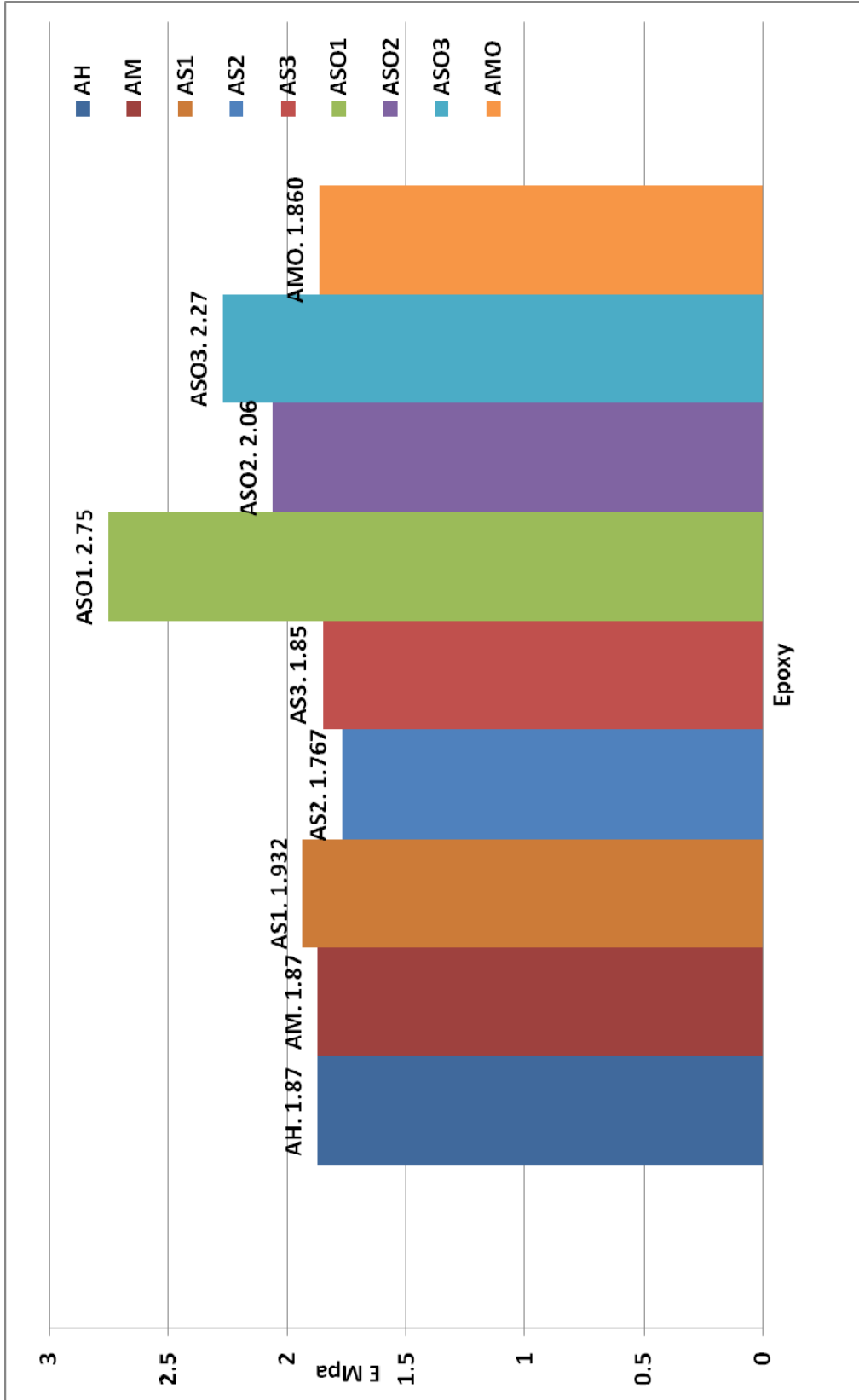


Figure 3.18 Effect of SiC on Araldite-420 elastic modulus

Figure 3.19 shows that the addition of SiC to Sikadur-30 by 1%wt will increase the strength from 18.6MPa and 22.8MPa, for hand-mixed and sonicated neat epoxy, to 25.9MPa. When the SiC percentage was increased, the strength decreased to a level lower than the hand-mixed epoxy: 16.4MPa and 17.4MPa for 2% and 3% SiC wt.

The modulus increased from 9.29MPa for the neat sonicated Sikadur-30 to 11.63, 10.56 and 11.39MPa for 1%, 2% and 3% SiC respectively.

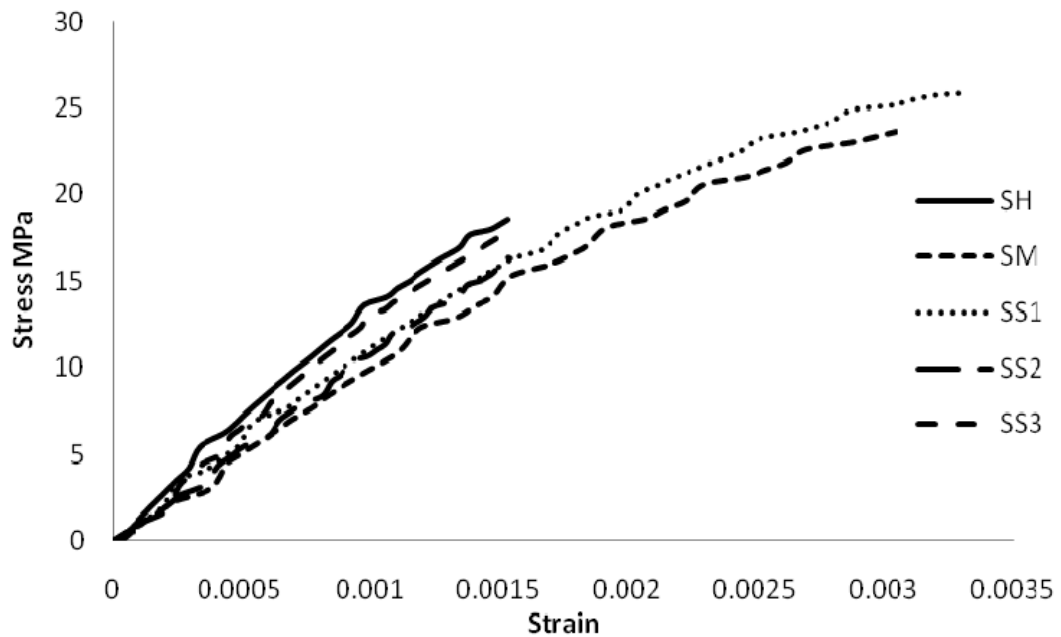


Figure 3.19 Effect of SiC on Sikadur-30

At a low strain level, the agglomerated particle increased the stiffness of the material, but at a high strain level, the stress concentration caused by the agglomerated particle initiated cracks, which caused the sample to fail quickly (Zhou, et al. 2009).

As mentioned before, adding SiC to the epoxy will increase the modulus of elasticity due to its irregular shapes that prevent the movement of epoxy bundles.

Figures 3.20 and 3.21 summarize the effect of SiC on Sikadur-30's strength and elastic modulus.

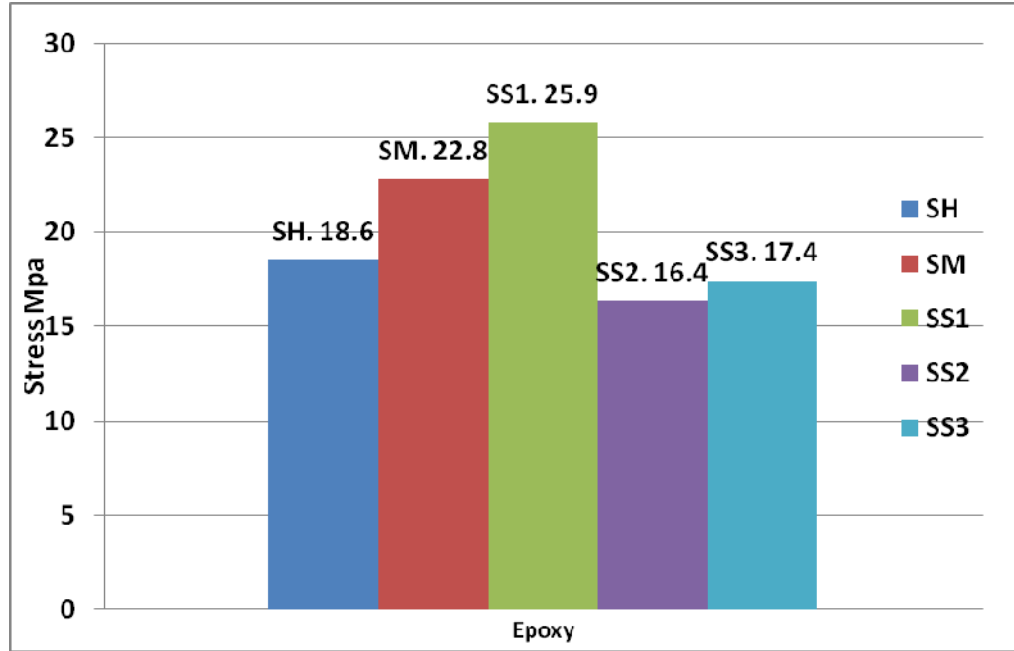


Figure 3.20 Effect of SiC on Sikadur-30 strength

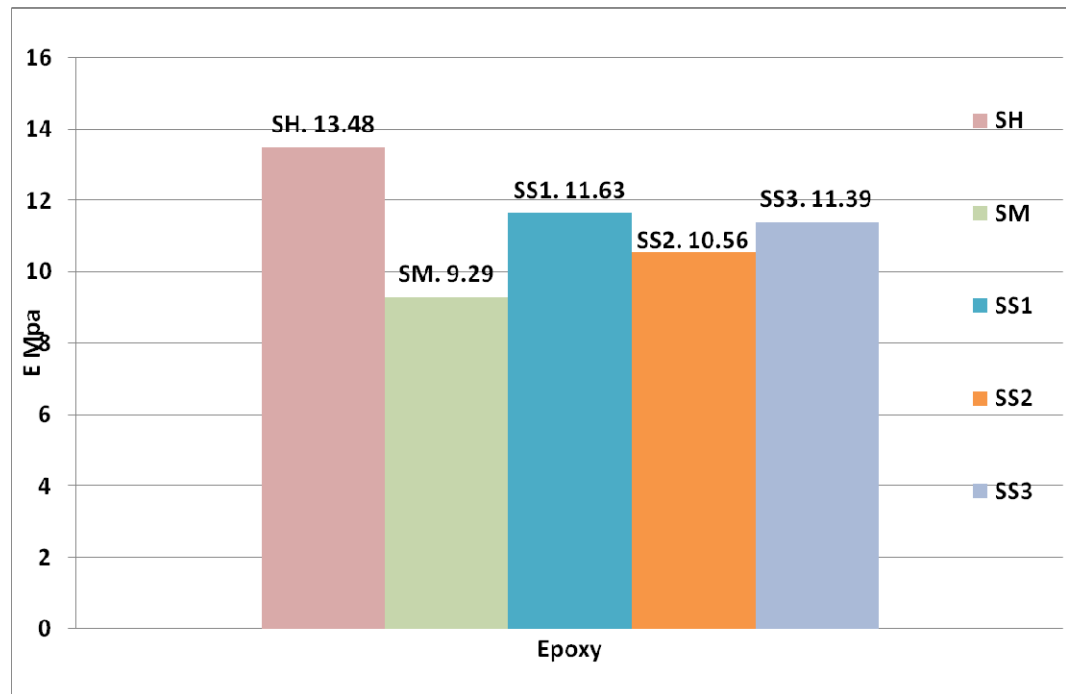


Figure 3.21 Effect of SiC on Sikadur-30 elastic modulus

3.2.9 Dispersion analysis

To evaluate the dispersion situation of the nanoparticles inside the epoxies, and to check whether the nanoparticles agglomerate inside the epoxies, a scanning electron microscope (SEM) was used to examine some of the samples. This method is the only direct way to analyse whether the nanoparticles are fully imbedded inside the epoxy and the agglomeration is incoherent. In most research to date, optical microscopes, scanning electron microscopes, and transmission electron microscope image-analysis have been employed to qualitatively assess the state of dispersion. However, these methods cannot yield the overall dispersion since the images show only very small fractions of the sample's cross-section.(Kim,et al. 2009-B)

This method gives only an indication of the dispersion because the observed area cannot be larger than 1 millimetre square. Figures 3.22, 3.23 and 3.24 show images from the SEM for sonicated, neat Araldite-420, 1% and 3% MWCNT in Araldite-420.

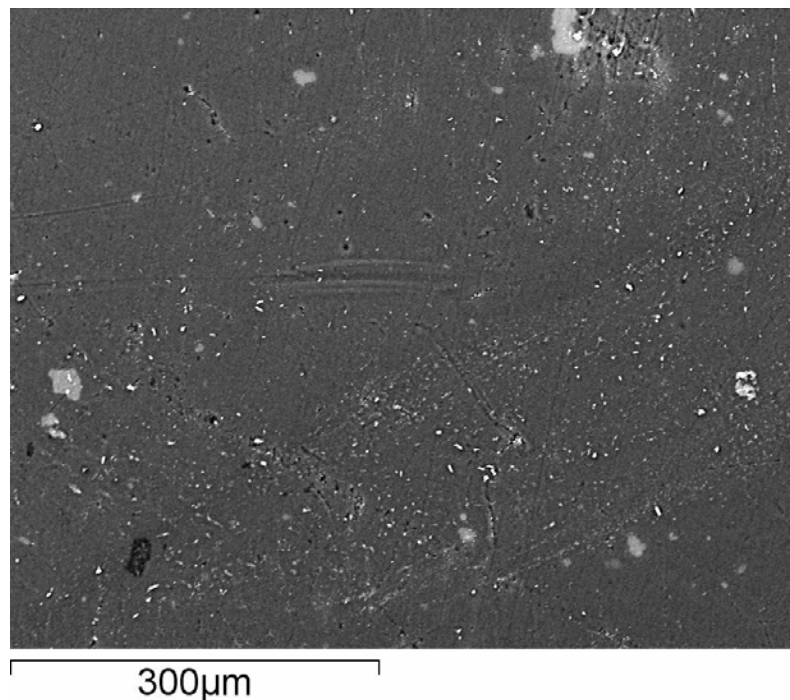


Figure 3.22 Hand-mixed Araldite-420 under SEM

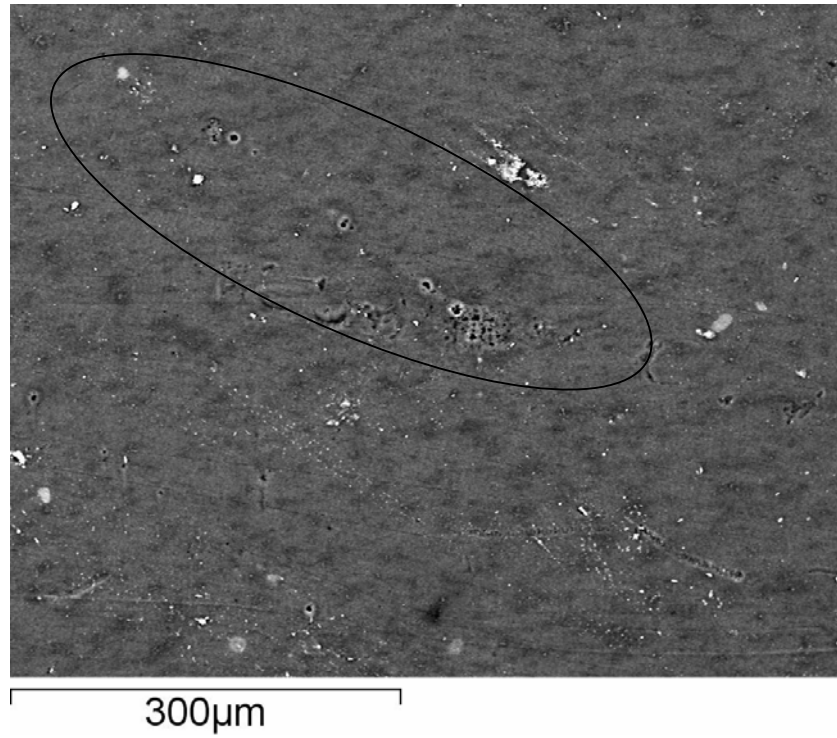


Figure 3.23 1% MWCNT embedded in Araldite-420 under SEM

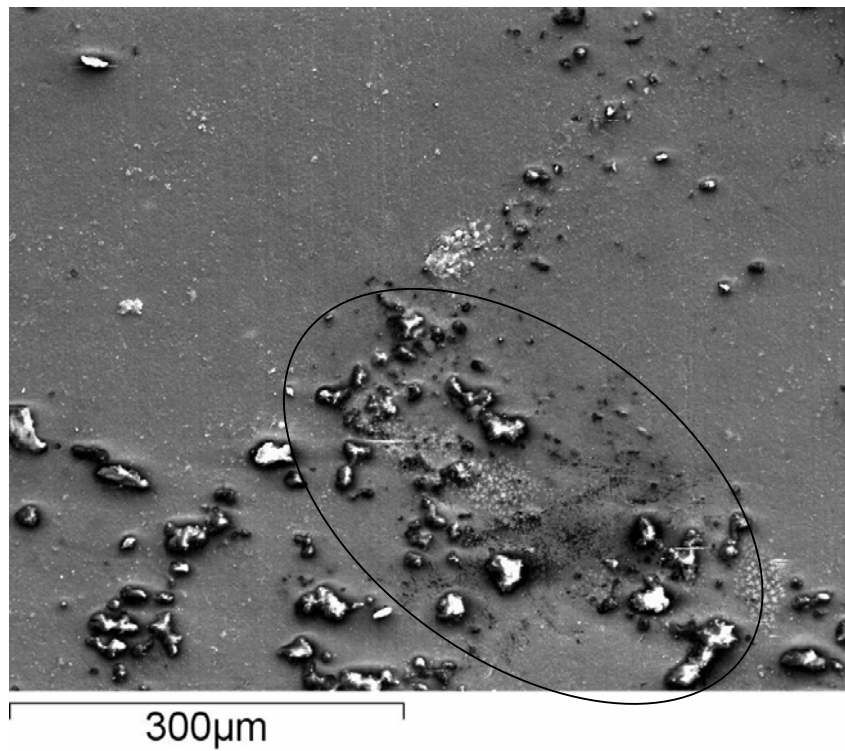


Figure 3.24 3% MWCNT embedded in Araldite-420 under SEM

Comparing Figures 3.23 and 3.24 with 3.22, the MWCNTs are clearly observed: for 1% MWCNT, the particles are barely recognizable. This is because nanotubes wetted by block copolymer are well separated so that the electrical conductivity (discharge) across the sample is blocked, and no contrast builds up between the CNTs and the epoxy matrix.

When the MWCNT percentage is increased to 3% (Figure 3.24) the agglomeration between the MWCNT is clear, but still distributed evenly across the examined section.

This indicates that the mixing method works efficiently and the density of energy and mixing time are sufficient to infuse MWCNT into Araldite-420.

3.2.10 Glass transition temperature tests

The glass transition T_g is a reversible change of the polymer between rubbery and glassy states, and the temperature at which this occurs. T_g can be measured accurately by Dynamic Mechanical Thermal Analysis (DMTA). In fact, DMTA is considered the most sensitive method for measuring a T_g .

The T_g is detected as a sudden and considerable change in the elastic modulus and an attendant peak in the $\tan \Delta$ curve. The damping property ($\tan \Delta$) is the ratio of the dynamic loss modulus to the dynamic storage modulus, and is related to the molecular motions and phase transitions. $\tan \Delta$ is therefore sensitive to all molecular movement occurring in polymers. $\tan \Delta$ is therefore sensitive to all molecular movement occurring in polymers. This underscores the importance of T_g as a material property, for it shows clearly the substantial change in rigidity that the material experiences in a short span of temperatures.

To find the effect of adding different nanomaterials to different epoxies, two samples of Araldite-420 and Sikadur-30, containing 0wt%, 1wt%, 2wt% and 3wt% from each nano additive (MWCNT and SiC) were tested using a Rheometric Scientific Inc. DMTA IV machine shown in Figure 3.25a. The samples (with dimensions of 40mm in length×5mm width×2 thickness) were placed in the DMTA fixture as illustrated in Figure 3.25b.

An oscillating strain (sinusoidal or other waveform) was applied to the samples with increasing surrounding temperature and the resulting stress developed in the sample was measured. The strain amplitude was set at 0.05 % with 1 Hz frequency. The temperature was raised from 25 °C to 150 °C with a heating ramp rate of 2 °C/minute. The output signals were analysed, and the rheological parameters were computed using established mathematical methods,.

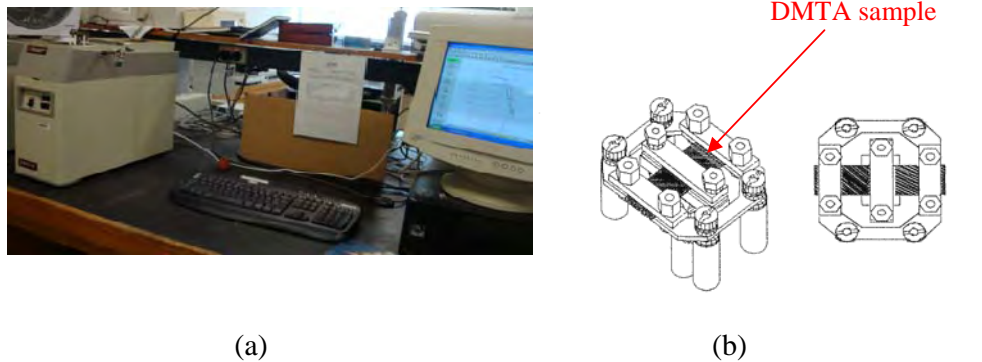


Figure 3.25 Dynamic Mechanical Thermal Analysis (DMTA) machine

All the specimens showed a glassy state followed by the rubbery state. Figures 3.26 to 3.29 show the recorded values from the DMTA data: the $\tan\Delta$ values varied with the temperature and reached their peak at almost the same temperature range as the pure epoxy.

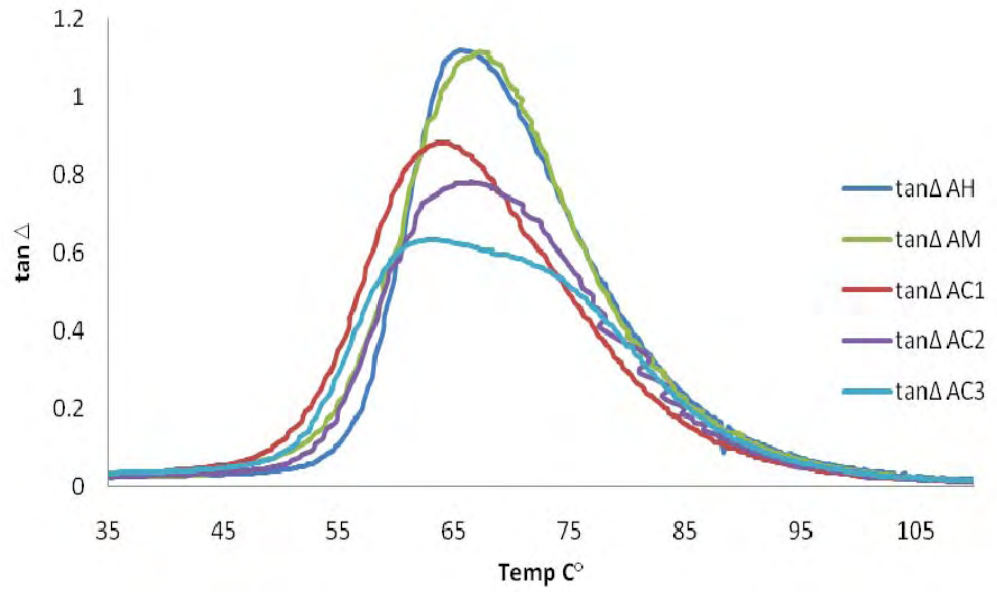


Figure 3.26 tan Δ variation with temperature for various MWCNT % in Araldite-420

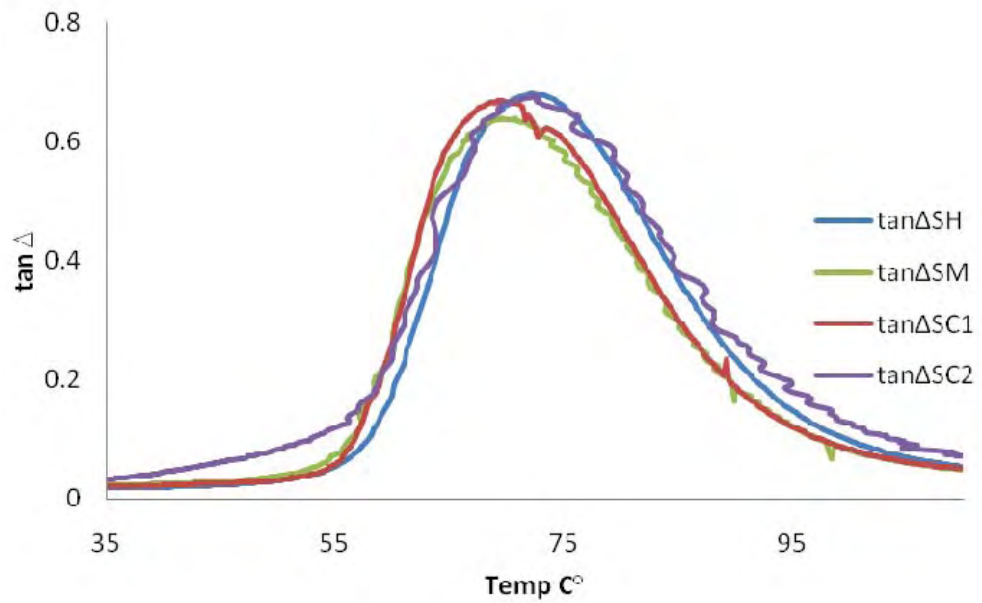


Figure 3.27 tan Δ variations with temperature for various MWCNT % in Sikadur-30

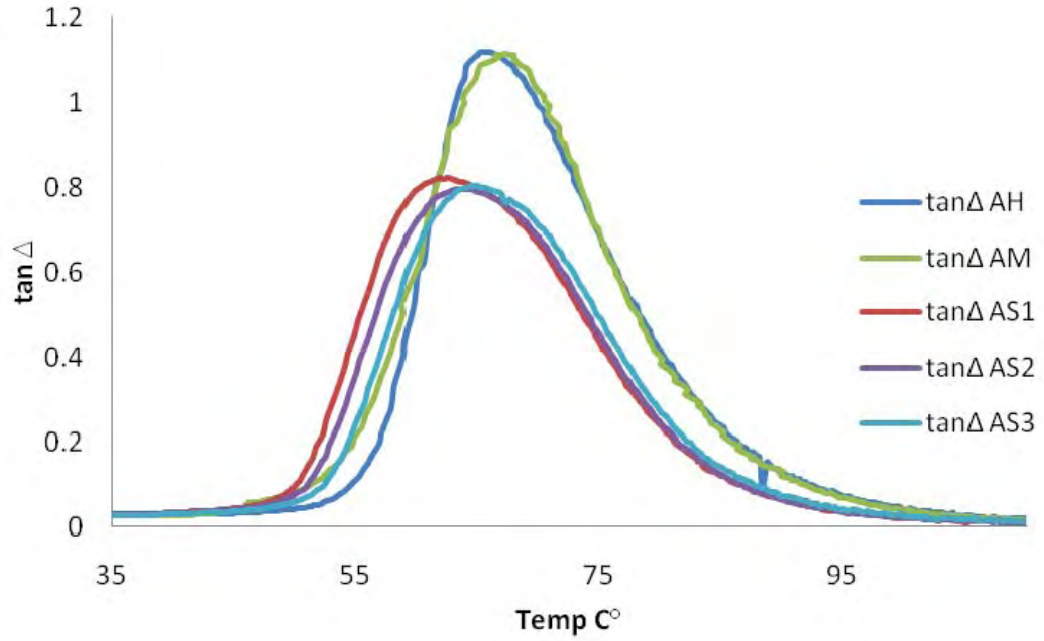


Figure 3.28 $\tan \Delta$ variations with temperature for various SiC% in Araldite-420

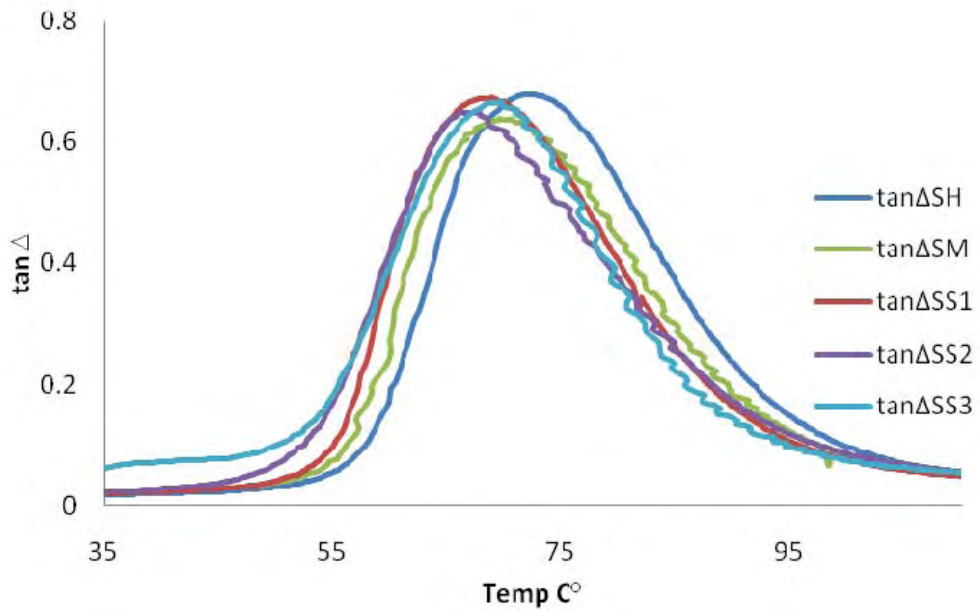


Figure 3.29 $\tan \Delta$ variations with temperature for various SiC % in Sikadur-30

The peak factor, Γ , is defined as the full width at half maximum of the $\tan \Delta$ peak divided by its height, and it can be qualitatively used to assess the homogeneity of the epoxy network. The neat epoxy had a high peak factor, which indicated low homogeneity in the epoxy network. For the nanophased epoxy, the peak factor decreased with higher MWCNT weight percentages. The lower peak factor for the nanophased epoxy indicates greater homogeneity. (Zhou et al.,2007).

From the results, the effects of the CNT and SiC nanopowder are negligible as can be seen in Table 3.3.

Table 3.3 T_g results for different epoxies and different nanomaterials using DMTA

		Araldite 420	Sikadur 30
Multi-wall Carbon Nanotubes (MWCNT)	0% Hand mixing	65	71
	1%	63	70
	2%	66	66
	3%	63	N/A
Silicon Carbide nanopowder (SiC)	0% Ultrasonic mix	68	70
	1%	63	69
	2%	64	67
	3%	65	69

This small (and even negligible) effect is due to the presence of nanoparticles in epoxy which will create a strong molecular interaction between them and resin molecules, which will hinder the interaction between the resin and hardener molecules.

This will impede the formation of the final cross-linked structure of the matrix during curing. As a result, the cross-linking density decreases, thereby lowering the T_g of the material.

In our nanoparticle-epoxy samples, two competing processes occur: nanomaterials limit the mobility of epoxy resin macromolecules, which reduce the T_g , but simultaneously reduce the cross-linking density and loosen the interfacial layers because of the under-cured binder in the material.

3.3 Carbon fibre reinforced polymer

3.3.1 General

With increased use, CFRP composite materials can have acquisition costs competitive with those of traditional construction materials while offering significant potential for reducing overall life-cycle costs. Additionally, CFRP composites are very light-weight, and the construction techniques used for CFRP composites can greatly speed the construction or repair process, offering significant savings in costs for both the owner and the user of the facility.

Finally, through careful selection of the fibres and resins used to manufacture CFRP plate, tailoring of the fibre architecture and selection of the appropriate manufacturing techniques and environments, CFRP composites can be fabricated with the desired structural properties and geometry.

CFRP laminates or plates essentially combine two constituent materials, i.e. the reinforcing carbon (or graphite) fibres and the polymeric matrix. The fibres contribute to the strength and stiffness of the composite, whereas the resin matrix holds the fibres together, providing toughness and environmental resistance. Laminates are expected to be more suitable for field applications where flat uniform surfaces are available for bonding.

The CFRP plates used in this project were supplied by MBrace Co.

3.3.2 Measured properties of CFRP

There is always a gap between manufacturer's claimed properties and the actual properties of materials. In order to obtain an accurate value for material properties, testing must be conducted on similar material. A series of tensile coupon tests were conducted to determine the actual properties of the materials used in the present study. The CFRP composite elastic modulus was determined using testing procedures in accordance with ASTM:D 3039.

Each CFRP plate test coupon had an overall length of 300 mm and average width of 50 mm. Two aluminium plates with a 3mm thickness had been attached to the coupon ends to distribute the load from the loading machine to the CFRP plate. The aluminium plate surfaces were sandblasted before the bonding application. Araldite-420 adhesive was used for bonding.

The adhesive was then allowed to cure according to the manufacturer's recommendation (7 days at least). Tension tests were carried out using the Shimidzu testing machine. Two strain gauges were installed at the centre of both sides of the specimen. The strain reading was used to find the modulus of the CFRP. An additional strain gauge attached perpendicular to the loading direction to read the transverse strains was needed to calculate Poisson's ratio. Figure 3.30 shows a schematic view of the specimen and Figure 3.31 shows the test set-up.

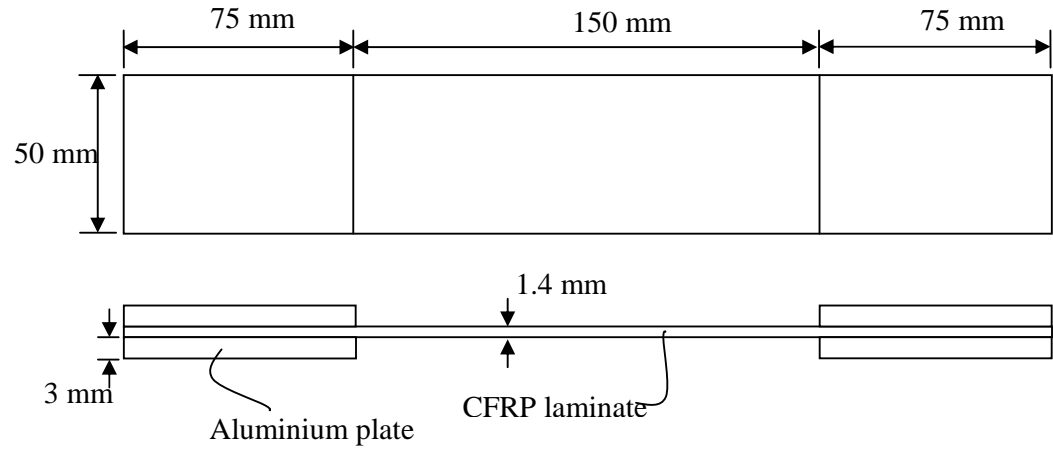


Figure 3.30 Schematic view of CFRP coupon (not to scale)



Figure 3.31 Test set-up on the Shimidzu testing machine

The tensile strengths for the specimens ranged from 2859MPa for CP1 to 2868 MPa for CP2 with modulus of elasticity of 208 and 209 GPa for CP1 and CP2 respectively, as shown in Table 3.4.

Table 3.4 Test results of CFRP laminate (BASF Construction Chemicals)

CFK 200/2000 CFRP Laminate	Manufacturer properties	C1 test results	C2 test results
Ultimate tensile strength	2400MPa (min)	2859MPa	2868MPa
Ultimate strain	1.2%	1.4%	1.5%
Modulus of elasticity	205 GPa (min)	208GPa	209GPa

Similar failure modes were observed in the tests. Failure modes of CFRP laminate specimens are shown in Figure 3.32, which shows ruptured and shredded fibres near the centre of the specimen. A smell of burning plastic was noticed at the failure times which indicated the large amount of energy that was released.



Figure 3.32 Failure modes of the CFRP laminate coupon specimens

Figure 3.33 shows the stress-strain diagram for CFRP plates compared with steel. Poisson's ratio was calculated to be 0.21. As can be seen in Figure 3.34, the laminate coupon shows a linear elastic behaviour until failing in a brittle mode.

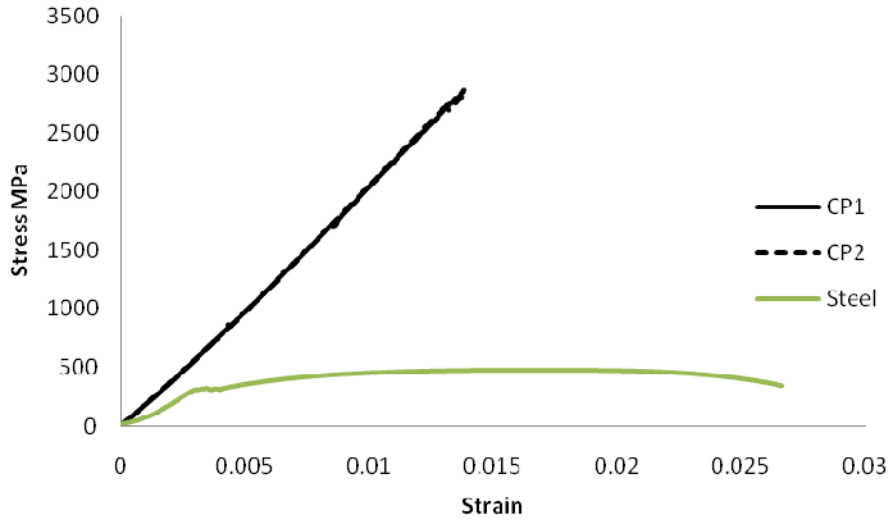


Figure 3.33 Stress strain curve for CFRP laminate and mild steel (measured)

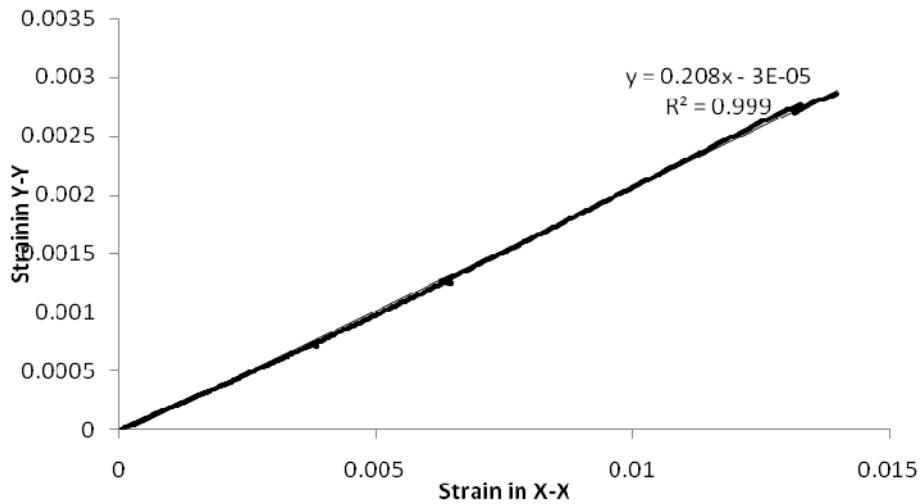


Figure 3.34 Strain curve for CFRP laminate in two perpendicular directions

3.4 Measuring properties of steel

Figure 3.35 shows a steel coupon specimen and the tested stress-strain responses of the steel are illustrated in Figure 3.36. Steel plates came in different

batches for the whole project. Coupon tests were performed in accordance with AS 1391 (SAA 1991). The tensile strength of different batches of steel ranged around 480MPa.



Figure 3.35 tested steel coupon specimen

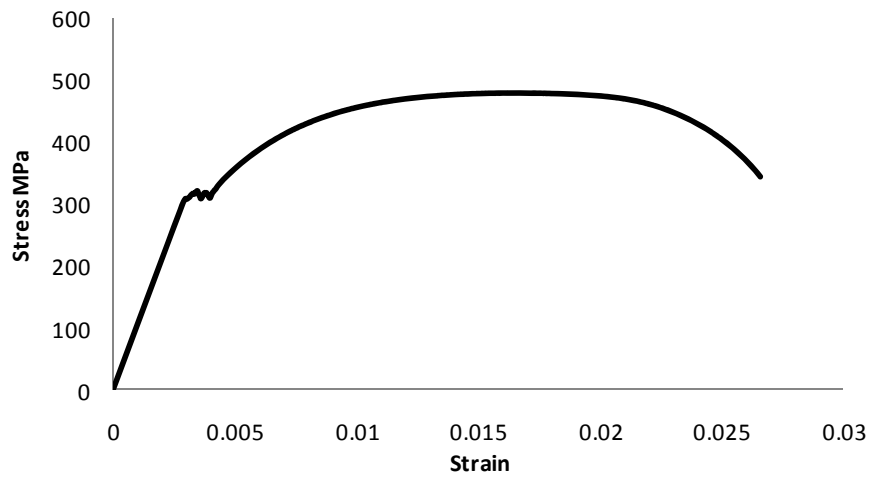


Figure 3.36 stress-strain curve of the tested steel

3.5 Summary

In this chapter, results of mechanical and thermal tests have been reported to find the effect of adding MWCNT and SiC nanopowder to commercial construction epoxies, Araldite-420 and Sikadur-30. The results show:

- Probe sonication is not only an efficient method to infuse MWCNT and SiC powder into the chosen epoxies, as indicated directly by SEM and indirectly by the $\tan\Delta$ curve shapes, but also increases epoxy homogeneity.
- The optimum percentage of MWCNT added to Araldite 420 is 2% wt. less than this percentage of MWCNT is not sufficient as a reinforcement and starts to work as impurities when the percentage exceeds this figure.
- Sonication of 1% of SiC powder then vacuuming Araldite-part-A gives the optimum increment for the elastic modulus of 2.75MPa compared to 1.86MPa for vacuumed, neat samples.
- The increments in strength and elastic modulus of Sikadur-30 when adding MWCNT and SiC nanopowder are due to the sonication process, and the effect of nanoparticles is negligible.
- The addition of MWCNT and SiC to the studied epoxies has a negligible effect on the T_g .

Chapter Four

Experimental Investigation of CFRP-steel Joints Using Different Nanoparticle-enhanced Epoxies

4.1 Introduction

The construction boom after World War II resulted in a mature infrastructure network across the world. Lately, the issue of maintenance and repair/upgrading of existing structures has become a major issue, particularly in the area of bridges (Hii and Al-Mahaidi,2006). Due to their high strength and stiffness combined with lightness, CFRPs represent a better rehabilitation choice than the typical metallic fixing process for structures (Kostopoulos et al., 2008).

However, the adhesive material is a key parameter for failure in CFRP systems. Therefore, enhancement of the adhesive properties can lead to an overall enhancement in structural behaviour.

In this project, different weight fractions and types of MWCNT and SiC nano-powder were mixed with structural epoxies to produce toughened adhesives, which lead to enhancement of the performance of CFRP-steel joints. Single-lap joint specimens were prepared, using enhanced epoxies, and the ultimate failure strengths were experimentally measured.

The 3D image correlation photogrammetry system (ARAMIS) was chosen to measure the strain along the bond length of the single lap CFRP-steel joints. While the theory and

development of the algorithms for image correlation are presented elsewhere (Mikhail et al., 2001 and Linder,2006, among others). A comparative study of a conventional strain measurement device, such as a strain gauge, was used to test the robustness and accuracy of the technique.

4.2 Specimen materials, preparation and testing set-up

In the present experimental program, specimens of 50mm width, MBrace 2000/200 CFRP laminate were selected to be attached to steel plate by Araldite-420 and Sikadur-30 adhesive. The steel plates used in the experimental series had dimensions of 250 mm length, 50 mm width and 12 mm thickness. The measured properties for all materials are reported in Chapter Three.

In every adhesive-containing bond, cleaning and sometimes roughening of the bonding surface is essential to ensure no impurities will affect the bond and to create additional bonding area to maximize bond strength.

The bonded steel surface was cleaned of oil or dust particles using acetone then sandblasted to remove the stain particles and to maintain better mechanical interlock. To ensure the thickness of the adhesive layer, 5 pieces of 2-3 mm long, 0.5mm diameter wires were attached on the four corners and centre of the steel bonding surface. These wires prevented the epoxy layer from becoming thinner after pressing the CFRP onto the steel plate. The CFRP laminates were cut to 300mm length and the adhesives mixed according to the previously-mentioned procedure (see Chapter three). The pre-prepared mixed part A and B adhesive was then applied along the bond length of the steel plate for

100mm bonding length. Then, the CFRP laminate was placed on top of the adhesive and gentle pressure was applied. The extra epoxy and air bubbles were wiped from the sides of the steel plate. A 300kg/m^2 pressure was applied on the face of the CFRP laminate and left for 24 hrs. Then the pressure was removed and the samples were left to cure at room temperature for 7 days. Meanwhile, two aluminium plates 3mm thick 100mm long and 50mm wide were attached to the CFRP laminate free end on both sides using Araldite-420. These two plates worked as a gripping end and helped distribute the stress across the gripping area without stress concentration.

Before the test took place, another steel plate 50mm wide, 100mm long and 14mm thick was pin attached to the steel plate free end. This additional plate increased the total gripped thickness of the original plate to assure the loading axis was aligned such that it passed through the tested sample without any moment. A schematic view of a specimen is shown in Figure 4.1.

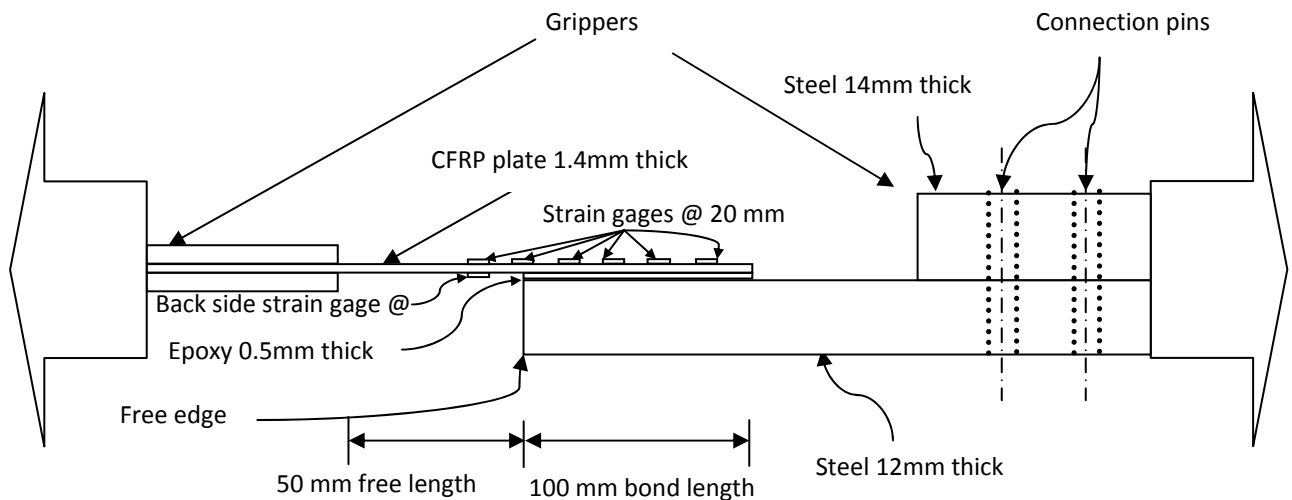


Figure 4.1 schematic view of a specimen

A total of 47specimens were prepared. The samples are summarized in Table 4.1.

Table 4.1 specimen test programme

Nanoparticles	Percentages	Araldite-420	Sikadur-30
MWCNT manufactured by Sigma-Aldrich Co	0% Hand mixing	3samples	2 samples
	1%	6 samples	2 samples
	2%	2 samples	2 samples
	3%	2 samples	NA
MWCNT manufactured from NTP (N series)	1%	4 samples	NA
	2%	4 samples	NA
	3%	4 samples	NA
Silicon Carbide (SiC)	0% Ultrasonic mix	2 samples	2 samples
	1%	2 samples	2 samples
	2%	2 samples	2 samples
	3%	2 samples	2 samples

Due to the differences between the adhesives used, the nanoparticles (types and percentages) and mixing methods, a coding scheme is used to differentiate between the specimens. The first letter C differentiates the code from the adhesive naming system. Then the epoxy type (A for Araldite-420 and S for the Sikadur-30) is followed by the additives: C for the MWCNT and S for SiC powder. Then, the mixing method is recognized by M for mechanical-ultrasonic mixing without additives, H for the normal hand mixing without additives refers to MWCNT purchased from NTP suppliers. The first number is for the weight concentration percentages of the additives (1%, 2% and 3%), and the last number is for the sample number. Figure 4.2 shows the coding scheme.

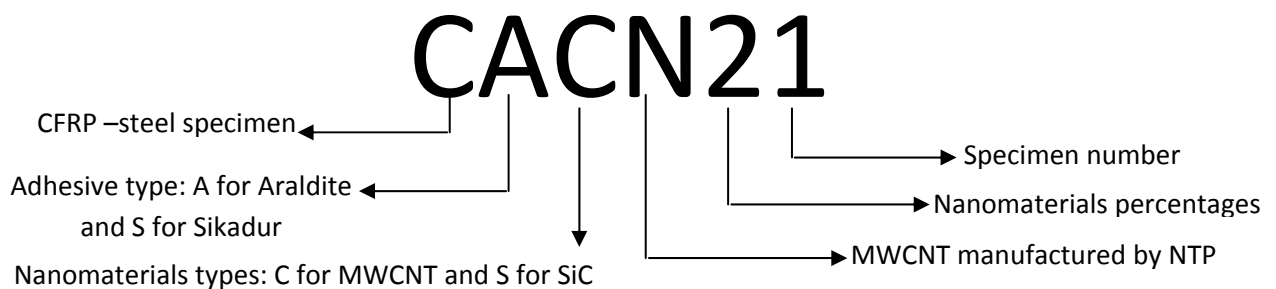


Figure 4.2 Specimen coding scheme

Six foil strain gauges were attached on the top of the CFRP laminate surface; one at the joint, one at the free length and 4 others every 20 mm along the bonded length, as shown in Figure 4.1.

Each specimen was loaded in tension on a 500 kN capacity Shimidzu testing machine with a loading rate of 2 mm/min at room temperature. Figure 4.6 shows the test set-up in the Shimidzu testing machine.

4.3 Evaluation of testing setup

To ensure the effectiveness of specimen arrangements , and to assure that there were no bending created through the CFRP laminate, a sample with the same properties as that in Figure 4.1 was tested with strain gauges only at the free length of the CFRP laminate across the CFRP width on top and bottom. These gauges checked whether there were stress differences due to misalignment of the tensioning process across the thickness of the laminate. Araldite-420-hand mixing was used to attach the CFRP laminate to the steel plate. The strain gauges arrangement on the CFRP laminate free length on both sides is shown in Figure 4.3.



Figure 4.3 Top-view for CAH03 specimen

In Figure 4.4, the strains of three different positions of CFRP laminate from top and bottom sides are calculated. The figure shows that the strain curves for the three different positions are approaching the 45° line, which confirms the equality of the collected strain readings for three different positions. Hence, as there are no stress differences across the CFRP laminate, no moment changes were expected.

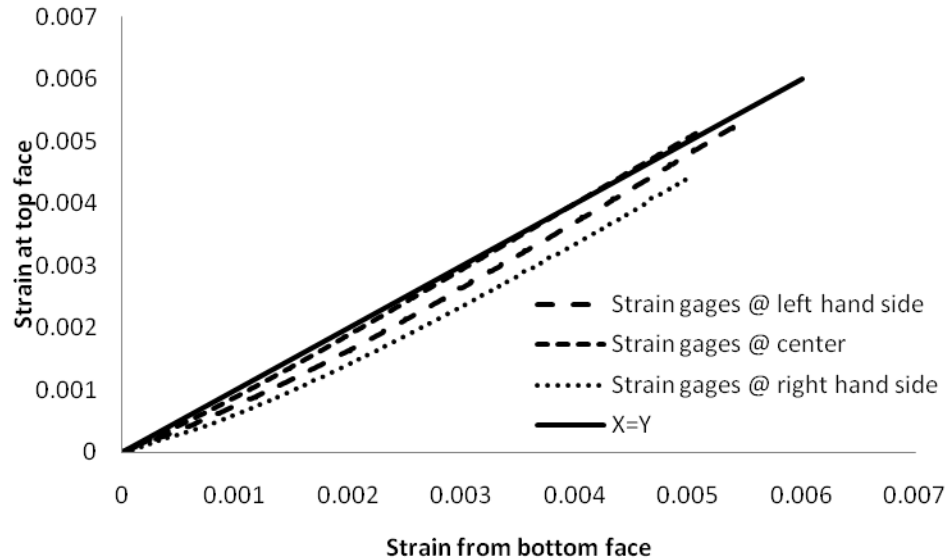


Figure 4.4 Strain from top and bottom sides of the specimen

4.4 Strain calculation method: Photogrammetry

4.4.1 Introduction

Photogrammetry is a technique for determining the three-dimensional geometry (location, size, and shape) of physical objects by measuring and analysing their two-dimensional photographs. (Fraser, 2001)

Photogrammetry has many attributes which make it an ideal tool for many engineering fields like topographic mapping, architecture, manufacturing, and quality control.

The advantages of using the non-contact strain measuring methods can be summarized as follows:

- (1) It is a non-contact technique that is capable of measuring difficult-to-access structures;
- (2) It is less labour-intensive;
- (3) It records a large amount of geometric information in a short time period by acquiring images;
- (4) It allows revisiting the visual records and performing additional analysis at a later time; and
- (5) It can be used as a convenient tool for routine measurement applications.

Another advantage of photogrammetry over traditional gauges is that the former can measure 3-dimensional displacement, while the latter measure deflection in only one direction.(Ruinian,et.al.,2008)

Many researchers at Monash University have used the ARAMIS system to study CFRP behaviour with different materials: Hii and Al-Mahaidi, (2006) used it to investigate the torsional strengthening of solid and box-section reinforced concrete beams with externally-bonded CFRP. ARAMIS has also been used to investigate the load-deformation characteristics of reinforced concrete T-beams strengthened with CFRP plates (Lee and Al-Mahaidi ,2008) and to study the effect of changing the bond length and epoxy type on strength in double lap steel joint (Sabrina,2007).

4.4.2 Principles and components of the Photogrammetry system

In photogrammetry, images are taken from camera stations positioned at close range to the object.

The technique in the ARAMIS system used in the present research is based on photogrammetry and uses ordinary light, rather than coherent laser light. The major components of the ARAMIS system are:

- Two digital high-speed cameras: 4M cameras with 50mm macro focal length lenses, computer-controlled, with resolution of 2048x2048 pixels. The maximum standard measuring volume for these cameras is 2000x2000x2000 mm³. The range of strain measurement is 0.05% to 100% and strain accuracy is 0.01%. These cameras work as digital data measurement devices that record and store information about the positions of the individual targets.
- High performance PC system to evaluate the signals from the cameras

Figure 4.5 shows the ARAMIS system components used in the present research.

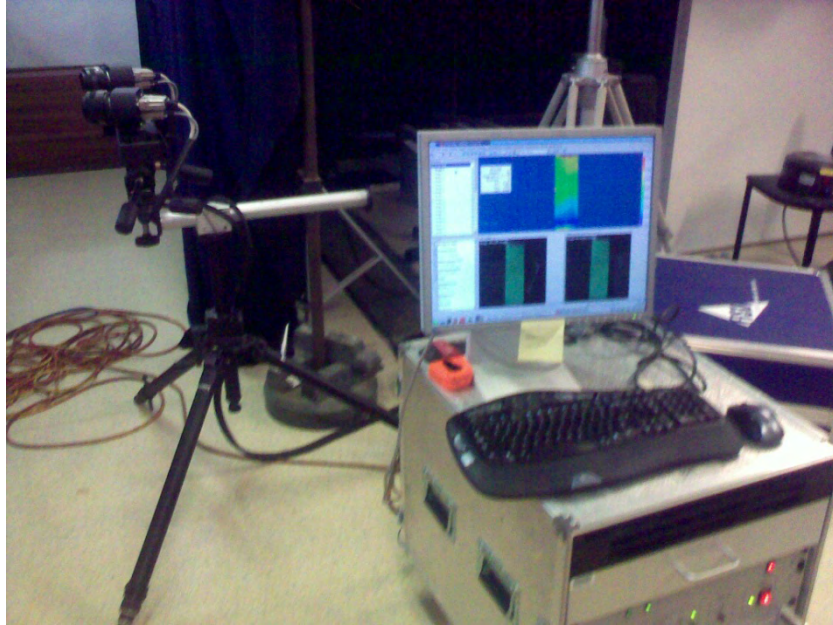


Figure 4.5 ARAMIS photogrammetry system

A random pattern with good contrast (white matt painting with a sprinkling of black spray) is applied along the surface of the bond length of the tested sample and deformed along the bond length. The collection of the data from the sample start by initial image processing to define a set of unique correlation areas known as macro-image facets, which are then tracked in each successive image with sub-pixel accuracy. The deformation of this sample under different load conditions is recorded by the cameras and evaluated using digital image processing. Using photogrammetric principles, the 3D coordinates of the surface of the specimen, which are related to the facets at each stage of load, can be calculated precisely. The results are the 3D contour of the component, the displacement, as well as the plane strain tensor. The strain distribution graph can be created for every stage (load level) individually and it is possible to see the image of every step of loading until failure.

Then, a secondary strain analysis is carried out using Microsoft EXCEL to synchronize the data from image processing with the data from the loading machine and, if applicable, with the strain gauges.

4.4.3 Comparing Photogrammetry and strain gauges results

To test the robustness of the ARAMIS system, two CFRP-steel samples were prepared and tested using foil strain gauges and the ARAMIS system simultaneously to collect the strain from the top surface of the CFRP laminate. Figure 4.6 shows the test set-up in the Shimidzu testing machine. The wiring shown from the bond length side connects the strain gauges mounted on the CFRP laminate. The cameras were calibrated prior to the test. The strain gauges were set to provide data 3 times per second. Images were recorded at various load stages of the specimen according to the input value of delay, which was 5 sec in this study. Therefore, the fifteenth reading from the strain gauges matched the first reading of the photogrammetry system and so on. In this way, testing was continued until failure of the specimen. Every effort was made to start the two systems (photogrammetry and load machine) at the same time.



Figure 4.6 Specimen fixed to test machine ready for testing with aid of strain gauges and ARAMIS system

Figures 4.7 and 4.9 show the comparison between the foil strain gauges readings and the ARAMIS system readings across the CFRP-steel bond length. The figures indicate that e ARAMIS results were in very close correlation compared with the strain gauges. Therefore, the photogrammetry system was used for the testing of the rest of the specimens reported in this chapter, except for the “N-type” MWCNT-Araldite-420 series.

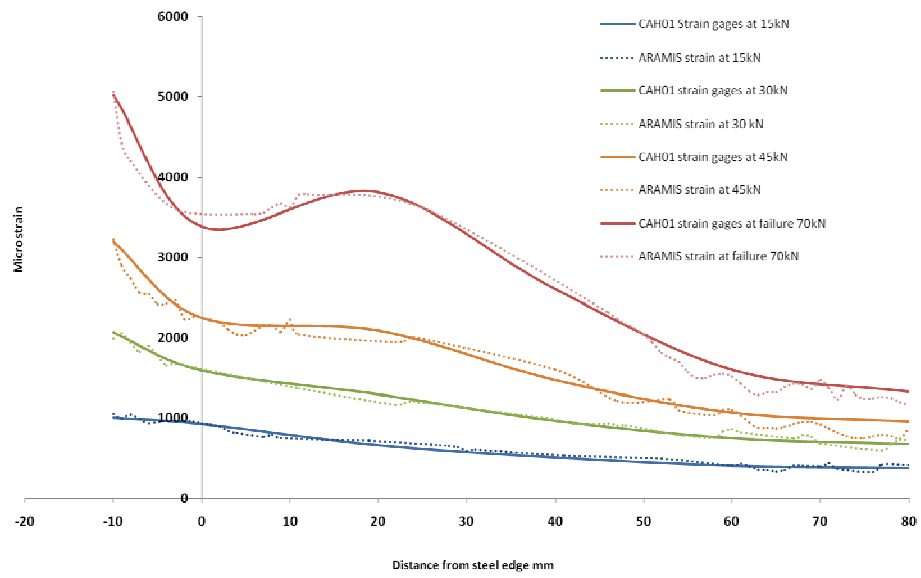


Figure 4.7 Strain distribution of CAH01 specimen along CFRP laminate surface by strain gauges and ARAMIS system

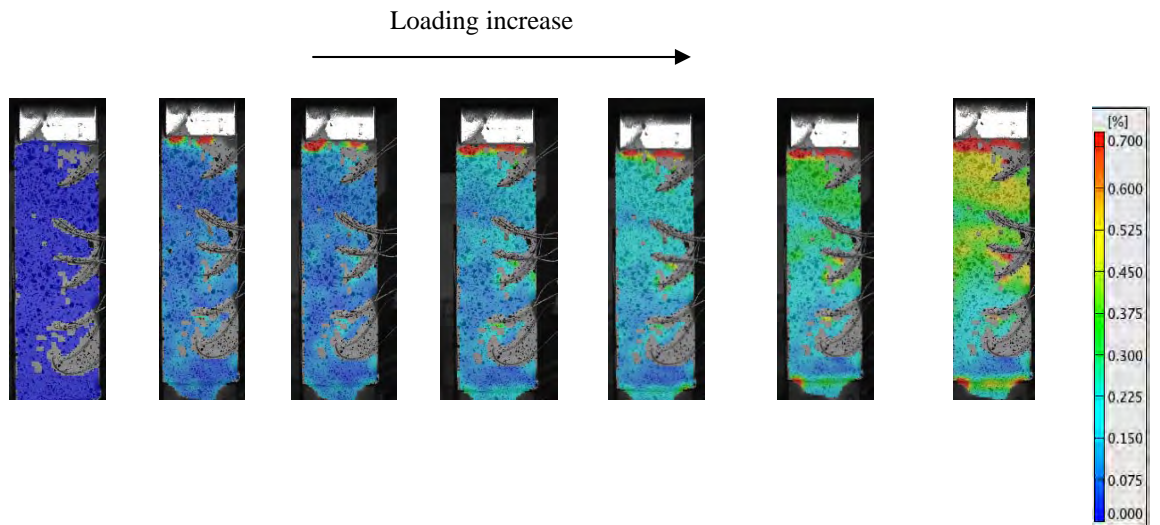


Figure 4.8 ARAMIS stages for CAH01

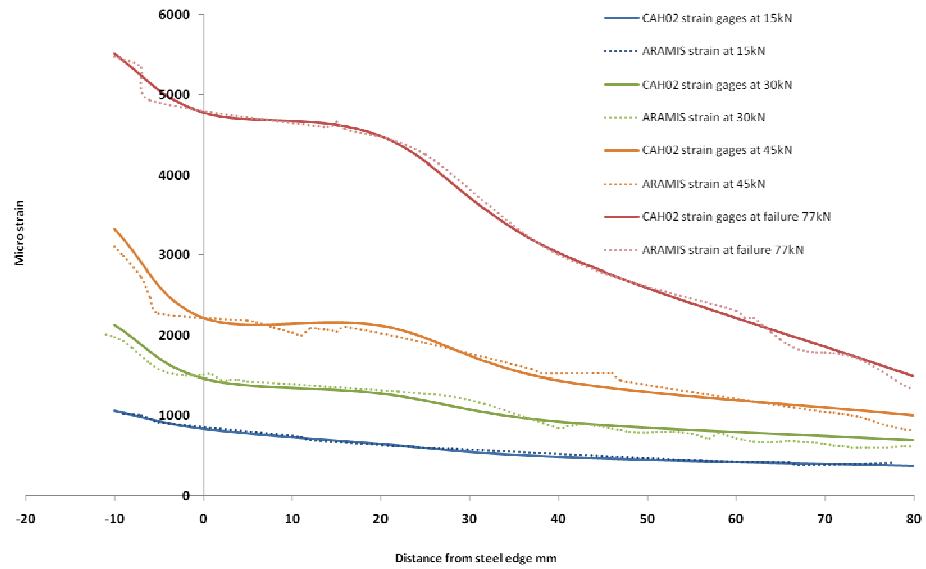


Figure 4.9 Strain distribution of CAH02 specimen along CFRP laminate surface by strain gauges and ARAMIS system

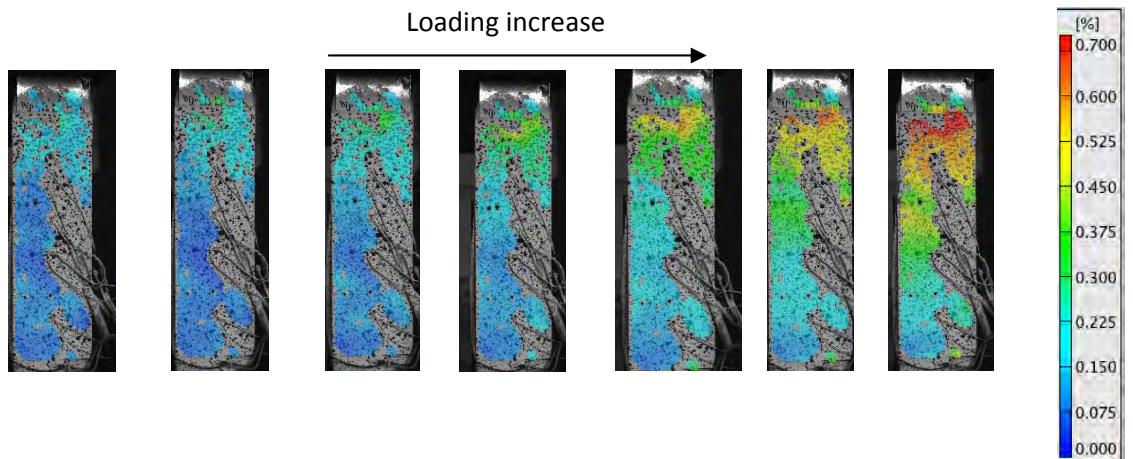


Figure 4.10 ARAMIS stages for CAH02

Figures 4.8 and 4.10 show the increments of the strain along bond length through the load stages as the loading increased compared with the original stage image.

It can be seen from the contour that the strain decreases from the loading edge to the end of the CFRP plate.

4.5 Effect of mixing method

As mentioned in Chapter 3, nanoparticles were mixed in the epoxies using the sonication mixing method. Since the sonication-only process does not affect Araldite-420 epoxy samples and has a positive effect on Sikadur-30 epoxy samples, it is worth studying the effect of sonication-only epoxies when used to bond CFRP laminates to steel. Also, it is essential to create reference data to study the nanoparticles additives effect.

Table 4.2 summarises the ultimate strength of the tested specimens:

Table 4.2 Ultimate stress of pure epoxy specimens

Araldite-420 specimens	Ultimate stress MPa	Sikadur-30 specimens	Ultimate stress MPa
CAH01	874.3	CSH01	654.3
CAH02	995.7	CSH02	661.4
CAH03	977.1	CSM01	735.7
CAM01	988.6	CSM02	725.7
CAM02	922.9		

Figure 4.11 shows the stress-strain diagram at unbounded length of CFRP laminate for hand- and sonication-mixed pure Araldite-420 specimens. The figure clearly shows that the failure mode is brittle, which becomes elastic all the way then breaks.

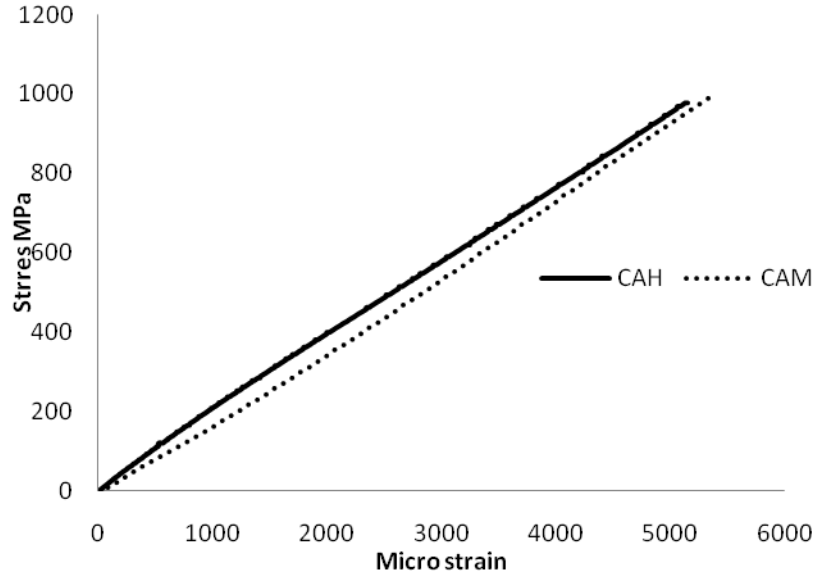


Figure 4.11 Effect of different mixing methods on Araldite-420 pure epoxy

Due to the homogeneity of Araldite-420 part-A particles, sonication has an impervious affect on the behaviour of the specimens compared to hand-mixed specimens. Figure 4.12-C shows failure surface images for CAM zooming using a light microscope up to 50X. The image shows clearly that the failure happened at the first layers of the CFRP laminate, and their traces can easily be identified on the failure surface. The epoxy thickness wire is partially covered by couples of CF that support the previous conclusion. This type of failure was repeated for CAH and CAM specimens as shown in Figure 4.12.

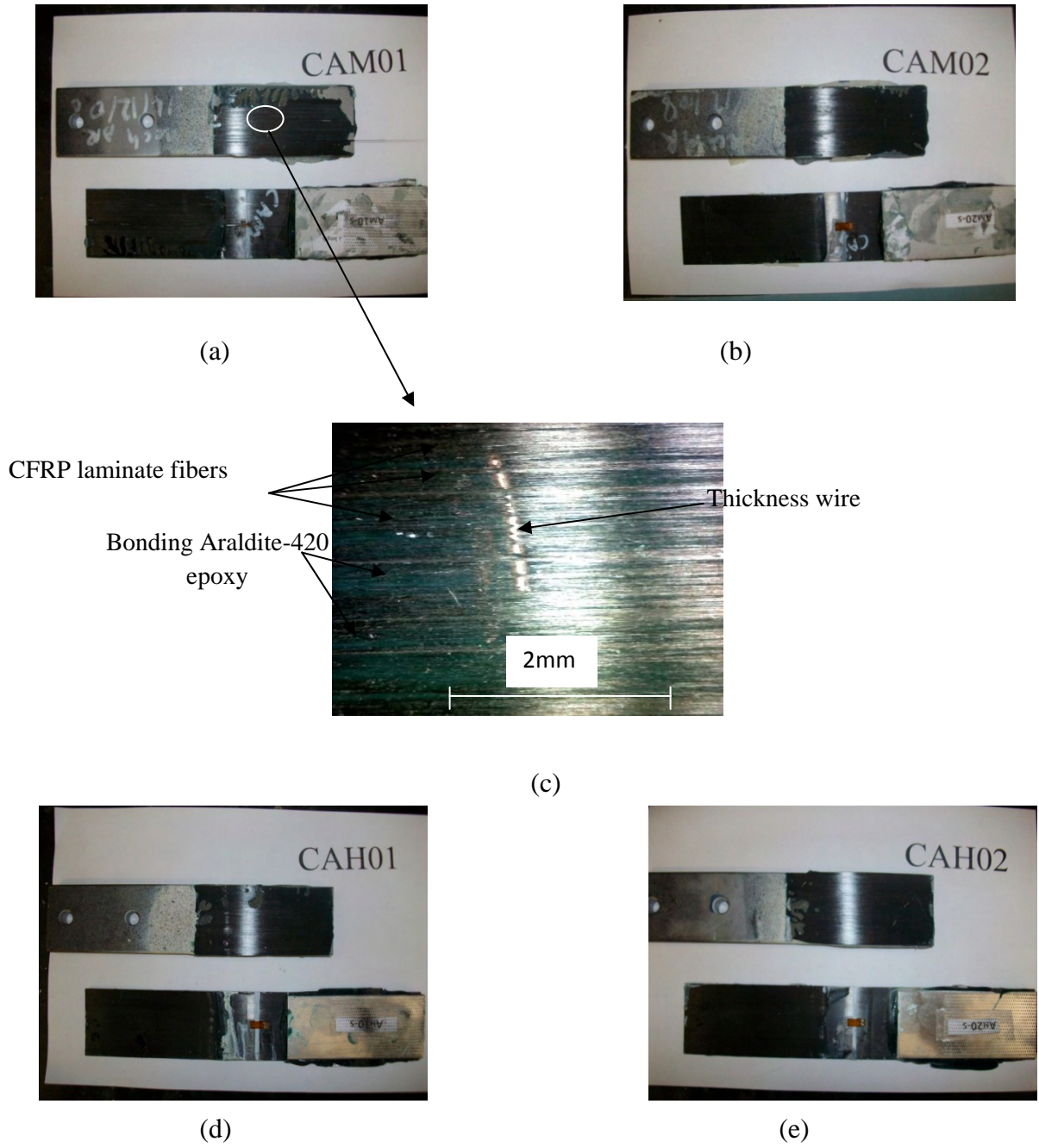


Figure 4.12 Failure surface of Araldite-420 pure specimens

Strain distribution across bonding length for CAM specimens is shown in Figure 4.12:

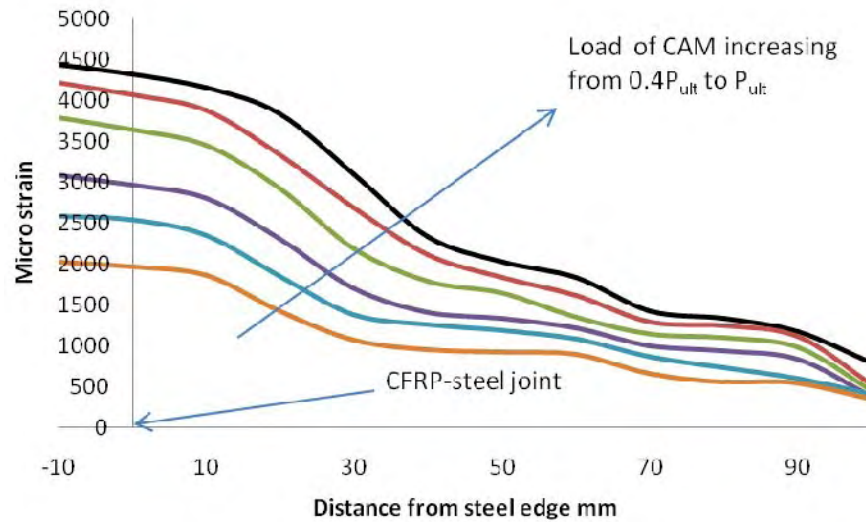


Figure 4.13 Strain distribution along pure sonicated Araldite-420 specimens

As with Araldite-420, Sikadur-30 pure specimens fail in a brittle pattern as shown in Figure 4.14. Sonication increases the homogeneity of Sikadur-30 particles, as previously explained in Chapter 3. However, the high filler content of the Sikadur-30 will effect negatively on the shear strength of the epoxy layer. The failure mode in Sikadur-30 specimens is partially delamination and partially failure in the epoxy layer, as shown in Figure 4.15.

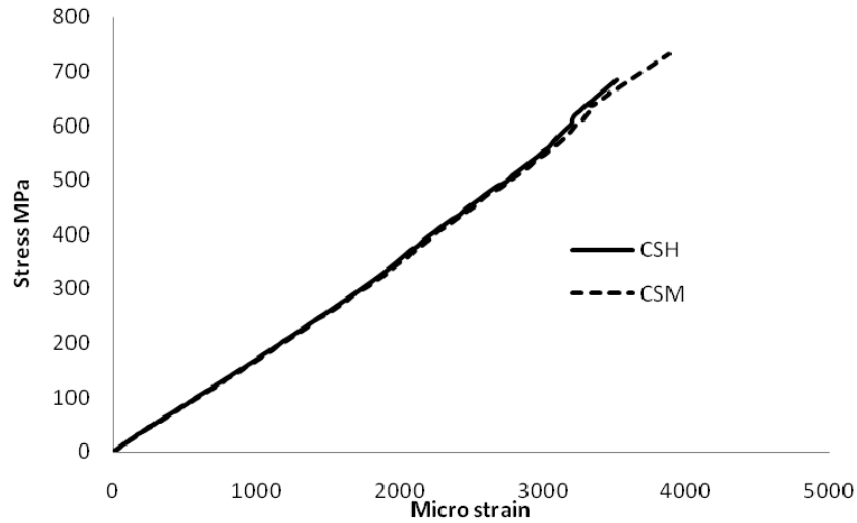


Figure 4.14 Effect of different mixing methods on Sikadur-30 pure epoxy

Figure 4.15 D and C, which shows images for CSH and CSM specimens taken by a light microscope, indicates that failures begin at the tip of the bonding length, near the steel edge, as a pure epoxy layer failure, where the thickness wires are free of epoxy or even embedded inside the epoxy. As the failure proceeds along the bond length, the failure mode changes to CF breakage and a trace of CFRP laminate embedded inside the epoxy layer starts showing at two thirds of bonding length. These fibres increase until a full layer of carbon fibre covers the epoxy layer.

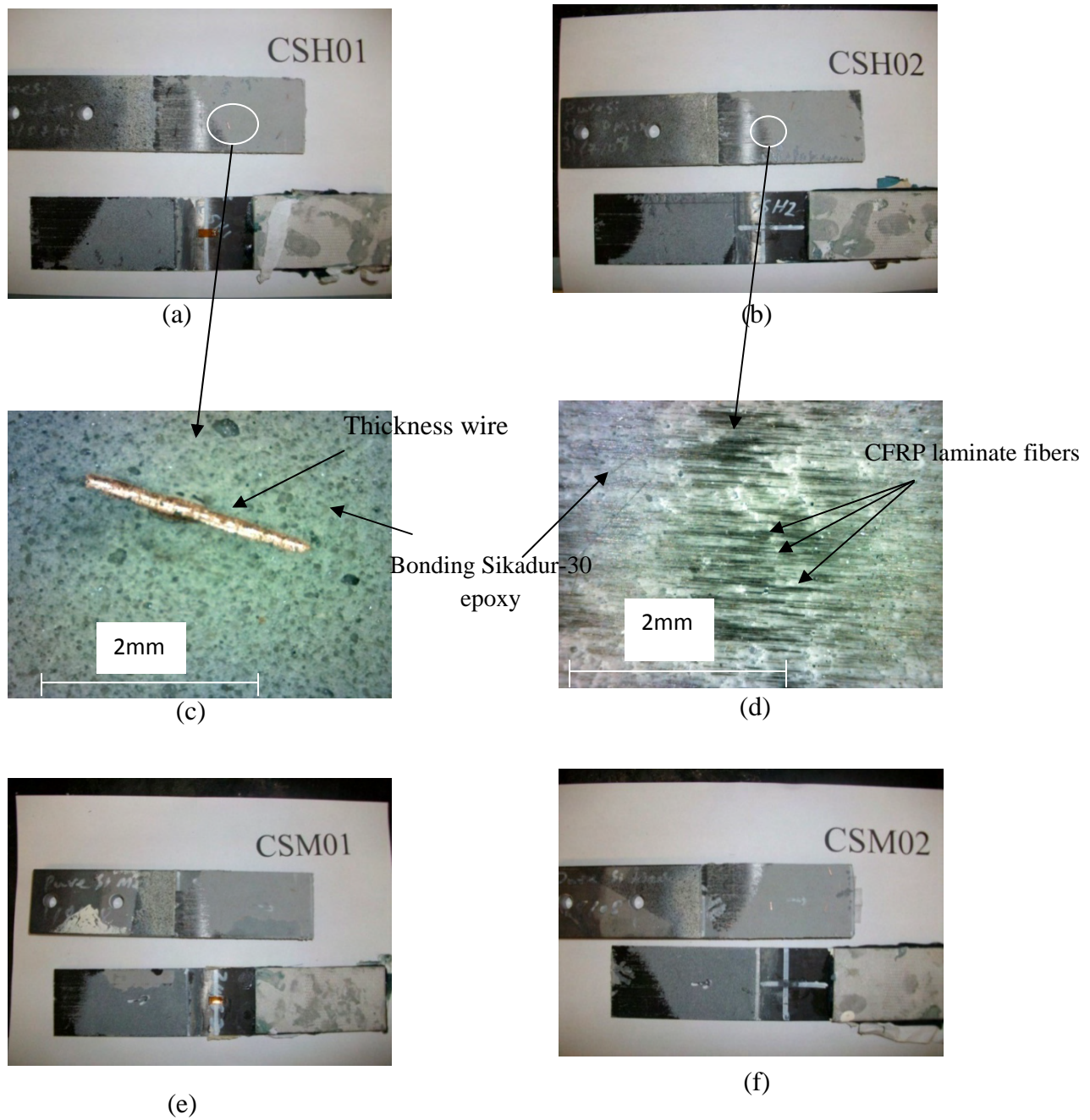


Figure 4.15 Failure surface of Sikadur-30 pure specimens

Figures 4.16 shows the strain distribution, using the ARAMIS system, along the bond lengths of CSH and CSM respectively. It is clear from the figure that strain gradually

decreases as the distance increases from the joint between the CFRP laminate and the steel.

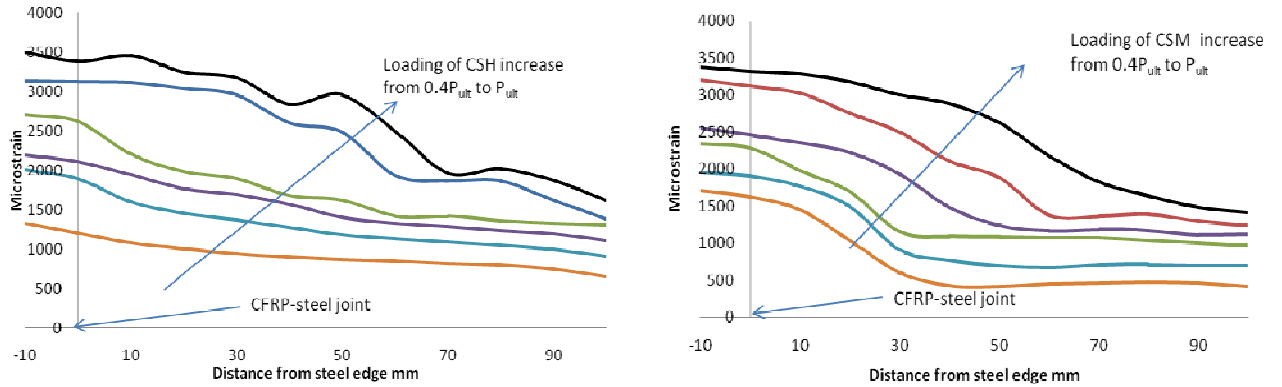


Figure 4.16 Strain distribution along pure sonicated and hand-mixed Sikadur-30 specimens

As demonstrated in Section 4.3, due to the small thickness of CFRP laminate, the strain variation across the laminate thickness, and both longitudinal and shear deformations of the steel plates are sufficiently small to be ignored. Therefore, the strain recorded at the outer laminate face can be considered bonding adhesive strain.

The stain is almost constant for the first 10 mm from the edge, because there is no resistance that may reduce or distribute the stresses. The constancy continues for a certain length of the bonding length; as the loading increases, this distance increases toward the middle of the bonding length then suddenly drops. A “drop point” is recognised at the first 20mm of the bonding length, increasing to reach 50 or 60mm as it approaches ultimate load.

This drop point is the point where the epoxy particles start distributing the stress across the bond length. As the load increases, the epoxy particles start to resist the stresses and distribute it to their neighbours which, in turn, resist and distribute, until the stress in the epoxy reaches a “saturation” point (epoxy ultimate strength) where it loses its ability to resist stress and distribute it across the bond length. This will happen when failure occurs.

In the CAH and CAM samples, the drop point started at 10mm from bonding length for $0.4P_{ult}$ and gradually increased to reach 25mm from the bonding length as the load reached P_{ult} . This small difference, compared with CSM and CSM specimens, is due to the small amount of elastic modulus that will affect stress distribution.

For CSM specimens, the drop point reached nearly 50mm along the bonding length, and 60 mm for CSH. The decrement in drop point location for CSM leads to the conclusion that as sonication increases the strength and decreases the elastic modulus (as mentioned in Chapter three), it also increases the strain distribution and shear strain resistance of Sikadur-30 particles.

4.6 Effect of adding nanoparticles

In recent years, CFRP systems modified with nanoparticles, known as “multiscale” composites as they are reinforced with micro-scale fibres and nanoscale particles, have drawn significant attention in the field of advanced, high-performance materials. Most of the efforts in multiscale composites research have been focused on improving the strength properties by dispersing nanoparticles in the bulk of the matrix.

This approach benefits from the micro-scale reinforcement provided by traditional fibres and from the complementary reinforcement on the nanoscale offered by nanoparticles.

To separate the effect of nanoparticles in epoxy used as adhesive from their effect if used as matrix, this study used nanoparticles of different types and percentages of MWCNT and SiC nano-powder to reinforce structural epoxies (Araldite-420 and Sikadur-30) to bond CFRP laminate on steel plates. The results are reported in the following section.

4.6.1 Effect of MWCNT

MWCNT has different effects on the epoxies used in the present study, as mentioned in Chapter 3. These effects are repeated when the epoxies are used to attach CFRP laminates to steel.

The MWCNT used had the following characteristics: diameter of 110-170nm, length 5-9micrometer and 90+% purity, manufactured by Sigma-Aldrich Co. The same procedure of mixing MWCNT with epoxies was followed. The ultimate strength results from the testing of CAC group specimens are summarised in Table 4.3.

Table 4.3 Ultimate stress of MWCNT specimens

1% MWCNT	Ultimate stress MPa	2% MWCNT	Ultimate stress MPa	3% MWCNT	Ultimate stress MPa
CAC11	1282.9	CAC21	1475.7	CAC31	1131.4
CAC12	1235.7	CAC22	1322.9	CAC32	1098.6
CAC13	1255.7				
CAC14	1152.9				
CAC15	1234.3				
CAC16	1282.9				

When the 1% of MWCNT is added to Araldite-420 epoxy, strength increases by 34% on average for hand-mixed Araldite-420 specimens. 2% of MWCNT gives the optimum increment in bonding of nearly 50% on average for hand-mixed samples. Only 20% increment in bond strength occurs when 3% MWCNT is added to the Araldite epoxy. Figure 4.17 shows the effect of adding different percentages of MWCNT to Araldite-420 epoxy. The figure shows brittle failure as different MWCNT percentages are added to Araldite-420.

Figures 4.18-4.20 show the failure surface images and the zoomed failure sections.

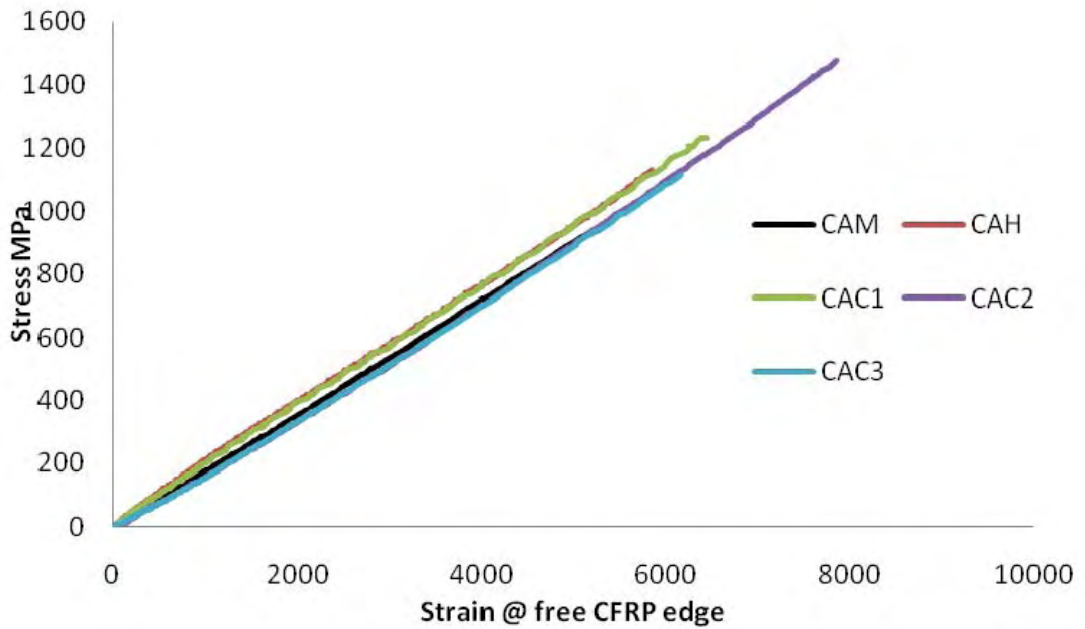


Figure 4.17 Effect of adding MWCNT to Araldite-420

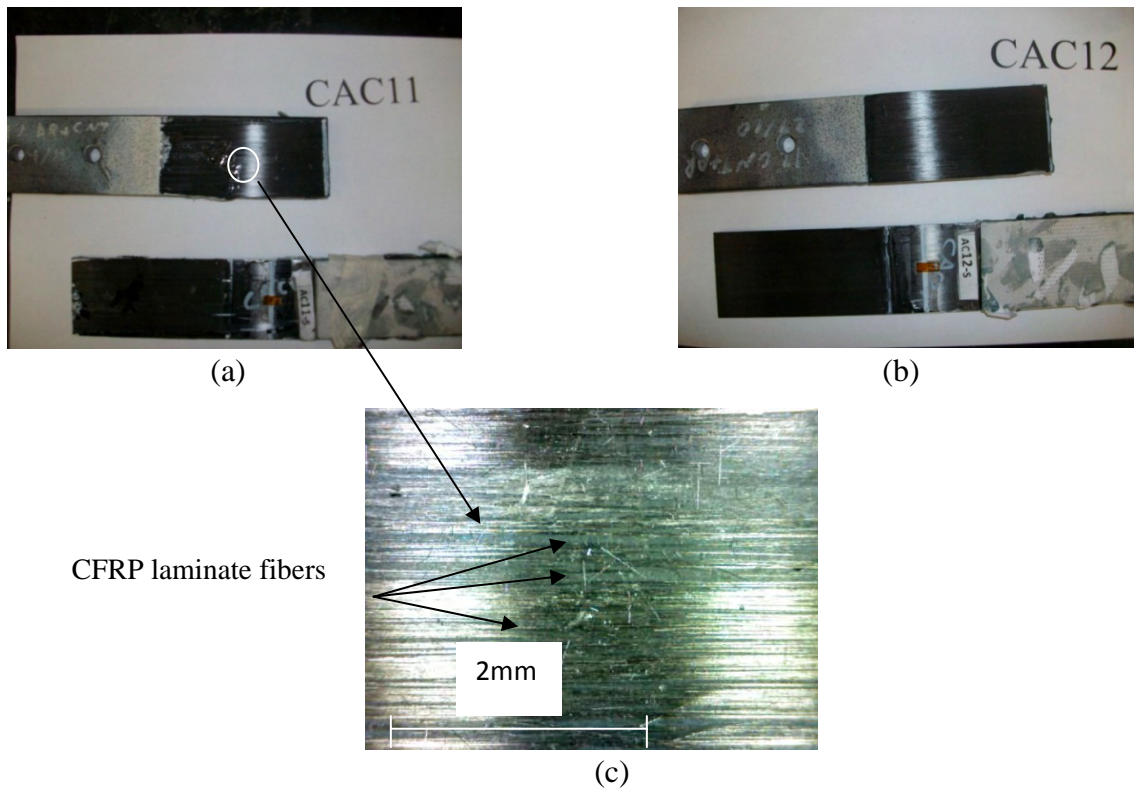


Figure 4.18 Failure surface of CAC1

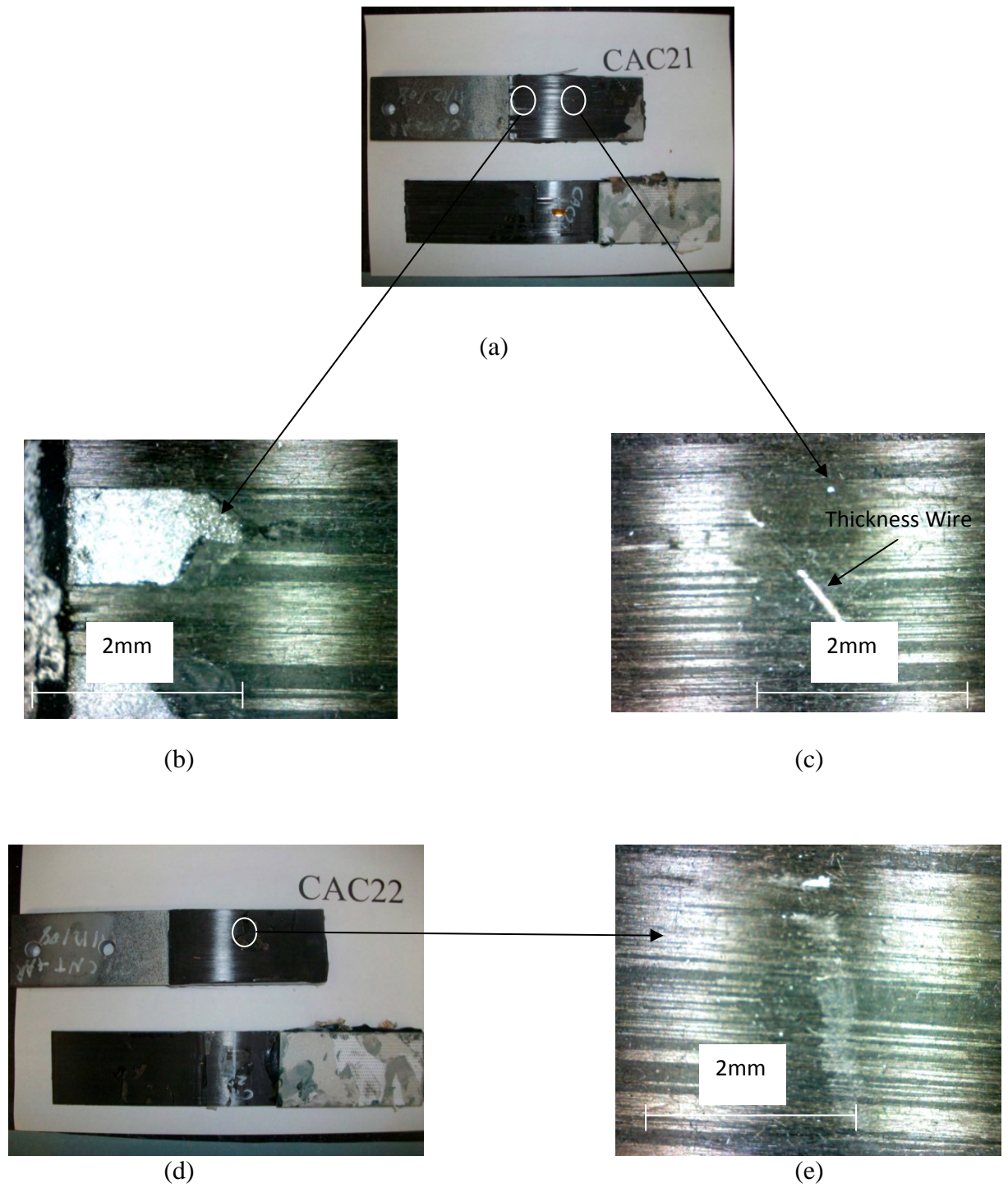


Figure 4.19 Failure surface of CAC2

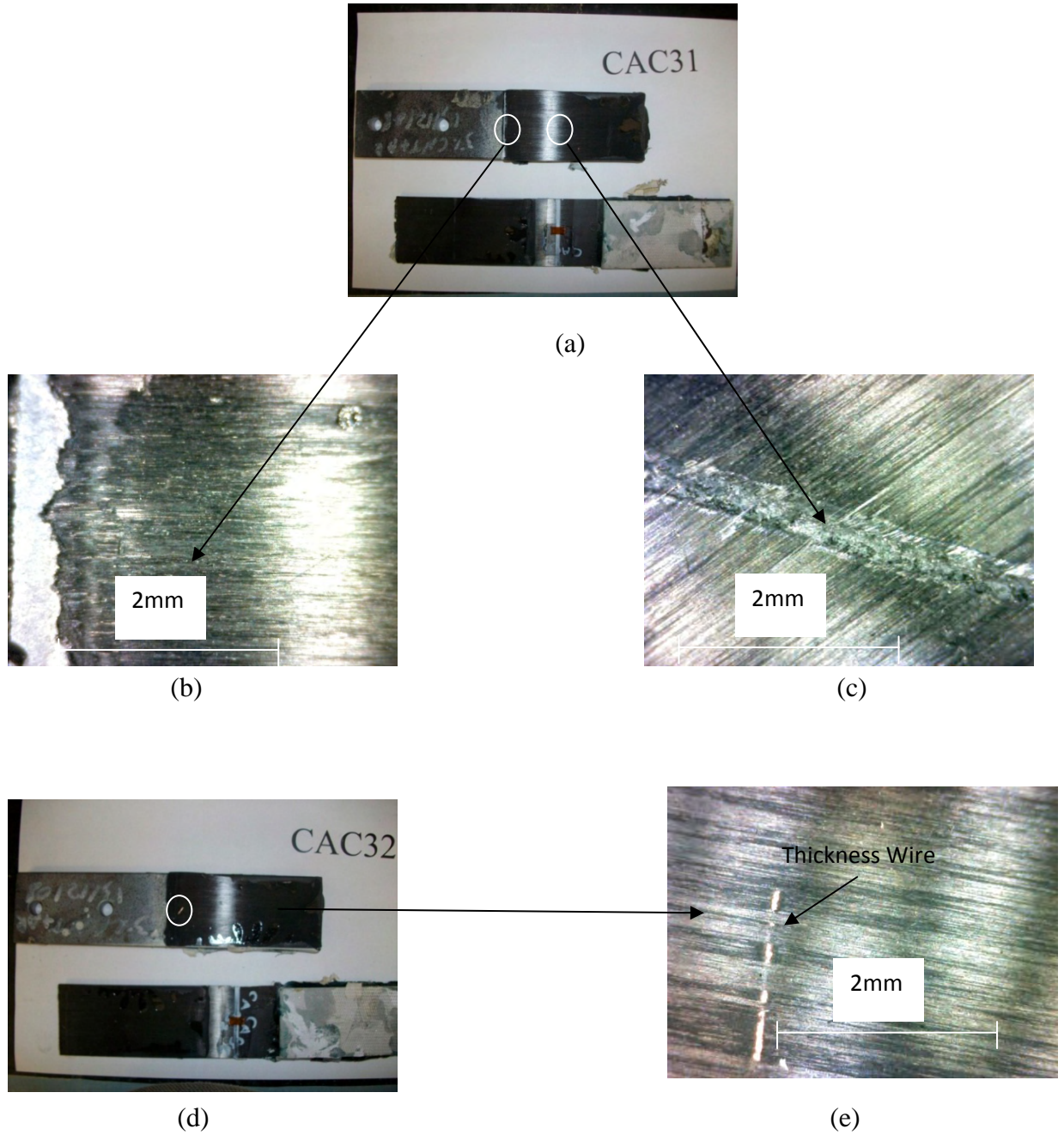


Figure 4.20 Failure surface of CAC3

In general, the failure mode is a brittle-delamination failure in the first layer of CFRP laminate. The zoomed image of failure surfaces shows a full layer of CF attached

strongly to the epoxy layer. The failure surface shows different features when the MWCNT percentages increase: 1% MWCNT-Araldite specimens fail by pure delamination the CFRP laminate and the first few layers are lifted at the failure surface. It is not easy to recognize the bonding epoxy layer due to the thick CF debonded layer as shown in Figure 4.18-C.

For 2% MWCNT, the epoxy is so strong that the delamination failure develops to steel-epoxy layer failure, as shown in Figure 4.19-E. Figure 4.19-B shows the thickness wire half covered with CF. The delaminated laminate is thicker than for the 1% and 3% MWCNT and the laminate breaks at the middle of the bond length as shown in Figure 4.19-E.

When the percentage of MWCNT is increased to 3%, the failure becomes a fracture in the CFRP laminate at the middle of the bond length as shown in Figure 4.20-B. The laminate then delaminates from the adhesive surface and continues to the end of the bonding length as shown in Figure 4.20-C. Figure 4.21 shows the strain distribution along the CFRP laminate surface.

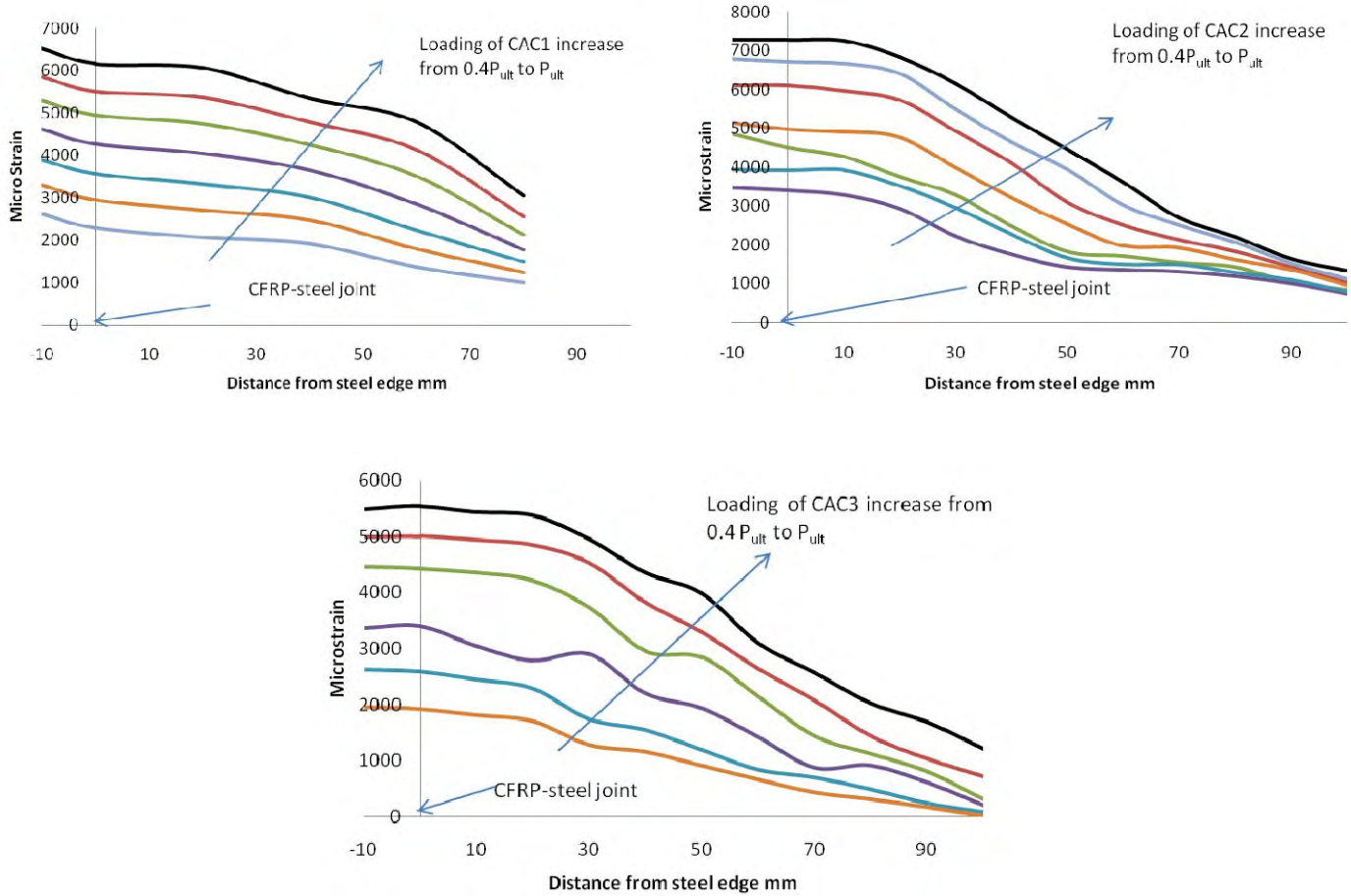


Figure 4.21 Strain distribution along CAC specimens

As mentioned before, the strain along the CFRP laminate remains constant until it reaches the steel edge. Then the adhesive continues to distribute the stresses until the strain reaches 20-40mm from the free edge, at which point the strain starts to absorb and distribute stress until it reaches the other end of the joint.

4.6.2 Effect of different types of MWCNT:

To test the effect of using another type of MWCNT with Araldite-420, the MWCNT purchased from NTP Co. with diameter of 60-100nm, length 1-2micrometers and 95+% purity was used. 1%, 2% and 3% of the new MWCNT was mixed with Araldite-420 to prepare a new test series.

Table 4.4 summarises the percentages and the ultimate loads for the new series.

Table 4.4 Ultimate stress of new MWCNT type specimens

1% NTP MWCNT	Ultimate stress MPa	2% NTP MWCNT	Ultimate stress MPa	3% NTP MWCNT	Ultimate stress MPa
CACN11	1068.6	CACN21	1307.1	CACN31	1207.1
CACN12	902.9	CACN22	1414.3	CACN32	1142.9
CACN13	918.6	CACN23	1534.3	CACN33	1088.6
CACN14	1035.7	CACN24	1465.7	CACN34	1165.7

Figure 4.22 which show the effect of adding different MWCNT percentages manufactured by NTP Co. The failure mode continues to be brittle and the ultimate stresses are near the averages of the previous MWCNT type.

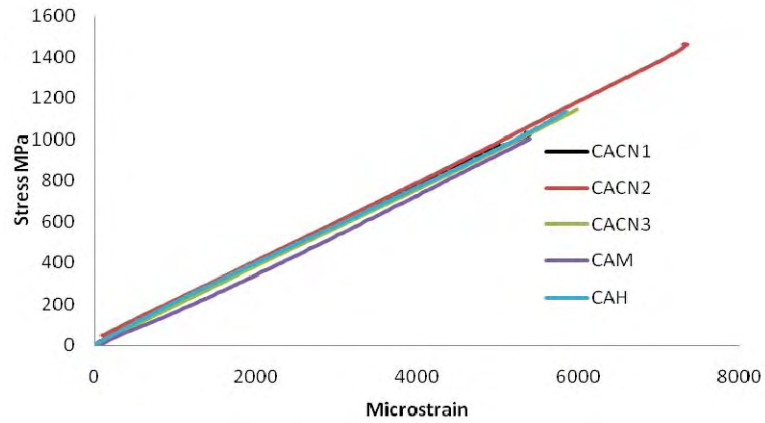


Figure 4.22 Effect of “NTP” MWCNT type on Araldite-420

Figure 4.23 shows the strain distribution along bond length. This figure shows no have major changes from the results for the old MWCNT.

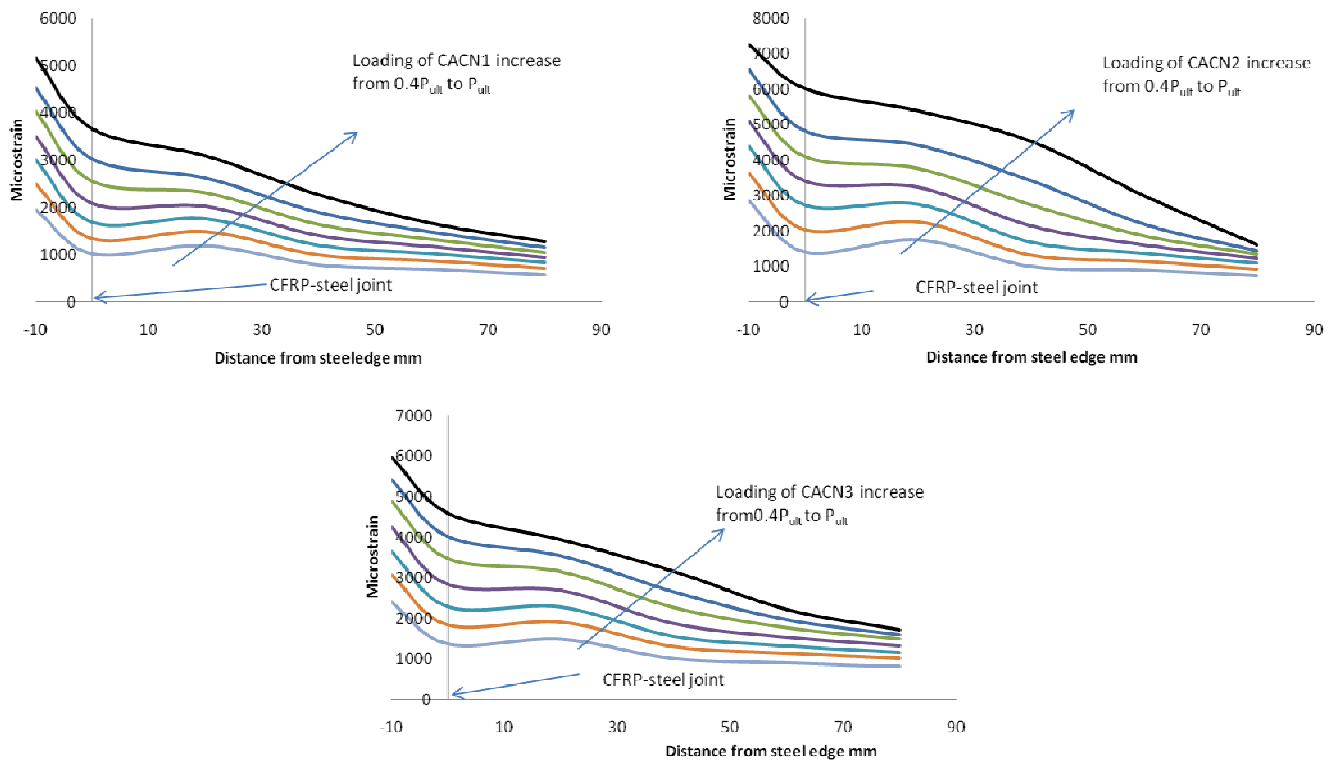


Figure 4.23 Strain distribution along CACN specimens

Adding MWCNT to Sikadur-30 has a different effect. The results show a slight increment from hand mixing and even a reduction in ultimate strength of MWCNT (manufactured by Sigma-Aldrich Co) mixed with Sikadur-30 compared with hand-mixed and sonicated pure Sikadur-30 specimens. Table 4.5 and Figure 4.24 summarise the effect of adding 1% and 2% of MWCNT to Sikadur-30.

Table 4.5 Ultimate stress of CSC specimens

1% MWCNT	Ultimate stress MPa	2% MWCNT	Ultimate stress MPa
CSC11	761.4	CSC21	640.0
CSC12	744.3	CSC22	620.0

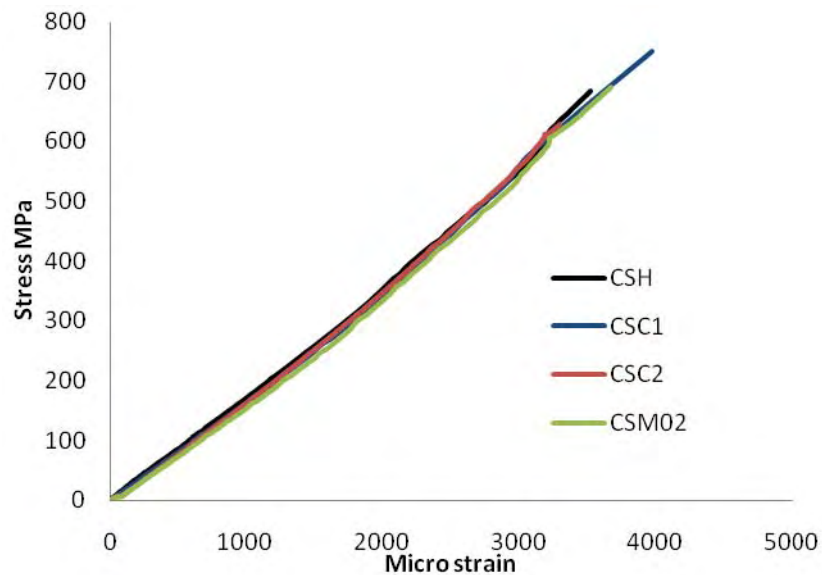


Figure 4.24 Effect of adding MWCNT to Sikadur-30

1% of MWCNT mixed with Sikadur-30 will enhance the strength from an average of 47.2kN for sonication only specimens to an average of 47.3kN. Averages of 44.1kN are

measured when the MWCNT percentage is increased to 2%. As explained in the previous chapter, negligible effects, and even a reduction, are expected when MWCNT is mixed with Sikadur-30. A further reduction is reported due to the small adhesive thickness (0.5 mm), resulting in the MWCNT being easily distributed inside this thickness in large numbers, but not the micro-fillers contained in Sikadur-30. The strain distribution along bonding length is summarised in Figure 4.25.

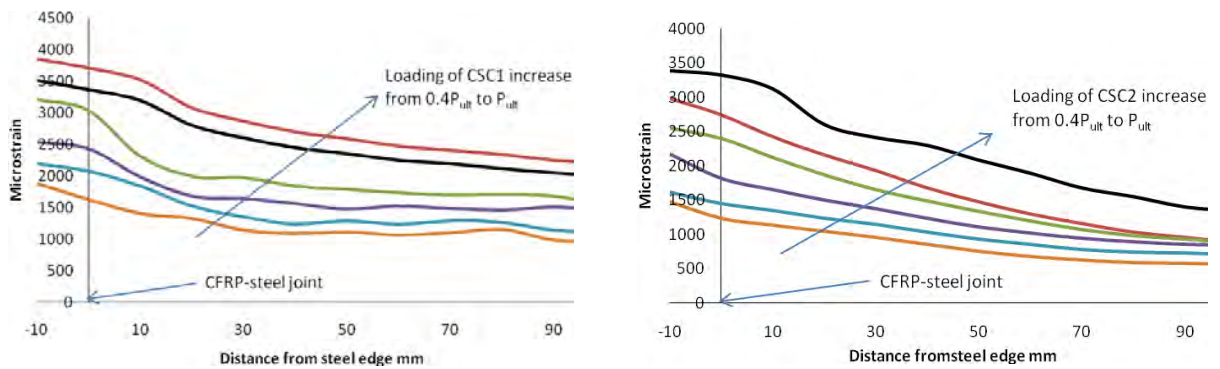


Figure 4.25 Strain distribution along CSC specimens

The same failure mode is repeated as for the hand-mixed and pure sonicated specimens: epoxy layer failure developed after 20-50mm from bonding length to a full plate delamination, as is clearly shown in Figure 4.26.



Figure 4.26 Failure surfaces of CSC specimens

4.6.3 MWCNT specimens failure

Any failure mechanisms activated by fibre breakage or delamination are directly related to the bonding adhesive. These mechanisms include adhesive yielding or cracking beneath the broken fibre tip, where the maximum stress concentration occurs, followed by crack propagation or increase of the matrix volume where shear yielding occurs (Kostopoulos, 2009).

Fibre damage, fibre breakage and adhesive layer cracking are the phenomena responsible for resistance increases. Adhesive layer cracking is the main damage mechanism in the early stage of loading.

With delamination failure, and in the presence of MWCNTs, even low contents of 1% and 2% by weight, lead to a significant increase in the fracture energy of the laminates (about 50%). This trend is closely connected to initial crack bridging by MWCNT, which requires extra energy, additional to that needed for crack initiation and propagation within the material. The MWCNT-enhanced adhesive transfers the stress efficiently, such that no stress concentrations are seen through the CFRP laminate except for the first layers of CF where the high stress could not re-distribute across the laminate depth.

Nevertheless, for large addition of MWCNT, the viscosity of the resin increased leading to high shear during sonication. As a consequence, the MWCNT agglomerations are not under high shear forces and therefore it is not possible to break them and achieve an even MWCNT dispersion, resulting in a material with agglomerations, which act as defects in adhesive, and thus low mechanical properties.

4.7 Effect of adding SiC

In the search for materials which enhance epoxy behaviour, bulk SiC is known as a ceramic material with high hardness, wear resistance, high temperature stability, and chemical inertness. However, the lack of anchoring between the SiC particles and the epoxies sometimes has some negative effects, as explained in Chapter 3.

In this section, test results for a set of CFRP laminates attached to steel plate by SiC enhanced epoxies are reported.

1%,2% and 3 % by weight of SiC nanofillers, with particle sizes < 100nm, and density of 3.22 g/ml at 25 °C, were mixed with Araldite-420 and Sikadur-30 following the mixing

procedures set out in Chapter 3, were used in this test set. Table 4.6 shows the test results.

Table 4.6 Ultimate stress of CAS specimens

1% SiC	Ultimate stress MPa	2% SiC	Ultimate stress MPa	3%SiC	Ultimate stress MPa
CAS11	992.0	CAS21	574.4	CAS31	863.0
CAS12	954.0	CAS22	522.9	CAS32	746.0

A strength reduction in CFRP-steel joint using SiC was expected as the major properties had been reduced when tested under direct tensile, as reported in Chapter 3.

Figure 4.27 shows the stress-strain behaviour for different percentages of SiC mixed with Araldite-420 compared with hand-mixed and sonicated pure Araldite-420

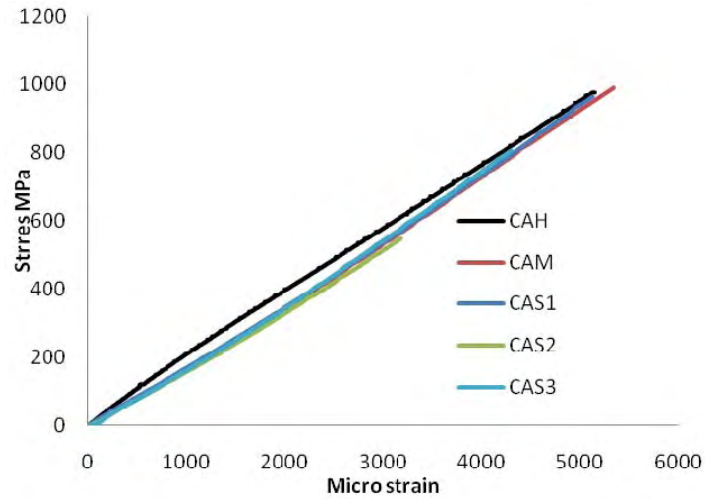


Figure 4.27 Effect of different SiC percentages on Araldite-420 specimens

Although the failure load for 1% SiC mixed Araldite-420 doesnot increase much from the hand-mixed and sonication pure epoxy, the failure mode is full delamination for the first layer of CFRP laminate with a large trace of CF on the adhesive surface, as shown in Figure 4.28.

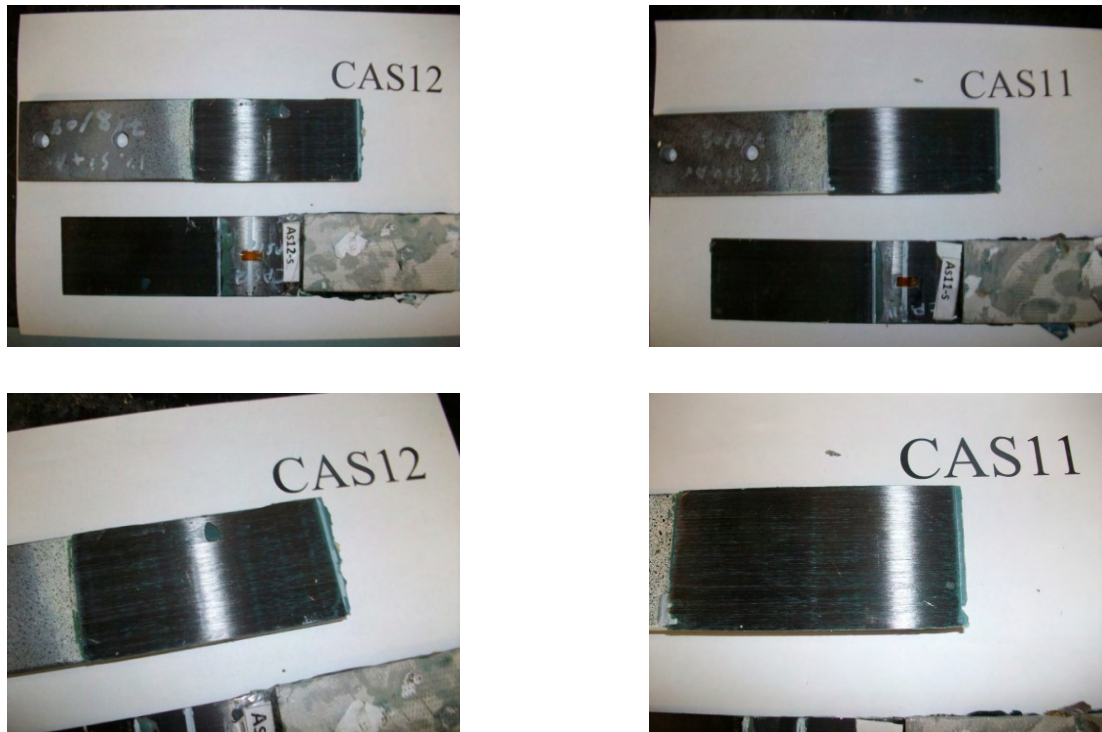


Figure 4.28 Failure surface of CAS1

2% SiC specimen failure does not changed from the previous test series: pure delamination failure for the first plate layer with a trace of CF still attached to the epoxy, as shown in Figure 4.29.



Figure 4.29 Failure surface of CAS2 specimens

When the SiC percentages increase to 3%, the ultimate strength remains less than the pure epoxy specimens. However, the failure mode begins to be a breakage in the CF , and the delaminated layer starts to become thicker, resulting in some full thickness laminates remaining attached to the adhesive surface, as shown in Figure 4.30.



Figure 4.30 Failure surface of CAS3

Adding SiC to Araldite-420 does not increase the strength or the elastic modulus of the epoxy, on which the delamination depends. However, the friction between the SiC nanoparticles, due to their wear-resistance and the laminate surface is so significant that the stress concentrates on the tips of the CF, which creates major stress leading to breakage of the fibres.

Figure 4.31 shows the strain distribution along the bonding length of Araldite-420 SiC enhanced epoxy.

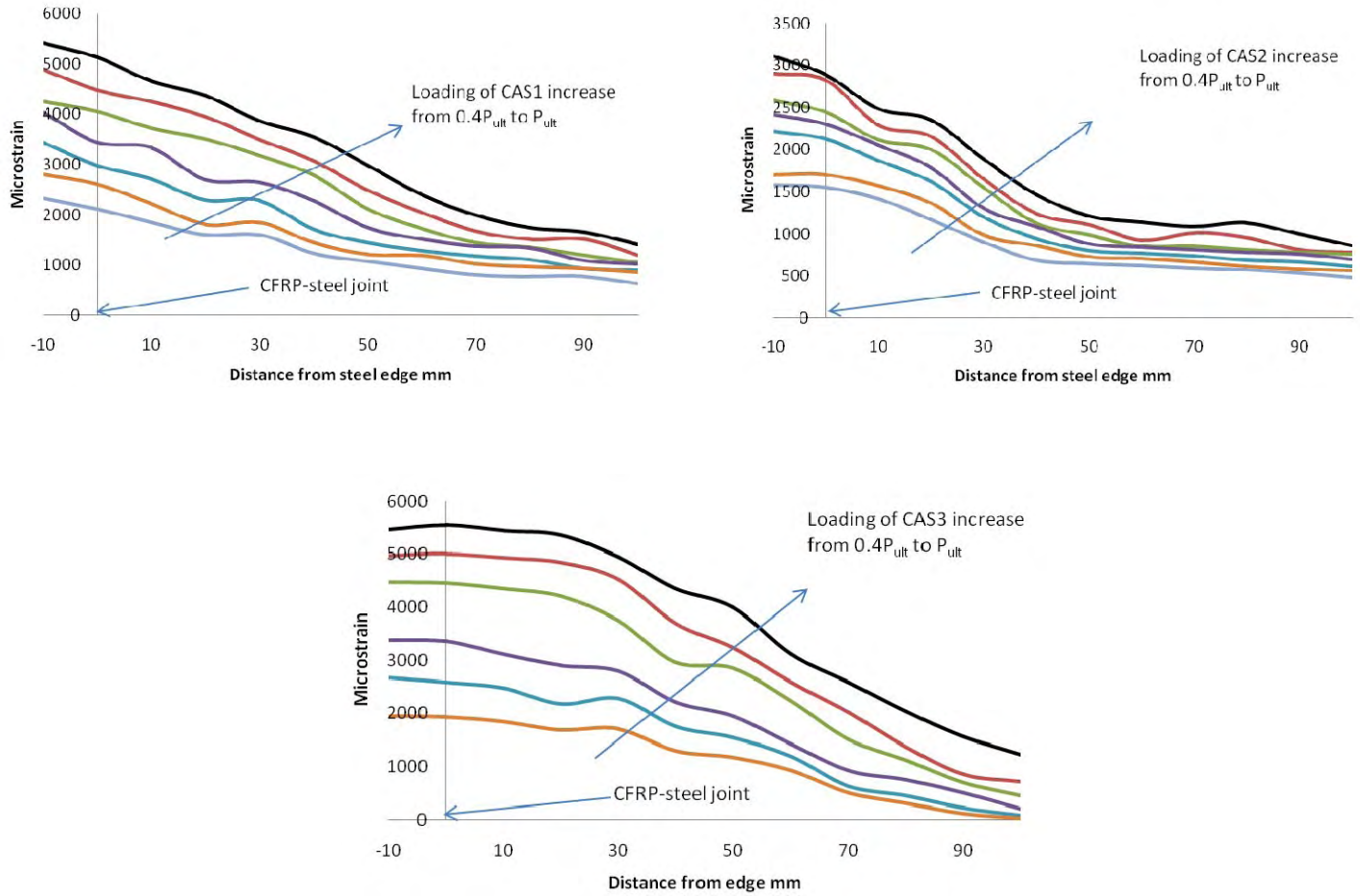


Figure 4.31 Strain distribution along CAS specimens

Adding SiC to Sikadur-30 has a positive effect on ultimate strength when 1% wt is added. This increment is followed by a decrement when 2% is added, while the addition of 3% SiC returns the ultimate strength to the pure epoxy level, as summarised in Table 4.7.

Table 4.7 Ultimate stress of CSS specimens

1% SiC	Ultimate stress MPa	2% SiC	Ultimate stress MPa	3%SiC	Ultimate stress MPa
CSS11	782.9	CSS21	554.3	CSS31	620.7
CSS12	752.9	CSS22	579.0	CSS32	666.7

Figure 4.32 shows the effect of adding SiC to Sikadur in different percentages on the stress-strain behaviour.

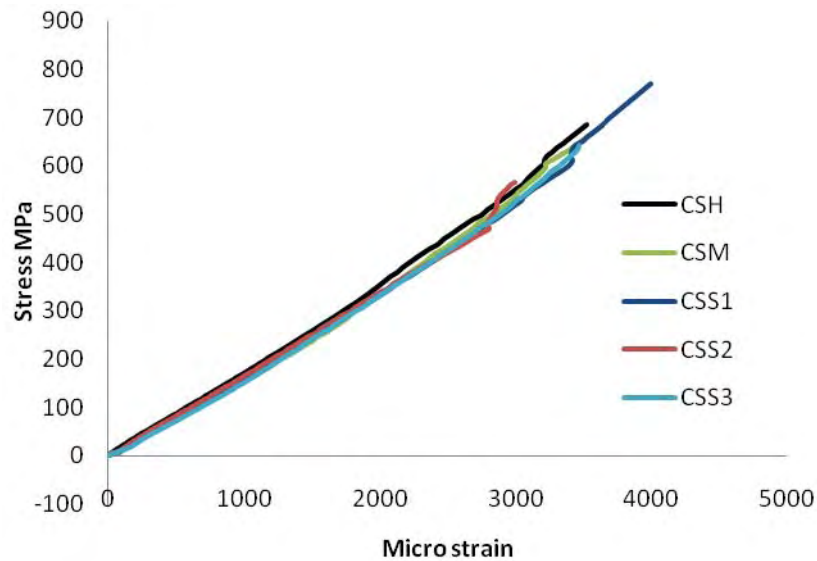


Figure 4.32 Effect of SiC on Sikadur-30

Due to their size, the SiC nanoparticles can be present in significant numbers in a small zone such as adhesive thickness, while the micro-fillers, with which Sikadur-30 is filled, barely fit in such small zone. These fillers prevent the nanoparticles from working as reinforcement elements and even reduce the superior wear resistance properties of SiC nanoparticles by working as rollers that the CFRP laminate tumbles along on the

adhesive surface. The slight increments in strength for 1% SiC and the unchanged strength for the 3% SiC are due to the ability to transfer the stress from the laminate to the steel which depends on the tensile strength and elastic modulus. These two properties are tested in Chapter 3 and the decrement in strength in 2%SiC is due to these decrements of strength and elastic modulus.

Figures 4.33-4.4.35 show a single failure mode that recurred for different SiC percentages, regardless of adhesive strength, modulus of elasticity and ultimate strength of the system. The failure mode is typical as it starts with adhesive epoxy layer failure. Then the depth of the failure surface becomes shallower, reaching the CFRP laminate, where its first layer starts to delaminate, leaving a trace of CF on the adhesive surface.

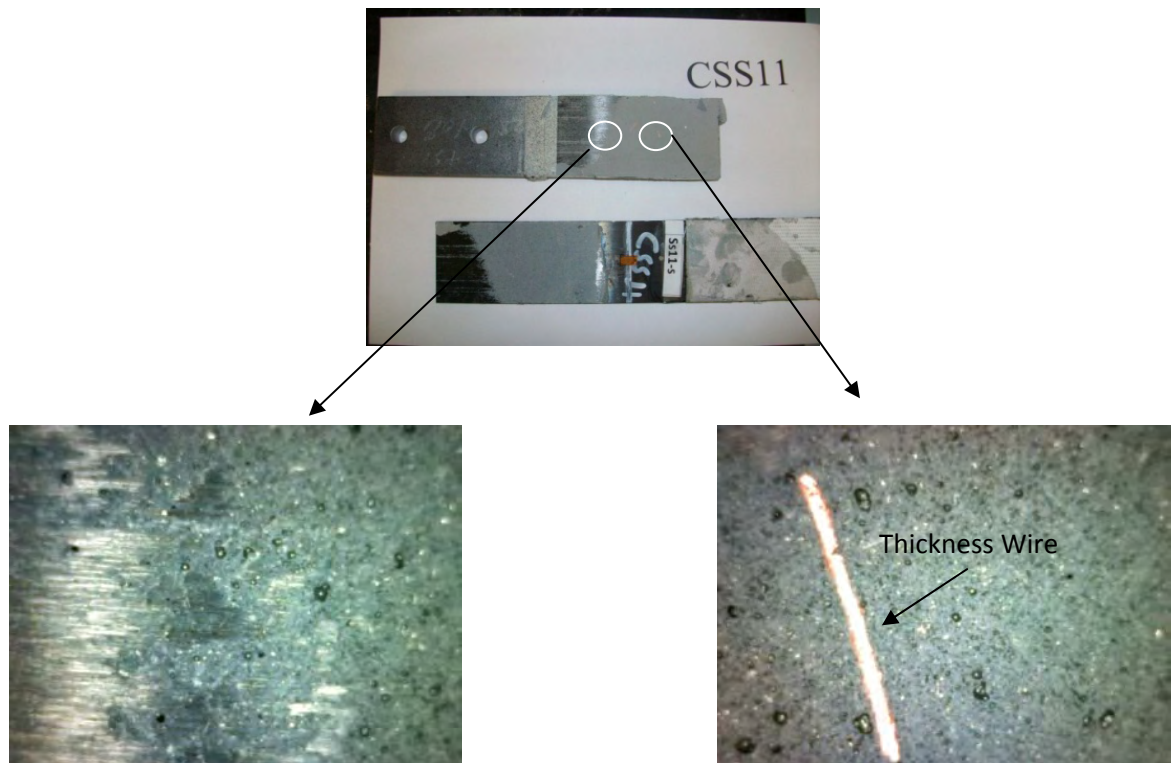


Figure 4.33 Failure surface of CSS1

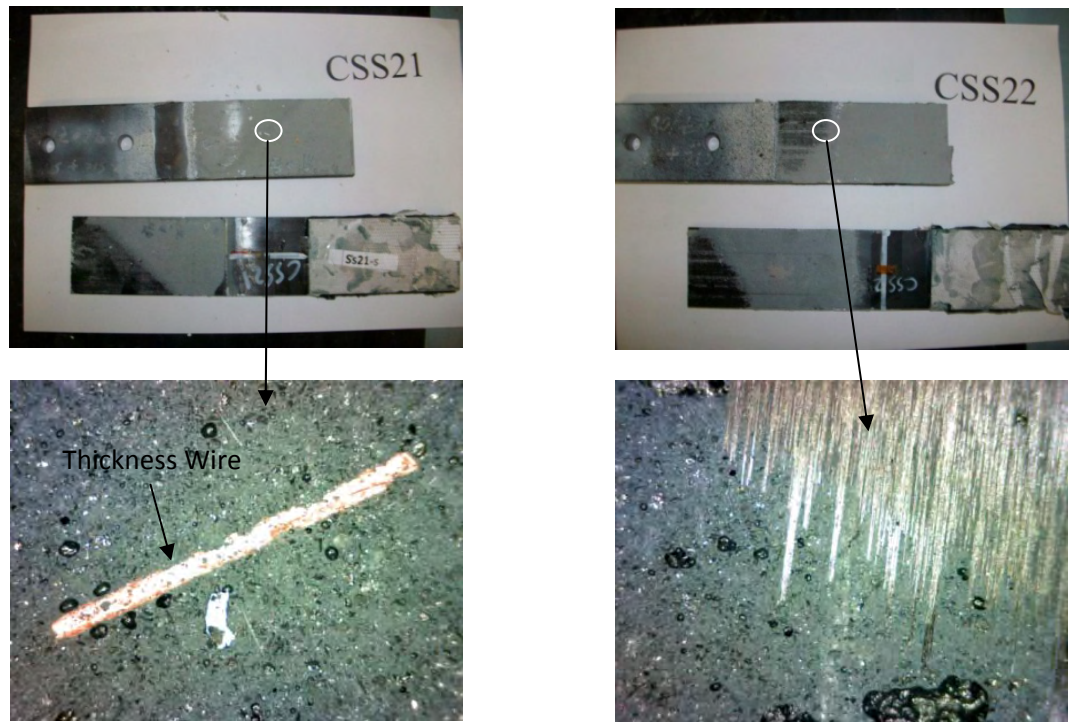


Figure 4.34 Failure surface of CSS2

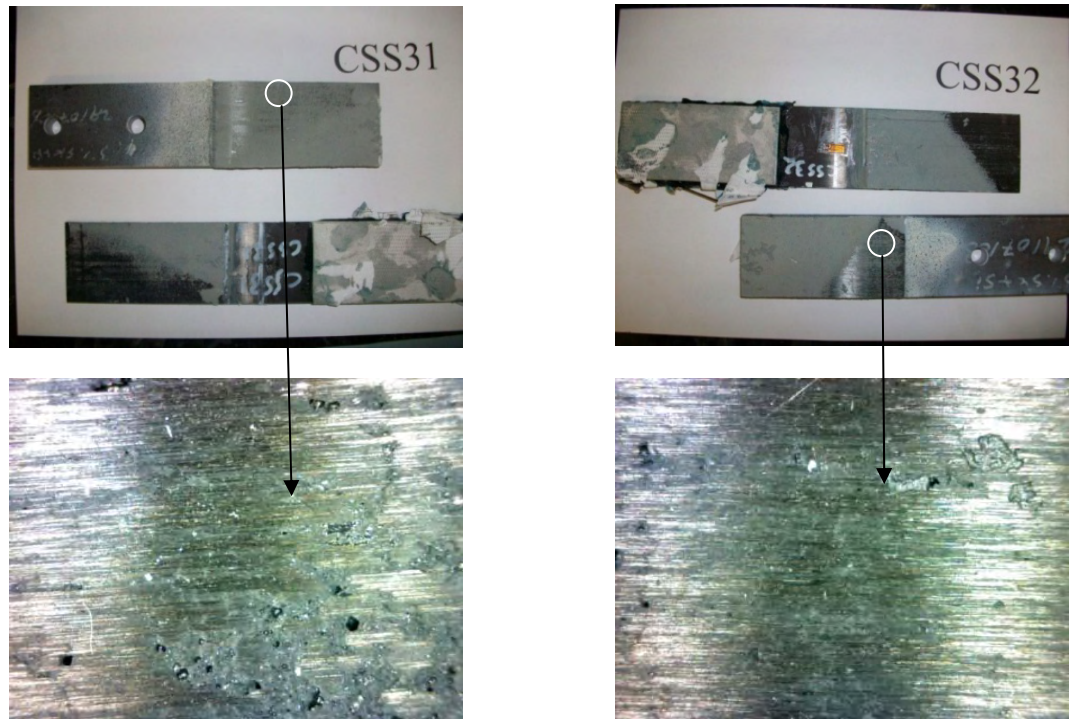


Figure 4.35 Failure surface of CSS3 specimens

This type of failure can be traced through strain distribution along the bonding length, as shown in Figure 4.36.

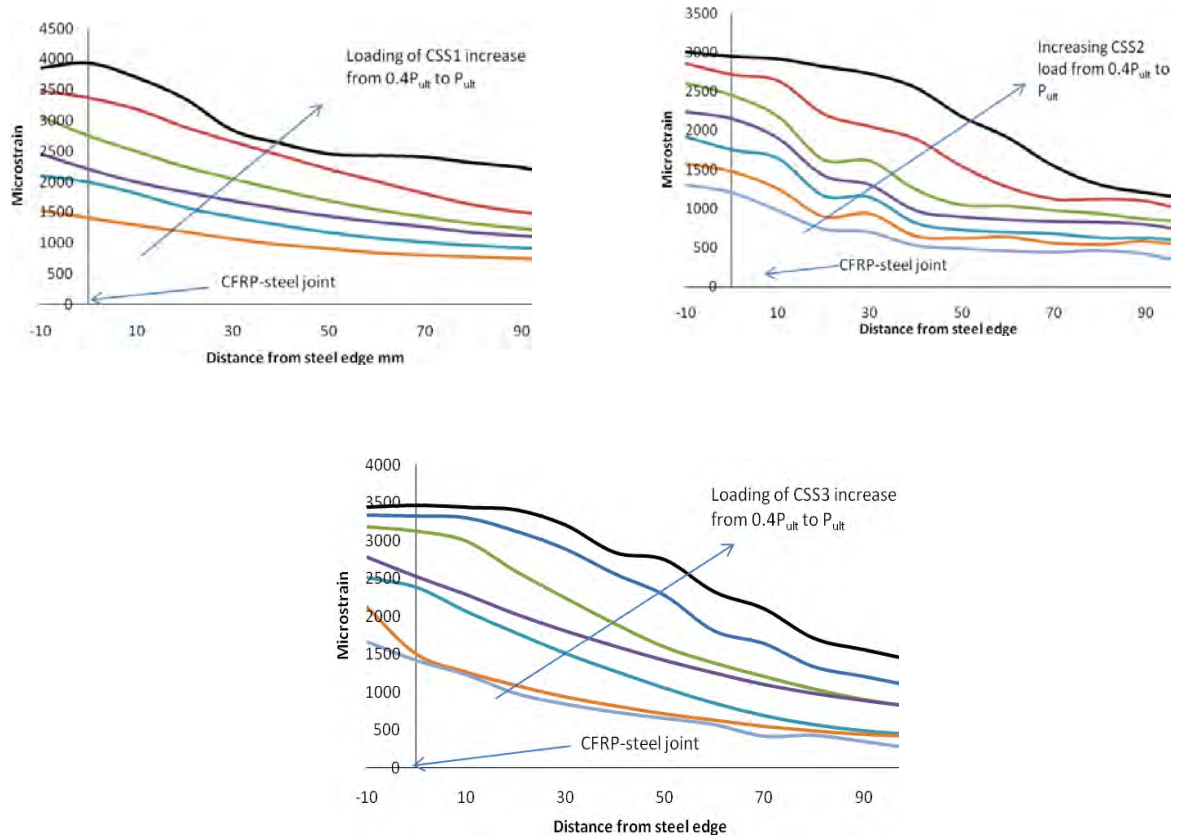


Figure 4.36 Strain distribution along CSS specimens

The strain distributions for the Sikadur specimens differ from those of Araldite in that the Sikadur samples have a sudden, easily-recognised drop in strain near the middle of the bond length, where the failure starts to transfer to delamination.

At the beginning of the bond length, the stress levels are high, and the weakest point at that place is the epoxy layer, which has micro-fillers. These work as rollers and help the adhesive's accumulated particles around the SiC to roll on each other and create micro-

cracks that store stress at its tips, but not enough to fail. Due to the superior wear resistance properties of the SiC, the CF are attached strongly to it.

When the stress level increases, the adhesive micro cracks at the beginning of the bonding length develop to become total failure and the stress starts to transfer to the remaining bond length. The stress level is so high that the CF cannot continue to transfer and distribute the stress and therefore fails at its weakest point. The CF tips start to break and failure starts at the middle of the bond length and smear both sides. The CF continues to delaminate up to the end of the bonding length due to the direction of the stress redistribution and fails in the adhesive layer due to the presence of micro cracks, which hoard the stress at their tips.

4.8 Summary

In the present research, a series of single lap samples were tested. The adhesives used were modified by the addition of different types and percentages of nanoparticles. The following conclusions can be drawn from the tested specimens:

- The comparisons of the strain distribution obtained by measurements by gauges and the photogrammetry system show that the latter technique not only can complement, but also replace traditional measurement techniques.
- When Araldite-420 is used, joint strength increases as the percentage of MWCNT increases until it reaches 2%, which is the optimum percentage with strength

increase of 50%. Then the strength decreases due to the agglomeration of the nanoparticles.

- Slight differences in the length, diameter and purity of mixed MWCNT have a negligible effect on joint strength.
- SiC nanopowder has a negative effect on the strength of Araldite-420 joints due to agglomeration that prevents the epoxy from distributing the strength.
- Sikadur-30 joints have the same failure pattern because of the micro- fillers in the epoxy and prevent nanoparticles from playing a reinforcing role. The nanoparticles also play a role in the acceleration of CFRP laminate delamination failure.

Chapter Five

A Model-Based Simulation of CFRP-Steel Bond Failure Using the Material Point Method

5.1 Introduction

Although the use of the lightweight CFRP instead of heavy and bulky steel plates in retrofitting old or damaged steel structures has increased, this increment has been limited due to the absence of a clear understanding of how the epoxy layer in CFRP-steel joints behaves at each loading stage. Therefore, many experimental (Fawzia et al., 2005; 2007; Schnerch et al., 2004; Colombi and Poggi 2006; Jiao and Zhao 2004; Xia and Teng 2005 among others) and theoretical studies (Fawzia et al., 2006; Wu et al., 1998; Yin and Wu 2001) have been conducted to investigate the mechanical responses of CFRP-steel joint systems under various loading conditions. However, many of the past numerical studies (Fawzia et al., 2006; Liu et al., 2008; Teng and Hu 2007; among others) focused on the design and structural performance of the CFRP-steel joint systems and paid limited attention to the mechanical behaviour of the adhesive layer, which results in an inadequate understanding of how the adhesive layer between the CFRP and steel performs during the loading and failure stages. This situation is partially due to the absence of an effective interfacial debonding model for the simulation of the failure of CFRP-steel bonds.

A detailed numerical study using the Material Point Method (MPM), focusing on CFRP-steel double lap and single lap joints is thus proposed in this chapter to gain a better understanding of the CFRP-steel debonding failure mechanism.

In the proposed approach, an elasto-plasticity model with linear hardening and softening laws is used to model the bonded materials. The MPM, which does not employ fixed mesh-connectivity, is adopted as a robust spatial discretisation method to accommodate the multi-scale discontinuities involved in the CFRP-steel bond failure process.

To demonstrate the potential of the proposed model-based simulation approach, a parametric study is conducted on previously investigated CFRP-steel specimens reported by other researchers, to investigate the effects of bond length and loading rate on the failure modes of CFRP-steel joint systems. Then, the MPM is used to simulate the currently tested pure epoxy CFRP-steel specimens. The simulation results not only well match the available experimental data but also provide a better understanding of the physics underlying the combined CFRP/epoxy layer delamination process.

5.2 Material Point Method

5.2.1 Background

Recently, several kinds of meshless methods for spatial discretization have been proposed in the computational mechanics community. Since these meshless methods do not use grid mesh connectivity as compared with conventional mesh based methods, such as FEM and the finite difference method, they have been applied to some complex problems of current interests such as impact, contact, localization, crack propagation, penetration, preformation, and fragmentation.

As one of the innovative spatial discretization methods, MPM is an extension to solid mechanics problems of a hydrodynamics code called FLIP that, in turn, evolved from the Particle-in-Cell Method dating back to the pioneering work of Harlow (1964). The motivation of the development was to simulate challenging problems such as im-

pact/contact, penetration and machine processing with history dependent internal state variables ,as shown in various publication about MPM(Sulsky et al.,1994;1995; Shen and Chen,2005; Zhou et al., 1999 ; Ionescu et al., 2006 and Guilkey et al., 2003; among others).

The main difference between the FEM and the MPM in modelling delamination type of failure is there is no fixed mesh connectivity involved in the MPM. Therefore, the complete decohesion or separation would occur if the material strength is totally or nearly totally lost. In other words, a material point would be separated from the original continuum body (which may occur in experiments) if there is no internal interaction between the fully failed point with zero or near zero strength and the body with non-zero strength.

The key advantage of MPM is to make use of both the Eulerian and Lagrangian methods while avoiding the shortcomings of each. In comparison with other meshless methods, the MPM appears to be less complex with a cost factor of at most twice that associated with the use of corresponding finite element (Chen et al .,2005). In addition, the use of the single –valued mapping function in the MPM results in a natural no-slip contact/impact scheme without invoking master/slave nodes so that no interpenetration would occur in multi-body interaction problems. Without using the fixed mesh connectivity in the MPM, the complete decohesion or separation of material can be effectively modelled after the material strength is totally lost.

5.2.2 MPM governing equations and their weak forms

In the MPM, a mesh of Lagrange material points is used to discretise one or more solid bodies. The interaction of the material point is calculated on a background Eulerian or spatial finite element mesh on which the momentum equation is solved. Mate-

rial point quantities are updated from the solution on the Eulerian mesh with mapping function.

The complete algorithm consists of the following steps: an initialisation phase where information is transferred from the material points to a grid; a Lagrangian phase where the equations of motion are solved in an updated Lagrangian frame on the grid; followed by a convective phase where the particles are updated and the grid is redefined. (Chen et al., 2002).

The key feature of the MPM is the use of the same set of nodal basis functions for both the mapping from material points to cell nodes, and the mapping from cell nodes to material points. As a result, the use of the single-valued mapping functions yields a natural no-slip contact/impact scheme so that no inter-penetration would occur for penetration problems.

The MPM discretises a continuum body with the use of a finite set of N_p material points in the original configuration that are tracked throughout the deformation process. Let \mathbf{x}_p^t ($p = 1, 2, \dots, N_p$) denote the current position of material point p at time t . Each material point at time t has an associated mass M_p , density ρ_p^t , displacement \mathbf{u}_p^t , velocity \mathbf{v}_p^t , Cauchy stress tensor \mathbf{s}_p^t , strain \mathbf{e}_p^t , and any other internal state variables necessary for constitutive modelling. Thus, these material points provide a Lagrangian description of the continuum body.

The governing equations are based on the conservation equation for momentum:

$$\mathbf{s}^s \cdot \nabla + \rho \mathbf{b} = \rho \mathbf{a} \quad (5.1)$$

and the mass conservation equation:

$$\rho \nabla \cdot \mathbf{v} + \frac{d\rho}{dt} = 0 \quad (5.2)$$

supported by suitable constitutive equations and kinematic relations between displacement and strain. $\mathbf{s}^s(\mathbf{x},t)$ denotes the specific stress which is defined to be the Cauchy stress divided by density, $\rho(\mathbf{x},t)$. The specific body force is $\mathbf{b}(\mathbf{x},t)$, $\mathbf{v}(\mathbf{x},t)$ is the velocity and the acceleration is $\mathbf{a}(\mathbf{x},t)$. \mathbf{x} is the current position of material point at certain time t .

The weak form of the conservation of momentum can be found, based on the standard procedure used in the finite element method, to be

$$\int_{\Omega} \rho \mathbf{w} \cdot \mathbf{a} d\Omega = \int_{\Omega} \rho \mathbf{w} \cdot \mathbf{b} d\Omega + \int_{S^c} \rho \mathbf{c}^s \cdot \mathbf{w} dS - \int_{\Omega} \rho \mathbf{s}^s : \nabla \mathbf{w} d\Omega \quad (5.3)$$

in which \mathbf{w} denotes the test function, \mathbf{c}^s is the specific traction vector (i.e., traction divided by mass density), Ω is the current configuration of the continuum, and S^c is that part of the boundary with a prescribed traction. The test function \mathbf{w} is assumed to be zero on the boundary with a prescribed displacement. Since the whole continuum body is described with the use of a finite set of material points (mass elements), the mass density term can be written as

$$\rho(\mathbf{x}, t) = \sum_{p=1}^{N_p} M_p \delta(\mathbf{x} - \mathbf{x}_p^t) \quad (5.4)$$

where δ is the Dirac delta function with dimension of the inverse of volume. The substitution of Equation 5.4 into Equation 5.3 converts the integrals to the sums of quantities evaluated at the material points; namely

$$\sum_{p=1}^{N_p} M_p [\mathbf{w}(\mathbf{x}_p^t, t) \cdot \mathbf{a}(\mathbf{x}_p^t, t)] = \sum_{p=1}^{N_p} M_p [-\mathbf{s}^s(\mathbf{x}_p^t, t) : \nabla \mathbf{w}|_{\mathbf{x}_p^t} + \mathbf{w}(\mathbf{x}_p^t, t) \cdot \mathbf{c}^s(\mathbf{x}_p^t, t) h^{-1} + \mathbf{w}(\mathbf{x}_p^t, t) \cdot \mathbf{b}(\mathbf{x}_p^t, t)] \quad (5.5)$$

with h being the thickness of the boundary layer . The interactions among different material points are reflected only through the gradient terms, which necessitates the use of a background mesh, as can be observed from Equation 5.5.

To do so, the computational mesh is constructed of 2-mode cells for one-dimensional problems, 4 node cells for 2-dimensional and 8 for 3-dimensional problems. These cells are employed to define standard nodal basis function $N_i(\mathbf{x})$, associated with spatial nodes $\mathbf{x}_i(t), i=1,2,\dots,N_n$ with N_n being the total number of mesh nodes.

The nodal basis functions are assembled from conventional finite element shape functions. For instance, the shape functions for a 4-node cell is given by:

$$N_1 = (1 - \xi)(1 - \eta) \quad (5.6A)$$

$$N_2 = \xi(1 - \eta) \quad (5.6B)$$

$$N_3 = \xi\eta \quad (5.6C)$$

$$N_4 = (1 - \xi)\eta \quad (5.6D)$$

in which ξ and η are the natural coordinates of a material point in the cell along x and y directions, respectively The coordinate of any material point in a cell can be represented by:

$$\mathbf{x}_p^t = \sum_{i=1}^n \mathbf{x}_i N_i(\mathbf{x}_p^t) \quad (5.7)$$

If the displacements of any material point in a cell are defined by the nodal displacements, $\mathbf{u}_i^t(t)$, the displacement

$$\mathbf{u}_p^t = \sum_{i=1}^n \mathbf{u}_i N_i(\mathbf{x}_p^t) \quad (5.8)$$

Since the same basic functions are used for both spatial coordinates and displacements, kinematic compatibility demands that the basis functions must advect with the material, as in an updated Lagrangian framework. In other words, the material time rates of the basis functions must be zero.

Hence, it follows that the velocity, acceleration and test function for any material point in a cell are represented by

$$\mathbf{v}_p^t = \sum_{i=1}^n \mathbf{v}_i N_i(\mathbf{x}_p^t) \quad (5.9)$$

$$\mathbf{a}_p^t = \sum_{i=1}^n \mathbf{a}_i N_i(\mathbf{x}_p^t) \quad (5.10)$$

and

$$\mathbf{w}_p^t = \sum_{i=1}^n \mathbf{w}_i N_i(\mathbf{x}_p^t) \quad (5.11)$$

with \mathbf{v}_i^t , \mathbf{a}_i^t and \mathbf{w}_i^t being nodal velocities, accelerations and test functions respectively.

The use of Equations 5.7-5.11 ensures that the associated vectors are continuous across the cell boundary. However, the gradients of these vectors are not continuous across the cell boundary due to the use of linear shape functions. The variables evaluated at material points are related to the nodal values through the shape functions, as can be seen from Equations 5.7-5.11. Substituting Equations 5.10 and 5.11 into Equation 5.5 yields:

$$\sum_{i=1}^{N_n} \mathbf{w}_i^t \cdot \sum_{j=1}^{N_n} m_{ij}^t \mathbf{a}_j^t = \sum_{i=1}^{N_n} \mathbf{w}_i^t \cdot \mathbf{c}_i^t + \sum_{i=1}^{N_n} \mathbf{w}_i^t \cdot \mathbf{b}_i^t - \sum_{i=1}^{N_n} \mathbf{w}_i^t \cdot \sum_{p=1}^{N_p} \mathbf{M}_p \mathbf{s}_p^{s,t} \cdot \nabla N_i \Big|_{\mathbf{x}_p^t} \quad (5.12)$$

at time t , in Equation 5.12, the consistent mass matrix is given by

$$m_{ij}^t = \sum_{p=1}^{N_p} M_p N_i(\mathbf{x}_p^t) N_j(\mathbf{x}_p^t) \quad (5.13)$$

with corresponding lumped nodal masses

$$m_i^t = \sum_{p=1}^{N_p} M_p N_i(\mathbf{x}_p^t) \quad (5.14)$$

The discrete specific traction and body force takes the form of

$$\mathbf{c}_i^t = \sum_{p=1}^{N_p} M_p \mathbf{c}_p^{s,t} h^{-1} N_i(\mathbf{x}_p^t) \quad (5.15)$$

$$\mathbf{b}_i^t = \sum_{p=1}^{N_p} M_p \mathbf{b}_p^t N_i(\mathbf{x}_p^t) \quad (5.16)$$

with $\mathbf{c}_p^{s,t} = \mathbf{c}^s(\mathbf{x}_p^t, t)$, and $\mathbf{b}_p^t = \mathbf{b}(\mathbf{x}_p^t, t)$.

Alternatively, if the vector \mathbf{b} is a known function of position and time, as for gravity, then the nodal body force can be computed directly by

$$\mathbf{b}_i^t = \mathbf{b}(\mathbf{x}_p^t, t) m_i^t \quad (5.17)$$

Since \mathbf{w}_i^t are arbitrary except where the components of displacement are prescribed,

Equation 5.12 becomes

$$m_i^t \mathbf{a}_i^t = (\mathbf{f}_i^t)^{\text{int}} + (\mathbf{f}_i^t)^{\text{ext}} \quad (5.18)$$

for a lumped mass matrix, where the internal force vector is given by

$$(\mathbf{f}_i^t)^{\text{int}} = - \sum_{p=1}^{N_p} M_p \mathbf{s}_p^{s,t} \cdot \mathbf{G}_i(\mathbf{x}_p^t) \quad (5.19)$$

with $\mathbf{s}_p^{s,t} = \mathbf{s}^s(\mathbf{x}_p^t, t)$ and $\mathbf{G}_i(\mathbf{x}_p^t) = \nabla N_i|_{\mathbf{x}_p^t}$ and the external force vector is

$$(\mathbf{f}_i^t)^{\text{ext}} = \mathbf{c}_i^t + \mathbf{b}_i^t \quad (5.20)$$

As can be observed from Equations 5.14 - 5.16, and 5.19, the shape function is used to map the information from material points to the nodes of the cell containing these points. The information from the particle would be equally mapped to the cell nodes, if the material point is located in the centre of a cell, as can be found from the shape functions defined in Equation 5.6.

An explicit time integrator is used to solve Equation 5.17 for the nodal accelerations, with the time step satisfying the stability condition, i.e., the critical time step, Δt , being the smallest ratio of the cell size to the wave speed inside modelled material given by

$$\Delta t = \frac{\Delta x}{\sqrt{E/\rho}} \quad (5.21)$$

Where Δx is smallest cell dimension, E is elastic modulus for the material.

For small displacements, the spatial discretisation via the MPM is equivalent to that via the FEM using Gauss points at the same locations as those of the material points in each cell. Therefore, the convergence behaviour of the explicit time integrator used to solve Equation 5.17 is similar to that employed to integrate the corresponding equation in the FEM. However, no consistent theoretical results have been obtained for the convergence behaviours of time integrators when large deformations and the transition from continuous to discontinuous failure modes occur.

After the solution of the motion equations on the cell nodes, which also controlled by boundary conditions, the new nodal values of velocity are then used to update the position of the material points. The gradient of the nodal basis function evaluated at the material point position is used to determine the strain increment for each material point. The corresponding stress increment can be found from the constitutive model. The material points can carry and transport any internal state variables that are assigned to them. The computational cycle for this time step is complete when the mate-

rial points are completely updated. The computational mesh used in the current cycle is discarded, and a new mesh is defined for the next time step, in the spirit of the updated Lagrangian frame.

5.3 MPM evaluation

5.3.1 Pre-tested specimens simulation

In this section, the effectiveness of the MPM for investigating the failure mechanism of the CFRP-steel system is verified by comparing the MPM simulation results with the previous experimental data of double lapped CFRP-steel system under shear loading (Fawzia, 2007).

In the experimental programme (Fawzia , 2007), each CFRP layer consisted of three CFRP sheets 50 mm wide with lengths of 40, 50, 70 or 80 mm. The CFRP sheets were bonded together using 0.2 mm thick epoxy layers. One CFRP layer was then attached to each side of two 5mm thick, 50mm wide steel plates using a 0.2 mm thick epoxy layer, as demonstrated in Figure 5.1.

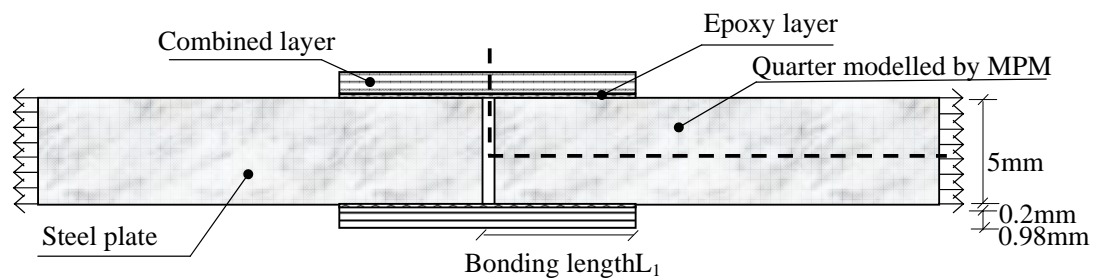


Figure 5.1 Side view of the CFRP-steel double lap joint tested in (Fawzia,2007)

All specimens were tested up to failure under tensile loading at the rate of 2mm/min. Since the total thickness of specimen (7 mm) is much smaller than its width (50 mm),

it is reasonable to assume that no significant stress or strain changes will occur in the width direction under uniformly distributed load at the ends of the steel plates. Therefore, the MPM simulation could be simplified into a two-dimensional plane strain problem. Due to the symmetrical conditions in the X and Y directions, only a quarter of the CFRP-steel system is modelled in the MPM, as illustrated in Figure 5.2.

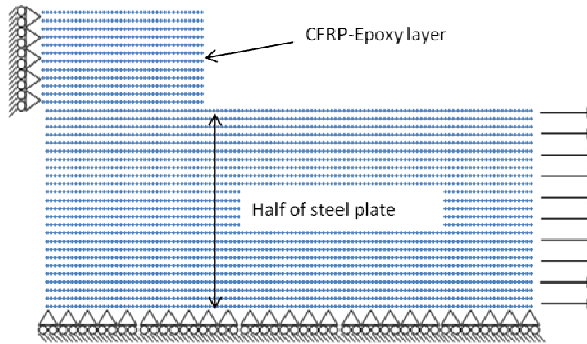


Figure 5.2 Schematic of (Fawzia,2007) specimens modelled using the MPM.

In the MPM, the specimen is divided into three different materials layers, namely, 2.5 mm thick steel layer, 0.2 mm thick epoxy layer, and 0.98 mm thick combined CFRP/epoxy layer, as shown in Figure 5.2. Figure 5.2 and all Figures shows deformed shape of tested specimens magnified by a factor of 10 in Y direction compared to X direction. This magnification increases the chance to follow up the studied failure surfaces(usually on the CFRP or adhesive layers). To ensure that there are, at least, two material point layers in each part along the thickness direction, a mesh size of 0.1 mm high and 1 mm long is chosen to discretise the CFRP-steel joint system. A constant velocity of 2mm/min is applied to the right edge of the steel plate to simulate the displacement controlled loading in the experiment.

Since the combined CFRP/epoxy layer consists of 3 CFRP sheets and 2 epoxy layers, the mechanical properties of the combined CFRP/epoxy layer are dependent on its

components and their corresponding thicknesses. Following the work of Fawzia et.al (2006), the equivalent mechanical properties such as strength, elastic modulus and Poisson's ratio are used in this study. For example, the equivalent modulus of the combined CFRP/epoxy layer is calculated by

$$E_{\text{CFRP}} = \frac{E_e t_e + E_f t_f}{t_e + t_f} \quad (5.22)$$

where E_e and E_f are the elastic moduli of the epoxy and CFRP sheet, respectively, t_e the thickness of the epoxy, and t_f the thickness of the CFRP sheet. For the purpose of simplicity, a linear elasto-plasticity model is adopted to describe steel, CFRP and epoxy. The proposed elasto-plasticity model with linear hardening and softening laws for epoxy is presented in Figure 5.3 and the models for the steel and combined CFRP/epoxy layer are shown in Figure 5.4.

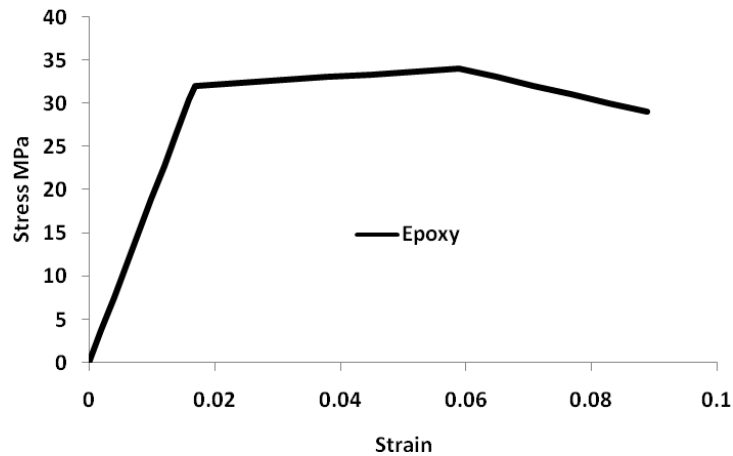


Figure 5.3. An elasto-plasticity model with linear hardening and softening laws for epoxy layer.

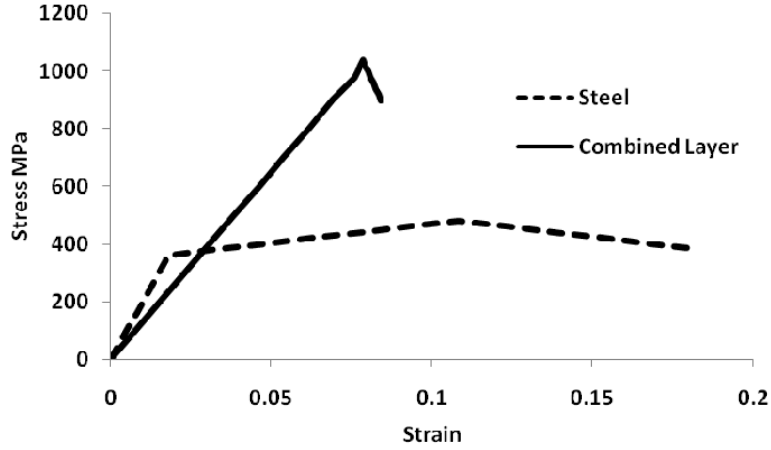


Figure 5.4. Linear elasto-plasticity constitutive model for steel and combined CFRP-epoxy layer.

The key mechanical properties of steel, CFRP and epoxy used in this study are given in Table 5.1.

Table 5.1. Mechanical properties for the materials of double lap shear specimens

	CFRP sheet	Steel plate	Epoxy	CFRP/epoxy Combined Layer
Elastic Modulus (GPa)	215	195	1.9	130
Yield Strength (MPa)	1610	360	30	979
Plastic Strength (MPa)	1710	484	32	1040
Poisson Ratio	0.28	0.25	0.21	0.25

The uniaxial and homogenized stress-strain curve of Figures 5.3 and 5.4 has been extended to a biaxial stress state using von Mises' yield criterion to predict the yielding stage of the materials.

5.3.2 Simulation results

5.3.2.1 Bond length effect

The MPM simulation is evaluated by comparing the simulation results with available experimental data. The load-deflection curves for 40mm, 50mm, 70mm and 80mm

bond lengths obtained from the experiments (Fawzia, 2007) are compared with the corresponding MPM simulations in Figures 5.5, 5.6, 5.7 and 5.8, respectively.

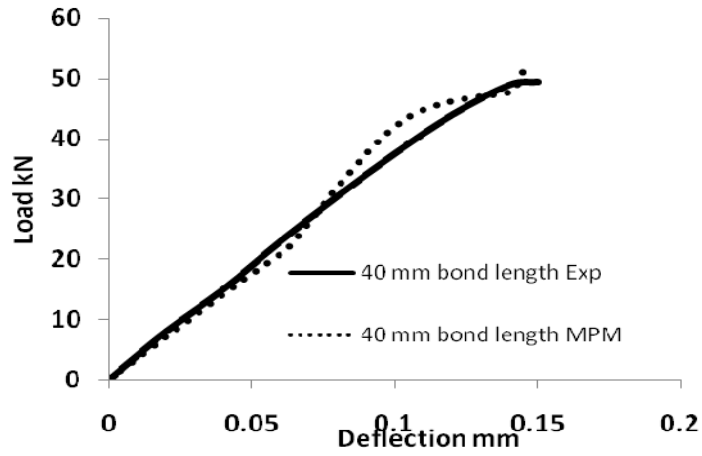


Figure 5.5. Comparison of load displacement behaviour of bond length 40mm.

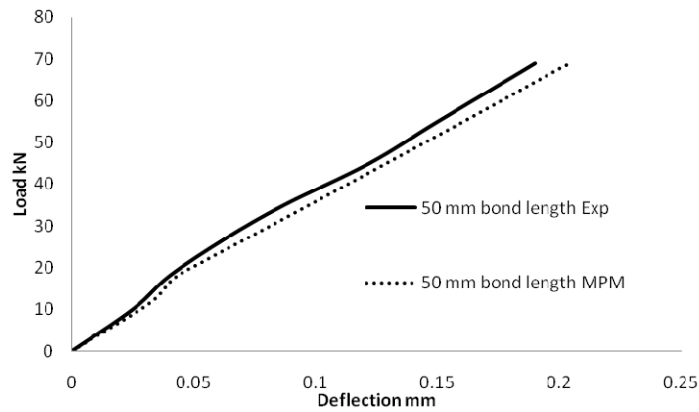


Figure 5.6. Comparison of load displacement behaviour of bond length 50mm.

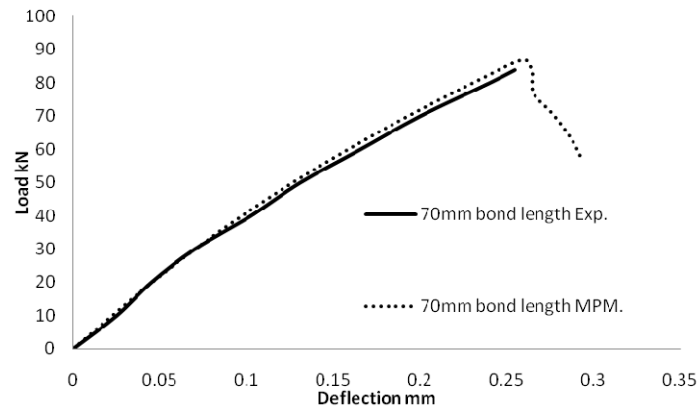


Figure 5.7. Comparison of load displacement behaviour of bond length 70mm.

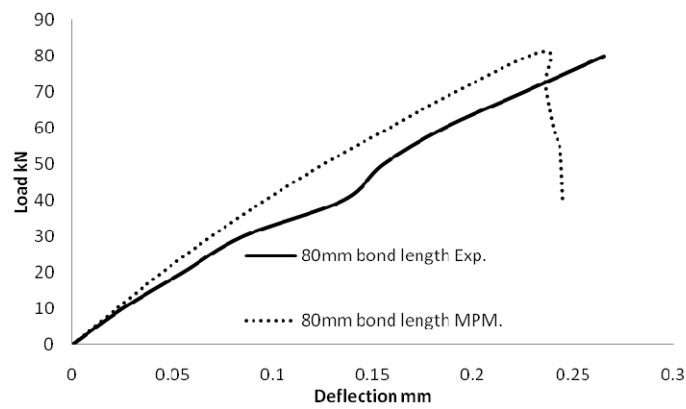


Figure 5.8 Comparison of load displacement behaviour of bond length 80mm.

As can be seen from the figures, for the CFRP-steel joint under loading rate of 2mm/min, the MPM simulation results match the experimental data well. Furthermore, the MPM simulation is able to provide the unloading section of the load-deflection curve with the use of the constitutive models containing softening regime. The comparisons of the ultimate loads of the steel-CFRP joints predicted by the MPM and measured in the experiment are given in Table 5.2.

Table 5.2 Comparisons of experimental data and MPM results

Bond Length L_1 (mm)	Ultimate Load (kN)			
	Test 2mm/min	MPM 2mm/min	MPM 20mm/min	MPM 200mm/min
40	49.90	51.99	69	72
50	69.80	68.9	78.6	82.4
70	80.80	86.91	90.55	93.11
80	81.3	81.39	90.8	94.5
90	NA	74.14	87.7	90.3
100	NA	79.3	85.9	90.6

With a difference ranging from -1.3% to 7.02%, the simulated load carrying capacity is in close agreement with experimental measurements.

To study the effect of increasing the bonding length above the effective length, 90mm and 100mm bonding lengths have been modelled as shown in Figures 5.9 and 5.10.

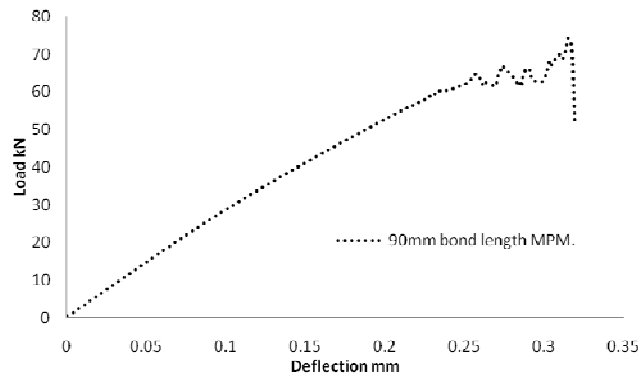


Figure 5.9 Load displacement behaviour of simulated bond length 90mm

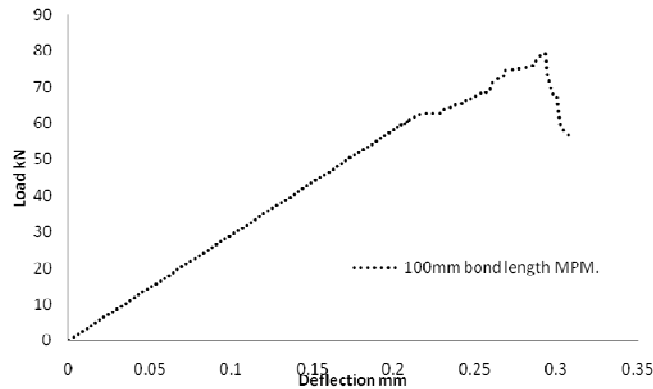


Figure 5.10 Load displacement behaviour of simulated bond length 100mm

As the bond length increases above the optimum bond length, the ultimate strength ceases increasing. However, the behaviour of the specimens becomes more ductile and the displacements continue to increase.

Furthermore, the numerically simulated and experimentally measured distributions of the normal strain ϵ_{xx} along the top surface of the combined CFRP/epoxy for the bond lengths of 70mm and 80mm at time $t=t_{\text{failure}}$ are compared in Figures 5.11 and 5.12, respectively. It is evident that the simulated strain distributions are consistent with those measured experimentally.

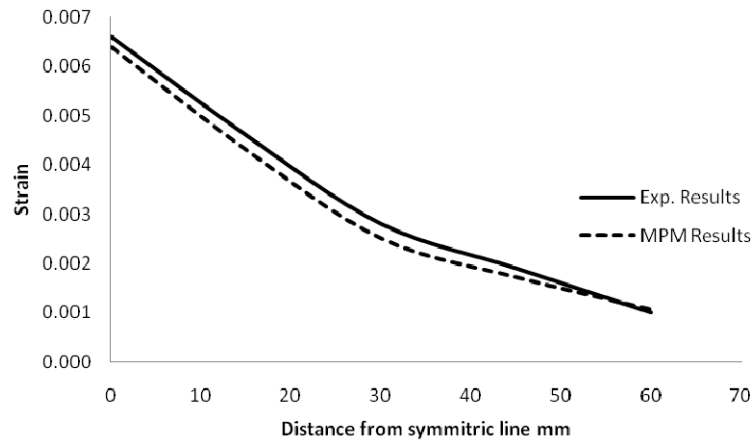


Figure 5.11 Normal strain distribution in the combined CFRP/epoxy layer with bond length of 70mm.

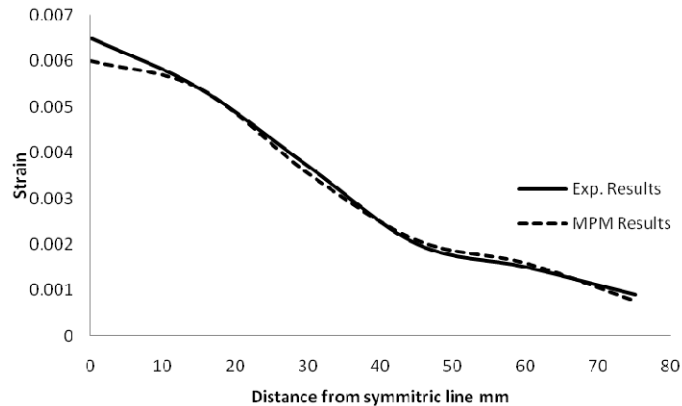


Figure 5.12 Normal strain distribution in the combined CFRP/epoxy layer with bond length of 80mm.

The failure pattern is very important for understanding the performance of the steel-CFRP joint system because it provides a detailed view of the evolution of the system failure. Figures 5.13-5.16 show the actual deformation patterns of the specimens with bond lengths of 40mm, 50mm, 70mm and 80mm, respectively.

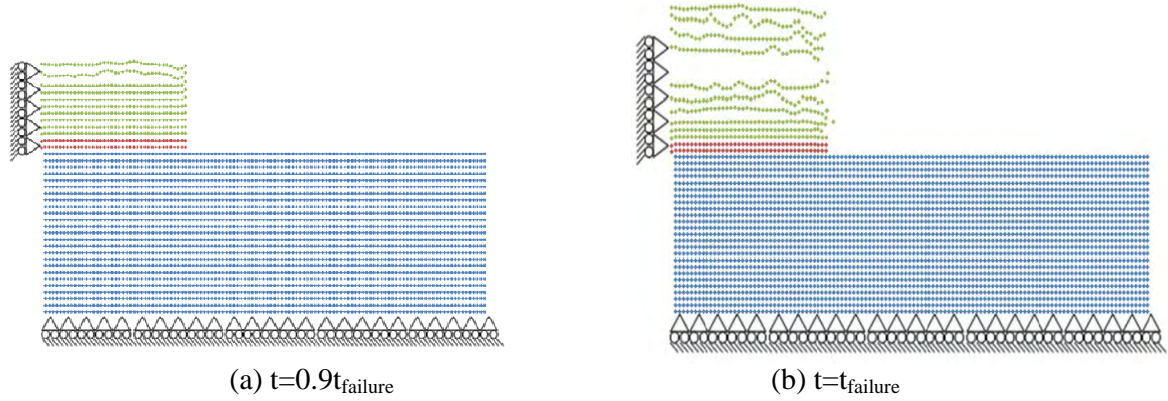


Figure 5.13 Deformed shapes for 40mm bond length at different times.

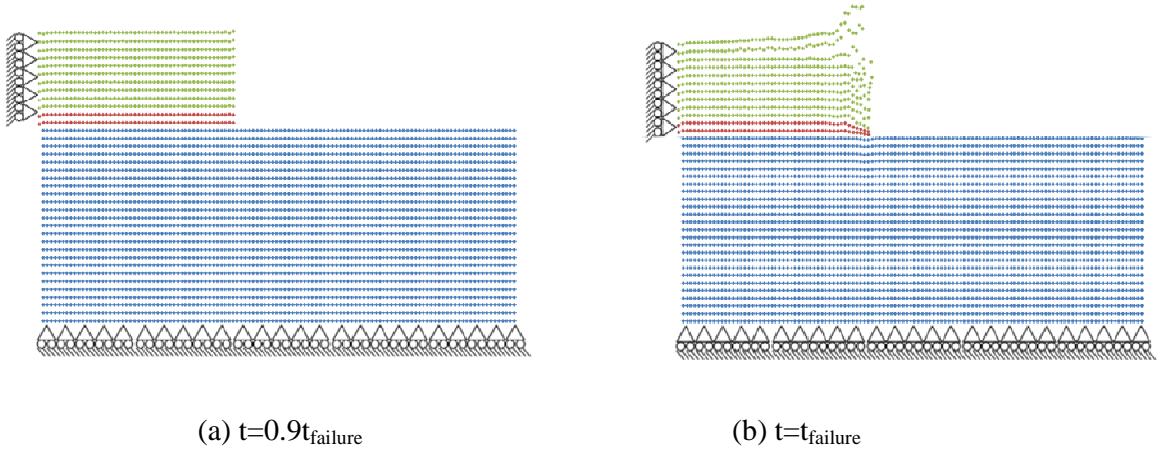


Figure 5.14 Deformed shape for 50mm bond length at different times.

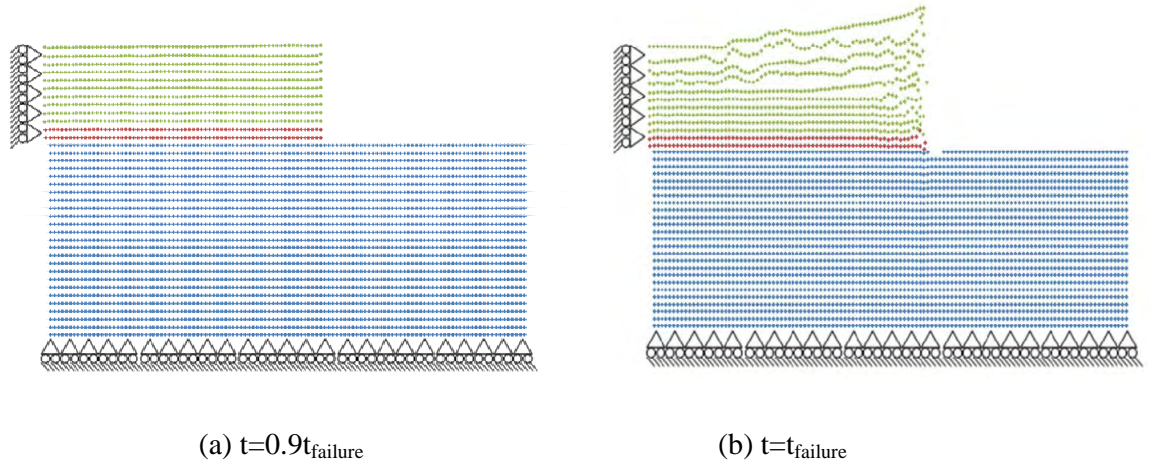


Figure 5.15 Deformed shape for 70mm bond length at different times.

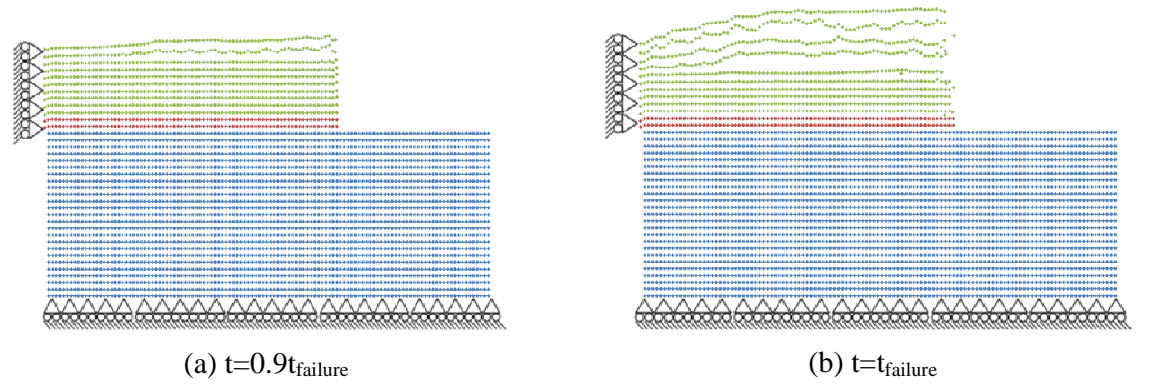


Figure 5.16 Deformed shape for 80mm bond length at different times.

In the experiments (Fawzia , 2007), the main failure scheme was a bonding failure inside the combined CFRP/epoxy layer, as shown in Figure 5.17.

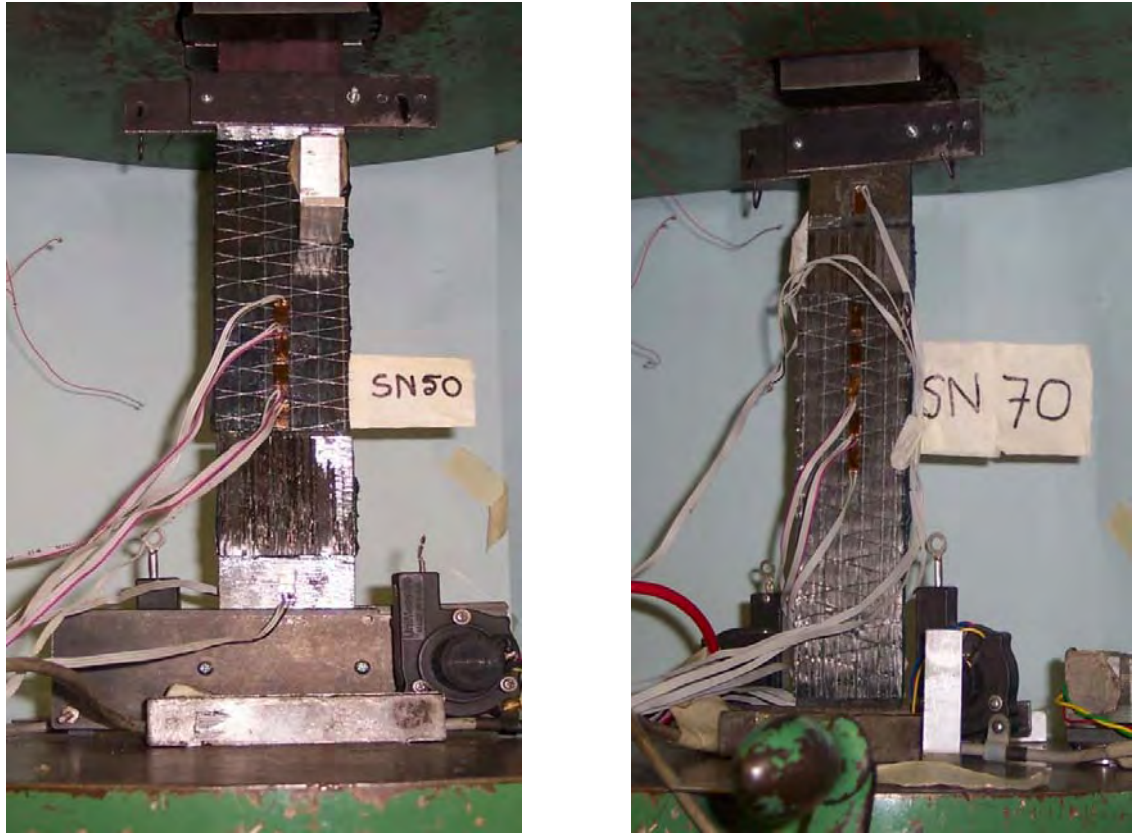


Figure 5.17 Experimental failure mode for 50 and 70 mm bond length (Fawzia,2007)

These failure patterns are effectively simulated by the MPM, as shown in Figures 5.13-5.16. It appears from Figures 5.13(a), 5.14(a), 5.15(a) and 5.16(a) that the samples start to show a distortion at the upper part of the composite layer when time t is at 90% of the complete failure time. This distortion is observed in all simulated specimens with different degrees of clarity when the bond length varies. In the 40 mm bond length case, the distortion evolves to become a full and clear delamination within the composite layer lower than where the distortion starts as reported in Figure 5.13(b). In the 50mm and 70 mm bond length samples, the distortion develops to become a combination of separation within the combined layer and a rupture near the end of the bonding length, as presented in Figures 5.14(b) and 5.15(b). When the bond

length increases to 80mm, which is the optimum bond length according to Fawzia (2007), the failure becomes a delamination pattern similar to but not as clear as that of 40mm bond length as demonstrated in Figure 5.16(b).

Generally, the failure is brittle and the brittleness of the system decreases as the bond length increases. This may be due to the ductile properties of the epoxy bond affecting the mechanical properties of the combined CFRP/epoxy layer. The change of the failure mode from delamination to a combination of delamination and rupture failure is due to the different stress distribution along the bond length direction. As the epoxy layer length increases, the effectiveness of transferring the stress from steel plate to the CFRP layer increases due to the high ductility of the epoxy layer compared with the CFRP layer. Figures 5.18-5.21 demonstrate the normalized shear stress τ_{xy} distribution along the bond length direction at time $t=0.9t_{\text{failure}}$ and $t=t_{\text{failure}}$ for bond lengths of 40mm, 50mm, 70mm and 80mm respectively.

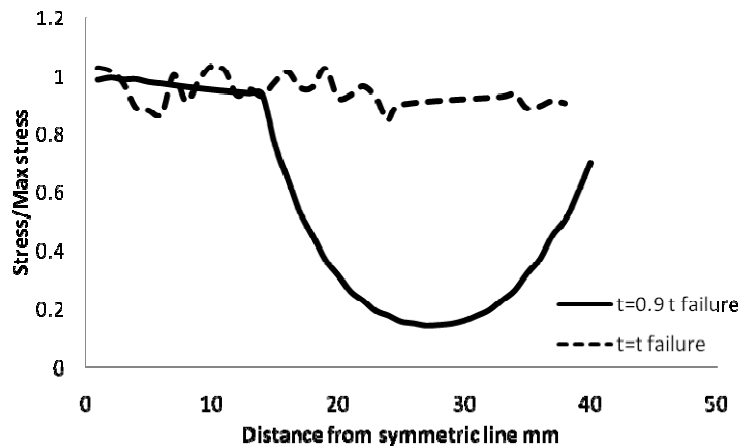


Figure 5.18 Shear stress distribution along 40 mm bond length samples at the failure layer.

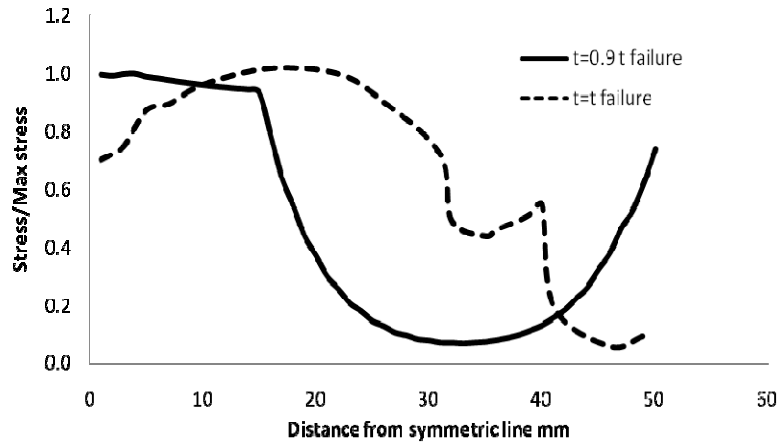


Figure 5.19. Shear stress distribution along 50 mm bond length samples at the failure layer.

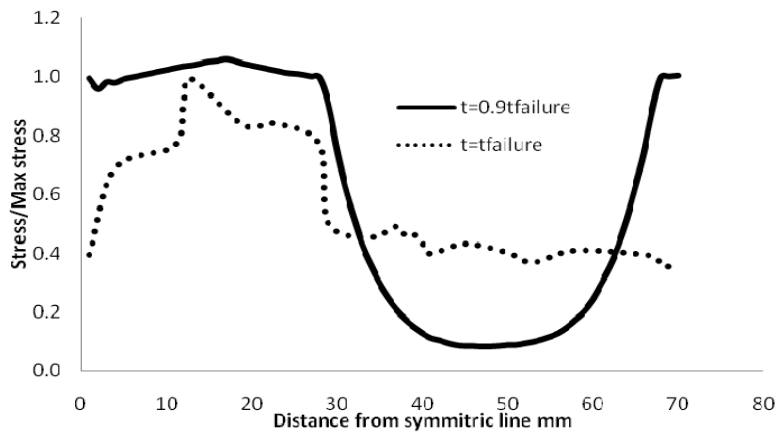


Figure 5.20. Shear stress distribution along 70 mm bond length samples at the failure layer.

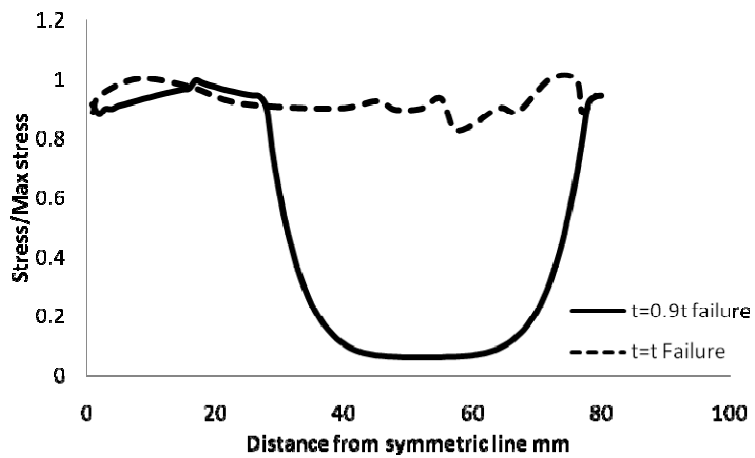


Figure 5.21. Shear stress distribution along 80 mm bond length samples at the failure layer.

The straight part of the $0.9t_{\text{failure}}$ curve shows that the stresses are fully transferred from steel plate to the CFRP layer. Figures 5.18-5.21 clearly show that the straight part of the stress on $0.9 t_{\text{failure}}$ ends at 15 mm for 40 mm bond length, increasing to 30 mm for 70 mm bond length and stays constant as the bond length increases. This constancy is consistent with the fact that the optimum bonding length falls between 70mm and 80mm, when the epoxy layer reaches its limit of stress transfer. As the time approaches failure, the shear stress is more evenly distributed in the short bond specimen than in the long bond specimen. Therefore, in a CFRP-steel system with a short bond, the concentration of shear stress is not sufficient to cause a rupture failure. Instead, the shear stress will be evenly distributed along the bond length, which allows more material points in the epoxy bond layer to reach the failure stress almost simultaneously, as shown in Figure 5.18, and leads to a clear delamination, which can be observed in Figure 5.11. For the specimen with the longer bond, the maximum shear stress is reached before the shear stress is evenly distributed along the bond length, as presented in Figures 5.19 and 5.20, which will lead to a rupture failure at the stress concentration point. This point (around 25 mm from the steel edge for 50 mm bond length and 30mm for 70 mm bond length) works as a separation point that stops stress distribution, which leads to the build up of stress before it and the disappearance of stress after it. Therefore, failure occurs due to stress concentration on the bonding length before this point.

For the even longer bond length (80 mm), the shear stress will first concentrate at a certain point and cause a rupture failure at that point, as previously clarified. However, the un-delaminated part of the bond will be long enough to allow for stress redistribution and to cause delamination, as can be seen in Figure 5.21.

5.3.2.2 Loading rate effect

The mechanical behaviour of CFRP is known to be loading-rate sensitive (Jiang et al. 2006). Hence, it is important to understand the effect of loading rate on the failure mechanism of CFRP-steel joint systems. In this study, the MPM is used to study the loading rate effect on the ultimate load and failure mode of CFRP-steel systems with 40,50,70 and 100mm bond lengths. The simulated loading rates are 2, 20 and 200 mm/min.

Figure 5.22 shows the load-deflection curves of the CFRP-steel system with 40 mm bond length under different loading rates. As can be seen from the figure, when the loading rate increases from 2mm/min to 20mm/min, the ultimate load increases by more than 35%. However, when the loading rate increases further to 200mm/min, no significant increase of the ultimate load is observed. Furthermore, the displacement at the ultimate strength has been nearly doubled as the loading speed increased from 2mm/min to 20mm/min. The failure displacement increased the loading rate increased to 200mm/min to 3 times more than that of 2mm/min, due to the divergence part of the curve.

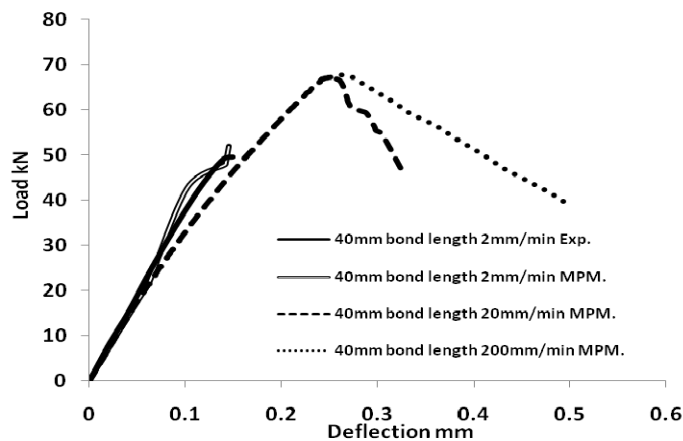


Figure 5.22 Loading rate effect on the load-deflection curve of 40 mm bonding length

Figures 5.23 and 5.24 demonstrate the failure evolution of the 40mm bonding length under loading rates of 20mm/min and 200mm/min, respectively. It appears from Figures 5.13 and 5.22 that when the loading rate increases from 2mm/min to 20 mm/min, delamination occurs at a deeper position inside the combined CFRP/epoxy layer. If the loading rate increases further to 200mm/min, the failure becomes a rupture at the steel plate, as shown in Figure 5.23, rather than delamination in the combined CFRP/epoxy layer. As the loading rate increases, the stress redistribution across CFRP layers increases and becomes more effective. The stress distribution leads to more particles reaching optimum strength and displacement. This distribution clarifies the displacement increments as the loading rate increases.

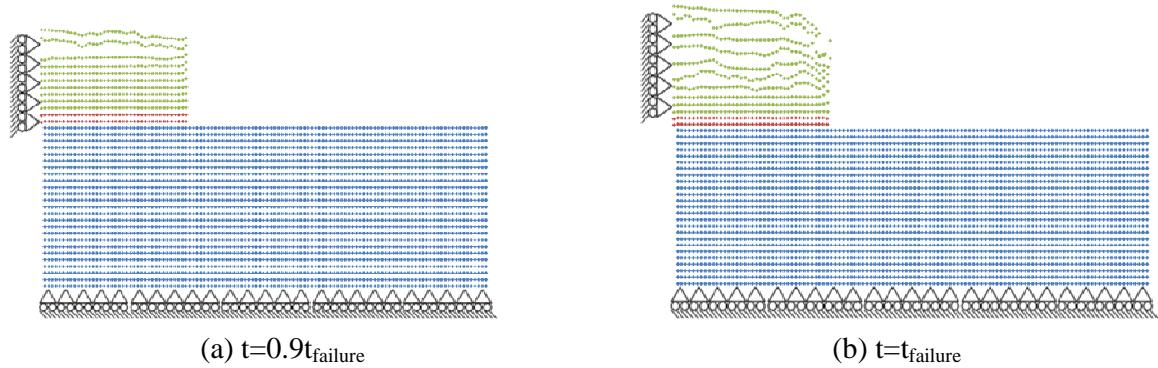


Figure 5.23. Deformed shape for 40mm bond length under 20mm/min loading speed at different times

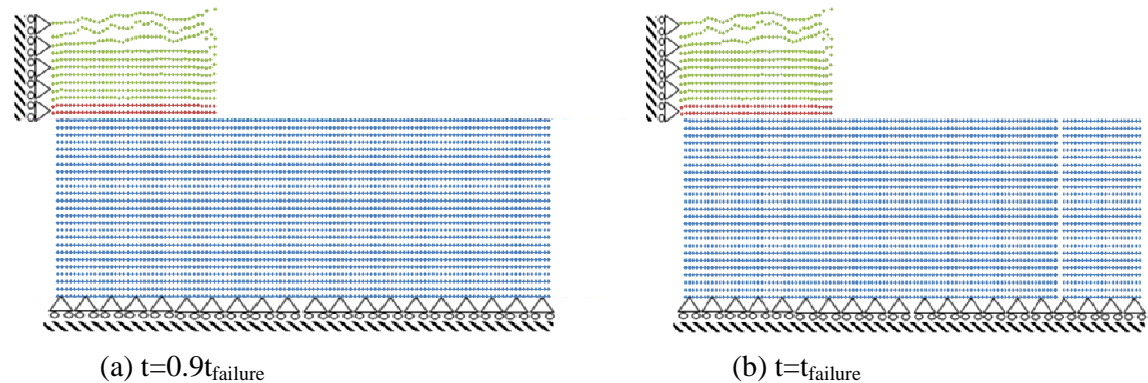


Figure 5.24. Deformed shape for 40mm bond length under 200mm/min loading speed at different times

As the bond length increase, the increasing effect of loading rate on ultimate strength decrease as shown in Figures 5.25-5.29.

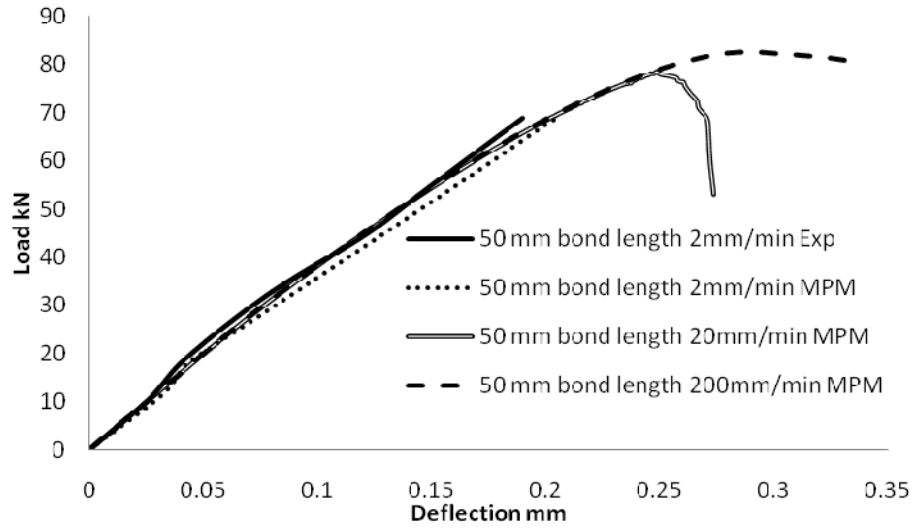


Figure 5.25. The effect of loading rate on the load-deflection curve of 50mm bonding length

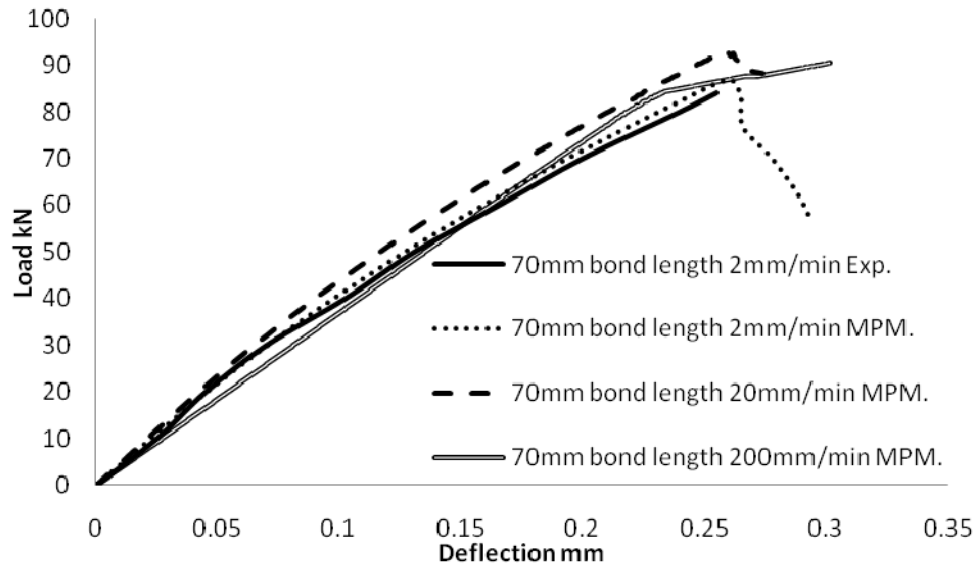


Figure 5.26. The effect of loading rate on the load-deflection curve of 70mm bonding length

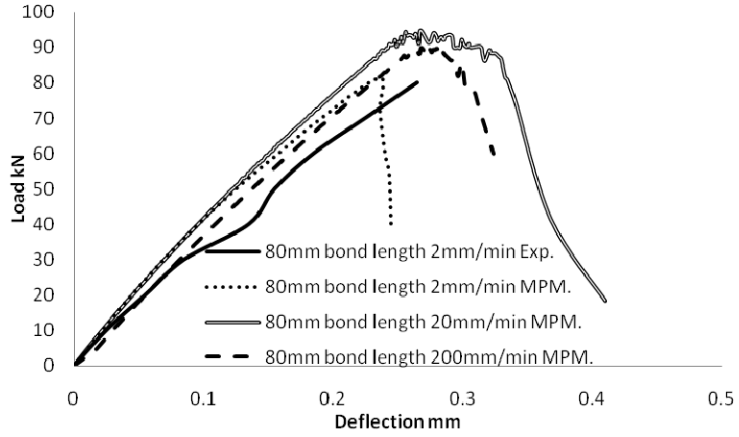


Figure 5.27. The effect of loading rate on the load-deflection curve of 80mm bonding length

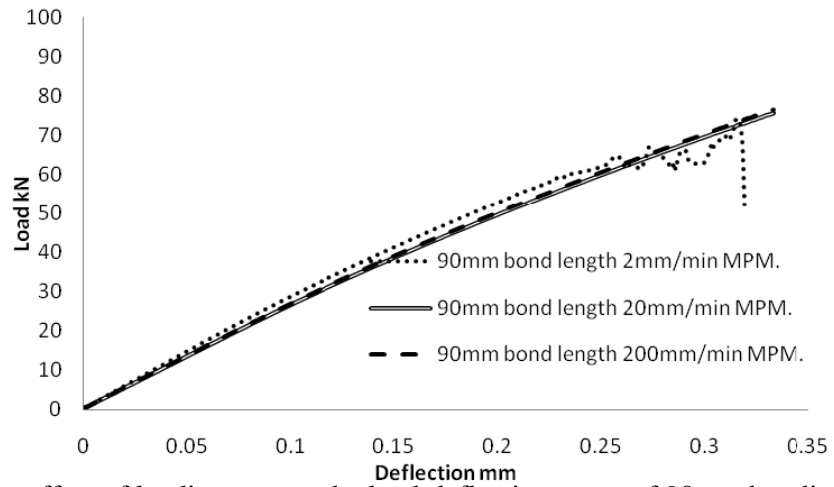


Figure 5.28. The effect of loading rate on the load-deflection curve of 90mm bonding length

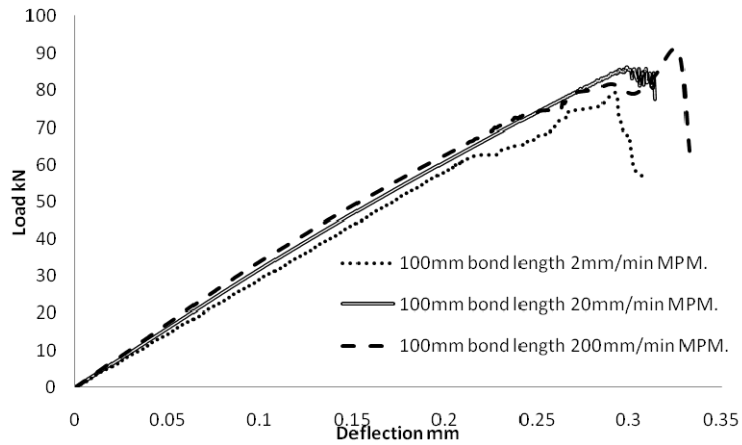


Figure 5.29. The effect of loading rate on the load-deflection curve of 100mm bonding length

As the loading rate increases, the ultimate load increases with a continuous displacement increment. The smaller loading rate, 2mm/min, still has smaller ultimate strength, but as the loading rate increases the ultimate load increases by a smaller percentage compared with the shorter bond length. For example: increasing the loading rate from 2mm/min to 20mm/min for the 40mm bond length increases the ultimate strength by 32%, but this percentage decreases to 18% and 8% for the 90mm and 100mm bond lengths respectively. These results match the Hart-Smith concept well by reaching the optimum bonding length, where the ultimate strength stays constant even the bond length increases. Figure 5.30 shows the modified Hart-Smith model for different loading rates.

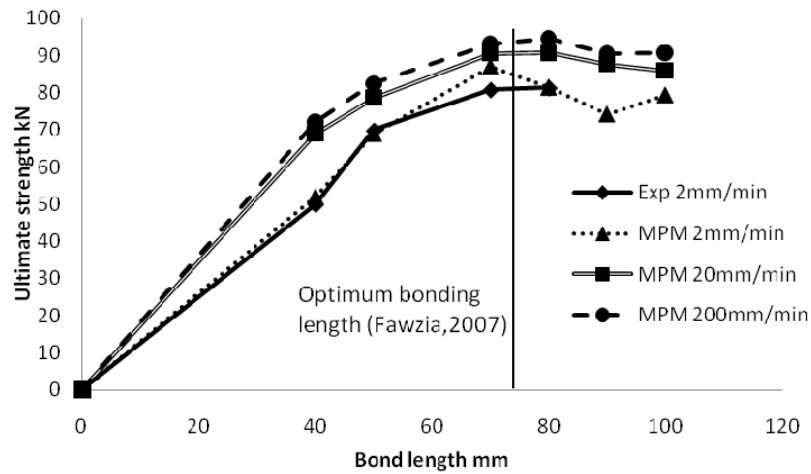


Figure 5.30 Loading rate effect on various bonding lengths

Figure 5.30 clearly shows that for every bond length there is a loading rate which gives optimum strength. Beyond this rate, the optimum strength is not affected by the loading rate. This loading rate is around the 20mm/min for the modelled specimens.

5.4 MPM simulation of different epoxy specimens:

MPM was used to simulate different types of epoxies used in CFRP-steel single lap shear specimens. The mechanical properties of Araldite-420 and Sikadur-30 were reported in Chapter three. Table 5.3 illustrates the mechanical properties of the modelled materials.

Table 5.3 Mechanical properties of the materials of single lap shear specimens

	CFRP plate	Steel plate	Araldite-420 Hand mix	Araldite-420 sonication	Sikadur-30 Hand mix	Sikadur-30 sonication
Elastic Mod-ules (GPa)	208	186	1.87	1.86	13.48	9.29
Yield Strength (MPa)	2750	320	15	15	13	15
Plastic Strength (MPa)	2865	484	26.7	26.4	18.6	22.8
Poisson Ratio	0.21	0.25	0.21	0.21	0.25	0.25

As reported in Table 5.3, the sonicated Araldite-420 material properties are similar to those of the hand-mixed Araldite-420. Therefore, only the sonication-mixed Araldite-420 will be modelled. The CFRP-steel specimens' dimensions match those reported in Chapter four. The simulated loading rate is 2mm/min, which is the same as that used in the experimental procedure. As mentioned in Section 5.3, the MPM simulation was simplified into a two-dimensional plane strain problem. The simulated specimen is divided into three different materials layers, namely, 12 mm thick steel layer, 0.5 mm thick epoxy layer, and 1.4 mm thick CFRP plate, as shown in Figure 5.31. The boundary conditions used in the MPM simulation are illustrated in Figure 5.31.

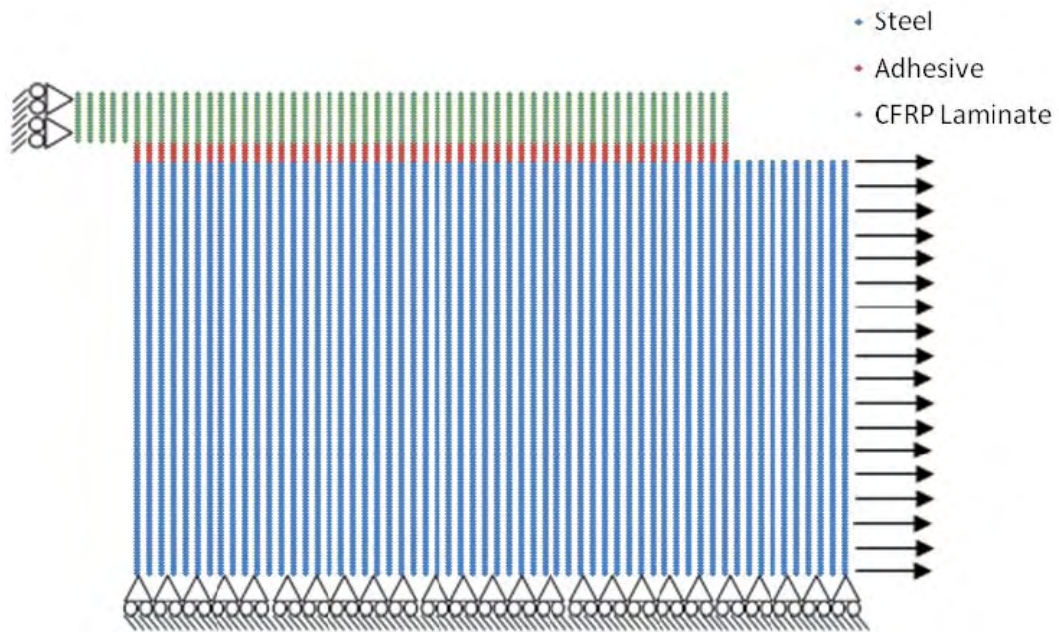


Figure 5.31 Schematic of Chapter four specimens modelled using the MPM.

To ensure that there are at least two material point layers in each part along the thickness direction, a mesh size of 0.05 mm high and 1 mm long is chosen to discretise the CFRP-steel joint system. A constant velocity of 2mm/min is applied to the right edge of the steel plate to simulate the displacement controlled loading in the experiment.

The strain and stress are taken from a point at the surface of the CFRP-free edge.

As mentioned before in Chapter Four, the hand-mixed specimens of Araldite-420 and Sikadur-30 were named CAH and CSH respectively. The sonicated-only Sikadur-30 specimen will be named CSM. Figures 5.32 to 5.34 show the stress-strain diagrams for the simulation of different epoxy specimens compared to the experimental results.

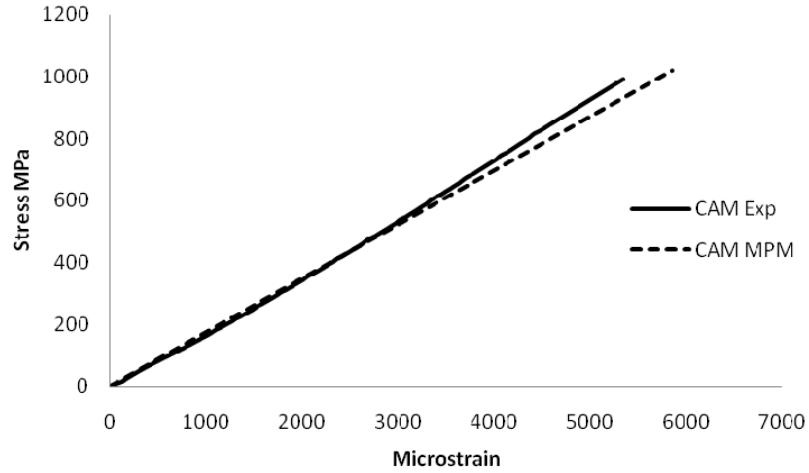


Figure 5.32 MPM modelling compared with experimental results for sonicated-only mixed Araldite-420 specimens

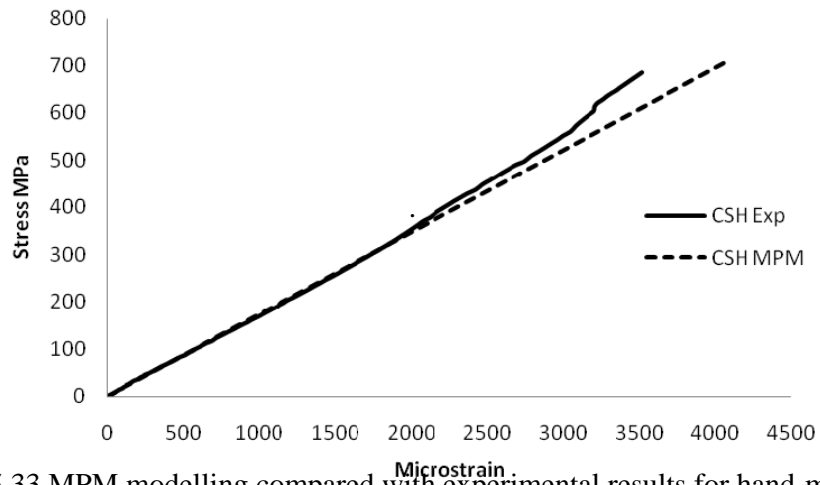


Figure 5.33 MPM modelling compared with experimental results for hand-mixed Sikadur-30 specimens

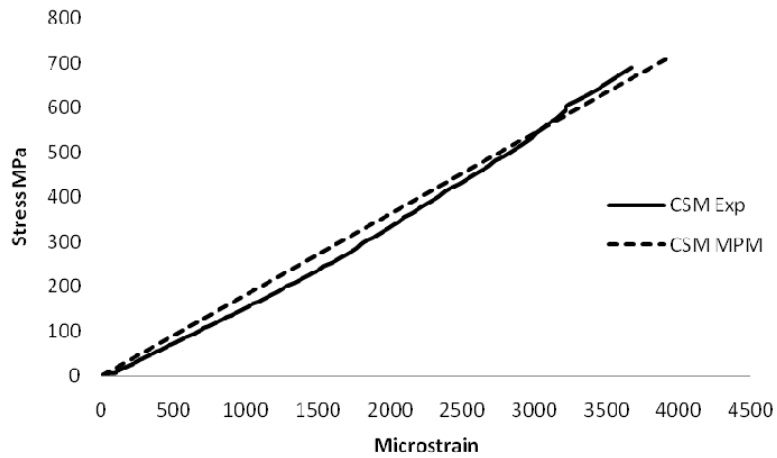


Figure 5.34 MPM modelling compared with experimental results for sonication mixed Sikadur-30 specimens

These figures clearly show that the MPM simulation results, which are very consistent with the experimental results, demonstrate very ductile and nearly linear behaviour up to failure. This behaviour is due to the ductile failure type that occurs all specimens. This failure is clearly modelled by the MPM and illustrated by Figures 5.35-5.37.

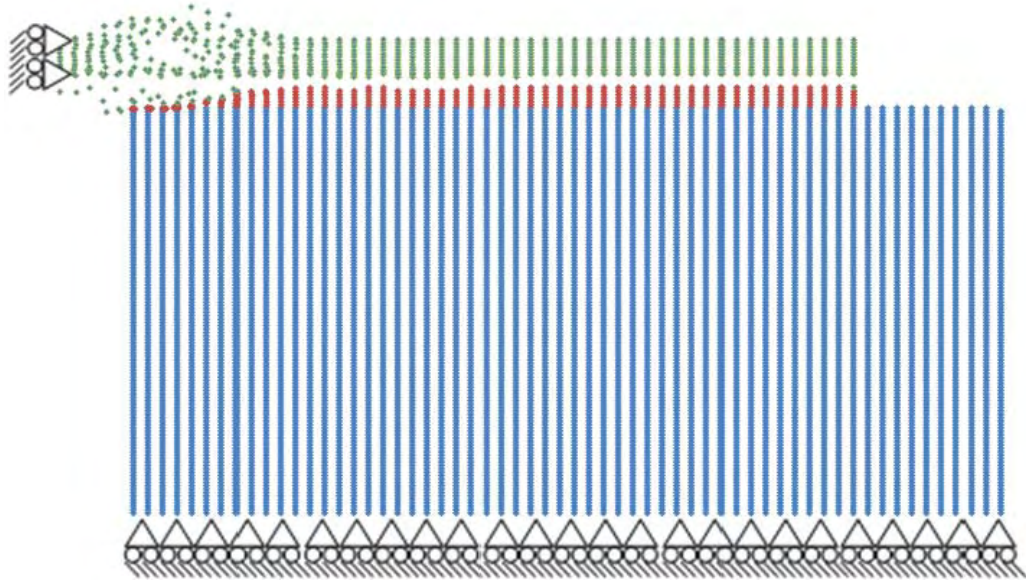


Figure 5.35 MPM model failure shape (side view) and failure image(top view) for CAM specimens

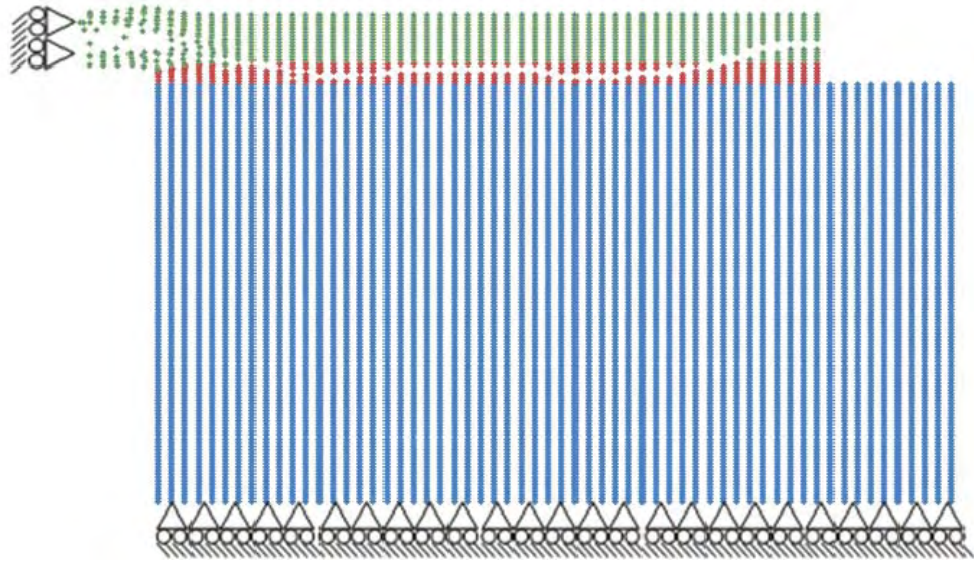


Figure 5.36 MPM model failure shape (side view) and failure image(top view) for CSH specimens

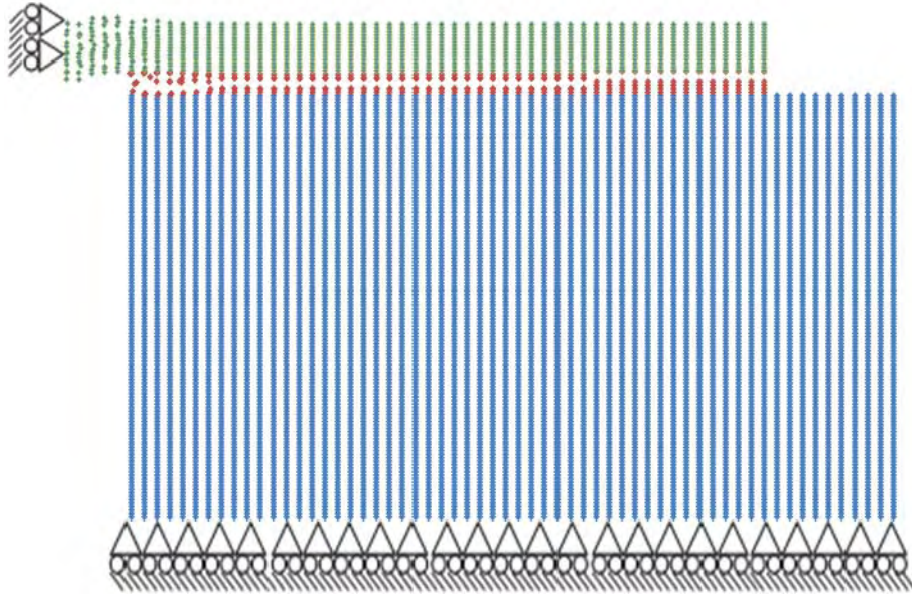


Figure 5.37 MPM model failure shape (side view) and failure image(top view) for CSM specimens

Figures 5.35-5.37 clearly show how the modelled failure shape has a similar failure type compared with the tested specimens: CFRP plate failure along bond length for

CAM and CAH specimens; failure at epoxy layer developing to CFRP plate failure when reaching the end of bond length for CSM and CSH specimens.

Furthermore, the plane strains along the CFRP surface collected in experiments have been modelled by MPM. Figures 5.38-5.40 show the comparisons between MPM results and test data.

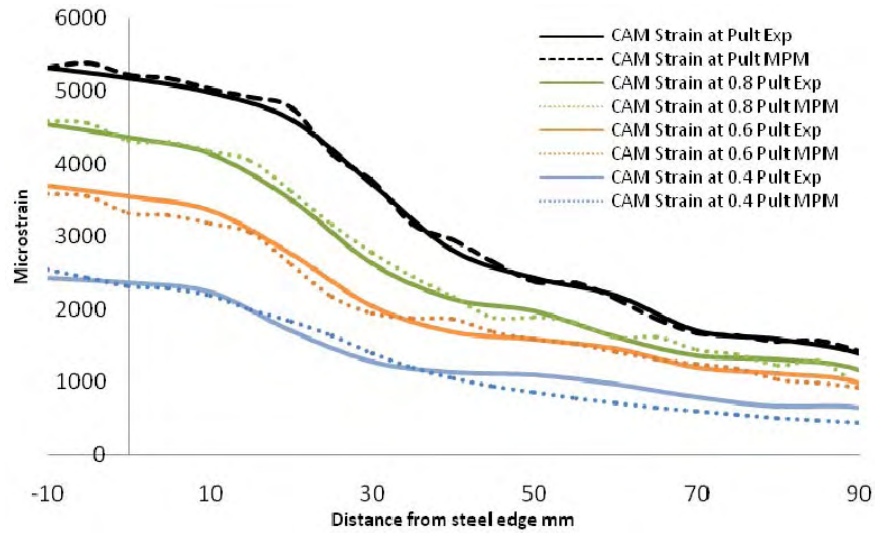


Figure 5.38 Normal strain distribution in the CFRP plate surface for CAM specimens.

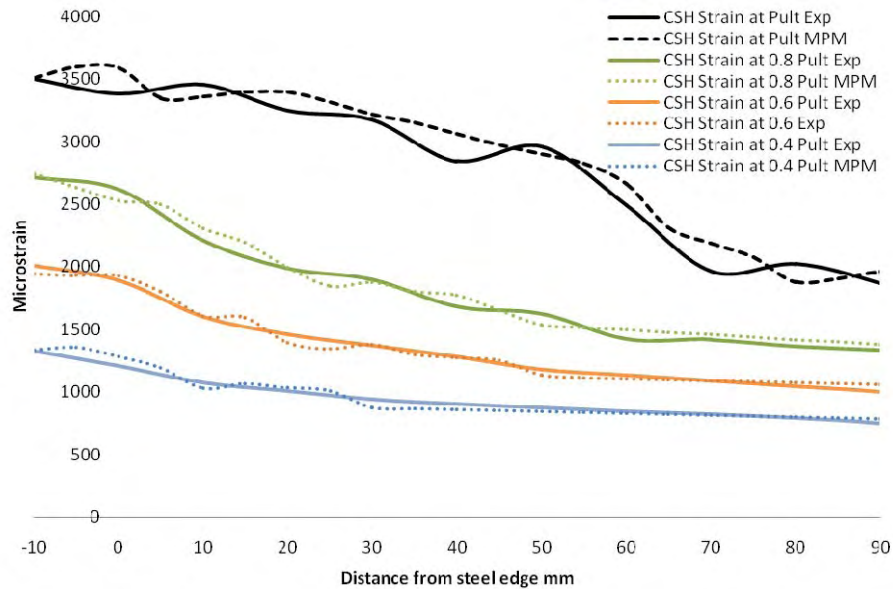


Figure 5.39 Normal strain distribution in the CFRP plate surface for CSH specimens.

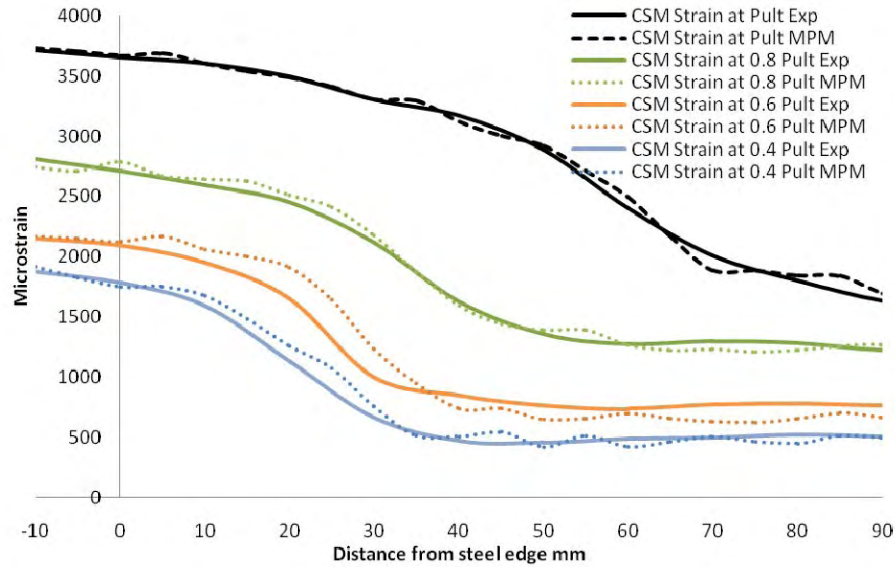


Figure 5.40 Normal strain distribution in the CFRP plate surface for CSM specimens.

Figures 5.38-5.40 show a good agreement between the experimental and MPM-modelled samples.

5.5. Summary

In this chapter, previously tested double lap and current single lap CFRP-steel systems under shear loading have been simulated using elasto-plasticity material models within the framework of the MPM. The effects of bond length, loading rate and different epoxy properties on the load carrying capacity and failure mode of the CFRP-steel joint system have been investigated. The simulated load-deflection, stress-strain curves and normal strain distributions at the top of combined CFRP/epoxy layers and CFRP plates are consistent with the available experimental data.

The simulation results show that if the bonding length is short enough, the development of the failure mode of the CFRP-steel joint system will be a “clear” delamination without any rupture within the layer. As the bond length increases, the failure mode starts to become a mixed delamination and rupture within the combined

CFRP/epoxy layer. For a given CFRP-steel system there is an optimum loading rate at which the system allows the stress to evenly distribute along the bond length and result in a single clear delamination or a multiple layer delamination. If the loading rate is further increased, the failure will occur in the steel plate.

From the parametric study on the effects of bond length and loading rate, it appears that the proposed model-based simulation procedure with the framework of the MPM is able to capture the essential failure mechanism of the CFRP-steel joint system under shear loading.

Chapter Six

Nanomaterial Enhanced CFRP-steel systems: Bond-Slip Models

6.1 Introduction

In common engineering practice, the numerical modelling approach is considered as numerical laboratories tests. The efficiency and accuracy of these tests depend on the suitable modelling of the material properties fed in, and the numerical approach to simulate the failure nature.

The Finite Element Method (FEM) is a mesh-based method and may have difficulties in modelling the transition from the continuous to discontinuous failure mode involved in the process of CFRP delamination from steel plate. Therefore, the Material Point Method (MPM), which is one of the meshless methods that do not employ fixed mesh connectivity, is adopted to model the discontinuous failure of CFRP-steel bond.

The main difference between the FEM and the MPM in modelling delamination failure is that there is no fixed mesh connectivity involved in the MPM. Therefore, complete decohesion or separation would occur if the material strength is totally or nearly lost. In other words, a material point would be separated from the original continuum body (which may occur in experiments) if there is no internal interaction between the fully failed point with zero or near zero strength and the body with non-zero strength.

It is worth noting that in most of the previous numerical simulations, an elastic-perfectly plastic scheme was used for the epoxy. In the present research, an elastoplastic model with a linear hardening and softening law is implemented in the MPM to simulate the CFRP and adhesive epoxy layers.

In this chapter, in order to gain further understanding of the debonding behaviour of single strap joints, MPM is used to simulate the nanomaterial-enhanced CFRP-steel system tested in Chapter Four. Stress-strain relationships and strain distribution along the CFRP bond length have been compared between experimental and MPM results. A bond slip model has been developed, based on experimental results for nanoparticle-enhanced CFRP-steel joints and an optimum percentage of nanoparticles have been found for maximum shear bond strength.

6.2 MPM simulation of nanomaterial-enhanced specimens

The tested specimens from Chapter Four have been modelled using MPM. The simulation process followed the same procedure detailed in Section 5.4. The naming scheme for the modelled specimens follows the naming scheme applied in Chapter Four and summarized in Figure 4.2. The tested specimens have the same joint geometrical properties as those reported in Figure 4.1, the only difference being the epoxy properties. The mechanical properties for the steel and CFRP used in the experimental tests have been reported in Chapter Three and summarized in Table 5.3. The material properties for the different epoxies used in the tests reported in Chapter Four and modelled by MPM have been reported in Chapter Three and are summarized in Table 6.1 below.

Due to the large number of specimens modelled, only the CAS1, CAC2, CSS1 and CSC2 specimens have been reported in this chapter.

Table 6.1 Mechanical properties for tested epoxy used in MPM simulation

	Elastic Modulus (GPa)	Yield Strength (MPa)	Plastic Strength (MPa)	Poisson Ratio
CAC1	2.1	20	27.9	0.21
CAC2	2.13	21	30.9	0.21
CAC3	1.92	15	27.2	0.21
CAS1	1.93	17	27.9	0.21
CAS2	1.77	15	23.5	0.21
CAS3	1.85	14	25.9	0.21
CSC1	12.37	13	23.5	0.25
CSC2	10.84	12	17.7	0.25
CSS1	11.63	16	25.9	0.25
CSS2	10.56	11	16.4	0.25
CSS3	11.39	9	17.4	0.25

The remaining sample simulation results are reported in Appendix A. The stress-strain curves and the strain distribution at the top of the CFRP plate along the bonding length have been compared from experimental results and MPM. Figures 6.1-6.4 compare the simulated and tested stress strain diagrams and strain distributions of CAS1 and CAC2 specimens.

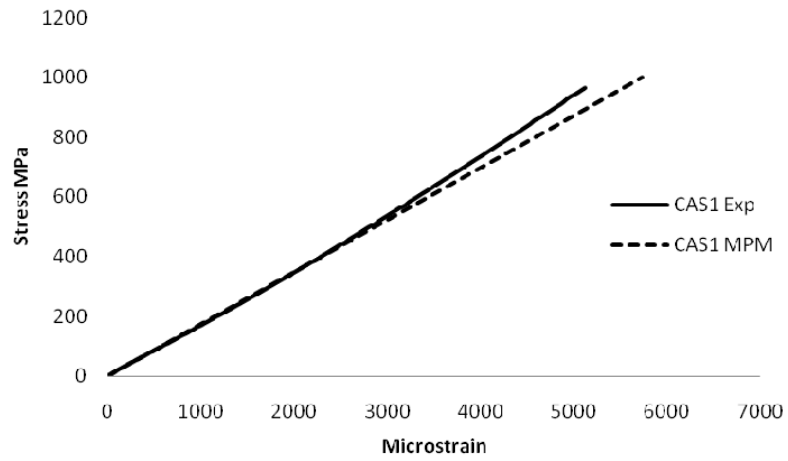


Figure 6.1 MPM specimens compared with experimental results for Araldite+1%SiC samples

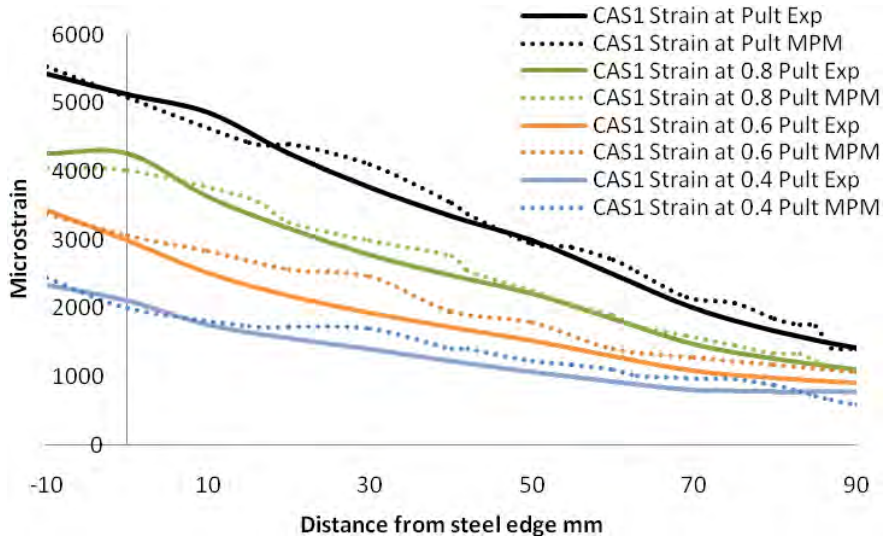


Figure 6.2 MPM-experimental strain distribution on CFRP surface along bonding length for CFRP-Araldite+1%SiC

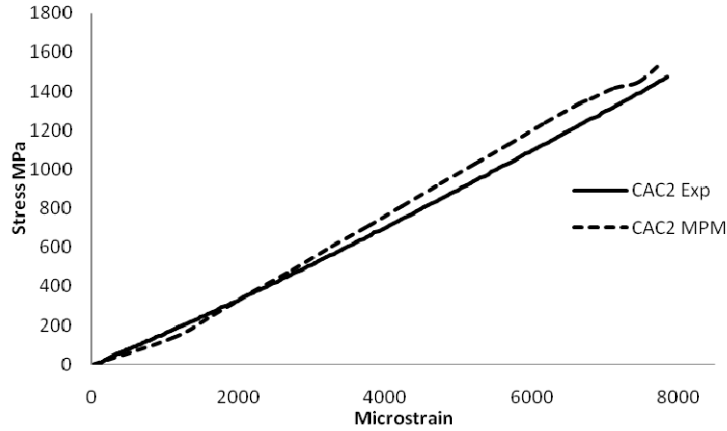


Figure 6.3 MPM specimens compared with experimental results for Araldite+2%MWCNT samples

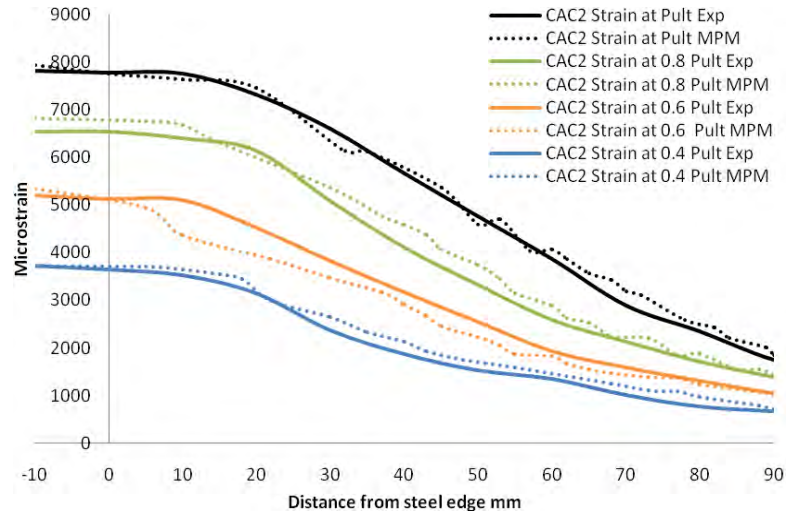


Figure 6.4 MPM-experimental strain distribution on CFRP surface along bonding length for CFRP-Araldite+2%MWCNT

Figures 6.1-6.4 show good agreement between the simulation results and the experimental data. The behaviour of the modelled specimens is ductile and nearly linear. This behaviour is due to the nature of the failure that occurs suddenly in the

experiments. The strain distribution curve starts with small slop until it reaches the first 10mm from the steel joint. This straightness is due to the constancy of the strain recorded for the free CFRP plate and its effect is passed beyond the steel joint.

Figures 6.5-6.8 compare the simulated and tested stress-strain diagrams and strain distributions of CSS1 and CSC2 specimens.

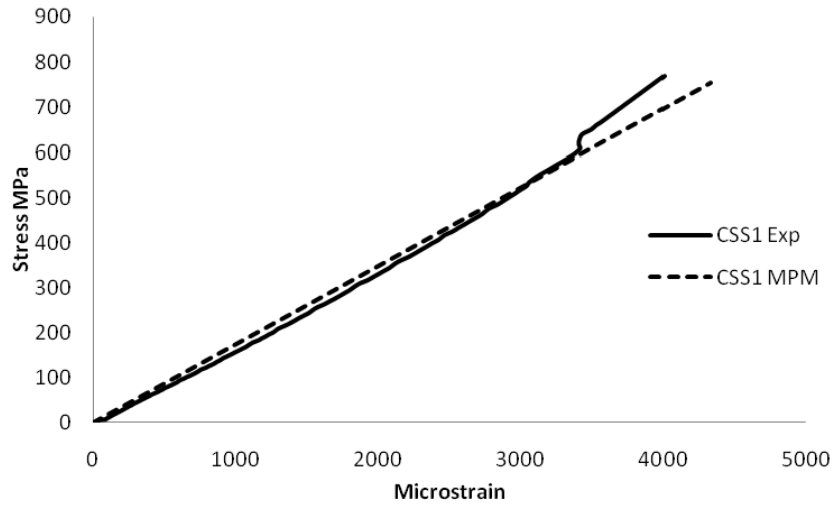


Figure 6.5 MPM specimens compared with experimental results for Sikadur-30+1%SiC samples

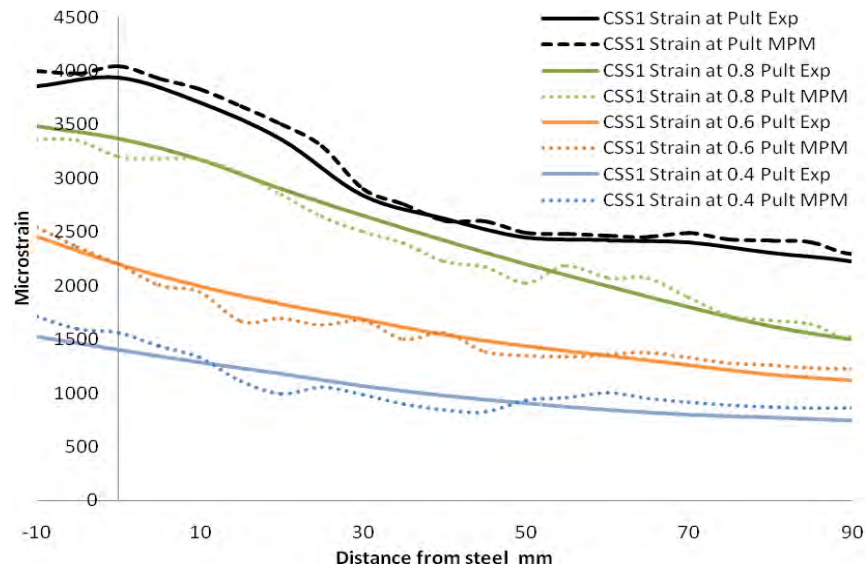


Figure 6.6 Compared MPM-experimental strain distribution on CFRP surface along bonding length for CFRP-Sikadur-30 +1%SiC

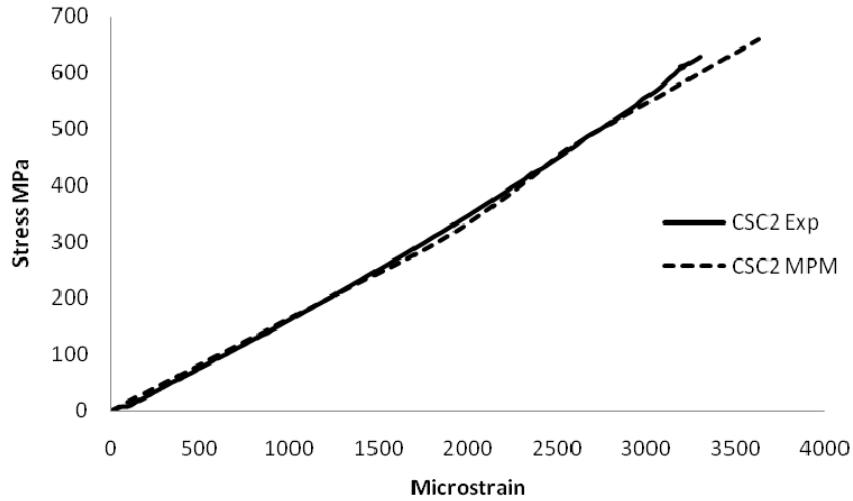


Figure 6.7 MPM specimens compared with experimental results for Sikadur-30+2%MWCNT samples

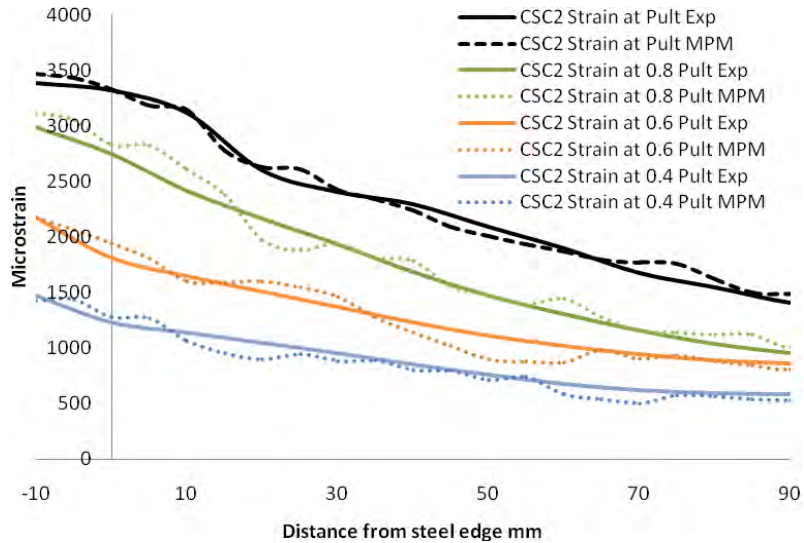


Figure 6.8 Compared MPM-experimental strain distribution on CFRP surface along bonding length for CFRP-Sikadur-30 +2%MWCNT

Figures 6.5-6.8 show a small and acceptable difference between the simulated and experimental data.

The good agreement between the MPM simulated specimens and the experimental data encouraged the simulation of specimens with the epoxy properties tested in Chapter Three and were not tested in Chapter Four. The ASO epoxy series specimens (Araldite-420 mixed with 1%, 2% and 3% SiC then oven-vacuumed) have been tested in the epoxy testing campaign but not used to build CFRP-steel samples. Therefore, the same dimensions and material properties for steel and CFRP plates used in previous simulations will be used, albeit with changes of the material properties of the joining adhesive to the material properties of the ASO properties from Chapter Three. Table 6.2 summarizes the material properties for ASO specimens.

Table 6.2 Mechanical properties of ASO epoxy

	Elastic Modules (GPa)	Yield Strength (MPa)	Plastic Strength (MPa)	Poisson Ratio
CASO1	2.75	16	28.9	0.21
CASO2	2.06	17	24.3	0.21
CASO3	2.27	14	27.7	0.21

Note that the letter ‘C’ has been added to the beginning of the epoxy names to differentiate them from the epoxy specimens.

Figures 6.9-6.11 show the stress-strain diagrams for CASO simulated specimens compared with the non-oven vacuumed specimens (CAS).

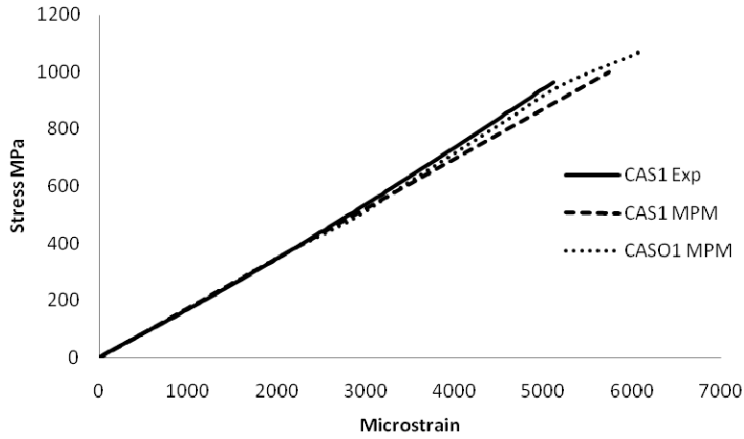


Figure 6.9 MPM specimens of oven-vacuumed specimens compared with experimental and MPM results of Araldite-420 +1% SiC

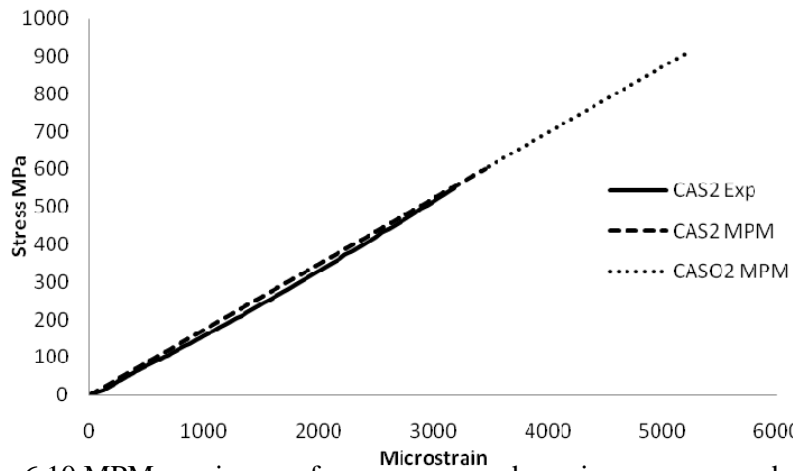


Figure 6.10 MPM specimens of oven-vacuumed specimens compared with experimental and MPM results of Araldite-420 +2% SiC

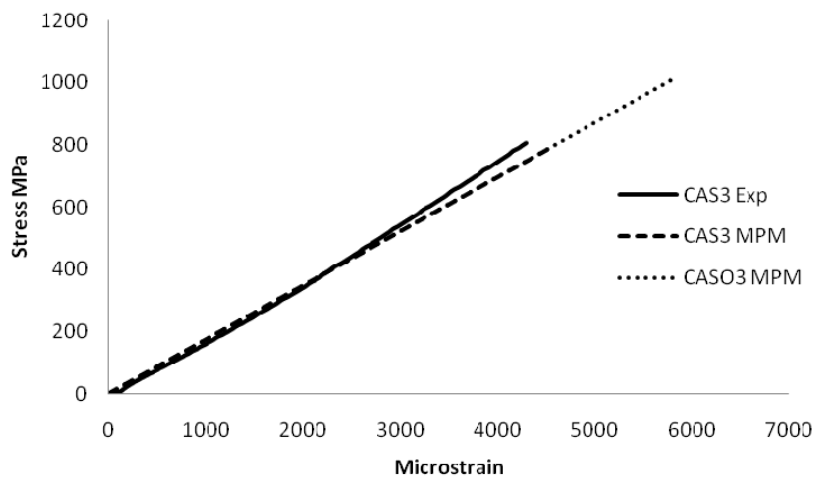


Figure 6.11 MPM specimens of oven-vacuumed specimens compared with experimental and MPM results of Araldite-420 +3% SiC

As expected, due to the increment in ultimate strength and the elastic modulus, ultimate stress and strength have increased compared with the non-vacuumed epoxy specimens. This increment is clearly shown in Figures 6.9 and 6.11, but unmistakably in Figure 6.10, where the failure stress level has been nearly doubled compared with the non-vacuumed data.

6.3 Bond slip model for nanomaterial-enhanced specimens

The bond strength of CFRP-concrete or steel systems is defined by the ultimate strength extracted from tested specimens divided by the interfacial area. Bond strength is usually used to conclude bond performance. However, such an approach is valid only under specific geometric conditions.

This section reports on the study of the local bond-slip relationship expanded from the experiments reported in Chapter Four.

The calculated strain distributions, measured by strain gauges and a photogrammetry system, for different nanoparticle percentages and types of enhanced adhesives, are used to quantify shear stress and slip. Based on the results, a bilinear bond-slip model is adopted in this section.

6.3.1 Shear stress distribution

To create the bond-slip relationship, it is essential to calculate shear stress distribution along the bond length. Lap-shear stress values were extracted analytically by integrating the measured strain distribution along the CFRP length. The major concern in determining shear stress from axial strains of the CFRP-concrete system is

that the axial strains measured on thin CFRP plate generally show violent variations due to the discrete nature of the concrete cracks and the heterogeneity of concrete (Lu et al., 2005). However, this may not be the case in the CFRP-bonded steel system. It has been demonstrated in Xia and Teng, (2005) and Fawzia (2007) that a bilinear model similar to that for concrete, could be adopted for the CFRP-bonded steel system.

In the present analytic study, the data from strain gauges represent the average shear stresses at each 20 mm along the bond length (i.e. strain gauge intervals = 20 mm).

The strain calculated from the photogrammatry system shows the exact strain at each specified point. To use these data at the same calculation scheme, the average strain along 10 mm from the bond length is calculated, and used to determine the shear stress.

The average bond stress between two adjacent readings from strain gauges and photogrammatry readings can be calculated by dividing the force difference by the bond area between those readings (per unit width of the bond), according to the following equation:

$$\tau = \frac{E_f (\varepsilon_{f,i+1} - \varepsilon_{f,i}) t_f}{\Delta L} \quad (6.1)$$

where E_f and t_f are the CFRP elastic modulus and thickness, respectively; $\varepsilon_{f,i+1}$ and $\varepsilon_{f,i}$ are the CFRP axial strains at two consecutive locations starting from $x = \ell$ reading; and ΔL is the distance between the consecutive strain readings (i.e. 20 mm for strain gages , and 10 mm for photogrammatry readings).

The shear stress calculation process is governed by certain assumptions to reduce affecting factors:

1. The measured strains at the surface were close to the average CFRP strains between the selected points.
2. Normal and shear strain variations across the CFRP thickness were ignored in describing the global behaviour of the bond.
3. Due to the difficulty of measuring the strain at the end of bonding length, the strain values were assumed to be zero at bond length end.

The calculated shear stress distributions along the distance away from the steel edge are shown in Figures 6.12 to 6.17. These figures show the shear distribution along bond length for CAH, CSM, CAS1, CAC2, CSS1 and CSC2 respectively.

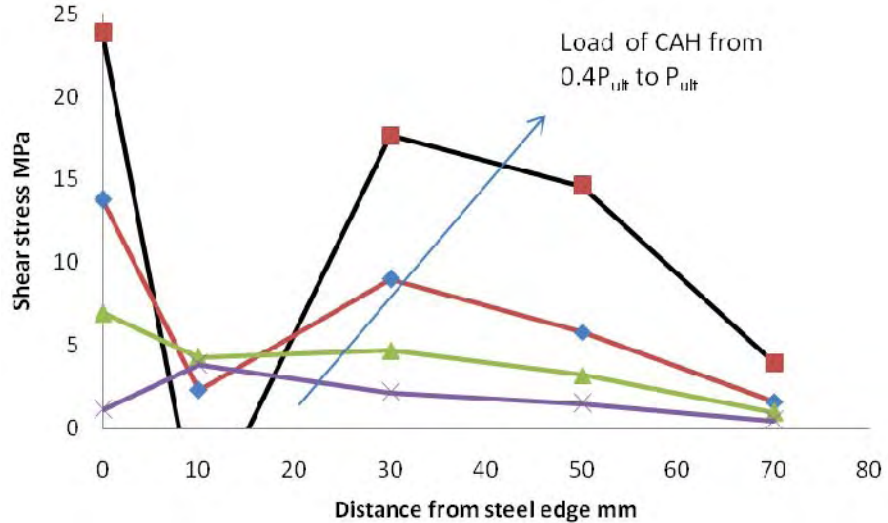


Figure 6.12 Shear stress distribution along CFRP bond length of Araldite-420 hand-mixed specimen

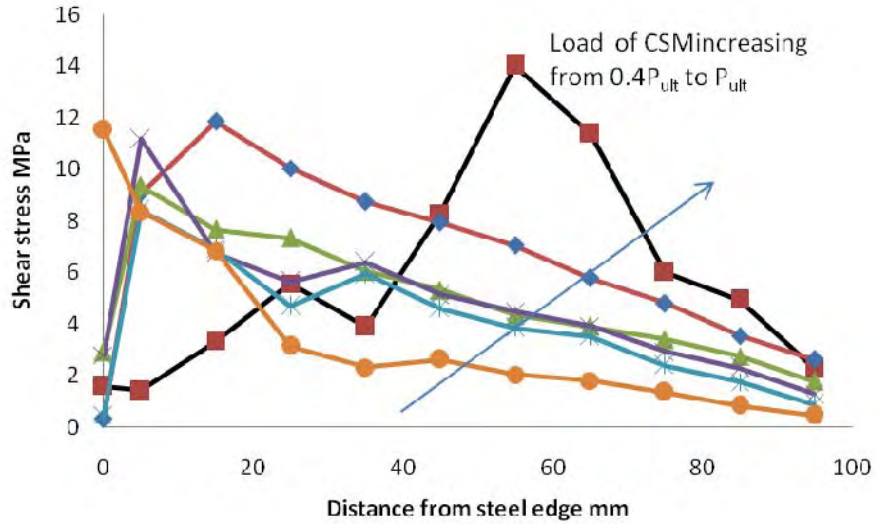


Figure 6.13 Shear stress distribution along CFRP bond length of Sikadur-30 sonicated-mixed specimen

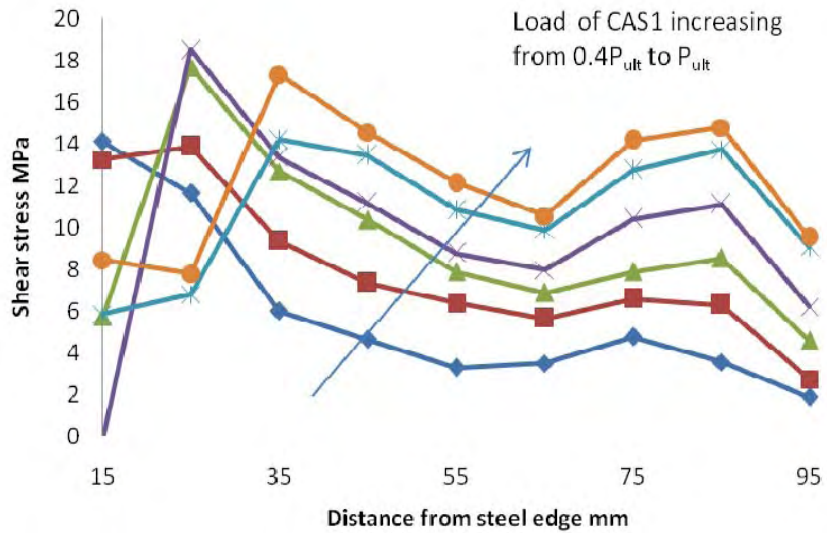


Figure 6.14 Shear stress distribution along CFRP bond length of Araldite-420+1%SiC specimen

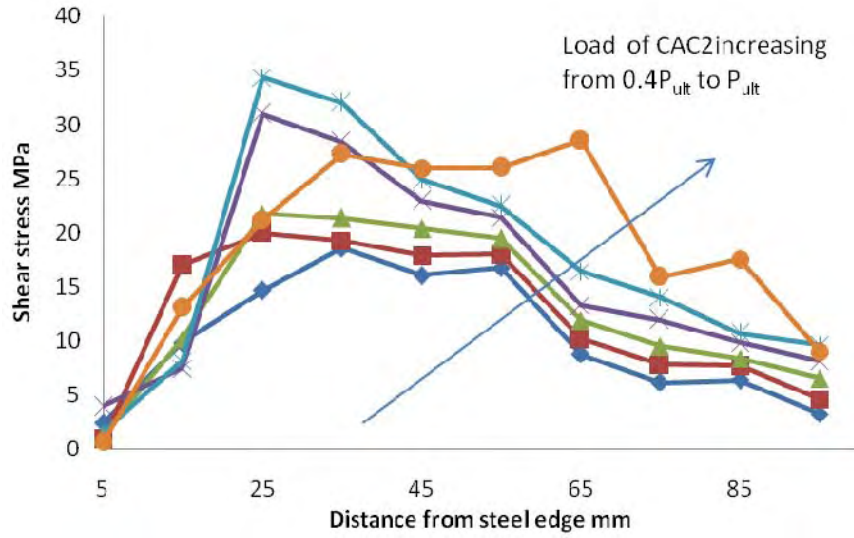


Figure 6.15 Shear stress distribution along CFRP bond length of Araldite-420+ 2% MWCNT specimen

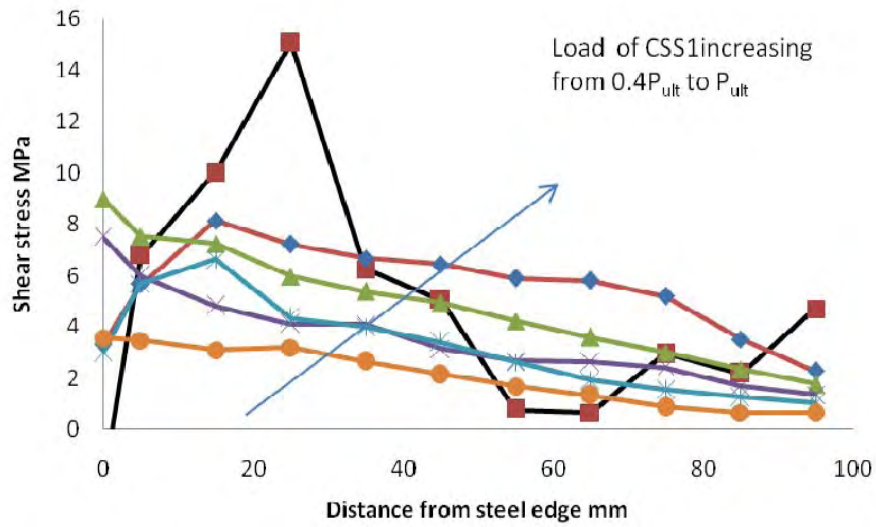


Figure 6.16 Shear stress distribution along CFRP bond length of Sikadur-30+ 1% SiC specimen

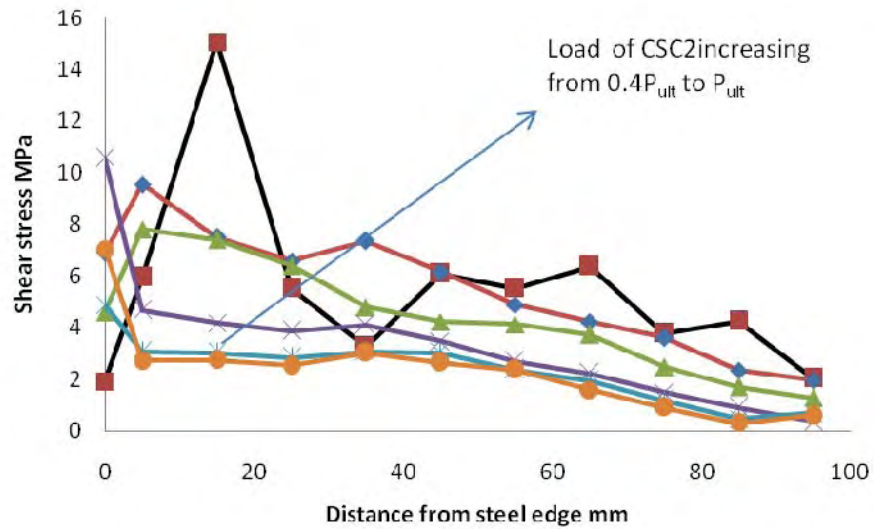


Figure 6.17 Shear stress distribution along CFRP bond length of Sikadur-30+2%MWCNT specimen

At a low load level, the shear stress is the largest near the steel edge, then gradually reduces to zero towards the unloaded plate end. As the load level increases, the shear stress at the loaded end starts to reduce. When the shear stress at the steel edge reduces to zero or near zero level, the ultimate load of the specimen reaches debonding then propagates towards the free end.

6.3.2 Bond slip model

For CFRP joints that fail by debonding in the adhesive layer, the bond-slip curves can be very closely approximated by a bi-linear model. According to this model, the shear stress increases linearly with the interfacial slip until it reaches the peak stress, τ_f at which the value of the slip is known as initial slip, δ_1 . Micro-cracking then starts, with the shear stress reducing linearly with the interfacial slip. The shear stress

reduces to zero when the slip exceeds maximum slip, δ_f signifying the debonding of a local bond element. Figure 6.18 shows a schematic view for a simple bi-linear bond-slip model.

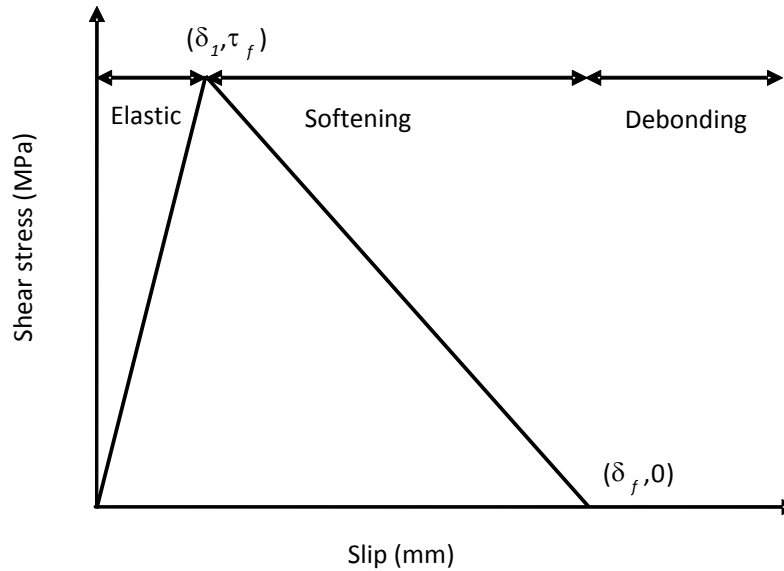


Figure 6.18 Bilinear bond-slip model approximation (Xia and Teng, 2005)

While researchers have focused on bond-slip relationships for CFRP sheet/plate bonded to concrete joints (Chen and Teng, 2001; Teng et al., 2002; Lee, 2003; Yuan et al., 2004; Lu et al., 2005; Pham and Al-Mahaidi, 2007 among others), research on CFRP sheet/plate to steel bonded joints is limited. The pioneering work of Xia and Teng (2005), which reported results of CFRP plate to steel bonded joints, suggests that the bilinear bond slip model can be used in CFRP-steel single lap joints. Fawzia (2007) studied the effect of bond lengths, adhesive maximum strain and adhesive thicknesses on the bond-slip relationship for CFRP sheets-double lap shear samples of steel plates and hollow tubes.

An example of the bond-slip relationship is shown in Figure 6.19 for the CFRP-concrete system, together with an example for the CFRP-steel system. The shear

strength in CFRP-steel system is clearly larger than that of the CFRP-concrete system, with a small difference in slip amount.

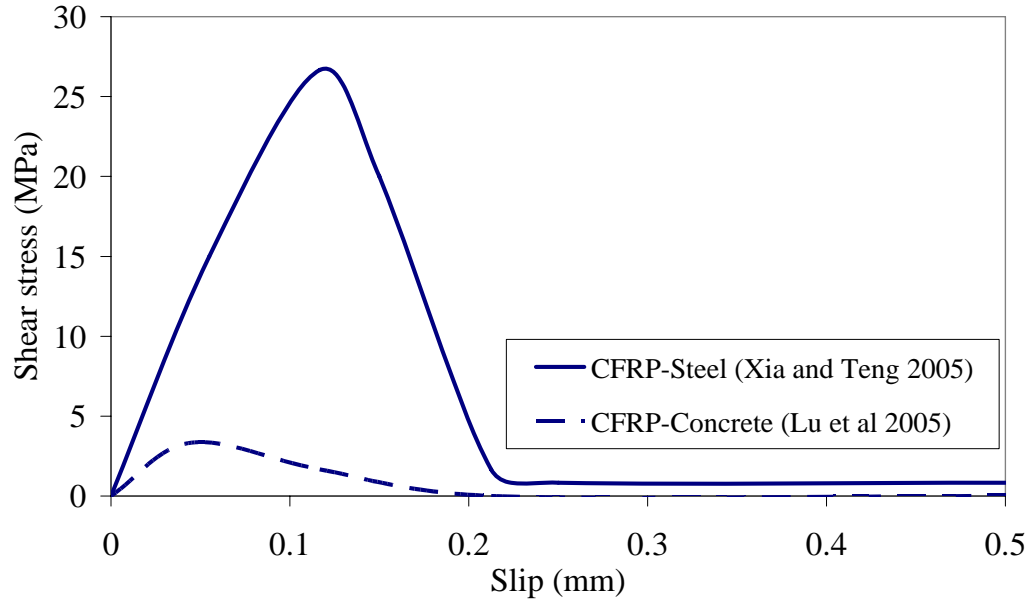


Figure 6.19 Comparison of the bond-slip model between CFRP strengthened concrete structure, Lu et al (2005) and steel structure, Xia and Teng (2005)

6.3.3 Bond-slip relationship

The local slip in CFRP is simplified as the relative displacement between the CFRP sheet and the steel plate. Local slips were calculated by integrating measured strain distribution along the bond length.

To obtain the shear stress-slip curve, the calculated shear stresses and slips should be combined. The local shear stress slip relationship is reasonably consistent between different locations on the same specimen (Xia and Teng,2005). Therefore, the model presented here shows maximum shear stress slip relationships from different locations on the same specimen.

The average slip values of the CFRP laminate at any load increment during the loading process can be calculated as the incremental sum of the CFRP's extension as follows:

$$S_i = \frac{\varepsilon_{f,i+1} + \varepsilon_{f,i}}{2} \Delta L + S_{i-1} \quad (6.2)$$

The same assumptions made for Equation 6.1 in the preceding section is valid for Equation 6.2.

The plots of the average lap-shear stress versus the average slip at different nanoparticle percentages and types for the CFRP-steel specimens are presented in Figures 6.20 to 6.23.

For all these figures, the bond-slip curves are calculated from the closest distance to the steel edge along the effective bond length (i.e. $x = 5$ mm), which may reflect a meaningful trend for lap-shear stress versus slip for the current bond configurations.

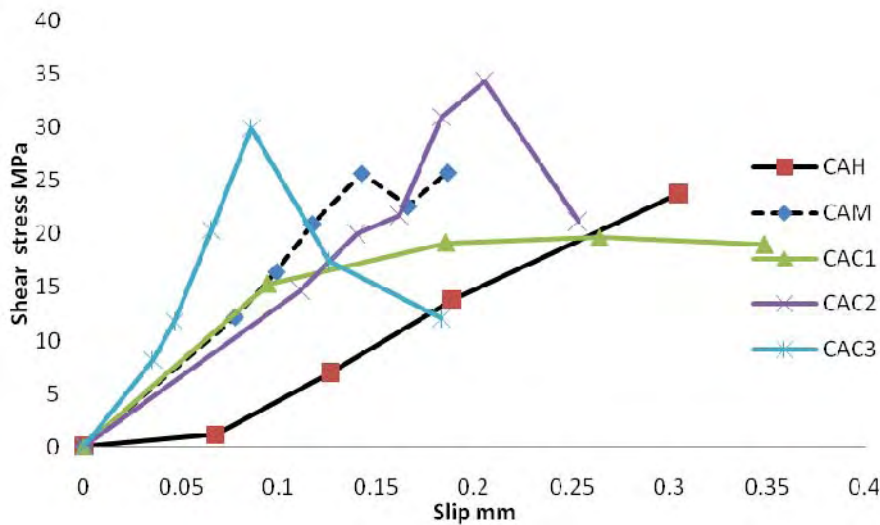


Figure 6.20 Effects of MWCNT percentages on bond-slip relationship of Araldite-420 specimens

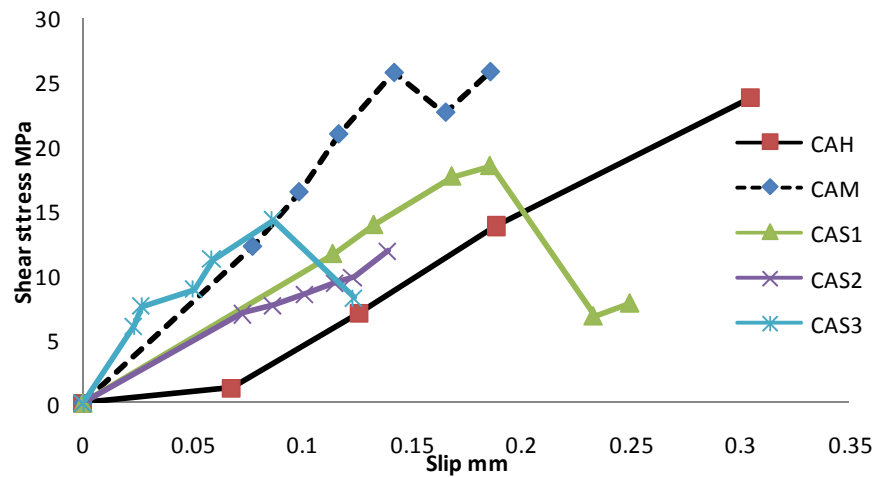


Figure 6.21 Effects of SiC percentages on bond-slip relationship of Araldite-420 specimens

For Araldite-420 specimens, the bond-slip relationship shows higher bond strength as the MWCNT is added, and increases the bond strength for 2 and 3% of MWCNT and increases the slip for 1%, compared with hand mixed specimens.

When SiC is added, 1%,2% and 3% of SiC do not improve the bonding strength nor the slip amount.

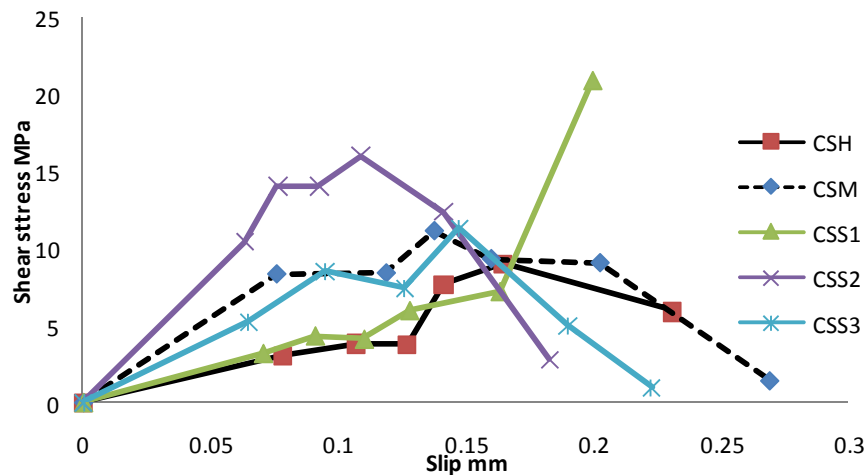


Figure 6.22 Effects of SiC percentages on bond-slip relationship of Sikadur-30 specimens

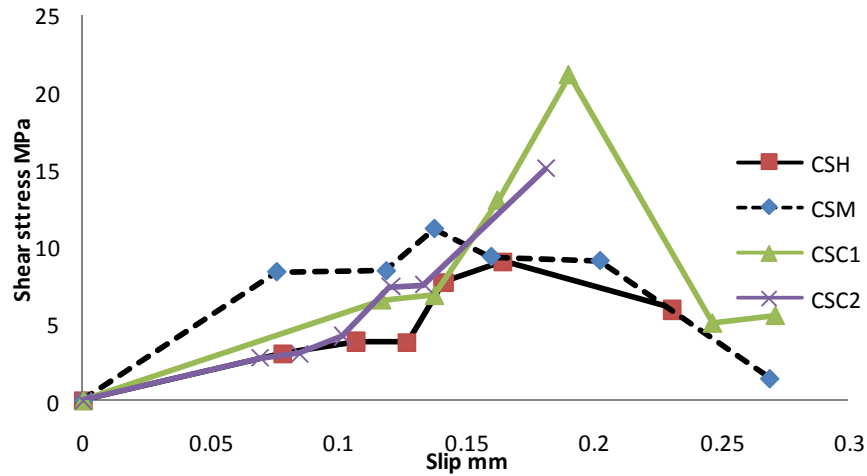


Figure 6.23 Effects of MWCNT percentages on bond-slip relationship of Sikadur-30 specimens

When the MWCNT percentages mixed with Sikadur-30 were increased, bond strength increased for both 1% and 2% without any change in the slip amount.

The same pattern was repeated for SiC enhanced Sikadur-30: the results showed increment in bond strength and small changes in slip amount.

Figures 6.24 and 6.25 show the effect of adding different percentages of nanoparticles with different epoxies on bonding strength.

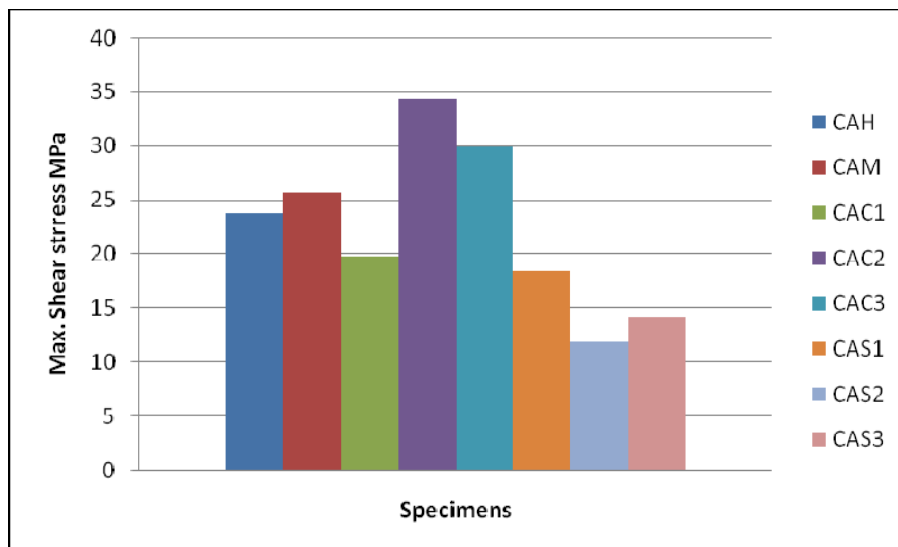


Figure 6.24 Effects of different nanoparticle types and percentages on bond strength of Araldite-420 specimens

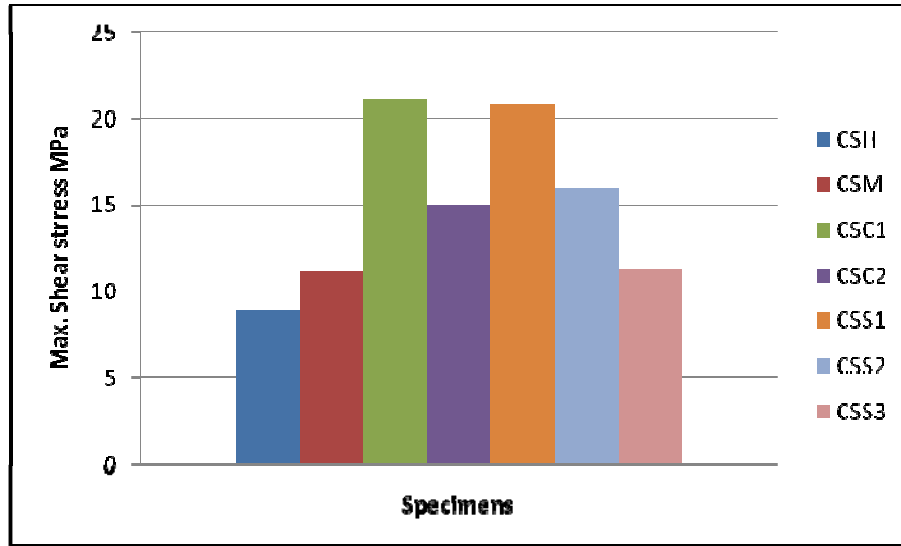


Figure 6.25 Effects of different nanoparticle types and percentages on bond strength of Sikadur-30 specimens

Figures 6.20,6.21 and 6.24 clearly show that sonication increases bonding strength by less than 10%. 2% of MWCNT added to Araldite-420 gives the optimum bonding shear strength for this configuration, followed by 2% then 1% of MWCNT. SiC had a negative effect on the bonding shear strength.

The nano-additives have, in general, a positive effect on shear bonding strength when mixed with Sikadur-30, as shown in Figures 6.22,6.23 and 6.25.

6.4 Summary

In this chapter, the tested specimens in Chapter Four have been modelled using MPM and the material properties from Chapter Three. Stress-strain curves and strain distributions along bond length have been compared between MPM and experimental results. The consistency of the modelled and tested results encouraged the modelling

of untested CFRP-steel specimens based on the material properties from Chapter Three.

The collected strain data from the series of experiments have been used to construct shear stress distribution along bond length and to build a bond-slip model. 2% MWCNT is the optimum weight percentage producing maximum shear bond strength for Araldite-420 specimens.

Chapter Seven

Conclusions and Future Work

7.1 Research summary

This thesis has addressed the effects of adding 1%, 2% and 3% of MWCNT and SiC nano-powder to two structural adhesives using the ultrasonication mixing method. These enhanced epoxies were used to bond CFRP and steel plates by a single lap joint.

The research has investigated issues relating to material properties, optimum nano-particle percentages, load-carrying capacity, strain and stress distribution, models for different loading rates, bonding length and bond-slip relationships.

The following is summary for this thesis:

- Many types of nano-particles can be added to enhance epoxy behaviour.
- The effects of adding small amounts of nano-particles varies from positive to negative on strength and T_g , depending on the agglomeration and distribution status.
- Slight differences in the length, diameter and purity of mixed MWCNT have a negligible effect on CFRP-steel joint strength.

- The distribution of nano-particles can be done by many mixing methods. The ultrasonic mixing method is adopted for the purposes of the present study owing to its simplicity and efficacy.
- Probe sonication is not only an efficient method to infuse MWCNT and SiC powder into the chosen epoxies, as indicated directly by SEM and indirectly by the $\tan\Delta$ curve shapes, but also increases epoxy homogeneity.
- The comparisons of the strain distribution obtained by measurements by gauges and the photogrammetry system show that the latter technique not only can complement, but also replace traditional measurement techniques.
- To understand the CFRP-steel joint behaviour, an active model is needed focusing on the epoxy. The key factors for such a model are the bond-slip relationship and strength of joint.
- The tested CFRP-steel joint have been modelled using MPM and the material properties from materials coupon tests. Stress-strain curves and strain distributions along bond length have been compared between MPM and experimental results. The consistency of the modelled and tested results encouraged the modelling of untested CFRP-steel specimens based on the material properties from Chapter Three.
- The effects of bond length, loading rate and different epoxy properties on the load carrying capacity and failure mode of the CFRP-steel joint system have been investigated. The simulated load-deflection, stress-strain curves and normal strain distributions at the top of combined CFRP/epoxy layers and CFRP plates are consistent with the available experimental data.

- From the parametric study on the effects of bond length and loading rate, it appears that the proposed model-based simulation procedure with the framework of the MPM is able to capture the essential failure mechanism of the CFRP-steel joint system under shear loading.
- For a given CFRP-steel system there is an optimum loading rate at which the system allows the stress to evenly distribute along the bond length and result in a single clear delamination or a multiple layer delamination. If the loading rate is further increased, the failure will occur in the steel plate.
- The collected strain data from the series of experiments have been used to construct shear stress distribution along bond length and to build a bond-slip model.

7.2 Conclusions

This thesis has proposed a method for the enhancement of adhesives used to attach CFRP and steel by adding nano-particles at different percentages and of different types. The behaviour of CFRP-steel joints through different loading times has been characterised using numerical analysis.

The findings of this thesis may form the basis for future nano-particle-enhanced epoxies for use in CFRP-strengthened steel structures. The main observations and conclusions are as follows:

- Ultrasonication is an effective method for the infusion of MWCNT and SiC into Araldite-420 and Sikadur-30 under the conditions provided in Chapter Three.
- Ultrasonication has a negligible effect on pure Araldite-420 properties and a considerable effect on pure Sikadur-30 properties.
- Vacuuming after sonication reduces the number of micro-bubbles inside Araldite-420, but does not remove all these bubbles.
- 2%wt is the optimum percentage of MWCNT infused in Araldite-420, which gives the ultimate strength and elastic modulus.
- Less than 2% wt MWCNT is insufficient to reinforce Araldite-420, and if the weight percentages are increased by more than 2%, MWCNT begins to agglomerate and start to work as impurities.
- Adding SiC has a small and even negative effect on Araldite-420's strength and elastic modulus due to the large number of bubbles created through the mixing process. If the epoxy is vacuumed, the elastic modulus is increased by 47% when 1wt% SiC is used.
- Due to its cement-like texture and relatively high degree of impurity in Sikadur-30, the application of ultrasonication to the pure epoxy increases its homogeneity, which leads to higher strength. Adding nano-particles (MWCNT or SiC nano-powder) does not affect the strength or elastic modulus. All the increment is due to the increment in homogeneity caused by ultra-sonication rather than the nano-particles. The nano-particles work as impurities and re-agglomerate with Sikadur-30 particles.
- The glass transition temperature is not affected by mixing methods, different types, or percentages of nano-particles for both Araldite-420 and Sikadur-30.
- The proposed single lap joint works to transfer the stress effectively from the CFRP plate to the steel through the epoxy layer without creating unwanted moment across the CFRP plate thickness.

- The close correlation between the results of the photogrammetry and conventional strain gauges indicates the robustness and accuracy of the photogrammetry technique. A non-contact strain measurement technique using photogrammetry could successfully replace traditional strain measurement techniques.
- The failure modes achieved for single lap joint, vary from adhesive layer failure to delamination of CFRP plate, depending on the enhanced adhesive's properties.
- The strain along the bond length decreases from the loaded end to the end of the CFRP attached to the steel plate.
- The shear stress decreases from the loaded edge away from the free steel edge. At the ultimate state, the shear stress becomes zero at the joint location and the peak shear stress is located away from the free edge of the steel.
- The behaviour of the joint through the loading process, and ultimate strength and strain distribution along the bond length are effectively simulated by the MPM numerical model.
- The failure shapes for single and double lap joints are successfully modelled using MPM.
- The parametric study was conducted to find the influence of different CFRP bond lengths and loading rates. It is assumed that the ultimate strength increases as the bond length increases until it reaches a certain value, after which no increase in the bond length affects the ultimate strength. Similarly, as the loading rate increases, the ultimate strength increases until it reaches a certain rate, after which increasing the rate does not affect the ultimate strength.
- The simulation results show that if the bonding length is short enough, the development of the failure mode of the CFRP-steel joint system will be a "clear" delamination without any rupture within the layer. As the bond length increases, the failure mode starts to become a mixed delamination and rupture within the combined CFRP/epoxy layer.

7.3 Future research

Research is needed on the effects of different types (i.e. carbon nano-fibres and nano-clay) and percentages of nano-particles on the ultimate strength and strain of CFRP-steel joints.

- To complete the research program, CFRP sheets prepared using nano-particle- enhanced epoxy will clarify the effect of nano-particles in the composite matrix.
- This research specifically investigated single lap joints under tension. Research can therefore be conducted using different joint configurations.
- Research is needed to study the effect of cyclic loading on CFRP-steel joints bonded by nano-particle-enhanced adhesive.
- Research is required to validate the loading rate effect on different CFRP-steel configurations. Enhancement in bonding strength through different loading rates is predicted when nano-particles are added to the attaching adhesive.
- Research is also necessary on the effects of loading under various short- term environmental effects (i.e. various temperature and humidity ranges) using nano-particle-enhanced adhesive joints.
- Research is needed to identify the effects of such adhesives on durability (i.e. long exposure periods) under extreme environmental conditions.

References

- Abenojar, J., del Real, J.C., Martinez, M.A., and Cano de Santayana, M. (2009), “Effect of Silane Treatment on SiC Particles Used as Reinforcement in Epoxy Resins”, *The Journal of Adhesion*, 85:pp.287-301.
- ACI 440, 2R-08 (2008). “Guide for the Design and Construction of Externally Bonded FRP Systems for Strengthening Concrete Structures.” Farmington Hills, MI: American Concrete Institute.
- Allaoui, A., Bai, S., Cheng, H.M. and Bai, J.B. (2002), “Mechanical and electrical properties of a MWNT/epoxy composite” , *Composites Science and Technology*, 62(15):pp:1993-1998.
- Al-Mahaidi, R. and Hii, A.K.Y. (2007), “Bond behaviour of CFRP reinforcement for torsional strengthening of solid and box-section RC beams”, *Composites: Part B* 38:pp.720-731.
- Al-Shawaf, A., Al-Mahaidi, R., and Zhao, X.L. (2006), “Study on bond characteristics of CFRP-steel double-lap shear joints at subzero temperature exposure”, CICE 2006, Third International Conference on FRP Composites in Civil Engineering Miami , Florida , USA.
- Amaratunga, G.A.J., Milne, K.B.K., Legagneux, P., Gangloff, L., Schnell, J.P., Semet, V., Thien, B.V., and Groening, O. (2004), “Carbon nanotubes as field emission sources”, *Journal of Materials Chemistry*, 14(6):pp.933-943.

References

- Andrews, R., Jacques, D., Rao, A.M., Rantell, T., Derbyshire, F., Chen, Y., Chen, J., and Haddon, R.C. (1999), “Nanotube composite carbon fibers”, *Applied Physics Letters*, 75(9): pp. 1329 -1331.
- Andrews, R., Jacques, D., Minot, M., and Rantell, T. (2002), “Fabrication of carbon multiwall nanotube/polymer composites by shear mixing”, *Macromolecular Materials and Engineering*, 287(6):pp.395-403.
- ASTM Designation D 638-01 (2000) “Standard Test Method for Tensile Properties of Plastics”, ASTM Standard, American Society for Testing Materials, USA.
- ASTM, Designation D 3039 (2000), “Standard test method for tensile properties of polymer matrix composite materials”, ASTM Standard, American Society for Testing Materials, USA.
- Bardenhagen, S.G., Brackbill, J.U. and Sulsky, D. (2000), “The material point method for granular material” *Computer methods in applied mechanics and engineering* 187:pp. 529-541.
- Barrau, S., Demont, P., Maraval, C., Bernes, A., and Lacabanne, C.(2005), “Glass Transition Temperature Depression at the Percolation Threshold in Carbon Nanotube–Epoxy Resin and Polypyrrole–Epoxy Resin Composites”, *Macromolecular Rapid Communications*, 26:pp. 390-394.
- BASF Construction Chemicals Austrilia Pty Ltd “MBrace S & P CFK Laminate”, Technical data sheet, 7 kingstone town close, Oakleigh, VIC 3166
- Baughman, R.H., Zakhidov, A.A. and de Heer, W.A. (2002), “Carbon Nanotubes-the Route Toward Applications”, *Science*, 297(2), :pp.787-792.

References

- Bekyarova, E., Thostenson, E.T., Yu, A., Kim, H., Gao, J., Tang, J., Hahn, H.T., Chou, T.W., Itkis, M. E. and Haddon, R.C. (2007), "Multiscale Carbon Nanotube Carbon Fiber Reinforcement for Advanced Epoxy Composites", *Langmuir* , 23:pp. 3970-3974.
- Bethune, D.S , Kiang, C. H., de Vries, M.S., Gorman, G., Savoy, R., Vazquez, J., and Beyers, R.(1993), "Cobalt-catalysed growth of carbon nanotubes with single-atomic-layer walls", *Nature*, 363(6430):pp.605-607.
- Bondar, A.M., Bara, A., Patroi, D., and Svasta, P.M. (2005), "Carbon Mesophase/Carbon Nanotubes Nanocomposite - Functional Filler for Conductive Pastes" *Polytronic 2005 - 5th International Conference on Polymers and Adhesives in Microelectronics and Photonics* Wroclaw, Poland.
- Borowiak-Palen, E., Ruemmel, M.H., Gemming, T., Knupfer, M., Biedermann, K., Leonhardt, A., Pichler, T., and Kalenczuk, R.J.(2005), "Bulk synthesis of carbon-filled silicon carbide nanotubes with a narrow diameter distribution", *Journal of Applied Physics*, 97(5): 56102(1-3).
- Brackbill, J.U. and Ruppel, H.M. (1986), "FLIP: A method for adaptively zoned, particle-in-cell calculations in two dimensions", *Journal of Computational Physics*, 65(2):pp. 314-343.
- Brackbill, J.U. , Kothe, D.B. and Ruppel, H.M. (1988), "FLIP:A low-dissipation, particle-in-cell method for fluid flow" *Computer Physics Communication*, 48:pp.25-38.
- Chen, J.F. and Teng, J.G. (2001), "Anchorage strength models for FRP and steel plates bonded to concrete", *Journal of Structural Engineering*, 127(7): pp.784-791.

References

- Chen, Z., Hu, W., Shen, L., Xin, X., and Brannon, R. (2002), “An evaluation of the MPM for simulating dynamic failure with damage diffusion”, *Engineering Fracture Mechanics*, 69:pp.1873-1890.
- Chen, Z., Shen, L., Mai, Y.W., and Shen, Y. (2005), “A bifurcation-based decohesion model for simulating the transition from localization to decohesion with the MPM”, *Zeitschrift für Angewandte Mathematik und Physik (ZAMP)*, 56:pp.908-930.
- Chen, H., Jacobs, O., Wu, W., Rüdiger, G., and Schädel, B.(2007a), “Effect of dispersion method on tribological properties of carbon nanotube reinforced epoxy resin composites”, *Polymer Testing*, 26 :pp.351-360.
- Chen, G.X, Li, Y., and Shimizu, H. (2007b), “Ultrahigh-shear processing for the preparation of polymer/carbon nanotube composites”, *Carbon*, 45(12):pp.2334-2340.
- Chikhi, N., Fellahi, S., and Bakar, M. (2002), “Modification of epoxy resin using reactive liquid (ATBN) rubber”, *European Polymer Journal*, 38(2):pp.251-264.
- Chisholm, N., Mahfuz, H., Rangari, V.K., Ashfaq, A., and Jeelani, S. (2005), “Fabrication and mechanical characterization of carbon/SiC-epoxy nanocomposites”, *Composite Structures*, 67:pp.115-124.
- Cho, J., Daniel, I.M., and Dikin, D.A.(2008), “Effects of block copolymer dispersant and nanotube length on reinforcement of carbon/epoxy composites”, *Composites: Part A* 39:pp. 1844-1850.
- Collins, P.G. and Avouris, P. (2000), “Nanotubes for electronics”, *Scientific American*, 283(6):62-69.

References

- Colombi, P., and Poggi, C. (2006), “Strengthening of tensile steel members and bolted joints using adhesively bonded CFRP plates”, *Construction and Building Materials*, 20(1–2):pp.22–33.
- Dalton, A.B., Collins, S., Mufloz, E., Razal, J.M., Ebron, V.H., Ferraris, J.P., Coleman, J.N., Kim, B.G. and Baughman, R.H. (2003), “Super-tough carbon-nanotube fibres”, *Nature*, 423:pp.703.
- Dalton, A.B., Collins, S., Razal, J., Munoz, E., Ebron, V.H., Kim, B.G., Coleman, J.N., Ferraris, J.P. and Baughman, R.H. (2004), “Continuous carbon nanotube composite fibres: properties, potential applications, and problems”, *Journal of Materials Chemistry*, 14 :pp.1-3
- Du, F., Scogna, R.C., Zhou, W., Brand, S., Fischer, J.E. and Winey, K.I. (2004), “Nanotube networks in polymer nanocomposites: rheology and electrical conductivity” , *Macromolecules*, 37(24):pp.9048-9055.
- Eftekhari, A., Jafarkhani, P., and Moztarzadeh, F. (2006), “High-yield synthesis of carbon nanotubes using a water-soluble catalyst support in catalytic chemical vapor deposition”, *Carbon*, 44(7):pp.1343-1345.
- Eitan, A., Jiang, K., Dukes, D., Andrews, R., and Schadler, L.S.(2003), “Surface Modification of Multiwalled Carbon Nanotubes: Toward the Tailoring of the Interface in Polymer Composites”, *Chemistry of Materials* , 15:pp.3198-3201.
- El Damatty, A.A., and Abushagur, M. (2003), “Testing and modelling of shear and peel behavior for bonded steel/FRP connections”, *Thin-walled structures* , 41(11):pp.987-1003.

References

- Eskin, G.I. (2001), “Broad prospects for commercial application of the ultrasonic (cavitation) melt treatment of light alloys”, *Ultrasonics Sonochemistry*, 8(3):pp.319-325.
- Evseeva, L. E. and Tanaeva, S. A. (2008), “Nanotubes(CNT) on the thermophysical properties of Epoxy/CNT nanocomposites at low temperature”, *Mechanics of Composite Materials*, 44(5) :pp.487-494.
- Fan, Z., Hsiao, K.T. and Advani, S.G. (2004), “Experimental investigation of dispersion during flow of multi-walled carbon nanotube/polymer suspension in fibrous porous media”, *Carbon*, 42(4):pp.871-876.
- Fawzia, S., Al-Mahaidi, R., Zhao, X.L., and Rizkalla, S. (2005), “Bond characteristics between CFRP and steel plates in double strap joints”, *Advances in Steel Construction*, 1(2), :pp.17-28.
- Fawzia, S., Zhao, X.L., and Al-Mahaidi, R. (2006), “Experimental and finite element analysis of a double strap joint between steel plates and normal modulus CFRP”, *Composite Structures*, 75: pp. 156-162.
- Fawzia, S., (2007), “Bond characteristics between steel and CFRP composites” Ph.D thesis, Department of Civil engineering, Monash University, Melbourne, Australia.
- Fawzia, S., Al-Mahaidi, R., Zhao, X.L., and Rizkalla, S. (2007), “Strengthening of circular hollow steel tubular section using CFRP sheets”, *Composites in Civil Engineering: Construction and Building Materials*, 21(4):pp. 839-845.
- Ferreira, J.A.M., Reis, P.N., Costa, J.D.M. and Richardson, M.O.W. (2002), “Fatigue behaviour of composite adhesive lap joints” , *Composites science and technology*, 62(10-11):pp1373-1379.

References

- Fiedler, B., Gojny, F.H, Wichmann, M.H., Nolte, M.C, and Schulte, K. (2006) , “Fundamental aspects of nano-reinforced composites” , Composites Science and Technology, 66 :pp. 3115-3125.
- Fraser, C. (2001), “A resume of some industrial applications of Photogrammetry” ISPRS Journal of Photogrammetry and Remote Sensing, 48(3):pp.12-23 .
- Gabriel, G., Sauthier, G., Fraxedas, J., Moreno-Manas, M., Martnez, M.T, and Miravittles, C., (2006), “Preparation and characterization of single-walled carbon nanotubes functionalized with amines”, Carbon, 44(10):pp.1891-1897.
- Ganguli, S., Aglan, H., Dennig, P. and Irvin, G., (2006), “Effect of Loading and Surface Modification of MWCNTs on the Fracture Behavior of Epoxy Nanocomposites”, Journal of Reinforced Plastic and Composites. 25(2):pp.175-188.
- García, E.J., John Hart, A., Wardle, B.L., and Slocum, A.H. (2007) “Fabrication and Nanocompression Testing of Aligned Carbon-Nanotube–Polymer Nanocomposites”, Advnced materials, 19:pp.2151-2156
- Geng, Y., Liu, M.Y., Li, J., Shi, X.M., and Kim, J.K.(2008) , “Effects of surfactant treatment on mechanical and electrical properties of CNT/epoxy nanocomposites”, Composites: Part A , 39 :pp.1876-1883.
- Giancaspro, J., Papakonstantinou, C., Nazier, M., and Balaguru, P. (2009), “Aerospace technology for strengthening of bridges.” Construction and Building Materials, 23: pp.748–757.

References

- Gojny, F.H. and Schulte, K.(2004), “Functionalisation effect on the thermo-mechanical behaviour of multi-wall carbon nanotube/epoxy-composites”, *Composites Science and Technology*, 64 :pp. 2303-2308.
- Gojny, F.H., Wichmann, M.H.C, Köpke, U., Fiedler, B., and Schulte, K.(2004) , “Carbon nanotube reinforced epoxy-composites: enhanced stiffness and fracture toughness at low nanotube content”, *Composites Science and Technology*, 64(15):pp.2363-2371.
- Gojny, F.H., Wichmann, M.H, Fiedler, B., Bauhofer, W., and Schulte, K. (2005) , “Influence of nano-modification on the mechanical and electrical properties of conventional fibre-reinforced composites.” *Composites:Part A*, 36(11):pp.1525-1535.
- Gong, X., Liu, J., Baskaran, S., Voise, R.D., and Young, J.S.(2000), “Surfactant-assisted processing of carbon nanotube/polymer composites”, *Chemistry of Materials*, 12:pp.1049-1052.
- Guadagno, L., Vertuccio, L., Sorrentino, A., Raimondo, M., Naddeo, C., Vittoria, V., Iannuzzo, G., Calvi, E. and Russo, S.(2009), “Mechanical and barrier properties of epoxy resin filled with multi-walled carbon nanotubes”, *Carbon*, 47(10):pp. 2419-2430.
- Guilkey, J.E., and Weiss, J.A. (2003). “Implicit time integration for the material point method: quantitative and algorithmic comparisons with the finite element method”, *International Journal for Numerical Methods in Engineering*, 57:pp.1323-1338.

References

- Guo, T., Nikolaev, P., Rinzler, A.G., Tomanek, D., Colbert, D.T., and Smalley, R.E. (1995-A), “Self-Assembly of Tubular Fullerenes”, *Journal of Physical Chemistry*, 99(27):pp.10694-10697.
- Guo, T., Nikolaev, P, Thess, A, Colbert, D and Smalley, R (1995-B), “Catalytic growth of single-walled nanotubes by laser vaporization”, *Chemical Physics Letters*, 243:pp.49–54.
- Guo, P., Chen, X., Gao, X., Song, H. , and Shen, H., (2007), “Fabrication and mechanical properties of well-dispersed multiwalled carbon nanotubes/epoxy composites” , *Composites Science and Technology*, 67 :pp. 3331-3337.
- Haque, A., Shamsuzzoha, M., Hussain, F. and Dean, D. (2003), “S2-Glass/Epoxy Polymer Nanocomposites: Manufacturing, Structures, Thermal and Mechanical Properties” , *Journal of Composite Materials*, 37: pp.1821-1837.
- Harlow, F.H. (1964), “The particle-in-cell computing method for fluid dynamics in fundamental methods in hydrodynamics”, *High-Speed Computations and Mathematics*, Academic Press, London, UK.
- He, C.N. and Tian, F. (2009), “A carbon nanotube alumina network structure for fabricating epoxy composites”, *Scripta Materialia* , 61 :pp. 285-288.
- Hii, A., and Al-Mahaidi, R. (2006), “Experimental Investigation on torsional behaviour of Solid and Box-Section RC Beams Strengthened with CFRP Using Photogrammetry”, *Journal of Composites for Construction ASCE*, 10(4):pp.321-329.

References

- Hollaway, L.C. and Cadei, J. (2002), “Progress in the technique of upgrading metallic structures with advanced polymer composites” , Progress in Structural Engineering and Materials, 4(2):pp.131-148.
- Hsiao, K.T., Alms, J. and Advani, S.G. (2003), “Use of epoxy/multiwalled carbon nanotubes as adhesives to join graphite fibre reinforced polymer composites”, Nanotechnology, 14:pp.791-793.
- Huntsman Advanced Materials “Araldite 420 A/B”, Technical data sheet.
- Iijima, S. (1991), “Helical microtubules of graphitic carbon”, Nature, 354:pp. 56-58.
- Iijima, S., and Ichihashi, T.(1993), “Single-shell carbon nanotubes of 1-nm diameter”, Nature, 363:pp.603–605.
- Iijima, S., Brabec, C., Maiti, A. and Bernholc, J.(1996), “Structural flexibility of carbon nanotubes”, Journal of Chemical Physics, 104(5):pp.2089–2092.
- Imanaka, M., Nakamura, Y., Nishimura, A. and Iida, T. , (2003) , “Fracture toughness of rubber-modified epoxy adhesives: Effect of plastic deformability of the matrix phase”, Composites Science and Technology, 63 (1):pp.41-51.
- Inami, N., Ambri, M.M., Shikoh, E., and Fujiwara, A. (2007), “Synthesis-condition dependence of carbon nanotube growth by alcohol catalytic chemical vapor deposition method”, Science and Technology of Advanced Materials, 8(4):pp.292-295.
- Inman, M. (2006), “Legendary Swords' Sharpness, Strength From Nanotubes, Study Says” National Geographic News, November 16, 2006.

References

- Ionescu, I., Guilkey, J.E., Berzins, M., Kirby, R.M., and Weiss, J.A. (2006), “Simulation of soft tissue failure using the Material Point Method”, *Journal of Biomechanical Engineering*, 128(6), pp. 917-924.
- Ishigami, N., Ago, H., Imamoto, K., Tsuji, M., Iakoubovskii, K., and Minami, N. (2008), “Crystal Plane Dependent Growth of Aligned Single-Walled Carbon Nanotubes on Sapphire”, *Journal of the American Chemical Society*, 130 (30): pp.9918-9924.
- Iwahori, Y., Ishiwata, S., Sumizawa, T., and Ishikawa, T. (2005), “Mechanical properties improvements in two-phase and three-phase composites using carbon nanofiber dispersed resin”, *Composites Part A*, 36(10):pp.1430-1439.
- Jacobs, O., Xub, W., Schä del, B. , and Wub, W. (2006), “Wear behaviour of carbon nanotube reinforced epoxy resin composites”, *Tribology Letters*, 23(1), :pp.65-75.
- Jia, Z., Wang, Z., Xu, C., Liang, J., Wei, B., Wu, D., and Zhu, S. (1999), “Study on poly (methyl methacrylate)/carbon nanotube composites”, *Materials Science and Engineering A*, 271, pp. 395-400.
- Jiang, W., Tsang, F., Tjong, S., Li, R., Kim, J., and Mai, Y. (2001), “Loading rate dependence of mode II fracture behaviour in interleaved carbon fibre/epoxy composite laminates”, *Applied Composite Materials*, 8(6):pp. 361-369.
- Jiao, H. and Zhao, X.L. (2004), “CFRP strengthened butt-welded very high strength VHS circular steel tubes”, *Thin-walled Structures*, 42(7):pp.963-978.

References

- Jones, S.C. and Civajan, S.A. (2003), “Application of fibre reinforced polymer overlays to extended steel fatigue life” , Journal of Composites for Construction ASCE, 7(4):pp.331-338.
- Kim, Y.J., Shin, T.S., Choi, H.D., Kwon, J.H., Chung, Y., and Yoon, H.G.(2005), “Electrical conductivity of chemically modified multiwalled carbon nanotube/epoxy composites”, Carbon, 43(1):pp.23-30.
- Kim, M., Park , Y.B. , Okoli, O.I., and Zhang, C.(2009-A), “Processing, characterization, and modeling of carbon nanotube-reinforced multiscale composites” Composites Science and Technology 69:pp.335-342.
- Kim, S.H., Lee, W.I., and Park, J.M. (2009b), “Assessment of dispersion in carbon nanotube reinforced composites using differential scanning calorimetry”, Carbon, 47(11):pp. 2699-2703.
- Kinemuchi, Y., Yanai, T., and Ishizaki, K.(1997), “In-situ formation of Si₃N₄-nano SiC composite”, Nanostructured Materials, 9(1-8):pp.23-32.
- Kostopoulos, V., Vavouliotisa, A., and Karapappas, P. (2008) “Carbon nanotube epoxy modified CFRPs: Towards improved mechanical and sensing for multifunctional aerostructures” Behavior and Mechanics of Multifunctional and Composite Materials Vol. 6929.
- Kostopoulos, V., Vavouliotis, A., Karapappas, P., Tsotra, P., and Paipetis, A. (2009), “A Damage Monitoring of Carbon Fiber Reinforced Laminates Using Resistance Measurements. Improving Sensitivity Using Carbon Nanotube Doped Epoxy Matrix” System Journal of Intelligent Material Systems and Structures, 20:pp.1025-1034.

References

- Krstic, V.D.(1992), “Production of Fine High-Purity Beta Silicon Carbide Powders”, *Journal of the American Ceramic Society*, 75(1):pp.170-174.
- Lahiff, E., Ryu, C.Y., Curran, S., Minett, A.I., Blau, W.J. and Ajayan, P.M. (2003), “Selective positioning and density control of nanotubes within a polymer thin film”, *Nano Letters*, 3(10): pp. 1333-1337.
- Lam, C.C.A. and Cheng, J.J.R. (2004), “Study of the tensile strength of CFRP/ steel double lap joints”, *Advanced Composite Material in Bridges Structures*, Calgary, Alberta, USA.
- Larpkittaworn, S., Ngerchuklin, P., Khongwong, W., Pankurdee, N. , and Wada, S.(2006), “The influence of reaction parameters on the free Si and C contents in the synthesis of nano-sized SiC”, *Ceramics International*, 32 (8):pp. 899-904.
- Lau, K.T., and Hui, D.(2002), “The revolutionary creation of new advanced materials carbon nanotube composites”, *Composites:part B*, 33:pp.263-277.
- Lee, Y.S., Cho, T.H., Lee, B.K., Rho, J.S., An, K.H., and Lee, Y.H. (2003), “Surface properties of fluorinated single-walled carbon nanotubes”, *Journal of Fluorine Chemistry*, 120(2):pp.99-104.
- Lee, T.K. (2003), “Shear strength of reinforced concrete T-beams strengthened using carbon fibre reinforced polymer (CFRP) laminates”, *Ph.D Thesis*, Monash University, Melbourne, Australia.
- Lee, T., and Al-Mahaidi, R. (2008), “An experimental investigation on shear behaviour of RC T-beams strengthened with CFRP using Photogrammetry”, *Composite Structures* , 82:pp.185-193

References

- Lenwari, A., Thepchatri, T. and Watanabe, E. (2002), “Prediction of premature separation of bonded CFRP plates from strengthened steel beams using a fracture criterion” *Structural Engineering and Mechanics*, 14(5):pp.565-574.
- Li, X., Gao, H., Scrivens, W.A., Fei, D., Xu, X., Sutton, M.A., Reynolds, A.P., and Myrick, M.L. (2004), “Nanomechanical characterization of single-walled carbon nanotube reinforced epoxy composites” , *Nanotechnology*, 15, pp. 1416-1423.
- Liang, W., Bockrath, M., Bozovic, D., Hafner, J.H., Tinkham, M. and Park, H.(2001), “Fabry-Perot interference in a nanotube electron waveguide”, *Nature*, 411, 665-668
- Liao, Y.H., Liang, Z., Park, Y.B., Wang, B., Zhang, C. (2006), “Fabrication and characterization of carbon nanotube/glass fiber-reinforced multiscale composites” , 47th AIAA/ ASME/ASCE/AHS/ASC Structures, Structural Dynamics, and Materials Conference, Newport, RI, 2006.
- Linder, W. (2006), “Digital Photogrammetry: A Practical Course” Second Edition. Berlin, Heidelberg: Springer-Verlag Berlin, Heidelberg.
- Liu, Z., Cousins, T., Lesko, J., and Sotelino, E. (2008), “Design recommendations for a FRP bridge deck supported on steel superstructure”, *Journal of Composites for Construction*, Vol. 12, No.6, pp. 660-668.
- Liu, H. (2008), “Fatigue behaviour of CFRP reinforced steel plates”, Ph.D thesis, Department of Civil Engineering, Monash University, Melbourne, Australia.
- Lourie, O., Cox, D.M., and Wagner, H.D.(1998), “Buckling and collapse of embedded carbon nanotube”, *Physical Review Letters*, 81(8):pp.1638-1641.

References

- Lozano, K. , Bonilla-Rios, J., and Barrera, E.V. (2001), “A Study on Nanofiber-Reinforced Thermoplastic Composites (II): Investigation of the Mixing Rheology and Conduction Properties”, *Journal of Applied Polymer Science*, 80:pp.1162-1172.
- Lu, K.L., Lago, M., Chen, Y.K., Green, M.L.H., Harris, P.J.F., and Tsang , S.C.(1996), “Mechanical damage of carbon nanotubes by ultrasound”, *Carbon*, 34(6):pp.814-816.
- Lu, J.P. (1997), “Elastic properties of single and multilayered nanotubes”, *Journal of the Physics and Chemistry of Solids*, 58(11):pp.1649–1652.
- Lu, X.Z., Teng, J.G., Ye, L.P. and Jiang, J.J. (2005), “Bond-slip models for FRP sheets/plates bonded to concrete”, *Engineering Structures*, 27(6): pp.920-937.
- Ma, P.C., Kim, J.K., and Tang, B.Z. (2006), “Functionalization of carbon nanotubes using a silane coupling agent”, *Carbon*, 44(15):pp.3232-3238.
- Ma, P.C , Kim, J.K, and Tang, B.Z, (2007) “Effects of silane functionalization on the properties of carbon nanotube/epoxy nanocomposites”, *Composites Science and Technology*, 67:pp.2965-2972.
- Mamedov, A.A., Kotov, N.A., Prato, M., Guldi, D.M., Wicksted, J.P. and Hirsch, A. (2002), “Molecular design of strong single-wall carbon nanotube/polyelectrolyte multiplayer composites”, *Nature Materials*, 1:pp.190-194
- Matta, F., Rizzo, P., Karbhari, V. M., and Di Scalea, F.L.(2006), “ Acoustic Emission Damage Assessment of Steel/CFRP Bonds for Rehabilitation”, *Journal of Composites for Construction ASCE*, 10(3):pp. 265-274.

References

- Mikhail, E., Bethel, J., and Chris, J. (2001), “Introduction to Modern Photogrammetry” McGraw-Hill New York; Chichester: Wiley.
- Miller, T.C., Chajes, M.J. , Mertz, D.R. and Hastings, J.N. (2001), “Strengthening of a steel bridge girder using CFRP plates”, Journal of Bridge Engineering ASCE , 6(6):pp.514-522.
- Milne, W.I. , Teo, K.B.K., Amaratunga, G.A.J., Legagneux, P., Gangloff, L., Schnell, J.P., Semet, V., Thien Binh, V., and Groening, O. (2004), “Carbon nanotubes as field emission sources”, Journal of Materials Chemistry, 14(6):pp.933-943.
- Moy, S. (2001) “Practice design and practice guides-frp composites life extension and strengthening of metallic structures” Thomas Telford Publishing, London, UK.
- Mraz, S.J. (2005), “A new buckyball bounces into town”, Machine Design, 77(8):pp.70-74.
- Nadler, M., Mahrholz, T., Riedel, U., Schilde, C., and Kwade, A.(2008), “Preparation of colloidal carbon nanotube dispersions and their characterisation using a disc centrifuge”, Carbon, 46(11):pp.1384 -1392.
- Nhuapeng, W., Thamjaree, W. , Kumfu, S., Singjai, P., and Tunkasiri, T.(2008), “Fabrication and mechanical properties of silicon carbide nanowires/epoxy resin composites”, Current Applied Physics, 8 :pp.295-299.
- Nikolaev, P., Bronikowski, M.J., Bradley, K., Rohmund, F., Colbert, D.T., Smith, K.A., and Smalley, R.E.(1999), “Gas-phase catalytic growth of single-walled carbon nanotubes from carbon monoxide”, Chemical Physics Letters, 313(1-2):pp.91-97.

References

- Niyogi, S. , Hamon, M.A., Perea, D.E., Kang, C.B., Zhao, B., Pal, S.K., Wyant, A.E., Itkis, M.E., and Haddon, R.C. (2003), “Ultrasonic dispersions of single-walled carbon nanotubes”, *Journal of Physical Chemistry:B*, 107(34):pp.8799-8804 .
- O’Connell, M. J., Boul, P., Ericson, L. M., Huffman, C., Wang, Y., Haroz, E., Kuper, C., Tour, J., Ausman, K. D., and Smalley, R. E.(2001), “Reversible water-solubilization of single-walled carbon nanotubes by polymer wrapping”, *Chemical Physics Letters*, 342(3-4), 265-271.
- Park, C. , Ounaies, Z., Watson, K.A., Pawlowski, K., Lowther, S.E., Connell, J.W., Siochi, E.J., Harrison, J.S., and St.Clair, T.L, (2002), “Polymer-single wall carbon nanotube composites for potential spacecraft applications”, *Materials Research Society Symposium – Proceedings*, 706:pp.91-96.
- Park, K.C., Hayashi, T., Tomiyasu, H., Endo, M., and Dresselhaus, M.S.(2005), “Progressive and invasive functionalization of carbon nanotubes sidewalls by diluted nitric acid under supercritical conditions”, *Journal of Materials Chemistry*, 15(3):pp.407-411.
- Peng, J., Binner, J., and Bradshaw, S.(2001), “Microwave initiated self-propagating high temperature synthesis of SiC” , *Journal of Materials Synthesis and Processing*, 9(6):pp.363-368.
- Pham, H. and Al-Mahaidi, R. (2004), “Experimental investigation into flexural retrofitting of reinforced concrete bridge beams using frp composites” , *Composite Structures*, 66 :pp.617-625.

References

- Pham, H. and Al-Mahaidi, R. (2007), “Modelling of CFRP-concrete shear-lap tests”, *International Journal of Construction and Building Materials*, 21(4): pp.727–735.
- Photiou, N.K., Hollaway, L.C., and Chryssanthopoulos, M.K. (2006), “Selection of Carbon-Fiber-Reinforced Polymer Systems for Steelwork Upgrading”, *Journal of Materials in Civil Engineering ASCE* September:pp.641-649.
- Poncharal, P., Wang, Z.L., Ugarte, D., and De Heer, W.A.(1999), “Electrostatic deflections and electromechanical resonances of carbon nanotubes”, *Science*, 283(5407):pp.1513-1516.
- Price, G.J. (2003), “Recent developments in sonochemical polymerisation” , *Ultrason Sonochem*, 10(4-5):pp.277-283.
- Qian, D., Dickey, E.C., Andrews, R., and Rantell, T. (2000), “Load transfer and deformation mechanisms in carbon nanotube-polystyrene composites”, *Applied Physics Letters*, 76(20):pp. 2868-2870.
- Qiu, J., Zhang, C., Wang, B. and Liang, R.(2007), “Carbon nanotube integrated multifunctional multiscale composites”, *Nanotechnology*, 18:pp.275708-275719.
- Rahimi, H. and Hutchinson, A. (2001), “Concrete beams strengthened with externally bonded frp plates” , *Journal of Composites Construction*, 5(1): pp.44–56.
- Ren, Z.F., Huang, Z.P., Xu, J.W., Wang, J.H., Bush, P.; Siegal, M.P., and Provencio, P.N. (1998), “Synthesis of Large Arrays of Well-Aligned Carbon Nanotubes on Glass”, *Science*, 282 (5391): 1105-1107.
- Rinzler, A.G, Liu, J., Dai, H., Nikolaev, P., Huffman, C.B., Rodriguez-Macias, F.J., Boul, P.J., Lu, A.H., Heymann, D., Colbert, D.T., Lee, R.S., Fischer, J.E.,

References

- Rao, A.M., Eklund, P.C., and Smalley, R.E. (1998), "Large-scale purification of single-wall carbon nanotubes: Process, product, and characterization" , *Applied Physics A: Materials Science and Processing*, 67(1):pp.29-37.
- Rizkalla, S., Hassan, T., and Hassan, N. (2003), "Design recommendations for the use of frp for reinforcement and strengthening of concrete structures", *Progress in Structural Engineering and Materials*, 5(1):pp.16-28.
 - Rodgers, R.M., Mahfuz, H. , Rangari, V.K. Chisholm, N., Jeelani, S.(2005), "Infusion of SiC Nanoparticles Into SC-15 Epoxy: An Investigation of Thermal and Mechanical Response", *Macromolecular Materials and Engineering*, 290(5):pp: 423-429.
 - Ruinian, J., David, V., and Kenneth, R., (2008), "Close-range photogrammetry applications in bridge measurement: Literature review", *White Measurement*, 41:pp.823-834.
 - SAA (1991), "Methods for tensile testing of materials" Australian Standard AS1391, Sydney, Standards Association of Australia, Australia.
 - Saito, Y., and Nishikubo, K. (1996), "Radial single-wall carbon tubes growing on surfaces of Pd particles", *Journal of Physics and Chemistry of Solids*, 57(2): pp.243-246.
 - Saito, Y., Nishikubo, K., Kawabata, K., and Matsumoto, T. (1996), "Carbon nanocapsules and single-layered nanotubes produced with platinum-group metals (Ru, Rh, Pd, Os, Ir, Pt) by arc discharge", *Journal of Applied Physics* , 80(5):pp.3062-3067.
 - Salvetat, J.P., Kulik, A.J., Bonard, J.M., Briggs, G.A.D., Stockli, T., Metenier, K., Bonnamy, S., Beguin, F., Burnham, N.A., and Forro, L. (1999), "Elastic modulus

References

- of ordered and disordered multiwalled carbon nanotubes”, *Advanced Materials*, 11(2):pp.161-165.
- Sandler, J.K.W., Shaffer, M.S.P., Prasse, T., Bauhofer, W., Schulte, K., and Windle, A.H. (1999), “Development of a dispersion process for carbon nanotubes in an epoxy matrix and the resulting electrical properties”, *Polymer*, 40(21):pp.5967-5971.
 - Sandler, J.K.W., Kirk, J.E., Kinloch, I.A., Shaffer, M.S.P., and Windle, A.H. (2003), “Ultra-low electrical percolation threshold in carbon–nanotube– epoxy composites”, *Polymer*, 44:pp.5893–5899.
 - Sangermano, M., Borella, E., Priola, A., Messori, M., Taurino, R., and Petra, P.(2008), “Use of Single-Walled Carbon Nanotubes as Reinforcing Fillers in UV-Curable Epoxy Systems”, *Macromolecular Materials and Engineering*, 293(8):pp.708-713.
 - Schadler, L.S., Giannaris, S.C. and Ajayan, P.M.(1998), “Load transfer in carbon nanotube epoxy composites”, *Applied Physics Letters*, 73:pp.3842-3844.
 - Schnerch, D., Stanford, K., Summer, E., and Rizkalla, S. (2004), “Strengthening steel structures and bridges with high modulus carbon fiber reinforced polymers: resin selection and scaled monopole behaviour”, *Transportation Research Record*, 1892:pp.237-245.
 - Schreyer, H.L., Sulsky, D. and Zhou, S.J. (2002), “Modelling delamination as a strong discontinuity with the material point method” *Computer Methods in Applied Mechanics and Engineering*, 191:pp.2483-2507.

References

- Seeger, T., Kohler-Redlich, P., and Ruhle, M. (2000), “Synthesis of Nanometer-Sized SiC Whiskers in the Arc-Discharge”, *Advanced Materials* , 12(4):pp. 279-282.
- Seo, M., Park, S., and Lee, S. (2005), “Influence of atmospheric plasma on physicochemical properties of vapor-grown graphite nanofibers”, *Journal of Colloid Interface Science* , 285(1):pp.306-313.
- Sham, M.L. and Kim, J.K. (2006), “Surface functionalities of multi-wall carbon nanotubes after UV/ozone and TETA treatments”, *Carbon* , 44(4):pp.768-777.
- Shelimov, K.B., Esenaliev, R.O., Rinzler, A.G., Huffman, C.B., and Smalley, R.E.(1998), “Purification of single-wall carbon nanotubes by ultrasonically assisted filtration”, *Chemical Physics Letters*, 282(5-6): pp.429-434.
- Shen, L. and Chen, Z. (2004), “An investigation of the effect of interfacial potentials on the stress transition in thin films” *Modelling and Simulations in Materials Science and Engineering*, 12:pp. 347-369.
- Shen, L. and Chen, Z. (2005), “A silent boundary scheme with the material point method for dynamic analyses”, *Computer Modelling in Engineering and Sciences*, 7:pp. 305-320.
- Shen, G.Z., Bando, Y., Ye, C.H. , Liu, B.D., and Golberg, D.(2006), “Synthesis, characterization and field-emission properties of bamboo-like β -SiC nanowires”, *Nanotechnology*, 17(14):pp.3468-3472.
- Shi, Z., Lian, Y., Liao, F.H., Zhou, X., Gu, Z., Zhang, Y., Iijima, S., Li, H., Yue, K.T., and Zhang, S.L.(2000), “Large scale synthesis of single-wall carbon

References

nanotubes by arc-discharge method” *Journal of Physics and Chemistry of Solids*, 61(7):pp.1031-1036.

- Sika Australia Pty Ltd “Sikadur 30”, Technical data sheet, 33 Fiveways Boulevard, Keysborough, VIC 3175, Australia
- Song, Y. S., and Youn, J. R. (2005), “Influence of dispersion states of carbon nanotubes on physical properties of epoxy nanocomposites”, *Carbon*, 43(7): pp.1378-1385.
- Song, Y.S. (2007), “Multiscale Fiber-Reinforced Composites Prepared by Vacuum-Assisted Resin Transfer Molding” , *Polymer Composites*, 28:pp.458-461.
- Song, Y.S, Oh, H., Jeong, T.T, and Youn, J.R (2008), “A Novel Manufacturing Method for Carbon Nanotube/Aramid Fiber Filled Hybrid Multi-component Composites”, *Advanced Composite Materials*, 17:pp.333-341.
- Sulsky, D., Chen, Z. and Schreyer, H. L. (1994), “A particle method for history-dependent materials”, *Computer Methods in Applied Mechanics and Engineering*, 118: pp.179-196.
- Sulsky, D., Zhou, S. J. and Schreyer, H. L. (1995), “Application of a particle-in-cell method to solid mechanics”, *Computer Physics Communications*, 87:pp.236-252.
- Sulsky, D. and Schreyer, H.L. (1996), “Axisymmetric form of the material point method with application to upsetting and Taylor impact problems”, *Computer Methods in Applied Mechanics and Engineering*, 139 :pp.409-429.

References

- Tao, K., Yang, S., Grunlan, J., C., Kim, Y.S., Dang, B., Deng, Y., Thomas, R.L., Wilson, B.L., and Wei, X.(2006), “Effects of Carbon Nanotube Fillers on the Curing Processes of Epoxy Resin-Based Composites”, *Journal of Applied Polymer Science*, 102:pp.5248-5254.
- Tavakkolizadeh, M. and Saadatmanesh, H. (2003), “Fatigue strength of steel girders strengthened with carbon fibre reinforced polymer patch”, *Journal of Structural Engineering ASCE*, 129(2):pp.186-196.
- Teng, J.G., Chen, J.F., Smith, S.T. and Lam, L. (2002), “FRP strengthened RC structures”, John Willey & Sons Ltd, West Sussex, UK
- Teng, J.G. and Lam, L. (2004), “Behaviour and modelling of fibre reinforced polymer-confined concrete”, *Journal of Structural Engineering*, 130(11):pp.1713-1723.
- Teng, J.G., and Hu, Y.M. (2007), “Behaviour of FRP-jacketed circular steel tubes and cylindrical shells under axial compression”, *Construction and Building Materials, Composites in Civil Engineering*, 21(4), pp. 827-838
- Thostenson, E.T., and Chou, T.W.(2002), “Aligned multi-walled carbon nanotube-reinforced composites: processing and mechanical characterization”, *Journal of Physics D: Applied Physics*, 35: pp.77-80.
- Thostenson, E.T., and Chou, T.W. (2006-A), “Carbon nanotube network: sensing of distributed strain and damage for life prediction and self healing”, *Advanced Materials*, 18(21):pp.2837-2841.
- Thostenson, E.T., and Chou, T.W. (2006-B), “Processing-structure-multi-functional property relationship in carbon nanotube/epoxy composites”, *Carbon*, 44(14):pp.3022-3029.

References

- Treacy, M.M.J., Ebbesen, T.W., and Gibson, T.M. (1996), “Exceptionally high Young’s modulus observed for individual carbon nanotubes”, *Nature* , 381:680-687.
- Vasconcelos, P.V., Lino, F.J., Magalhaes, A., and Neto, R.J.L. (2005), “Impact fracture study of epoxy-based composites with aluminium particles and milled fibres”, *Journal of Materials Processing Technology*, 170(1-2):pp.277-283.
- Vigolo, B., Penicaud, A., Coulon, C., Sauder, C., Pailler, R., Journet, C., Bernier, P. and Poulin, P. (2000), “Macroscopic fibres and ribbons of oriented carbon nanotubes” , *Science*, 290(5495):pp.1331-1334.
- Visco, A. , Calabrese, L., and Milone, C.(2009), “Cure Rate and Mechanical Properties of a DGEBA Epoxy Resin Modified with Carbon Nanotubes” , *Journal of Reinforced Plastics and Composites* , 28:pp. 937-949.
- Walters, D.A., Ericson, L.M., Casavant, M.J., Liu, J., Colbert, D.T., Smith, K.A., and Smalley, R.E. (1999), “Elastic strain of freely suspended single-wall carbon nanotube ropes”, *Applied Physics Letters*, 74(25):pp.3803-3805.
- Wang, Z., Liang, Z., Wang, B., Zhang, C. and Kramer, L. (2004), “Processing and Property Investigation of Single-walled Carbon Nanotube (SWNT) Buckypaper/Epoxy Resin Matrix Nanocomposites”, *Composites:Part A*, 35(10): pp.1225-1232.
- Wang, Q., Dai, J., Li, W., Wei, Z., and Jiang, J. (2008), “The effects of CNT alignment on electrical conductivity and mechanical properties of SWNT/epoxy nanocomposites”, *Composites Science and Technology* , 68:pp.1644-1648.

References

- Wang, S., and Qui, J.(2009), “Modification of Epoxy Resins via m-chloroperbenzoic Acid-Epoxidized Carbon Nanotubes”, *Journal of Applied Polymer Science*, 112:pp. 3322-3326.
- Wichmann, M.H.G, Sumfleth, J., Gojny, F.H., Quaresimin, M., Fiedler, B., and Schulte, K.(2006), “Glass-fibre-reinforced composites with enhanced mechanical and electrical properties – benefits and limitations of a nanoparticle modified matrix”, *Engineering Fracture Mechanics*, 73(16):pp.2346-2359.
- Wong, E.W., Sheehan, P.E., and Lieber, C.M. (1997), “Nanobeam mechanics: elasticity, strength, and toughness of nanorods and nanotubes”, *Science*, 277:pp.1971-1975.
- Wu, Z., Yin, J., and Asakura, T. (1998), “Fracture response simulation of FRP-reinforced concrete beams by mixed finite elements”, *Journal of Applied Mechanics*, 1(8):pp.337-344.
- Xia, S.H., and Teng, J.G. (2005), “Behaviour of FRP-to-steel bonded joints”, *Proceedings of the International Symposium on Bond Behaviour of FRP in Structures*, Hong Kong, China, December.
- Xian, G.J., Walter, R., and Hauptert, F. (2006), “Friction and wear of epoxy/TiO₂ nanocomposites: Influence of additional short carbon fibers, Aramid and PTFE particles”, *Composites Science and Technology*, 66(16):pp.3199-3209.
- Xie, S., Li, W., Pan, Z., Chang, B., and Sun, L. (2000), “Mechanical and physical properties of carbon nanotube”, *Journal of Physics and Chemistry of Solids*, 61(7):pp.1153-1158.

References

- Yang, K., Yang, Y., Lin, Z.M., Li, J.T. and Du, J.S. (2007-A), “Mechanical-activation assisted combustion synthesis of SiC powders with polytetrafluoroethylene as promoter”, *Materials Research Bulletin*, 42(9):pp.1625-1632.
- Yang, Y., Yang, K., Lin, Z.M. and Li, J.T. (2007-B), “Mechanical-activation-assisted combustion synthesis of SiC”, *Materials Letters*, 67(3):pp.671–676.
- Yao, Z., Kane, C. L., and Dekker, C. (2000), “High-Field Electrical Transport in Single-Wall Carbon Nanotubes”, *Physical Review Letters* , 84(13):pp.2941- 2944.
- Yasmin, A., Abot, J.L. and Daniel, I.M. (2003), “Processing of clay/epoxy nanocomposites by shear mixing”, *Scripta Materialia*, 49:pp.81–86.
- Yasmin, A., Luo, J.J., Abot, J.L. and Daniel, I.M. (2006), “Mechanical and thermal behavior of clay/epoxy nanocomposites”, *Composites Science and Technology*, 66:pp. 2415-2422.
- Yin, J., and Wu, Z. (2001), “Simulations on crack distribution in FRP-strengthened concrete beams with interfacial fictitious crack model”, *Proceedings of the Fourth International Conference of Fracture Mechanics of Concrete and Concrete Structure*, France
- Yokozeki, T., Iwahori, Y. and Ishiwata, S. (2007), “Matrix cracking behaviors in carbon fibre/epoxy laminates filled with cup-stacked carbon nanotubes (CSCNTs)”, *Composites Part:A*, 38(3):pp.917-924.
- Yong, V., and Hahn, H.T. (2004), “Processing and properties of SiC/vinylester nanocomposites”, *Nanotechnology*, 15:pp.1338–1343.

References

- York, I.I. , Allen, R. , Sulsky, D., and Schreyer, H.L. (1999), “The material point method for simulation of thin membrane” *International Journal for Numerical Methods in Engineering*, 44:pp.1429-1456.
- Yu, M.F, Lourie, O., Dyer, M.J., Moloni, K., Kelly, T.F., Ruoff, R.S.(2000-A), “Strength and Breaking Mechanism of Multiwalled Carbon Nanotubes Under Tensile Load”, *Science*, 287:pp.637-640.
- Yu, M.F., Files, B.S., Arepalli, S., and Ruoff, R.S.(2000-B), “Tensile loading of ropes of single wall carbon nanotubes and their mechanical properties”, *Physical Review Letters*, 84(24):pp.5552-5555.
- Yuan, H., Teng, J.G., Seracino, R., Wu, Z.S. and Yao, J. (2004), “Full-range behaviour of FRP-to-concrete bonded joints”, *Engineering Structures*, 26(5): pp.553-565.
- Zhang, Y., and Iijima, S. (1999), “Formation of single-wall carbon nanotubes by laser ablation of fullerenes at low temperatures”, *Applied Physics Letters* , 75(20):pp.3087-3089.
- Zhang, M., Yudasaka, M., Koshio, A., and Iijima, S. (2001) , “Effect of polymer and solvent on purification and cutting of single-wall carbon nanotubes”, *Chemical Physics Letters* , 349(1-2):pp.25-30.
- Zhang, F.H., Wang, R.G. , He, X.D. , Wang, C., and Ren, L.N. (2009) , “Interfacial shearing strength and reinforcing mechanisms of an epoxy composite reinforced using a carbon nanotube/carbon fiber hybrid”, *Journal of Materials Science*, 44(13):pp.3574-3577.

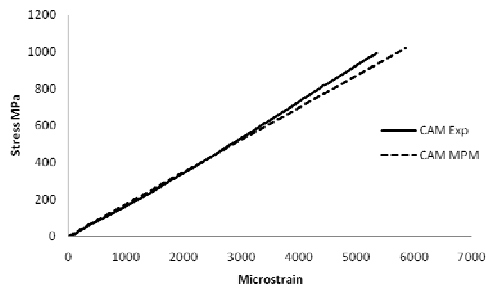
References

- Zheng, L.X., O'Connell, M.J., Doorn, S.K., Liao X.Z., Zhao Y.H., Akhadov E.A., Hoffbauer, M.A., Roop, B.J., Jia, Q.X., Dye, R.C., Peterson, D.E., Huang, S.M., Liu, J., and Zhu, Y.T. (2004), "Ultralong single-wall carbon nanotubes" , *Nature Materials*, 3:pp.673-676.
- Zhou, S.J., Stormont, J., and Chen, Z. (1999), "Simulation of geomembrane response to subsidence by using the material point method", *International Journal for Numerical and Analytical Methods in Geomechanics*, 23:pp.1977-1994.
- Zhou, T., Gu, M., Jin, Y., and Wang, J. (2005), "Effects of nano-sized carborundum particles and amino silane coupling agent on the cure reaction kinetics of DGEBA/EMI-2, 4 system" , *Polymer*, 46:pp.6216-6225.
- Zhou, Y., Pervin, F., Lewis, L., and Jeelani, S. (2007), "Experimental study on the thermal and mechanical properties of multi-walled carbon nanotube-reinforced epoxy", *Materials Science and Engineering-A*, 452–453:pp.657-664.
- Zhou, Y., Jeelani, M.I. and Jeelani, S.(2009), "Development of photo micro-graph method to characterize dispersion of CNT in epoxy", *Materials Science and Engineering A*, 506:pp.39–44.
- Zhu, J., Peng, H., Rodriguez-Macias, F., Margrave, J.L., Khabashesku, V.N., and Imam A.M. (2004), "Reinforcing epoxy polymer composites through covalent integration of functionalized nanotubes", *Advanced Functional Materials*, 14(7):pp.643-648.
- Zhu, J., Kim, J., Peng, H., Margrave, J.L., Khabashesku, V.N., and Barrera, E.V. (2003), "Improving the dispersion and integration of single-walled carbon

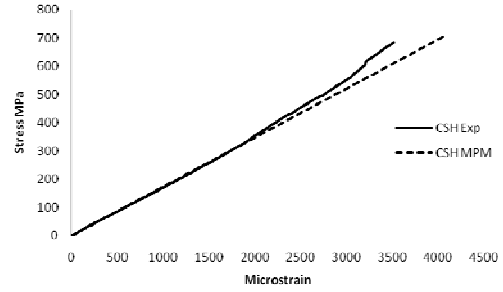
References

nanotubes in epoxy composites through functionalization.” *Nano Letters* ,
3(8):pp.1107-1113.

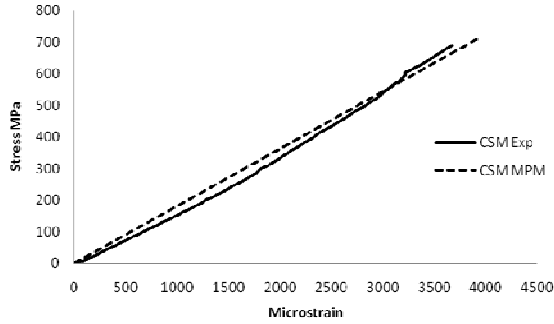
- Zou , W., Du, Z., Liu, Y.X, Yang, X., Li, H.Q., and Zhang, C. (2008),
“Functionalization of MWNTs using polyacryloyl chloride and the properties of
CNT–epoxy matrix nanocomposites”, *Composites Science and Technology*, 68
:pp.3259-3264.



(a)CFRP-Araldite mechanical mix

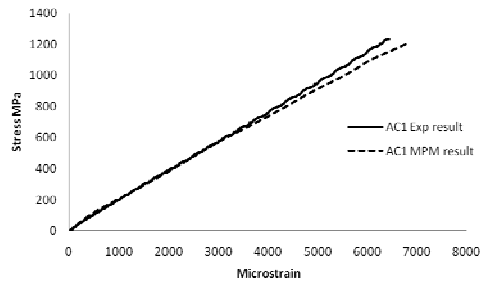


(b)CFRP-Sikadur hand mix

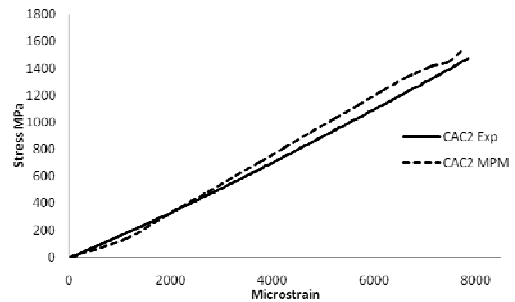


(c) CFRP-Sikadur mechanical mix

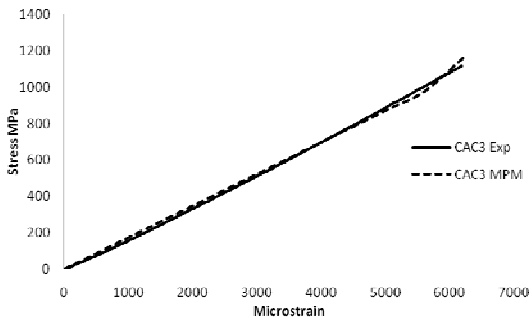
Figure A-1 MPM specimens compared with experimental results for hand and sonicated pure mixed epoxies.



(a) CFRP-Araldite+1% MWCNT

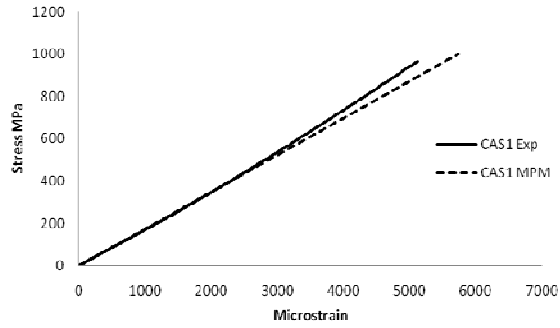


(b) CFRP-Araldite+2% MWCNT

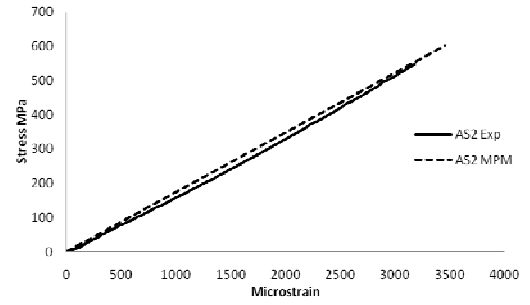


(c)CFRP-Araldite+3% MWCNT

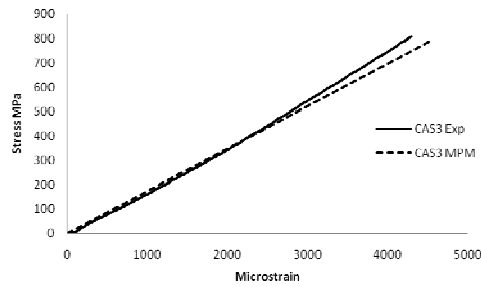
Figure A-2 MPM specimens compared with experimental results for Araldite-MWCNT samples



(a) CFRP-Araldite+1% SiC

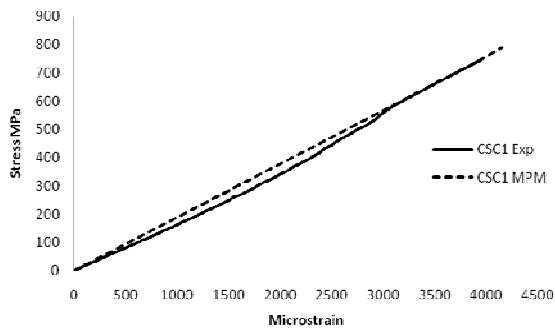


(b) CFRP-Araldite+2% SiC

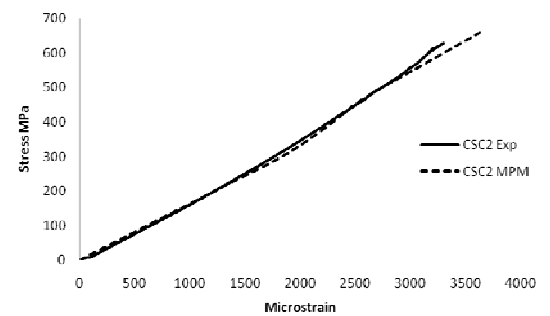


(c) CFRP-Araldite+3% SiC

Figure A-3 MPM specimens compared with experimental results for Araldite-SiC samples



(a) CFRP-Sikadur+1% MWCNT



(b) CFRP-Sikadur+2% MWCNT

Figure A-4 MPM specimens compared with experimental results for Sikadur-MWCNT samples

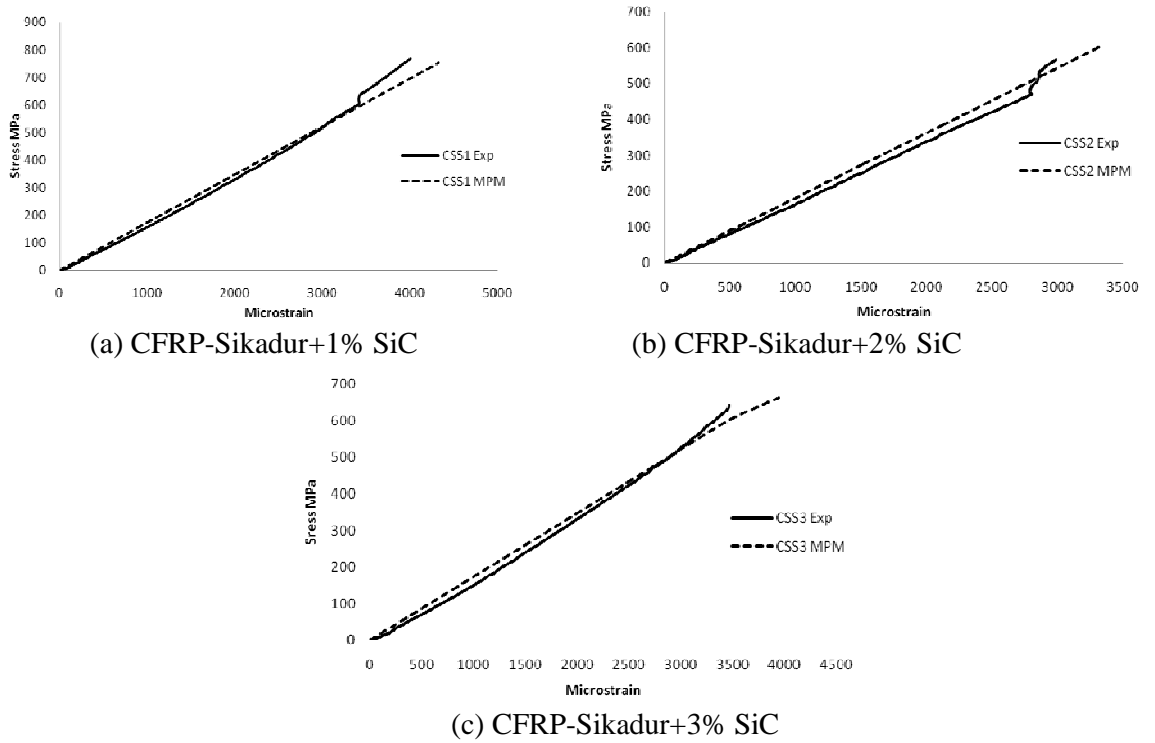


Figure A-5 MPM specimens compared with experimental results for Sikadur-SiC samples

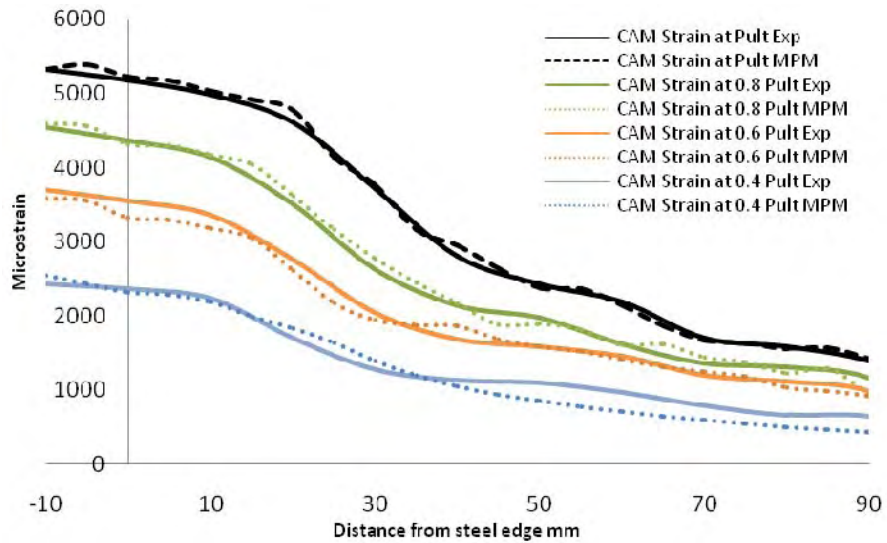


Figure A-6 MPM-experimental strain distribution on CFRP surface along bonding length for CFRP-mechanical mixed Araldite

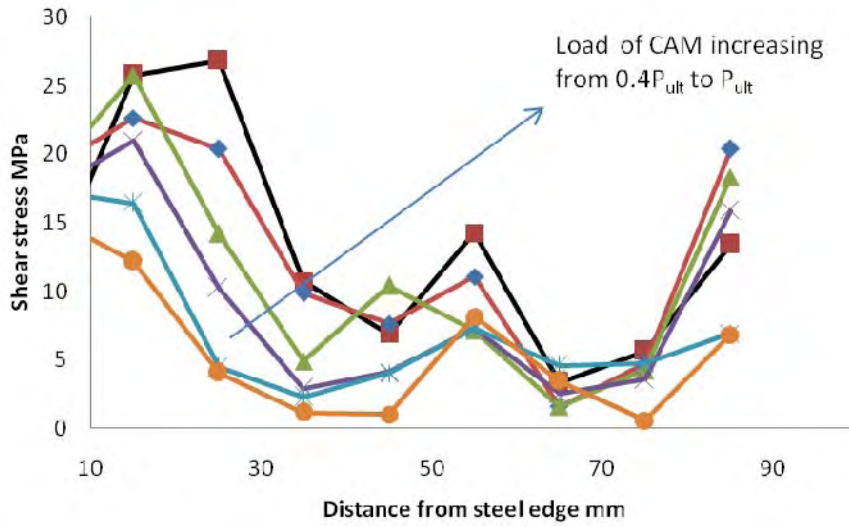


Figure A-7 Shear stress distribution along CFRP bond length of Araldite-420 sonication mixed specimen

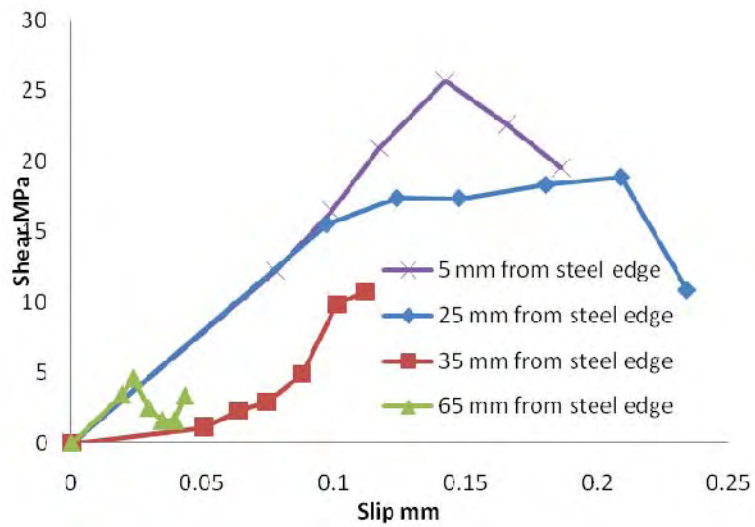


Figure A-8 Bond-slip plot of Araldite-420 sonication mixed specimen

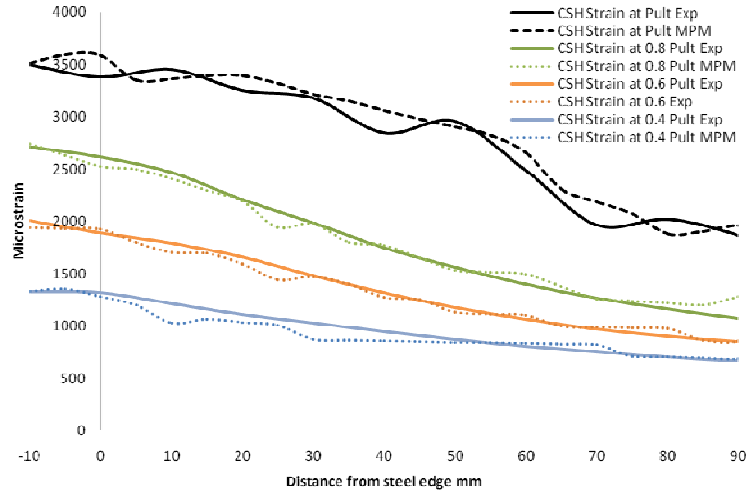


Figure A-9 MPM-experimental strain distribution on CFRP surface along bonding length for CFRP-hand mixed Sikadur

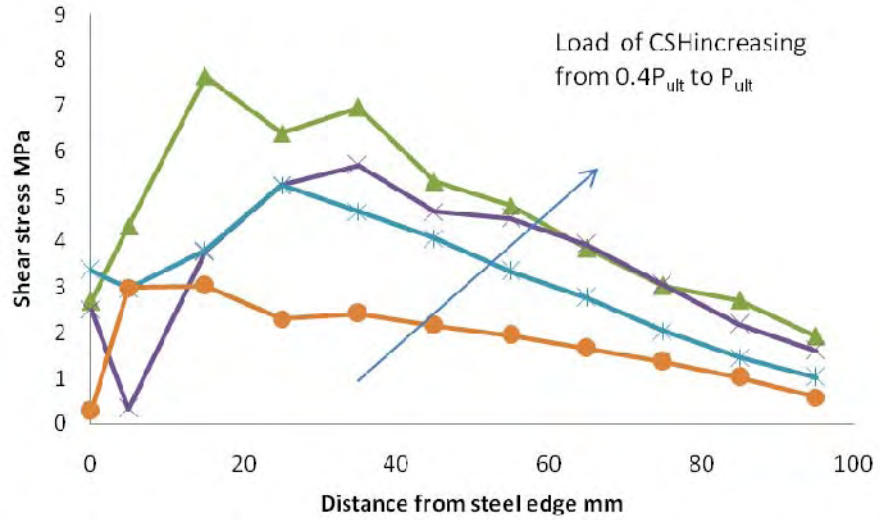


Figure A-10 Shear stress distribution along CFRP bond length of hand mixed Sikadur specimen

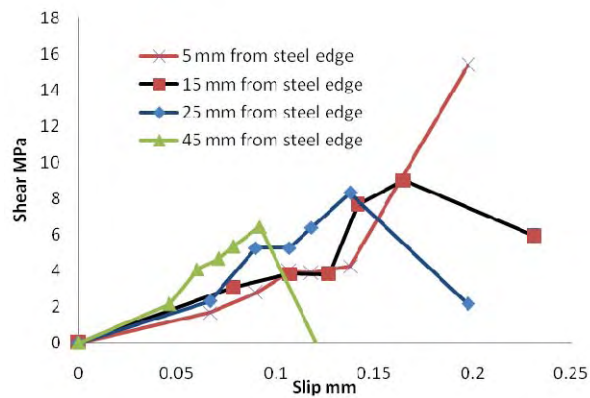


Figure A-11 Bond-slip plot of hand mixed Sikadur specimen

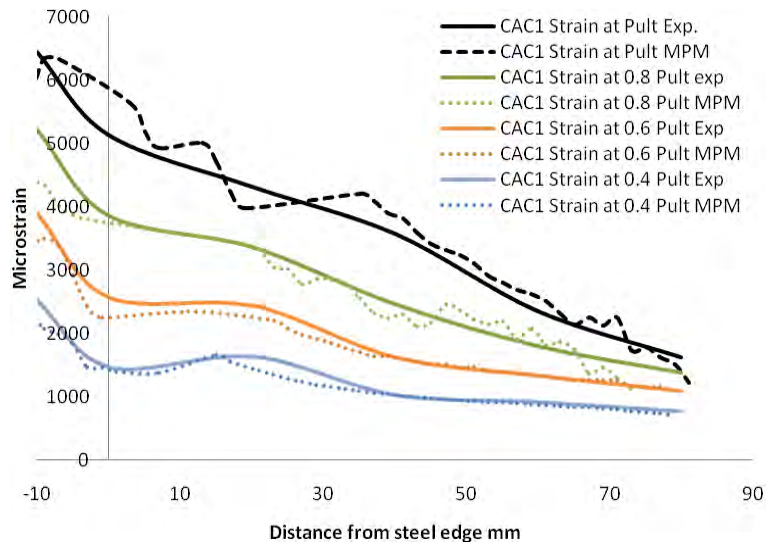


Figure A-12 Compared MPM-experimental strain distribution on CFRP surface along bonding length for CFRP-Araldite+1%MWCNT

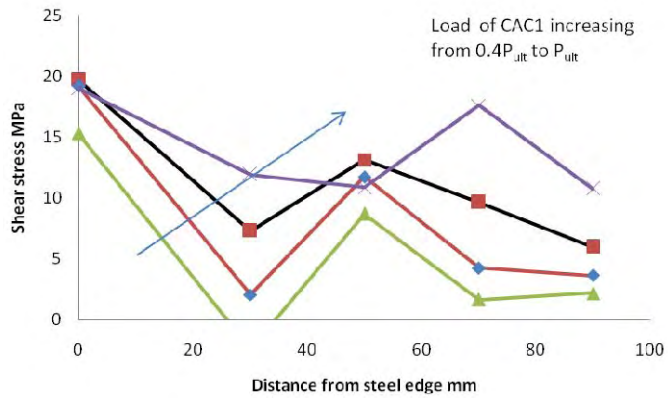


Figure A-13 Shear stress distribution along CFRP bond length of Araldite+1%MWCNT specimen

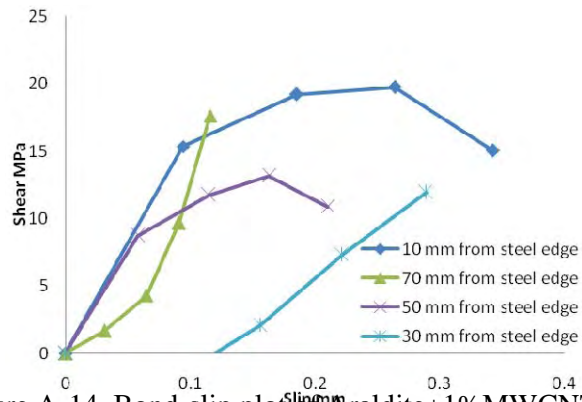


Figure A-14 Bond-slip plot of Araldite+1%MWCNT specimen

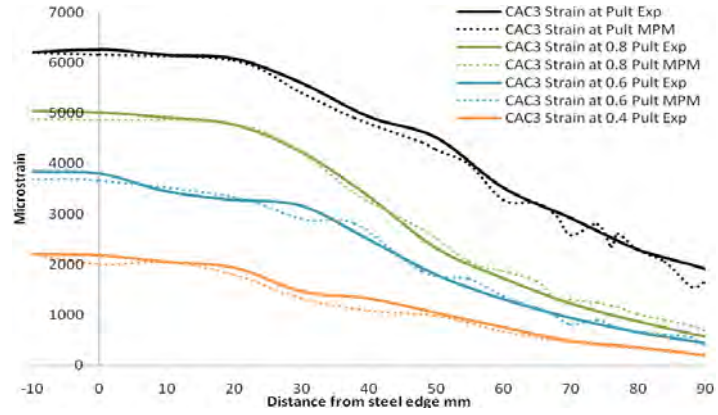


Figure A-15 Compared MPM-experimental strain distribution on CFRP surface along bonding length for CFRP-Araldite+3%MWCNT

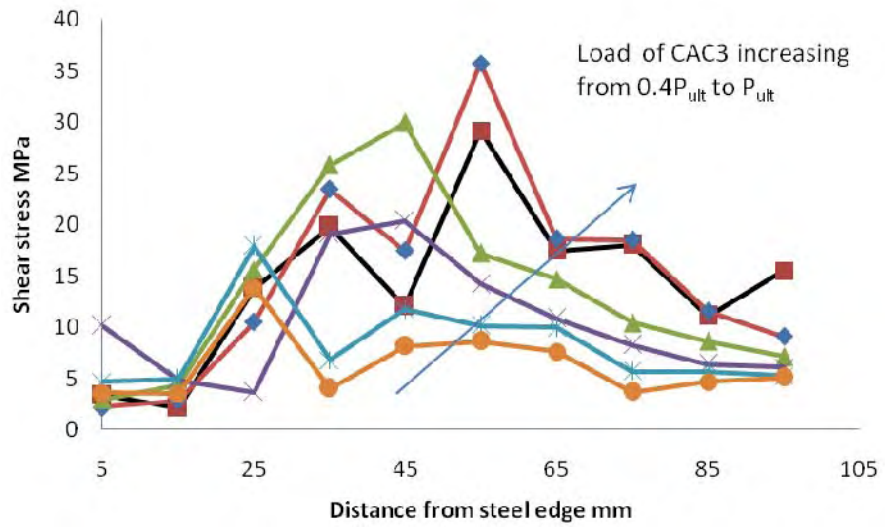


Figure A-16 Shear stress distribution along CFRP bond length of Araldite+3%MWCNT specimen

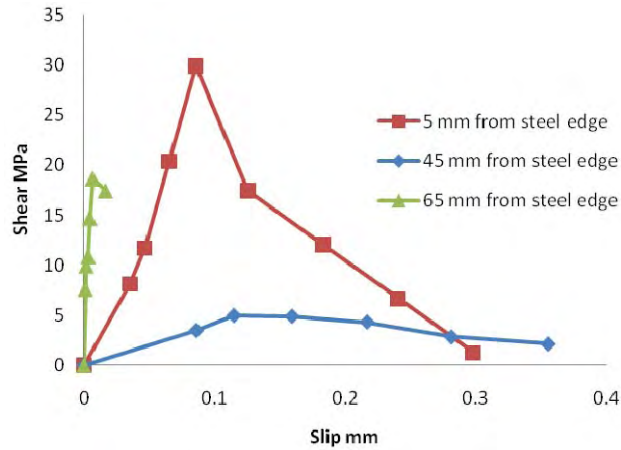


Figure A-17 Bond-slip plot of Araldite+3%MWCNT specimen

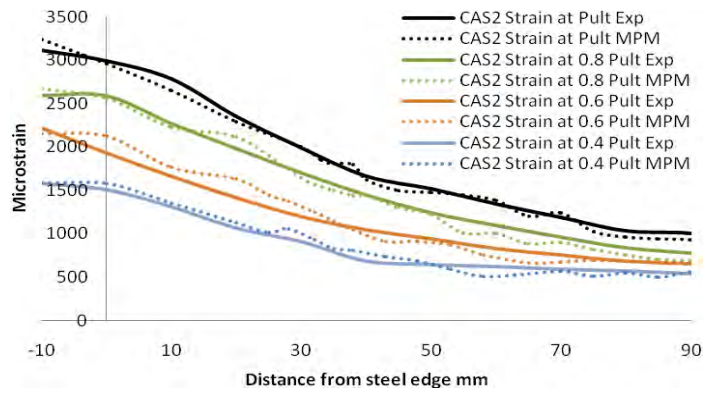


Figure A-18 Compared MPM-experimental strain distribution on CFRP surface along bonding length for CFRP-Araldite+2%SiC

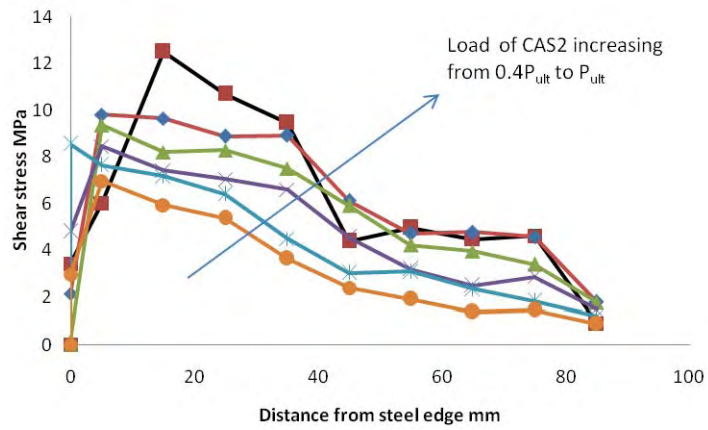


Figure A-19 Shear stress distribution along CFRP bond length of Araldite++2%SiC specimen

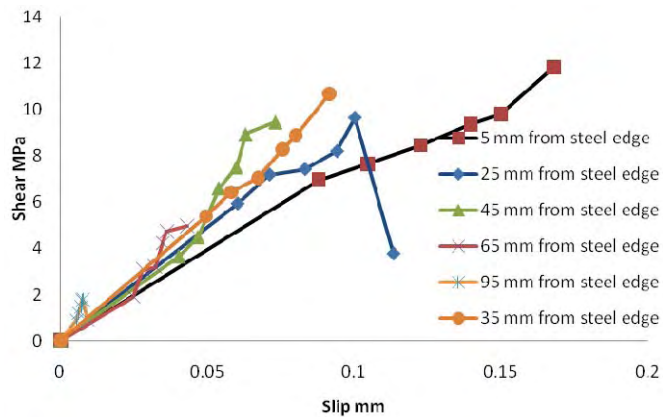


Figure A-20 Bond-slip plot of Araldite+2%SiC specimen

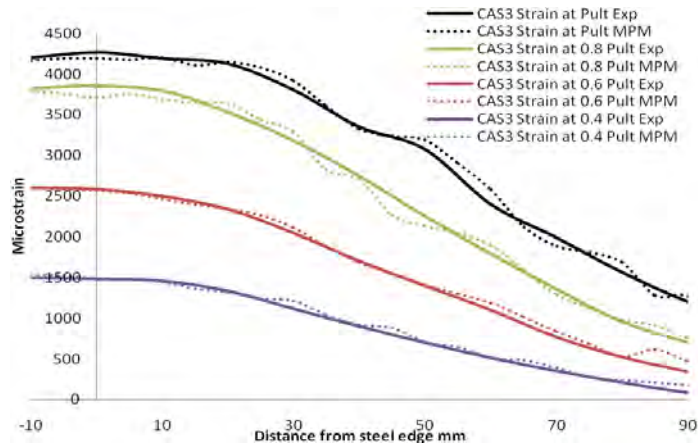


Figure A-21 MPM-experimental strain distribution on CFRP surface along bonding length for CFRP-Araldite+3%SiC

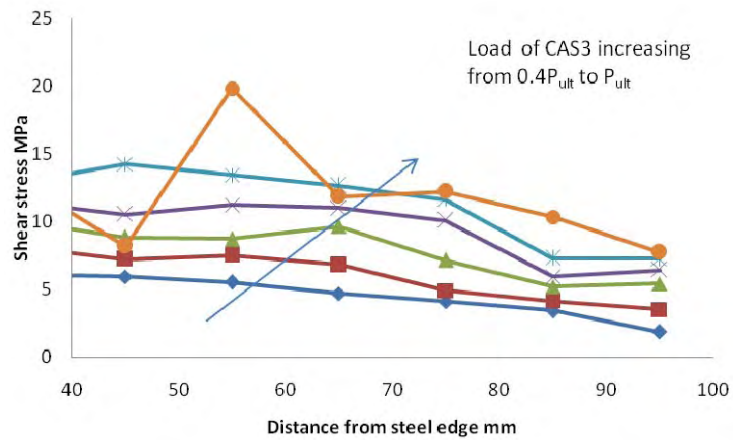


Figure A-22 Shear stress distribution along CFRP bond length of Araldite+3%SiC specimen

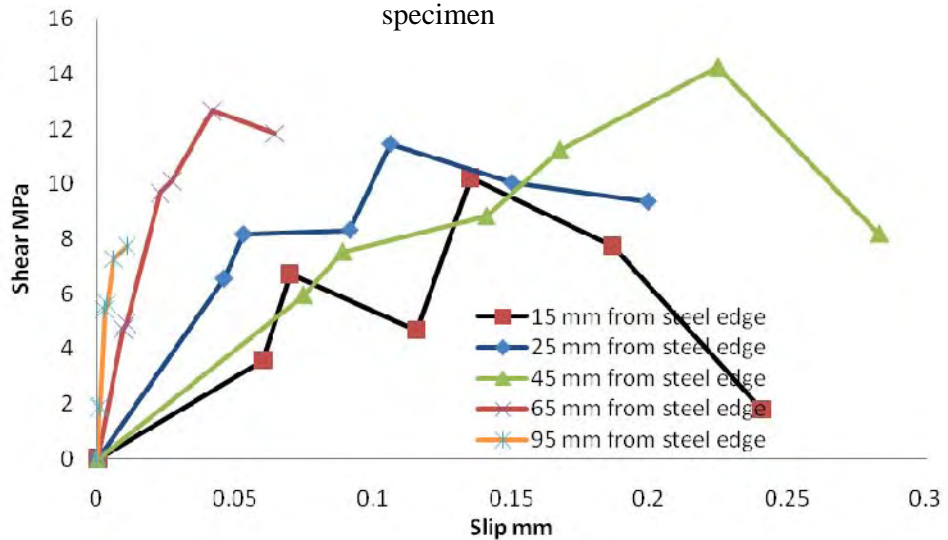


Figure A-23 Bond-slip plot of Araldite+3%SiC specimen

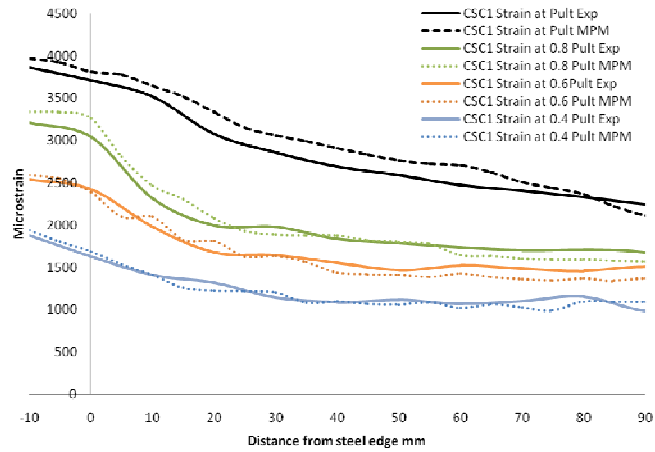


Figure A-24 MPM-experimental strain distribution on CFRP surface along bonding length for CFRP-Sikadur+2%MWCNT

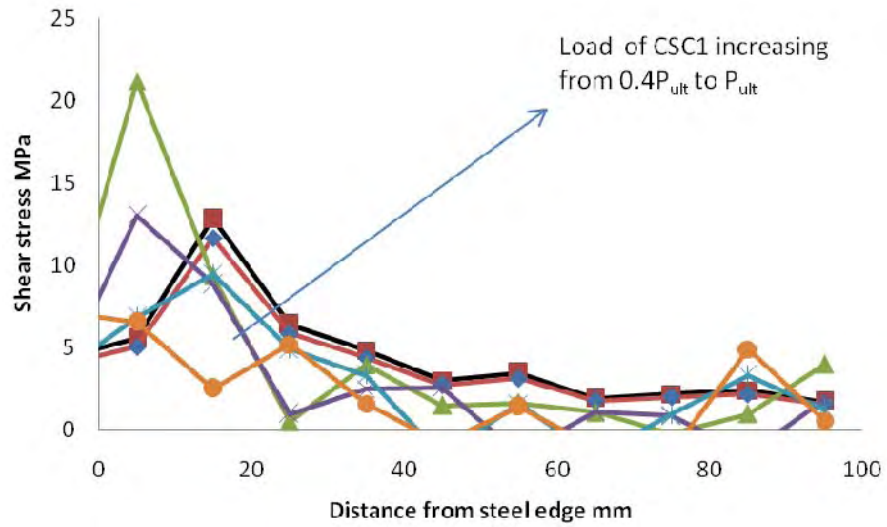


Figure A-25 Shear stress distribution along CFRP bond length of Sikadur+2%MWCNT specimen

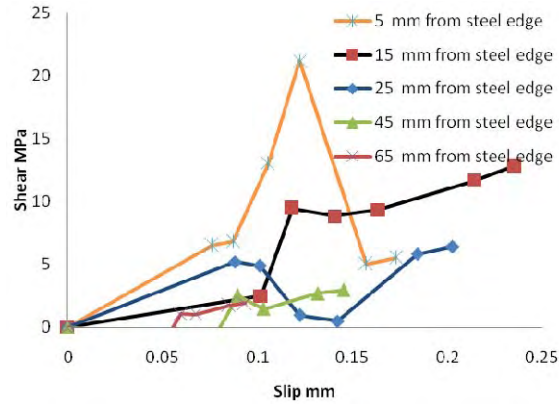


Figure A-26 Bond-slip plot of Sikadur+2%MWCNT specimen

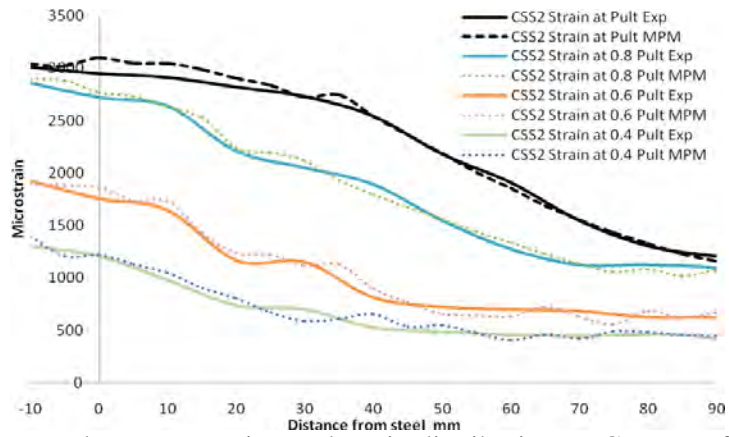


Figure A-27 Compared MPM-experimental strain distribution on CFRP surface along bonding length for CFRP-Sikadur+2%SiC

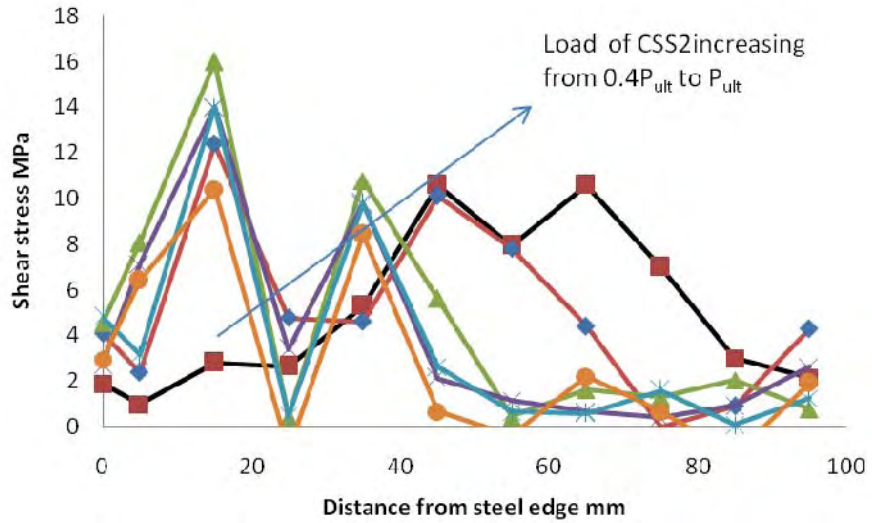


Figure A-28 Shear stress distribution along CFRP bond length of Sikadur+2%SiC specimen

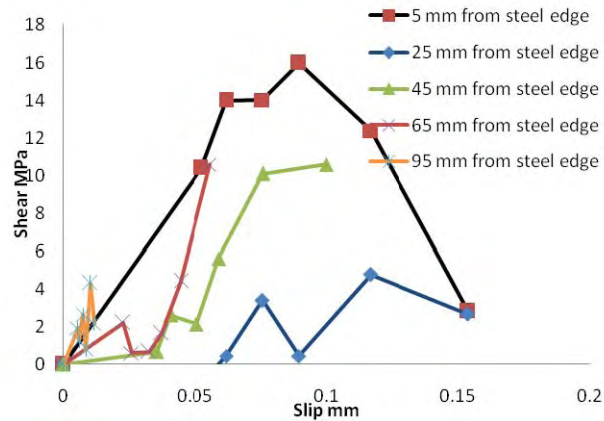


Figure A-29 Bond-slip plot of Sikadur+2%SiC specimen

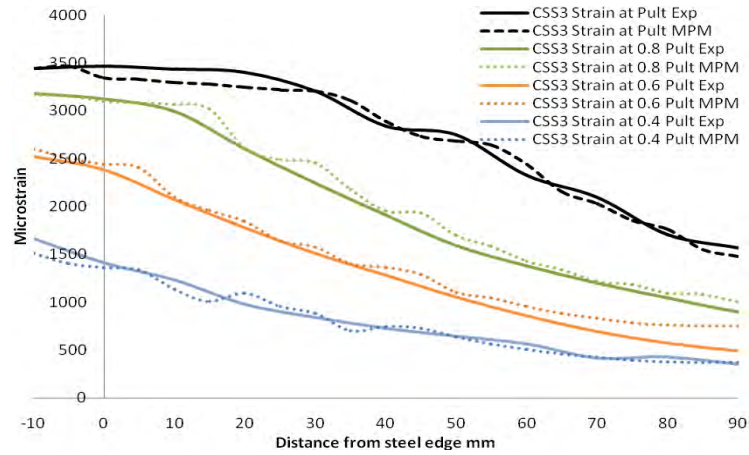


Figure A-30 Compared MPM-experimental strain distribution on CFRP surface along bonding length for CFRP-Sikadur+3%SiC

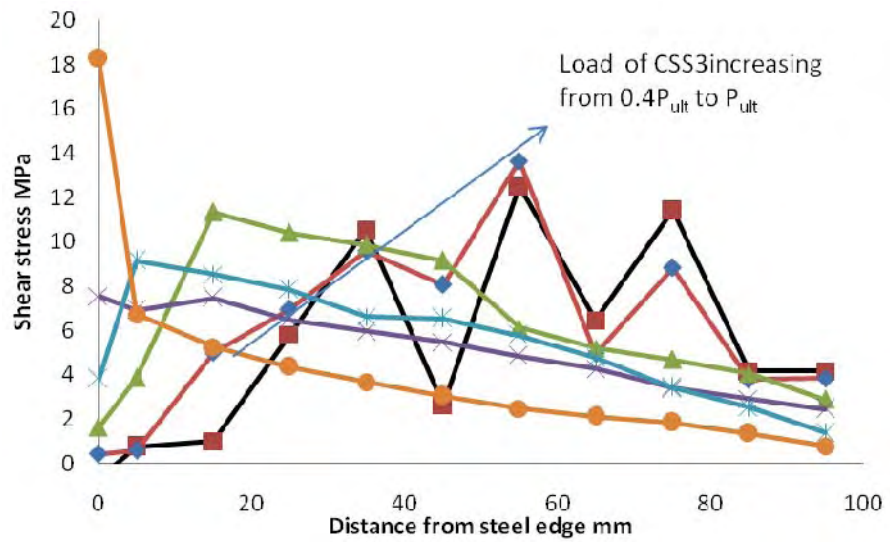


Figure A-31 Shear stress distribution along CFRP bond length of Sikadur+3%SiC specimen

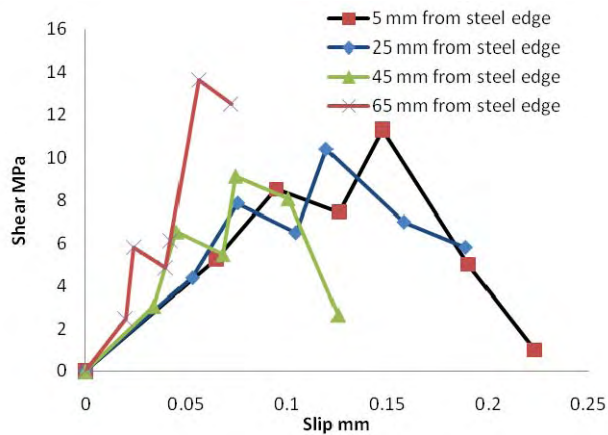


Figure A-32 Bond-slip plot of Sikadur+3%SiC specimen